# Quantitative, Non-Contrast MRI to Improve the Diagnosis of Breast Cancer


Isobel Gordon

New College

University of Oxford

A thesis submitted for the degree of

*Doctor of Philosophy*

Trinity 2025

# Acknowledgements

I would like to begin by thanking my wonderful supervisors, Professor Sir Michael Brady and Professor Sally Collins. Mike - it has been a privilege to be guided by your encyclopedic knowledge of MRI, breast cancer, and life. Thank you offering up your valuable time so freely and for your faith in me from the very beginning, without which this would not have been possible. Sally - thank you for your tireless championing of this project and for continually reminding me of the bigger picture. Thank you for your humour and enthusiasm, and for believing in me even when I didn't. I am sincerely grateful to you both for helping me to grow as a researcher and as a person, and I look forward to our continuing friendship.

I am indebted to the Royal Commission for the Exhibition of 1851, who awarded me an Industrial Fellowship to complete these doctoral studies. Their support enabled the dissemination of this research across three continents and even to HRH The Princess Royal. I am sincerely thankful for the many opportunities they have provided, and am grateful to always remain a member of the 1851 family.

I am deeply grateful to Perspectum Ltd. for their support in making this DPhil financially possible. Thank you especially to Dr. Rajarshi Banerjee for supporting my professional growth over the last eight years and to Dr. Paul Aljabar for his invaluable guidance throughout this project. I would also like to thank Dr. Matt Robson for introducing me to the fascinating world of MRI, and Dr. Michael Gyngell for his mentorship throughout the years.

I would like to thank the Nuffield Department of Women's and Reproductive Health for facilitating my studies and for the valuable feedback at symposiums over the years. I am proud to have been a part of a such an innovative and impactful department.

Thank you to the International Society for Magnetic Resonance in Medicine (ISMRM), the British Society of Breast Radiology (BSBR), and the Medical Image Understanding and Analysis conference (MIUA) for allowing me to present at their meetings. Thank you to ISMRM for the stipends which helped me to attend in person. Thank you to the Oxford Science and Ideas Festival and Oxford Pink Week for allowing me to talk directly with those affected by breast cancer, and to remember what this is really all about.

I am very grateful to Professor Sarah Vinnicombe, Dr. Richard Sidebottom,

Professor Iain Lyburn, and Dr. Amy Clare O'Brien for sharing their clinical expertise, and to Professor Gene Kim and Professor Pippa Storey for providing spectral data. I am also grateful to Dr. Keith A. Gillow, Dr. Sam Evans, and Dr. John McManigle for developing the "Oxford Thesis" LaTeX template which was used to typeset this document.

Thank you to all the teams at the sites taking part in the IMOGEN study. A sincere thank you must also go to all the volunteers and study participants who selflessly gave up their time to be involved in this research; without you, this work would not be possible.

I am very grateful for the support of my wonderful colleagues at Perspectum. I would particularly like to thank Dr. Amy Herlihy, Dr. George Ralli, Dr. Carolina Fernandes, and Dr. Alexandre Triay Bagur for offering up their time and expertise to support this research. Thank you for sharing ideas, code, and coffee with me and for putting up with my persistent questioning over the last few years. Thank you to Gemma Greenall, Bryn Horsington, and Sophie Bradshaw for your patience in teaching me the ways of clinical trial management and to all at Perspectum involved with the IMOGEN and RADIUS studies. Thank you to the brilliant Haley Fig, who generously provided many of the illustrations in this thesis, and to everyone in the Women's Health team over the years for your passion and encouragement. Thank you to Dr. Roberto Salvati, Dr. Adrienne Siu, Muddabir Zaidi, Anna Leung, and Mary Jean Solywoda for your help both on and off the scanner. Thank you also to Dr. John McGonigle and Dr. Markus Henningson for your insights and advice. Finally, thank you to everyone in the Imaging Science team for your invaluable feedback on this work, and for your patience whilst I determine my choice of meal deal from Tesco.

On a personal note, I would like to thank my wonderful friends, without whom I would be totally lost, and probably a lot more boring. Thank you to Will, Tamsin, Liora, Eleanor, and Lucy for your unwavering friendship and support over the last eleven years. Thank you to Katie, Alex, and Amy B-R for proving that fate does in fact exist. Thank you to Ariadne, Iris, Katherine, and Claudia, who I am so grateful to have met through these studies. A special thank you must go to Amy W for making life in the Big Flat so fun and for looking after me during particularly stressful times. Thank you to Allie for our many library sessions and our lunch breaks amongst the dinosaurs, and to James K for your friendship at ISMRMs. Thank you to the Manchester lot, and to Anna, Alice, and Embla for your continued camaraderie over the years. Finally, thank you to Kilda, James O, Julian, Zoulikha,

Ella, Suzy, Liz, and the many housemates who helped to make a house and its inflatable hot tub a home.

I am very grateful to have had such a wonderful family to support me during my DPhil. Firstly, thank you to my amazing dog Rudy, who I relied upon to get through these studies. Thank you for reminding me that persistence pays off by refusing to take "no" for an answer when requesting extra Bonios. Thank you to my brother, Rory, for our shared silliness and for reminding me that there are more stressful jobs out there, like those which involve handling venomous snakes. Thank you to my grandma, Ann Park, for your unwavering support for as long as I can remember, and to my granny, Ellen Gordon, whose career encouraged my interest in medical physics. Thank you to my grandfathers, Alan Park and Ronald Gordon, who I hope I have made proud. Finally, I am deeply grateful to my parents, Cathy and Phil Gordon, for championing every choice I ever have made in life but for prioritising my happiness above all else. Your generosity, humour, and kindness inspire me every day; I simply could not have asked for a better Mum and Dad.

Finally, I would like to thank my partner, Marcus, for his endless emotional and culinary support, and for proofreading this thesis. Thank you for making me laugh when I need it the most and for reminding me that you *know* I can do it. I am so grateful to have shared this journey with you.

Thank you all so much.

This thesis is dedicated to my parents

**Catherine Anne Gordon** and **Philip Henry Thomas Gordon**

and to the loving memory of

**Alan McBride Park**

# Abstract

Magnetic resonance imaging (MRI) is the most sensitive imaging modality for breast cancer diagnosis, but clinical protocols rely upon contrast injection, uncomfortable prone positioning, and qualitative image interpretation. Such protocols primarily identify tumours from increased neovascularity, which is only one manifestation of pathology.

This thesis addresses these limitations by developing non-contrast, quantitative MRI methodologies to characterise the breast. We focus on two biomarkers derived from chemical-shift-encoded MRI (CSE-MRI), proton density fat fraction (PDFF) and $T_2^*$. We particularly investigate their utility in characterising breast adipose tissue, which is increasingly recognised as a complex endocrine organ implicated in breast cancer. We also assess the feasibility of supine breast MRI through evaluation of a specialised support device, the "MR Bra".

The first two chapters provide necessary context, introducing breast disease, clinical imaging techniques, and essential MRI physics.

Chapters 3–5 then strive to determine the optimal implementation of CSE-MRI in the breast. First, *in silico* and *in vitro* analyses demonstrate the suitability of the two pulse sequences employed, showing accurate $T_2^*$ quantification and minimal $T_1$-related bias in PDFF at typical breast tissue values. Second, we present the first implementation of breast-specific fat spectra in CSE-MRI. We demonstrate improved map quality over alternative spectra, and show that a commonly employed subcutaneous fat spectrum produces significantly more fat-water swaps in breast adipose tissue. Finally, a hybrid-based post-processing algorithm and IDEAL-IQ outperform a magnitude-based algorithm, reducing fat-water swaps from 2.9% to $\leq 0.2\%$.

Chapters 6–9 explore applications of PDFF and $T_2^*$ in the breast. First, PDFF is evaluated in the quantification of breast density, a well-established breast cancer risk factor. Through developing five specialised phantoms, we demonstrate that PDFF-derived breast density is more accurate than conventional voxel classification-based techniques. *In vivo*, PDFF-derived density correlates strongly with BI-RADS® density category (R = 0.76), and distinguishes well between "fatty" and "dense" breasts (AUC = 0.89). Combining PDFF-derived density with a grey level co-occurrence matrix-based contrast metric further improves classification performance.

Second, we investigate PDFF as a marker of adipocyte hypertrophy, an indicator of adipose tissue quality linked to breast cancer. Breast adipose tissue PDFF correlates strongly with BMI (R = 0.70), suggesting sensitivity to the increased proportional fat content associated with hypertrophy, whereas $T_2^*$ shows negligible correlation (R = 0.15).

Third, we quantify PDFF and $T_2^*$ in perilesional breast adipose tissue. Perilesional PDFF is reduced more substantially around malignant lesions (median difference = -5.2%) than benign lesions (= -1.0%, p = 5.0e-4), suggesting that PDFF may be sensitive to cancer-associated adipocytes. Preliminary analyses indicate that PDFF distinguishes effectively between benign and malignant lesions (AUC = 0.98), whereas $T_2^*$ demonstrates limited performance (AUC = 0.65).

Finally, Chapter 9 evaluates the MR Bra. We demonstrate that supine imaging with the MR Bra is better tolerated than conventional prone imaging, with 86% of participants reporting a better overall experience. Quantitative imaging metrics demonstrate minimal positional bias and acceptable signal-to-noise ratio is achieved.

The thesis concludes by outlining future directions for this research, including proposed histological and epidemiological validations.

**Keywords** —- Breast Cancer – Magnetic Resonance Imaging (MRI) – Non-Contrast – Proton Density Fat Fraction (PDFF) – $T_2^*$ – Adipose Tissue – Breast Density – Supine

# Contents

# List of Research Contributions

## Papers

Gordon, I., Ralli, G., Fernandes, C., Herlihy, A., Brady, M. Proton Density Fat Fraction of Breast Adipose Tissue: Comparison of the Effect of Fat Spectra and Initial Evaluation as a Biomarker. *Medical Image Understanding and Analysis (Lecture Notes in Computer Science).* 2022; 13413: 28–45. DOI: 10.1007/978-3-031-12053-4_3

## Abstracts

Gordon, I., Ralli, G., Fernandes, C., Herlihy, A., Greenall, G., Collins, S., Brady, M. Non-Invasive Assessment of Breast Adipose Tissue with Quantitative MRI May Enable Detection of Cancer and Contribute to the Assessment of Cancer Risk *Meeting Abstracts from the British Society of Breast Radiology Annual Scientific Meeting 2022. Breast Cancer Research.* 2023; 25(S1): 73:O4. DOI: 10.1186/s13058-023-01659-8

Herlihy, A., Tiedeman, G., Gordon, I., Collins, S., Brady, M. Prone and Supine Quantitative MRI Measurement of Breast Density: Preliminary Results from Ongoing IMOGEN Study *Meeting Abstracts from the British Society of Breast Radiology Annual Scientific Meeting 2022. Breast Cancer Research.* 2023; 25(S1): 73:P14. DOI: 10.1186/s13058-023-01659-8

Gordon, I., Ralli, G., Herlihy, A., Fernandes, C., O'Brien, A., Collins, S., Brady, M. Quantitative Calculation of Breast Density with Proton Density Fat Fraction Enables Distinction between Latest Subjective BI-RADS Categories *Proceedings of the International Society for Magnetic Resonance in Medicine 2023.* 2023; 31: 2732. DOI: 10.58530/2023/2732

Gordon, I., Ralli, G., Herlihy, A., Fernandes, C., O'Brien, A., Triay Bagur, A., Collins, S., Brady, M. Assessment of Breast Density with Hybrid-Based Proton Density Fat Fraction Calculation Enables Distinction between BI-RADS Categories *British and Irish Chapter of the International Society for Magnetic Resonance in Medicine Postgraduate Symposium 2023.* 2023.

Gordon, I., Herlihy, A., Greenall, G., Collins, S., Brady, M. The "MR Bra": Development of A Support Device for Supine Breast Imaging with Commercially Available Flexible Body Coils *Proceedings of the International Society for Magnetic Resonance in Medicine 2024.* 2024; 32: 4766. DOI: 10.58530/2024/4766

Gordon, I., Ralli, G., Fernandes, C., Herlihy, A., Collins, S., Brady, M. In-Vitro Evaluation of the Performance of PDFF Against Classification-Based Algorithms in Calculation of Breast Density *Proceedings of the International Society for Magnetic Resonance in Medicine 2024.* 2024; 32: 0845. DOI: 10.58530/2024/0845

# Intellectual Property

PCT/EP2023/058670, Method and Apparatus for Characterisation of Breast Tissue using Multiparametric MRI.

UK Registered Design No. 6413500, Bra for Medical Imaging.

# List of Figures

# List of Tables

# List of Abbreviations

**1D, 2D, 3D** . . One-, Two-, or Three-Dimensional

**ACR** . . . . . American College of Radiology

**ADC** . . . . . Apparent Diffusion Coefficient

**AUC** . . . . . Area Under the Curve

**BFC** . . . . . Bias Field Correction

**BI-RADS** . . . Breast Imaging-Reporting And Data System

**BMI** . . . . . Body Mass Index

**BPE** . . . . . Background Parenchymal Enhancement

**BRCA1, 2** . . Breast Cancer Genes 1 or 2

**CAA** . . . . . Cancer-Associated Adipocyte

**CC** . . . . . Confounder-Corrected

**CC-CSE-MRI** Confounder-Corrected Chemical-Shift-Encoded Magnetic Resonance Imaging

**CI** . . . . . Confidence Interval

**CRLB** . . . . . Cramér-Rao Lower Bound

**CSE** . . . . . Chemical-Shift-Encoded

**DCE** . . . . . Dynamic Contrast Enhanced

**DCE-MRI** . . Dynamic Contrast Enhanced Magnetic Resonance Imaging

**DCIS** . . . . . Ductal Carcinoma In Situ

**DW** . . . . . Diffusion-Weighted

**DWI** . . . . . Diffusion-Weighted Imaging

**EPI** . . . . . Echo Planar Imaging

**ER+/-** . . . . . Estrogen Receptor Positive or Negative

**FA** . . . . . Flip Angle

**FCMC** . . . . . Fuzzy C-Means Clustering

**FDA** . . . . . Food and Drug Administration

**FF** . . . . . Fat Fraction

**FGT** . . . . . Fibroglandular Tissue

**FLASH** . . . . Fast Angle Low Shot

**FMS** . . . . . Field Map Smoothing

**FOV** . . . . . Field of View

**frFSE** . . . . . Fast Recovery Fast Spin Echo

**FSE** . . . . . Fast Spin Echo

**FSPGR** . . . . Fast Spoiled Gradient Echo

**GE** . . . . . General Electric

**GLCM** . . . . Grey Level Co-Occurrence Matrix

**GoF** . . . . . Goodness-of-Fit

**GRE** . . . . . Gradient-Recalled Echo

**HWLoA** . . . . Half-Width of the 95% Limits of Agreement

**HER2** . . . . . Human Epidermal Growth Factor Receptor 2

**HR+/-** . . . . Hormone Receptor Positive/Negative

**HRT** . . . . . Hormone Replacement Therapy

**IDC** . . . . . Invasive Ductal Carcinoma

**ILC** . . . . . Invasive Lobular Carcinoma

**IDEAL** . . . . Iterative Decomposition of Water and Fat with Echo Asymmetry and Least Squares Estimation

**IDEAL-IQ** . . Iterative Decomposition of Water and Fat with Echo Asymmetry and Least Squares Estimation with Iron Quantification

**IR** . . . . . Inversion Recovery

**LCD** . . . . . Liquid-Crystal Display

**LCIS** . . . . . Lobular Carcinoma in Situ

**LoA** . . . . . Limits of Agreement

**LMS** . . . . . Liver MultiScan™

**LMS MOST** . Liver MultiScan™ Magnitude Only Thin $T_2^*$

**MAD** . . . . . Mean Absolute Deviation

**MAGO** . . . . Magnitude-Only

**MASLD** . . . . Metabolic dysfunction-Associated Steatotic Liver Disease

**MR** . . . . . Magnetic Resonance

**MRI** . . . . . Magnetic Resonance Imaging

**MRS** . . . . . Magnetic Resonance Spectroscopy

**NHS** . . . . . National Health Service

**PD** . . . . . Proton Density

**PDFF** . . . . . Proton Density Fat Fraction

**PF** . . . . . Partial Fourier

**PR+/-** . . . . Progesterone Receptor Positive or Negative

**PVE** . . . . . Partial Volume Effect

**PIC** . . . . . Patient Identification Centre

**qMRI** . . . . . Quantitative MRI

**RC** . . . . . Repeatability Coefficient

**RF** . . . . . Radio Frequency

**REC** . . . . . Research Ethics Committee

**RESOLVE** . . Readout Segmentation of Long Variable Echo-trains

**ROI** . . . . . Region of Interest

**ROC** . . . . . Receiver Operating Characteristic

**SD** . . . . . Standard Deviation

**SE** . . . . . Spin Echo

**SFF** . . . . . Signal Fat Fraction

**SNP** . . . . . Single Nucleotide Polymorphism

**SNR** . . . . . Signal-to-Noise Ratio

**SPGRE** . . . . Spoiled Gradient-Recalled Echo

**TE** . . . . . Echo Time

**TR** . . . . . Repetition Time

**TSE** . . . . . Turbo Spin Echo

**UK** . . . . . United Kingdom

**USA** . . . . . United States of America

# 1 Introduction

## Contents



## 1.1 Preface

Breast cancer is the single most common cancer in the UK [1], with one in every seven women expected to receive a diagnosis in their lifetime [2]. Globally, incident cases of breast cancer nearly tripled between 1990 and 2021 [3], driven by an ageing population, changes to reproductive practices, and the rising obesity epidemic. Current estimates project new diagnoses to reach 3.2 million per year by 2050, highlighting the escalating global burden of this disease [4].

Breast cancer is the worldwide leading cause of cancer-related death amongst women [5]. Mortality is driven predominantly by metastasis to other organs; whilst the overall survival rates for breast cancer are relatively high, the 5-year survival rate for metastatic breast cancer is only $\sim$25% [6].

Early detection is vital to prevent breast cancer from progressing to the metastatic stage. This has lead to nationwide screening initiatives such as the NHS Breast Screening Programme, which has been shown to reduce mortality by 39% [7]. Mammography is typically employed in screening programmes, owing to its economic

feasibility as a quick and relatively inexpensive modality. However, mammography has reduced sensitivity for women with radiologically "dense" breasts [8], which have a high proportion of fibroglandular tissue compared to fatty tissue. Breast density is a well-established risk factor for breast cancer [9] and is typically assessed visually, a process which is associated with high inter- and intra- operator variability [10].

Women with dense breasts are increasingly offered breast MRI due to an increase in the number of MRI scanners per capita and the introduction of abbreviated protocols. MRI is widely regarded as the most sensitive imaging modality in breast cancer diagnosis, but clinical protocols necessitate the injection of a gadolinium-based contrast agent, which is an invasive and often unpleasant experience. Research indicates that deposits of gadolinium may remain in the brain, bone, skin, and liver [11], the long term effects of which are not yet known. The contrast agent is used to highlight potential tumour regions by indicating regions of increased neovascularity; clinical protocols therefore focus on identifying and characterising lesions directly rather than on assessment of the breast tissues themselves.

Interpretation of breast MRI currently relies on a clinician's experience to perform a qualitative assessment of the images. Significant inter-operator variability has been found in the interpretation of clinical breast MR images, particularly between newly-trained and more experienced radiologists [12]. Moreover, conventional MRI is performed in the prone position, with patients' breasts hanging into a specialised RF coil. This position is inaccessible for some women and uncomfortable for many more [13]. Furthermore, this breast-specific coil is only available at a fraction of clinical sites.

## 1.2 Purpose

The research presented in this thesis aims to address the limitations of clinical breast MRI by developing non-contrast, quantitative MRI methodologies to characterise the breast tissues, and by exploring the feasibility of supine positioning.

Historically, research into non-contrast MRI has focused upon diffusion-weighted imaging and measurement of the apparent diffusion coefficient (ADC) within lesions.

Instead, this thesis evaluates the utility of two metrics derived from chemical-shift-encoded MRI, proton density fat fraction (PDFF) and $T_2^*$. These metrics have shown substantial applicability in the characterisation of other organs [14–16], but have not yet been extensively applied in the breast. We particularly focus on the ability of these biomarkers to characterise breast adipose tissue, which is increasingly implicated in the development and progression of breast cancer [17]. In addition to developing biomarkers which negate the injection of contrast, this thesis further seeks to improve the patient experience by investigating the feasibility of performing breast MRI in the supine position through the use of a specialised support device, the "MR Bra".

If successful, this research could ultimately improve the comfort and accessibility of breast MRI, reduce variability in image interpretation, and inform the risk assessment and diagnosis of breast cancer through non-invasive characterisation of tissue features.

## 1.3 Objectives

The main objectives of this thesis are:

1. To determine the optimal implementation of chemical-shift-encoded MRI in the breast;

2. To evaluate PDFF in the measurement of breast density, considering its accuracy against other quantitative methods and its agreement with clinical categorisations;

3. To assess the capacity of PDFF and $T_2^*$ to characterise breast adipose tissue and thereby inform breast cancer risk assessment and lesion characterisation; and

4. To evaluate the feasibility of supine imaging using the "MR Bra" through comparison to conventional prone positioning.

## 1.4 Thesis Outline

The remainder of this thesis is structured as follows.

**Chapter 2** outlines the necessary context for the research presented in this thesis. Breast anatomy and disease are introduced, key determinants of breast cancer risk are described, and the imaging techniques employed in the clinical assessment of breast cancer are detailed. The chapter also introduces the fundamental concepts of MRI physics and quantitative imaging, and specifies the data sources employed for this work.

**Chapters 3**, **4**, and **5** seek to determine the optimal approach to chemical-shift-encoded MRI of the breast. **Chapter 3** assesses the effect of the choice of pulse sequence through *in silico* and *in vitro* analyses. **Chapter 4** considers the choice of the multi-peak fat spectrum in the CSE-MRI algorithm and details the first implementation of breast-specific fat spectra in CSE-MRI. Lastly, **Chapter 5** evaluates the impact of the choice of post-processing algorithm through which acquired data is fitted to the CSE-MRI signal model. These chapters define the method with which PDFF and $T_2^*$ maps are generated for the remainder of the thesis.

The subsequent three chapters explore applications of PDFF and $T_2^*$ in the breast. **Chapter 6** examines PDFF in the measurement of breast density. The development of five specialised breast density phantoms is detailed, which are used to compare the accuracy of PDFF-derived breast density against a conventional voxel classification approach. Subsequent *in vivo* analyses then compare quantitative PDFF-derived density against current clinical classifications to determine its clinical applicability.

**Chapter 7** considers PDFF and $T_2^*$ in the characterisation of breast adipose tissue hypertrophy, an indicator of mammary fat "quality" which is linked to breast cancer risk.

**Chapter 8** quantifies PDFF and $T_2^*$ in perilesional breast adipose tissue adjacent to benign and malignant lesions. The biomarkers' ability to reflect cancer-associated adipocytes is considered and their performance in discriminating between benign and malignant disease is evaluated.

**Chapter 9** reports the evaluation of a support device designed to enable supine breast imaging, the "MR Bra". Its performance against traditional prone positioning is compared through calculation of SNR, measurement of quantitative biomarkers, and reporting feedback from participants, radiographers, and radiologists.

**Chapter 10** summarises the contributions of this thesis, describes paths for the future development of the research, and concludes the thesis with final remarks.

# 2
# Background

The research described in this thesis spans several fields including MR physics, image analysis, cellular biology, and medicine. This chapter therefore aims to provide the technical and clinical context necessary to interpret the work described hereafter. Firstly, in Section 2.1, the anatomy of the breasts and the biological principles underpinning breast disease are described. Current risk prediction techniques and the clinical imaging of breast cancer are also discussed. In Section 2.2, an overview of relevant principles in MRI is provided, along with a description of clinical breast MRI protocols and a technical discussion of the MR parameters examined in this research. Lastly, in Section 2.3, the data sources employed in this thesis are described.

## Contents

## 2.1 Breast Cancer

### 2.1.1 Breast Anatomy

The breast is an organ with the primary function of lactation. Breast tissue may be categorised into two major components - fibroglandular tissue and fatty tissue (Figure 2.1). Breast fibroglandular tissue encompasses ducts, lobules, and connective tissues and is typically considered to be the functional component of the breast. The "fatty tissue" is the breast adipose tissue which surrounds the fibroglandular tissue. Once regarded as an inert energy storage depot, the adipose organ is now recognised as a complex endocrine system which influences both breast cancer risk and disease progression [17, 18].

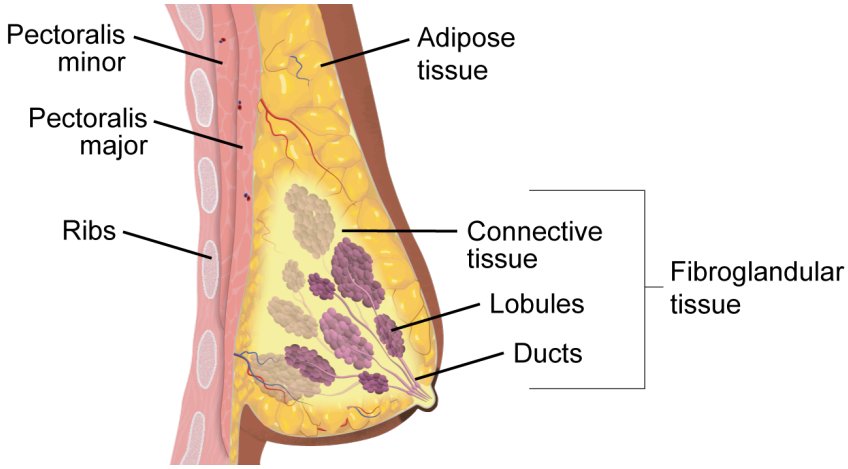


**Figure 2.1:** Illustration of breast anatomy, showing the breast fibroglandular tissue, which includes lobules, ducts, and connective tissues, and the adipose or "fatty" tissue which surrounds it. Image by Haley Fig.

The structure of the breast varies greatly throughout the course of a woman's life. During the menopause, the breasts undergo a gradual process of involution in which fibroglandular tissue atrophies and the relative proportion of fatty tissue increases. Involution of the breast also occurs after weaning to reflect the elimination of the need for lactation post-pregnancy. The structural composition of the breast also varies greatly across the population, with both genetics and lifestyle influencing the relative proportion of fibroglandular to fatty tissue.

### 2.1.2 Breast Disease

Breast disease encompasses multiple types of pathologies - both benign and malignant. In this section we provide a brief biological overview of common breast lesions, several of which are encountered in this thesis.

#### 2.1.2.1 Benign Breast Disease

**Cysts** Cysts are fluid-filled, round sacs which are thought to develop from failure in the continuous process of lobule and ductule formation [19]. Cysts are a common form of breast disease which are particularly prevalent in women between the ages of 30 to 50, and in post-menopausal women undergoing HRT. It is common for multiple cysts to be present within the breasts.

Cysts may be described as simple, complex, or complicated; these categories have varying risks of malignancy associated with them. Simple cysts are by far the most common and are filled entirely with fluid, have thin walls, and do not have malignant potential. Complex cysts have thick outer walls or contain solid components and must be investigated for the possibility of malignancy. Complicated cysts are fluid-filled but contain intracystic debris such as blood or pus; further diagnosis may be required as their appearance may mimic that of malignant lesions.

**Fibroadenomas** Fibroadenomas are solid benign lesions containing a mixture of glandular and connective tissues which are most commonly found in women of reproductive age [20]. They present as homogenous, well-circumscribed masses with a typically round shape. Complex fibroadenomas are a sub-category of fibroadenomas which are significantly less common than simple fibroadenomas but may harbour malignancy.

**Fat Necrosis** Fat necrosis is the death of adipose tissue which may be sustained by injury, surgery, or radiotherapy. Hard nodules of necrotic fat may be formed, microcalcifications may be present, and skin puckering may occur; these symptoms may lead to the suspicion of malignancy.

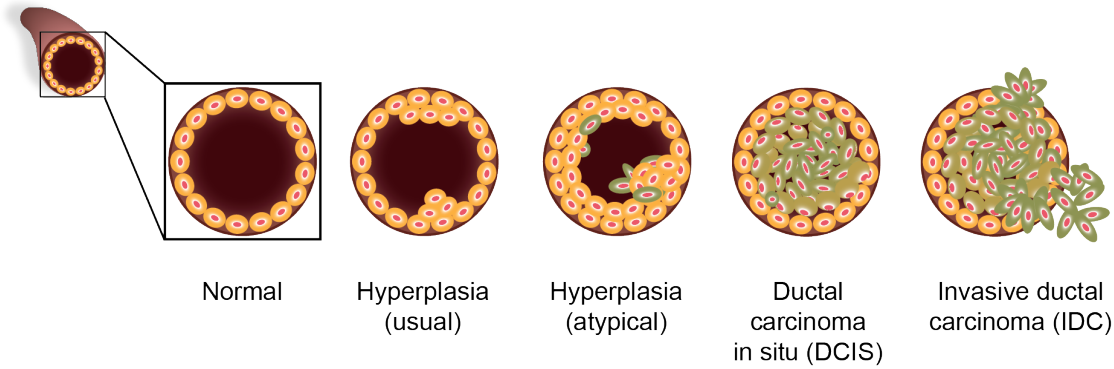


**Figure 2.2:** Illustration of cellular proliferation in the breast ducts. Image by Haley Fig.

**Lipomas** Lipomas are benign lesions which form due to an overgrowth of adipose tissue cells. They usually well-circumscribed, rounded masses which are soft and mobile.

**Hyperplasia** Hyperplasia describes an overgrowth of epithelial cells either in the breast ducts or lobules. Hyperplasia may be categorised as "usual", meaning that the cells present normally, or "atypical", meaning the cells are benign but show non-normal properties and have an increased risk of becoming malignant (Figure 2.2).

**Ductal Ectasia** Ductal ectasia is the abnormal dilation of the mammary ducts which may be accompanied by inflammation and fibrosis.

**Papillomas** Papillomas are benign tumours which occur from an overgrowth of ductal epithelial cells. They typically occur within a dilated major duct in the subareola region.

**Fibrocystic Breast Changes** The term "fibrocystic breast changes" encompasses the proliferation of a wide spectrum of structures in the breast. Most commonly this includes thickened regions of fibrous tissue with or without the presence of breast cysts, but may also include adenosis (enlarged lobules) or ductal hyperplasia. Fibrocystic breast changes are hormone-dependent and rarely occur post-menopause except in women undergoing hormonal replacement therapy.

#### 2.1.2.2 Malignant Breast Disease

Breast cancer is the rapid growth of abnormal epithelial cells within the breast. Breast cancer typically originates from either the mammary ducts or lobules and may be categorised into "invasive" or "in situ" sub-types. In situ cancer cells remain fully confined within a basement membrane, whilst invasive cancer cells have broken through this membrane to infiltrate other parts of the breast. In situ breast cancers are sometimes referred to as "pre-invasive" as they may be a precursor to invasive disease.

**Invasive Ductal Carcinoma** Invasive ductal carcinoma, or IDC, is the most common form of breast cancer and accounts for approximately 70-80% of diagnoses [21]. The cancerous cells of IDC originated within the ducts but have since broken through the ductal basement membrane and spread into the neighbouring breast stroma (Figure 2.2). IDC lesions are typically irregular in shape with ill-defined margins due to non-uniform tumour growth. Invasive ductal carcinoma may also be referred to as "invasive breast cancer of no special type", as histologically the cancer cells do not have distinguishing features relating to their point of origin.

**Ductal Carcinoma In Situ** Ductal carcinoma in situ, or DCIS, is the second most commonly diagnosed form of breast cancer, accounting for approximately 20-25% of diagnoses [22]. The cancerous cells are fully contained within the mammary ductal tree (Figure 2.2); DCIS is therefore often branching in shape. Microcalcifications resulting from secretions from the cancerous cells are a key indicator of DCIS; these are one of the earliest indications of malignancy.

**Invasive Lobular Carcinoma** Invasive lobular carcinoma, or ILC, describes cancerous cells which originated in the mammary lobules but have since infiltrated other breast tissues. ILC cells demonstrate a unique growth pattern in which the cancer grows in single-file lines. A palpable lump therefore rarely forms; instead, thickening of the breast tissue is more likely to be observed.

**Lobular Carcinoma in Situ** Lobular carcinoma in situ, or LCIS, refers to cancerous cells which have grown within the mammary lobules but remain fully contained within the lobular basement membrane. LCIS is clinically occult; it is typically found incidentally through histological analysis of other tissue.

Less common malignant conditions include inflammatory breast cancer, wherein the lymph nodes are blocked by cancer cells, and mucinous carcinoma, in which mucinous secretions accumulate around tumours.

Breast cancer may be further categorised by hormone receptor status and HER2 status. Breast cancer cells may include proteins ("receptors") which circulating oestrogen or progesterone may attach to. This attachment prompts these cells to divide, fueling disease progression. Hormone receptor positive (HR+) breast cancer cells are defined as those which are oestrogen receptor positive (ER+) and/or progesterone receptor positive (PR+). Approximately 80% of breast cancers are classed as oestrogen receptor positive, with 65% classed as both oestrogen and progesterone positive [23, 24].

Similarly, breast cancer cells may have upregulated expression of a protein called human epidermal growth factor receptor 2 (HER2). If cancer is found to be positive for oestrogen-receptors, progesterone-receptors, and HER2, it may be referred to as triple positive breast cancer, whilst conversely if the cancer tests negative for oestrogen and progesterone receptors and HER2, it may be referred to as triple negative breast cancer.

Hormone receptor status and HER2 status are used to inform breast cancer treatment. Hormone receptor positive cancers are key candidates for endocrine therapies, which aim to reduce the levels of oestrogen in the body, or to reduce the effect of oestrogen on the cancer cells. Meanwhile, anti-HER2 therapies attempt to stop or slow the growth of HER2 positive cancers by blocking the HER2 receptors from receiving the growth signals which trigger cell multiplication.

### 2.1.3 Risk Assessment

In clinical practice, breast cancer risk assessment is primarily based upon a woman's age. The NHS Breast Screening Programme offers population-based mammographic imaging to all asymptomatic women over the age of 50. In rare cases, younger women may be invited for screening if they are known carriers of high penetrance mutations in genes such as BRCA1 and BRCA2. These are known as "tumour suppressor genes" as they produce proteins involved in the repair of DNA damage; mutations in BRCA genes therefore lead to poor DNA repair and an accumulation of cellular mutations, increasing the likelihood that cells become cancerous. However, breast cancer risk has an array of predictive factors and cannot be defined through carrier status and age alone.

Personalised risk assessment models use multivariate data to quantify the likelihood of a woman receiving a diagnosis of breast cancer. This may be defined across a woman's lifetime or over a certain period of time, such as within the next 10 years. Higher risk women could be invited for earlier, more regular screening, may be imaged with alternative modalities, and may be invited to undergo preventative therapies.

Risk assessment models are typically based upon statistical regression, machine learning, or mathematical modelling. The risk factors, and their relative weightings, vary greatly between models. Common risk factors include familial history, nulliparity, age at first childbirth, and the use of hormonal replacement therapy, all of which may be obtained from a simple medical history.

Obesity and the metabolic syndrome are increasingly recognized as a significant predictive factors in breast cancer, particularly amongst post-menopausal women [17, 25–28]. Whilst these are complex diseases which affect endocrine system functionality and tissue composition, BMI is typically used as a simplified indicator of these diseases in risk prediction models.

In recent years, the integration of genomic data into risk predication models has become more common. In addition to the aforementioned high-risk genes such as BRCA-1 and BRCA-2, some models incorporate polygenic risk scores which

combine the risk from breast-cancer-associated single nucleotide polymorphisms (SNPs), which are lower risk mutations found across a much higher proportion of the population.

Imaging-derived biomarkers provide the opportunity to assess breast cancer risk through direct analysis of tissue composition. Two of the most commonly examined imaging-derived risk factors are background parenchymal enhancement (BPE) and breast density. BPE describes the degree of fibroglandular tissue enhancement under administration of a gadolinium-based contrast agent in DCE-MRI. Higher BPE is associated with an increased likelihood of breast cancer risk; whilst the biological mechanism behind this association is not clear, it is thought that elevated BPE may indicate higher glandular tissue concentration within the fibroglandular tissue (FGT) [29]. Meanwhile, breast density is a mammographic measure of the relative proportion of FGT to fatty tissue. Elevated breast density is a well-established risk factor for breast cancer in postmenopausal women, with recent studies suggesting a 2- to 3- fold increase in breast cancer risk between women with the highest and lowest breast densities [9].

Breast density and obesity are explored in further detail as risk factors for breast cancer in Chapters 6 and 7. We therefore describe the possible biological mechanisms behind these risk factors and their current place in clinical practice in further detail below.

#### 2.1.3.1 Breast Density

The term "breast density" typically refers to mammographic breast density. Mammographic breast density is a radiological assessment of the proportion of fibroglandular tissue to fatty tissue as examined through the difference in X-ray opacity of the two species; whilst fatty tissue appears transparent, fibroglandular tissue is highly attenuating of X-rays and therefore appears opaque (Figure 2.3). In clinical practice, breast density is assessed by eye and relies on operators' ability to classify the breasts into one of four categories defined by the American College of Radiology's (ACR) Breast Imaging Reporting & Data System (BI-RADS®) [30] (Table 2.1).

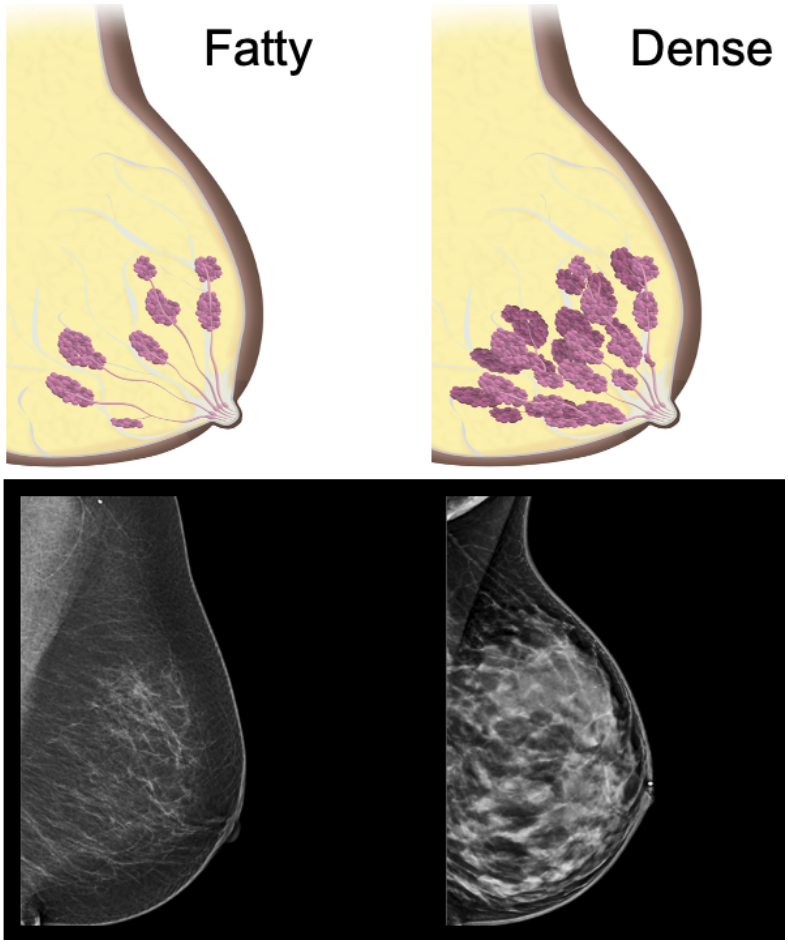


**Figure 2.3:** Visualisation of breast density, showing the difference in tissue content and mammographic appearance between "fatty" (left) and "dense" (right) breasts. Top: Images by Haley Fig. Bottom: Adapted from Cardona Ortegón et al. [31] under CC BY 4.0 [32].

This guidance provides a standardised method for the assessment and reporting of breast images.

The biological mechanism linking elevated breast density to increased breast cancer risk is unknown. Current hypotheses focus on the influence of fibroglandular tissue components on the transition of normal epithelial cells to malignant ones. The simplest hypothesized factor is that elevated breast density is associated with a greater number of epithelial cells, thereby increasing the probability of a mutation occurring [33]. Other hypothesized factors relate to the biological properties of stromal tissues, with collagen, fibroblasts, and the extracellular matrix all being associated with increased epithelial cell proliferation or tumour growth [34].

| BI-RADS® Category | Description |
|---|---|
| A | The breasts are almost entirely fatty. |
| B | There are scattered areas of fibroglandular density. |
| C | The breasts are heterogeneously dense, which may obscure small masses. |
| D | The breasts are extremely dense, which lowers the sensitivity of mammography. |

**Table 2.1:** The breast composition categories defined by the ACR BI-RADS® Atlas version 5 (2013) [30]. For further information, please see www.acr.org/Quality-Safety/Resources/BIRADS.

Somewhat counter-intuitively, whilst breast density typically decreases with age, breast cancer risk increases. The cause of this paradoxical relationship is unknown but it is thought that it is the cumulative exposure to biological factors in the FGT, as well as accumulation of cellular genetic damage, which influences cancer incidence [33, 35, 36]. Women who undergo delayed age-related involution of breast tissue are at higher risk of breast cancer [36]; this may also be explained through their increased cumulative exposure to biological factors in the FGT.

Regardless of mechanism, breast density has a proven relationship with breast cancer risk. The Tyrer-Cuzick model [37, 38] is a popular risk assessment model which is used to assess a woman's 10-year and lifetime risk of developing breast cancer. Later versions of the model incorporated a woman's breast density against the standard for her age and BMI as a variable. This improved the predictive power of the model by approximately 50% and accurately identified more high risk women [39]. Women with a high lifetime risk of breast cancer may be treated with preventative therapies such as Tamoxifen; this works to reduce the amount of epithelial tissue in the breast and is associated with a reduction in breast density.

As described in Section 2.1.4.1, elevated breast density is not only a strong risk factor for breast cancer but also decreases the sensitivity of mammography in breast cancer screening. Mammography is 98% effective in fatty breasts, however, its sensitivity is reduced to just 48% for breasts in the highest density category [8].

The screening of dense breasts may therefore be described as a "perfect storm", whereby there is an increased risk of breast cancer and an increased likelihood that any breast cancers present may be missed. In the USA, it is now mandatory in all states to inform women of their breast density after a mammogram, both to make women aware of the impact of breast density in screening sensitivity and to inform them of their breast cancer risk.

Reliable assessment of breast density is vital to inform the clinical pathway of the participant, to ensure that screening is performed with the appropriate frequency and imaging modality. The accuracy of breast density assessment is important when assessing longitudinal changes to the breast structure, such as tracking involution of the breast, monitoring the progress of preventative therapies, or assessing the effect of chemotherapy on healthy breast tissue. Conventional visual categorisation of breast density has high inter- and intra operator variability [10], and it is of course unable to track small changes in breast density over time. This has lead to demand for quantitative, automated techniques.

Mammographic breast density may be measured quantitatively using a computer-aided approach to segment fibroglandular tissue from fatty tissue. However, differences in X-ray calibration and the varying levels of compression employed across different scans limit repeatability. Volpara TruDensity® (Volpara Health Technologies Ltd., Wellington, New Zealand) [40] is an automated method for measurement of breast density which uses a model of the X-ray imaging chain to estimate the fibroglandular and fatty tissue volume in each pixel. This method is independent of the image acquisition technique and does not require operator intervention; it has been shown to be highly repeatable and to have close correlation with MRI-derived density. However, mammography is inherently limited in the measurement of breast density due to its use of ionising radiation and its two-dimensional nature. As described in Section 2.1.4.1, even three-dimensional tomosynthesis images are derived from projections of two-dimensional acquisitions; this may lead to tissue overlapping artefacts and affect breast density quantification.

The reader is directed to Chapter 6 for further discussion on breast density, including assessment of MRI-based methodologies for assessment of volumetric breast density.

#### 2.1.3.2 Obesity and the Metabolic Syndrome

Obesity is a complex condition which is typically categorised by the presence of excess body fat and a BMI above 30. Obesity is strongly linked to increased breast cancer incidence in post-menopausal women and to poorer outcomes in women of all ages [41, 42]. The metabolic syndrome is a type of metabolic disease classified by the presence of multiple factors, including obesity, insulin resistance, and dyslipidemia. Patients with the metabolic syndrome are three times more likely to have breast cancer than healthy participants [28], and are significantly more likely to suffer from relapse [43].

The link between obesity, the metabolic syndrome, and breast cancer incidence is thought to relate to the change in composition of the adipose tissue during weight gain. In childhood, weight gain primarily occurs through adipocyte hyperplasia - an increase in adipocyte number. However, in adulthood, weight gain primarily occurs through adipocyte hypertrophy [44] - the expansion of fat cells as they fill up with excess dietary lipids. This process is associated with altered adipose tissue function, adipocyte cell death, and a state of inflammation which provides a favourable environment for cancer genesis.

Whilst obesity is clearly associated with breast cancer incidence in post-menopausal women [45, 46], the link between obesity and breast cancer incidence in pre-menopausal women is less clear [17, 47, 48]. Some studies report a positive [49] or non-existent correlation [50], whilst others even suggest obesity may have a protective effect [51]. The mechanism for the difference in the effect of obesity pre- and post- menopause is not clear, but it is proposed to result from differences in oestrogen production. In pre-menopausal women, levels of aromatase, an enzyme responsible for oestrogen synthesis, are highest in the ovaries. However, aromatase is also expressed in the subcutaneous fat. During the menopause, oestrogen synthesis

in the ovaries ceases, but the aromatase levels in subcutaneous fat persist; in post-menopausal women, adipose tissue is therefore the primary source of oestrogen. In this cohort, greater adiposity therefore results in a relative increase in circulating oestrogen levels. However, in obese pre-menopausal women, the combination of increased oestrogen production from adipose tissue with the existing oestrogen production in the ovaries activates a negative feedback response in the hypothalamus pituitary axis of the brain, causing a reduction in ovarian oestrogen synthesis [52, 53]. A further hypothesis suggests that this negative feedback response decreases synthesis of progesterone, which may have a protective effect against HR-positive breast cancer [53]. Another contributing factor may be the type of oestrogen which is produced pre- and post- menopause. Estrone production dominates after the menopause and has a pro-inflammatory effect in adipose tissue, whilst estradiol, which dominates pre-menopause, has an anti-inflammatory effect [54].

Independent of menopausal status, obesity results in poorer prognoses across all breast cancer subtypes. The breast cancer mortality rate is increased by 35% in obese patients [55] and obesity is associated with a greater likelihood of breast cancer recurrence [56] and secondary malignancy [57]. These poorer outcomes are thought to be influenced by the local effect of adipose tissue inflammation on the tumour micro-environment, wherein the altered adipokine profile works to promote tumour growth [17]. Furthermore, as we discuss in Chapter 8, adipocytes in close proximity to tumours are remodelled and are referred to as cancer-associated adipocytes (CAAs) [58, 59]. These CAAs undergo delipidation, in which the lipid contents of the adipocytes are depleted and transferred to adjacent cancer cells, which provides energy for tumour proliferation [60, 61]. Hypertrophic adipocytes have greater lipid content which increases the influence of CAAs in obese patients.

Direct measurement of breast adipose tissue quality could improve risk prediction models and influence prognostic assessment. The reader is directed to Chapter 7 for investigation into non-invasive measurement of adipocyte hypertrophy, and to Chapter 8 for an investigation into measurement of adipose tissue quality within the tumour micro-environment.

### 2.1.4 Clinical Imaging Techniques

We now briefly describe the principles behind the key clinical imaging modalities employed in breast cancer detection and diagnosis.

#### 2.1.4.1 Mammography

Mammography is a quick and relatively inexpensive diagnostic procedure which passes low-dose X-rays through the breast. Historically, X-rays were received directly onto a photographic film plate; they are now more commonly received by a solid state detector which utilises computer-based reconstruction to generate images in a procedure known as digital mammography. Compression of the breast is required to improve the image contrast and visualisation of tissue near the chest wall, and to minimise motion artefacts. Breast compression is widely regarded as an uncomfortable and often painful procedure; efforts are therefore increasingly made to explore self-compression techniques [62].

Mammography exploits the fact that tumours are highly attenuating of X-rays, whereas fat is not. The attenuation coefficient of fibroglandular tissue is similar to that of tumours, rendering mammography ineffective at identification of tumours in dense breasts (Section 2.1.3.1). However, mammography is highly sensitive in the detection of calcifications, such as those associated with DCIS.

In standard mammography, two-dimensional projections of the breast are generated. Tomosynthesis refers to so-called "three-dimensional mammography" in which two-dimensional projections are acquired at multiple angles and computationally reconstructed into a three-dimensional image. Tomosynthesis is regarded to have improved diagnostic performance over standard mammography; in particular, the ability to detect tumours in dense breasts is improved. Tomosynthesis also does not require as severe breast compression as two-dimensional mammography. However, the technique is still fundamentally limited by the similarity in X-ray attenuation coefficient of tumours and fibroglandular tissue.

Mammography is often employed as the first port of call in breast imaging due to its low cost and propensity to identify calcifications. Alternative imaging

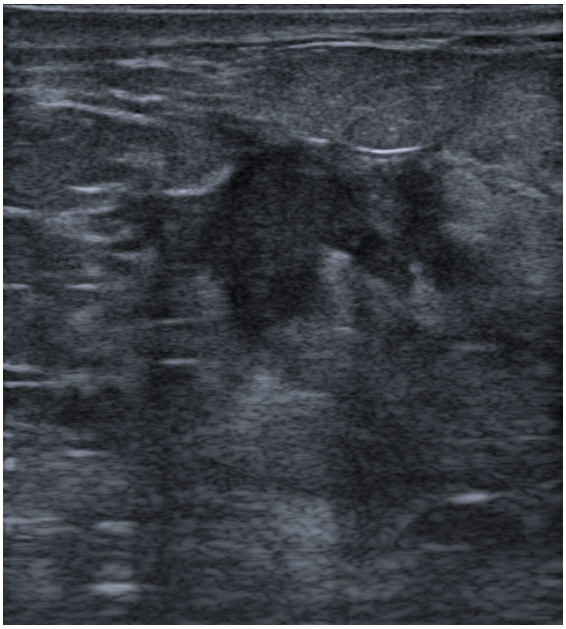

**Figure 2.4:** Example of a breast ultrasound image containing a lesion of invasive ductal carcinoma. Image from the dataset provided by Pawlowska et al. [63] under CC BY 4.0 [32].

modalities must be selected for women with dense breasts, and for those requiring frequent screening due to the ionising nature of the modality.

#### 2.1.4.2 Ultrasound

Breast ultrasound proposes a non-ionising solution for women with dense breasts, or for those who require investigation after mammography.

Ultrasound is performed by moving a probe across the breast. This probe ("transducer") houses a piezoelectric crystal which has the reversible ability to transform an electrical current into a mechanical pressure wave and vice versa. The former property is used to transmit high frequency sound waves into the breast. When an acoustic interface between two materials is encountered, reflections ("echoes") travel back and are received by the ultrasound probe. The ultrasound probe transforms the pressure waves received into an electrical current to construct digital images which are displayed in real time. Materials with higher density, such as tumours, reflect more sound and therefore appear more opaque ("hyperechoic"). Figure 2.4 shows an example ultrasound image of a lesion of invasive ductal carcinoma with its characteristic hyperechoic appearance.

Ultrasound is an inexpensive imaging modality which lends itself to adoption in resource-limited settings due to its portable nature, low maintenance costs, and facilitation of real time imaging for biopsy sampling of lesions. However, its performance may be dependent upon the individual's technique, with variables including the pressure applied to the probe and the selection of the imaging plane. Furthermore, as ultrasound samples the breast region by region, multifocal or contralateral disease may be missed, whilst its freehand acquisition can impede re-imaging the same plane at a later date, complicating longitudinal comparisons.

#### 2.1.4.3 MRI

MRI is widely regarded as the most sensitive imaging modality in breast cancer diagnosis. Figure 2.5 shows an example DCE-MRI image of invasive breast cancer, noticeable as a bright enhancing mass in the left breast [64]. Across ten studies of high risk women, the sensitivity of breast MRI ranged between 71-100% whilst that of mammography and ultrasound ranged between 25-58% and 33-52% respectively [65]. The DENSE study demonstrated the superior sensitivity of breast MRI through inviting high risk women with normal mammography results to a supplemental MRI scan; the interval cancer rate was reduced by 50% in those who underwent the additional MRI [66]. Historically, concerns have been raised over the specificity of breast MRI, indicating a higher risk of false positive diagnoses compared to other imaging modalities. More recent work disparages the association of breast MRI with inherently low specificity, but instead highlights the dependency of diagnostic accuracy on reader experience [67].

In clinical practice, breast MRI is typically reserved for the most difficult diagnostic cases and for high risk younger women. One barrier to its wider adoption is MRI's perceived expense compared to other imaging modalities. The introduction of abbreviated breast MRI protocols [68] and an increase in the number of MRI scanners per million inhabitants [69] has increased the economical feasibility of this modality, with a recent evaluation concluding that screening with breast

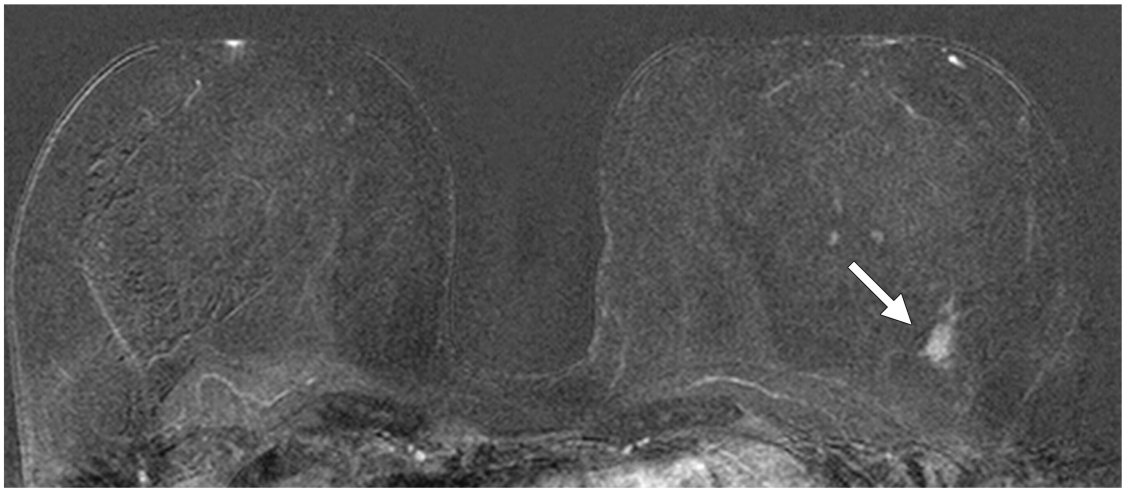

**Figure 2.5:** Example of a DCE-MRI image showing a suspicious enhancing mass in the left breast confirmed as invasive high-grade triple-negative cancer. Figure reproduced from Kuhl et al. [64] with permission from the Radiological Society for North America (permission conveyed through Copyright Clearance Center Inc.).

MRI for women with intermediate risk of breast cancer is cost-effective compared to mammography alone [70].

As we introduced in Chapter 1, clinical breast MRI protocols rely upon the intravenous injection of contrast agent and the uncomfortable prone position. Of the high-risk women who discontinued screening with MRI in the second round of the DENSE trial, 39% of reasons provided were MRI-related inconveniences and/or self-reported contraindications [71]. This stresses the need for methodologies to improve patient experience in breast MRI.

Before we describe clinical breast MRI and the work we intend to do to address its limitations, we must firstly introduce the key concepts of MRI physics. We return to clinical breast MRI in Section 2.2.3.

## 2.2 Magnetic Resonance Imaging

### 2.2.1 Principles of MRI

#### 2.2.1.1 The MRI Signal

Magnetic Resonance Imaging (MRI) is based on the phenomenon of nuclear magnetic resonance (NMR). The NMR principle dictates that nuclei in a strong,

constant magnetic field which are disturbed by a weak magnetic field will emit an electromagnetic signal. This signal is characteristic of both the nuclei and their surrounding environment. MRI exploits the NMR phenomenon by spatially encoding these electromagnetic signals to form images [72–74].

The formation of an NMR signal relies on the intrinsic spin angular momentum possessed by all particles, $\boldsymbol{J}$, which generates a magnetic moment, $\boldsymbol{\mu}$. The relationship between a particle's spin and magnetic moment is determined by its gyromagnetic ratio, $\gamma$:

$$\boldsymbol{\mu} = \gamma \boldsymbol{J} = \gamma \hbar \boldsymbol{I} \tag{2.1}$$

where $\hbar$ is the reduced Planck constant and $\boldsymbol{I}$ is the particle's quantum spin number. The gyromagnetic ratio is a property particular to each particle which is dependent upon its charge and mass.

Only particles with a non-zero spin number generate a non-zero magnetic moment $\boldsymbol{\mu}$ and may therefore be exploited for use in NMR. Due to the abundance of water in the human body, hydrogen nuclei, consisting of a singular proton ($\boldsymbol{I} = \frac{1}{2}$), are typically used as the element of interest in MRI.

In the absence of an external magnetic field, the magnetic moments of protons are aligned randomly, such that the net magnetic moment in an area of interest is near-zero. However, in the presence of an external magnetic field, $\boldsymbol{B_0}$, the Zeeman effect dictates that the number of potential quantum spin states possessed by a particle is equal to $2\boldsymbol{I} + 1$. For the proton, there are therefore two possible spin states, which are referred to as "spin up" and "spin down". In classical terms, the "spin up" state describes the alignment of a proton's spin parallel to $\boldsymbol{B_0}$ whilst the "spin down" state describes the alignment of a proton's spin anti-parallel to $\boldsymbol{B_0}$.

The energy of the spin down state is slightly higher than that of the spin up state, and the difference in energy possessed by the two states is described by the Zeeman equation:

$$\Delta\epsilon = \gamma \hbar B_0 \tag{2.2}$$

where $B_0 = |\boldsymbol{B_0}|$. The Boltzmann distribution describes the probability that a proton is in the spin up state compared to the spin down state. For a large number of protons, this probability can be equated to the ratio of the number of protons in the spin up state to the number of protons in the spin down state.

$$P \approx \exp\left(\frac{\Delta\epsilon}{kT}\right) \approx \frac{N_{up}}{N_{down}} \tag{2.3}$$

where $k$ is the Boltzmann constant and $T$ is the temperature. Incorporating Equation 2.2, and as $\gamma\hbar B_0 << kT$:

$$\frac{N_{up}}{N_{down}} \approx 1 + \frac{\gamma\hbar B_0}{kT} \tag{2.4}$$

There will therefore be a slightly larger ($\sim 0.0001\%$) number of protons with magnetic moments aligned parallel to $\boldsymbol{B_0}$ than anti-parallel. This gives rise to a net magnetisation along $\boldsymbol{B_0}$, referred to as $\boldsymbol{M_0}$. The net magnetisation resulting from these protons is the signal measured during MRI.

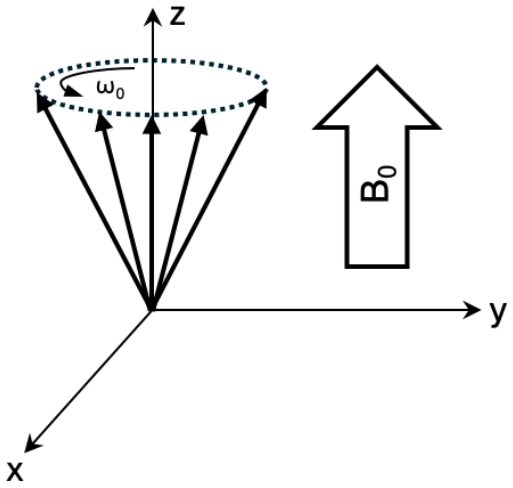


**Figure 2.6:** Illustration showing the precession of magnetisation around $B_0$ with angular momentum $w_0$. Figure inspired by Trakic [75].

#### 2.2.1.2 Measurement of the MRI Signal

The proton spins continually processes around the axis of $\boldsymbol{B_0}$, which is referred to as the z-direction (Figure 2.6), such that $\boldsymbol{B_0} = B_0\hat{\boldsymbol{z}}$. The angular frequency

of this procession may be found through applying the Planck-Einstein relation $\epsilon = \hbar\omega$ to Equation 2.2 such that

$$\omega_0 = \gamma B_0 \tag{2.5}$$

This precessional frequency is referred to as the Larmor frequency.

In equilibrium, spins are randomly oriented in the transverse (x-y) plane, such that the transverse magnetisation, $\boldsymbol{M_{xy}}, = 0$, leaving the net magnetisation fully aligned with the z-direction. To generate MRI images, the net magnetisation must be perturbed from the z-axis such that $\boldsymbol{M_{xy}}$ is non-zero. This is achieved through the application of an oscillating magnetic field, $\boldsymbol{B_1}$ which is perpendicular to $\boldsymbol{B_0}$. The $\boldsymbol{B_1}$ field is applied via a radio-frequency ("RF") pulse (Figure 2.7). For optimal energy transfer efficiency, the frequency of the RF pulse is set to the Larmor frequency. The angle to which the net magnetisation is tipped relative to the $B_0$ field is described as the flip angle, $\alpha$.

The MRI signal is detected as the $\boldsymbol{M_{xy}}$ vector rotates about the z-axis, which, due to the Faraday effect, induces an electric current in receiver coils which are sensitive to magnetic flux. The MRI receiver system detects two orthogonal signal components, denoted $I$ and $Q$. These signal components may arise from two physically orthogonal coils, or from a single coil with electronic quadrature demodulation, the latter of which is far more common today. The detection of these orthogonal signal components allows measurement of a complex MRI signal with both real and imaginary parts, which enables the computation of magnitude and phase images. The complex MR signal may be written as

$$S(\boldsymbol{r}, t) = |S(\boldsymbol{r}, t)| \exp(-i\phi(\boldsymbol{r}, t)) \tag{2.6}$$

where $\boldsymbol{r}$ is a location being imaged, $t$ is the time after application of the RF pulse, $|S(\boldsymbol{r}, t)|$ is the magnitude of the MRI signal and $\phi(\boldsymbol{r}, t)$ is the phase of the MRI signal.

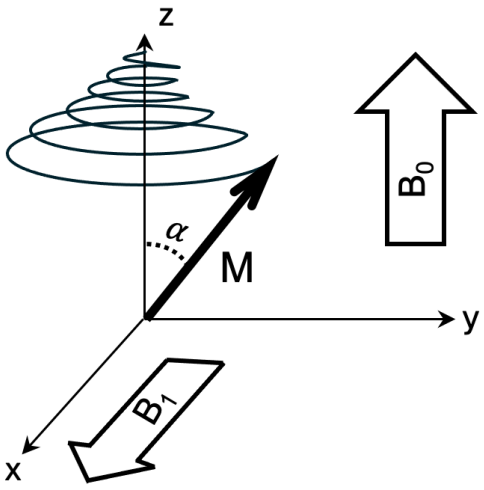


**Figure 2.7:** Illustration showing perturbation of the magnetisation by the $B_1$ field (RF pulse). The $B_1$ field flips the magnetisation by $\alpha$°where $\alpha$ is the flip angle. Figure inspired by Trakic et al. [75].

#### 2.2.1.3 Spin Relaxation

Once the RF pulse has been applied, the proton spins gradually return to a state of equilibrium, and begin to re-align themselves with $\boldsymbol{B_0}$. The environment of the protons dictates both the longitudinal (z-direction) and transverse relaxation of their spins.

**$T_1$ "Spin-Lattice" Relaxation** After the RF pulse, protons interact with nuclei, atoms, and molecules in the surrounding environment and thereby lose the energy absorbed from the RF pulse. The magnetisation along the z-axis experiences exponential recovery back to its equilibrium value of $M_0$, where $\boldsymbol{M_0} = M_0\hat{\boldsymbol{z}}$. The characteristic exponential time constant of this process is denoted $T_1$ and is defined as

$$M_z(t) = M_z(t=0)\exp\left(\frac{-t}{T_1}\right) + M_0\left(1 - \exp\left(\frac{-t}{T_1}\right)\right) \tag{2.7}$$

When $M_z(t = 0) = 0$, this simplifies to

$$M_z(t) = M_0\left(1 - \exp\left(\frac{-t}{T_1}\right)\right) \tag{2.8}$$

**$T_2$ "Spin-Spin" Relaxation** After the RF pulse, interactions also occur between neighbouring spins, leading to dephasing in the transverse plane and to exponential decay of $M_{xy}$ with a characteristic time constant $T_2$.

$$M_{xy}(t) = M_{xy}(t=0)\exp\left(\frac{-t}{T_2}\right) \tag{2.9}$$

**$T_2^*$ Relaxation** In practice, the transverse magnetisation decays more quickly than that described by Equation 2.9 due to an additional spin dephasing process incurred by the presence of any inhomogeneities in the magnetic field.

The effective transverse decay time constant is described as $T_2^*$ where $T_2^* < T_2$

$$\frac{1}{T_2^*} = \frac{1}{T_2} + \frac{1}{T_2'} \tag{2.10}$$

and $T_2'$ describes the contribution of the field inhomogeneities. $T_2^*$ characterises the free induction decay (FID) signal, that is, the signal induced in an RF coil after applying and switching off an RF pulse.

As the environment of the protons dictates the relaxation of the spins back to equilibrium, different tissue types have characteristic $T_1$, $T_2$, and $T_2^*$ values. These may either be measured exactly or used as a weighting in an image; that is, as a contrast in an image. This is explored further in Section 2.2.2.

#### 2.2.1.4 Spatial Encoding

The formation of an MRI image requires the distinction of signals from different regions in the species of interest. To do this, linear field gradients are applied over three orthogonal dimensions. The three field gradients are named the frequency encoding gradient, the phase encoding gradient, and the slice selection gradient.

Application of a magnetic field gradient changes the Larmor frequency of the protons along the direction of the gradient. This is because the total magnetic field experienced by each proton will vary according to its spatial location. This process is referred to as "frequency encoding". If a field gradient is applied along the x

axis, $G_x = dB_z/dx$, where $B_z$ is the z-component of the magnetic field which is determined by $\boldsymbol{B_0}$, then the Larmor frequency of a proton as a function of $x$ is

$$\omega(x) = \gamma(B_0 + G_x x) = \gamma(B_0 + \frac{dB_z}{dx}x) \tag{2.11}$$

$G_x$ is typically referred to as the frequency encoding gradient.

After frequency encoding, an additional field gradient must be applied along the y-axis in order to distinguish the signal location in two dimensions. This gradient, $G_y = \frac{dB_z}{dy}$, is applied for a short time only. During the application of $G_y$, protons will precess at different frequencies along $G_x$. When the phase encoding gradient is switched off, the protons return to their initial precessional frequencies but with an acquired phase offset which is dependent upon their location in the y-dimension. This gradient is therefore referred to as the phase encoding gradient.

To enable localisation of the MRI signal in all three dimensions, an additional field gradient must be applied along the z-axis. This gradient, $G_z = \frac{dB_z}{dz}$, enables the selection of a single slice along the z-axis and is therefore referred to as the slice selection gradient. Similarly to the frequency encoding gradient, this gradient alters the field strength along the z-axis and therefore the resonant frequencies of the protons along that dimension.

An RF excitation pulse is used alongside the application of $G_z$ which has a bandwidth that only contains the resonant frequencies required to excite protons within the desired slice. The waveform of the RF pulse can be changed to acquire different slice profiles, including simultaneously-acquired multi-slice data.

Using a slice selection gradient is referred to as 2D acquisition. In 3D acquisitions however, the RF pulse excites protons throughout the whole image volume and a second additional phase encoding gradient is applied to spatially encode the signal in the z-dimension.

#### 2.2.1.5 k-space

Through the application of these gradient fields, each spatial location may now be defined by a unique combination of frequency and phase. However, the reception of these encoded signals by the receiver coils does not immediately result in an image.

Instead, signals are received in a realm referred to as k-space, in which frequency is encoded along the x-axis ($k_x$) and phase is encoded along the y-axis ($k_y$) (Figure 2.8). Lower spatial frequencies, which contain the majority of the signal, are stored in the centre of k-space. Higher spatial frequencies, which contain the sharper edges of the image, are stored towards the periphery. Different trajectories may be used to fill k-space; the most common methods are row-by-row (rectilinearly), radially, and spirally.

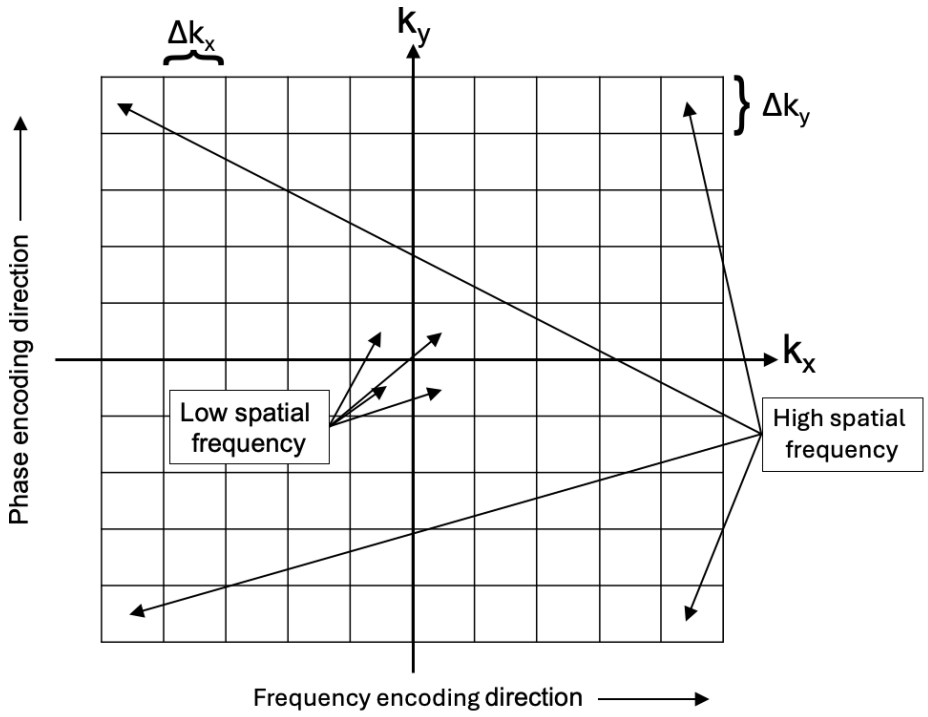


**Figure 2.8:** Illustration of k-space. Figure inspired by McClymont [76].

To convert the k-space data into an image, the Fourier transform is applied. The MR images produced will have the same dimensions as the k-space data; that is, an image of size A×B will be formed from A measurements acquired in the phase encoding direction and B measurements acquired in the frequency

encoding direction. Furthermore, the field of view in the x- and y- directions will be proportional to the resolution of the frequency encoding ($\Delta k_x$) and phase encoding measurements ($\Delta k_y$) respectively.

#### 2.2.1.6 MRI Pulse Sequences

A set of programmed magnetic gradient fields and RF pulses may be described as a "pulse sequence". The parameters in a pulse sequence are chosen according to the properties of the desired image, such as the weighting and resolution. Table 2.2 describes typical parameters employed in pulse sequence design.

Typically, echoes of the MRI signal are acquired rather than the FID signal directly. We describe below several common MRI pulse sequences which are used to generate these echoes.

**Spin Echo (SE)** In a spin echo sequence, a 90° pulse is firstly applied such that $M_0$ is rotated into the transverse x-y plane. The spins begin to dephase in the x-y plane. At a time equal to half the echo time (TE), a 180° RF pulse is applied. This pulse rotates the spins around the x-axis such that the spins refocus at the echo time, at which point the signal is measured. The spin echo is a fundamental MRI sequence. It has particular utility in measurement of true $T_2$, rather than $T_2^*$, due to the application of the "refocusing" 180° pulse which eliminates field inhomogeneity effects. For this reason, spin echo acquisitions demonstrate minimal susceptibility artefacts.

**Turbo Spin Echo (TSE)** A turbo spin echo sequence uses multiple 180° refocusing pulses after a single 90° pulse to generate a train of echoes. The phase encoding gradient is changed between echoes, such that multiple lines of k-space may be filled within a given repetition time (TR). This reduces imaging time compared to conventional spin echo sequences. Image blurring may occur when acquiring many echoes with short echo times, therefore TSE sequences are better suited to $T_2$-weighted acquisitions with longer TEs.

| MR Parameter | Description |
|---|---|
| Echo Time (TE) | The time between the excitation pulse and the peak of the signal induced in the receiver coil. |
| Echo Spacing ($\Delta$TE) | The time between successive signals induced in the receiver coil. |
| Repetition Time (TR) | The time between application of successive excitation pulses. |
| Flip Angle | The angle to which the net magnetisation is tipped relative to the $B_0$ field. |
| (Receiver) Bandwidth | The range of frequencies of the signal received by the RF coil. |
| Field of View (FOV) | The size of the image that contains the object of interest. |
| Matrix Size | The size of the matrix containing the k-space data which is defined by the number of samples in the frequency encoding and phase encoding directions. |
| Acquired In-Plane Resolution | The size of a pixel in the image prior to interpolation. This is equal to the field of view divided by the matrix size. |
| Reconstructed In-Plane Resolution | The size of a pixel after any interpolation which may be applied. |
| Slice Thickness | The thickness of an imaging slice, defined by the slice selection gradient and the bandwidth. |
| Slice Gap | The size of the gap between consecutive slices. |
| Imaging Plane | The orientation of the image with respect to the MR system - this is typically axial (wherein the image is taken in the x-y plane), coronal (x-z plane), or sagittal (y-z plane). |

**Table 2.2:** Descriptions of Commonly Employed MR Parameters

**Gradient-Recalled Echo (GRE)** Instead of a 180° RF pulse, a gradient-recalled echo (or "gradient echo") sequence uses magnetic field gradients to generate an echo. Firstly, an excitation pulse is applied to tip the magnetisation away from $\boldsymbol{B_0}$. Then, a dephasing ("negative") field gradient is applied. This causes the spins to dephase at a rate faster than free induction decay alone. A rephasing ("positive") field gradient is then applied which has the same strength but opposite polarity to the dephasing field. This causes the spins to rephase such that an echo is produced.

Gradient echo sequences are typically shorter than spin echo sequences as the gradient reversal after the initial RF pulse can be applied immediately once the gradient of opposite polarity has been applied. Spin echo sequences, however, necessitate waiting for TE/2 to apply an additional RF pulse, and for a further TE/2 before signal readout can occur. As a result, echoes may be recorded much more quickly in GRE sequences. When combined with the short TRs possible for GREs with small flip angles, this enables much shorter acquisition times. As the flip angle in GRE acquisitions is typically less than 90°, non-zero longitudinal magnetisation remains throughout the application of the gradient fields. Unlike spin echo sequences, GRE sequences do not eliminate field inhomogeneity effects, and are therefore useful in measurement of $T_2^*$ and in susceptibility-weighted imaging.

The flip angle which maximises the steady-state GRE signal is the Ernst angle, $\alpha_E = \arccos\left(e^{-TR/T_1}\right)$ where the $T_1$ is that of the tissue of interest. Increasing the flip angle towards the Ernst angle increases SNR and results in increased $T_1$-weighting of the sequence; in doing so, GRE sequences may be tuned to provide rapid acquisition of $T_1$-weighted images. In GRE applications where $T_1$-weighting is undesirable, such as in CSE-MRI (see Chapter 3), small flip angles ($<\alpha_E$) and/or longer TRs should be chosen.

An additional spoiler gradient may be applied to GRE sequences to eliminate any residual transverse magnetisation before application of the next excitation pulse. This reduces the repetition time of the sequence and is referred to as "spoiled" GRE.

**Echo Planar Imaging (EPI)** Echo planar imaging is a rapid imaging technique in which a large proportion of k-space is acquired after a single RF excitation using a rapid train of echoes. Single-shot EPI sequences acquire the entirety of k-space with one excitation, whilst multi-shot sequences split k-space acquisition over several shots to improve SNR and reduce blurring at the cost of time. EPI sequences typically provide the basis for diffusion-weighted imaging (DWI) as the strong gradients and long echo times required by DWI require rapid acquisition of k-space to reduce motion artefacts and signal decay.

#### 2.2.1.7 RF Receiver Coils

Multiple types of coil are present in an MRI system. The main field coil generates the static $B_0$ field, whilst shim coils are used to improve magnetic field homogeneity and gradient coils are used to generate the magnetic field gradients required for spatial localisation. RF coils are used to transmit the RF excitation pulse, and, as described in Section 2.2.1.2, to the detect the MRI signal through the induction of an electric current. RF coils may be able to solely transmit, solely receive, or to have both transmit and receive functionality.

**Figure 2.9:** Example of an RF receiver coil in position on a participant's abdomen; this is the flexible AIR Coil produced by GE Healthcare, Chicago, USA. Image from Perspectum Ltd.

Unlike the main field coil, shim coils, and gradient coils, which are built into the scanner, RF coils may be typically be added to and removed from the scanner

system as necessary. Exceptions to this include the body coil, which is built into the scanner's bore, and the spine coil, which is built into the patient table. Each RF receiver coil is tailored to the anatomy of interest; examples include the head coil, the abdominal coil, and the aforementioned breast coil. These coils are specialised in their shape, flexibility, and size to allow close proximity to the anatomy of interest to maximise the signal-to-noise ratio. An example of a flexible RF receiver coil manufactured by GE Healthcare is shown in Figure 2.9. The number of channels in a RF receiver coil describes the number of independent electronic chains which feed signal information back to the computer. The signals from each channel are combined to produce the final MR image.

#### 2.2.1.8 Acceleration in MRI

The speed of MR data acquisition may be increased through so-called "acceleration techniques". Reducing scan length is particularly important when imaging areas susceptible to respiratory motion, where effecting the scan within a breath hold can vastly reduce motion-induced artefacts. One acceleration technique, known as partial fourier (PF) acquisition, exploits the conjugate symmetry of k-space such that only part of it is acquired, with the remainder interpolated through mathematical equivalence. This can result in the imaging time reducing by up to half. Parallel imaging (PI) is another technique, in which k-space is undersampled and subsequently interpolated using spatial information from the coils. New acceleration techniques are emerging alongside advances in AI; networks trained on image and k-space data can infer high quality images given undersampled acquisitions [77].

#### 2.2.1.9 Signal-to-Noise Ratio (SNR)

The signal-to-noise ratio (SNR) is an important measure of image quality which should be considered in the acquisition and assessment of MRI images. Background noise in an MR system arises from different sources but is primarily thermal in nature, arising from resistance within the RF coils and losses from the imaged object.

SNR may be calculated either theoretically or practically. Theoretical SNR calculations are based upon the imaging parameters employed in the sequence,

such as voxel resolution and bandwidth, as well a term called the geometry factor ("g-factor"). The g-factor accounts for the heterogenous distribution of noise and is dependent upon the number and location of coils as well as the parallel imaging technique employed. Theoretical calculation of the g-factor can be difficult; for consistency, and to confirm real-world applicability, in this thesis we adopt a practical approach to SNR measurement. We employ a common approach to measurement of SNR [78, 79] such that

$$SNR = \frac{S_I}{\sigma_N} \tag{2.12}$$

where $S_I$ is the mean signal intensity in an ROI placed in a region of homogeneous high signal in the imaging object, and $\sigma_N$ is the standard deviation of the signal intensity within one or more ROIs placed in air. The specific placements of the ROIs for measurement of SNR will be discussed in each relevant section.

MRI-based noise is Gaussian in nature. In the output magnitude-only MRI images, however, noise is skewed into following a Rician distribution. Where the true signal is zero, the noise follows a special case of the Rician distribution known as the Rayleigh distribution. Whilst the signal within the anatomy of interest may still be approximated as Gaussian owing to its high SNR, the signal within the air follows this Rayleigh distribution. We therefore must introduce a statistical factor to correct for the different intensity distributions in measurement of SNR. This factor is is equal to 0.66 or $\sqrt{2 - \frac{\pi}{2}}$ and accounts for the relationship between the standard deviations of each statistical distribution. SNR is therefore finally calculated as

$$SNR = 0.66 \times \frac{S_I}{\sigma_N} \tag{2.13}$$

It should be noted that absolute measurement of SNR from MRI images can be difficult due to the aforementioned heterogenous distribution of noise, therefore it is usually best to compare SNR calculations relative to one another using a consistent method rather than being confident in a definitive stand-alone measurement of SNR.

#### 2.2.1.10 Imaging Artefacts

MRI images are subject to a variety of artefacts, which may arise from user error, hardware issues, or the imaging subject.

**Motion** It may not always be feasible for participants to remain completely stationary throughout a scan. Participant motion during an MR acquisition typically generates an artefact in the phase-encoding direction; this is because phase-encoding steps in k-space are acquired more slowly than frequency-encoding steps. If a participant changes position in between MR acquisitions this may lead to difficulties with any subsequent image registration or subtraction.

**Wrap Around** Wrap around artefacts occur when the dimensions of the object of interest exceed the field of view of the image. This can lead to parts of excluded anatomy folding over into the image, typically in the phase encoding direction.

**Fat-Water Swaps** Fat-water swaps may arise in chemical shift encoded (CSE) MRI techniques. These techniques aim to generate fat-only and water-only images and are explored extensively in Chapters 3, 4, and 5. Computational errors during signal processing may lead to misidentification of the dominant species (fat or water). This leads to incorrect interpretation of voxel content, such that the content of fat and water appears inverted, or "swapped".

**Partial Volume Effect** The partial volume effect arises from the limited resolution of an MRI acquisition; it occurs when a voxel contains more than one tissue type. This causes the signals in the voxel to be averaged or "blurred", which may lead to inaccuracies in image interpretation and a loss of visualisation of fine structures.

### 2.2.2 Quantitative Imaging

As described in section 2.2.1.2, different tissue types have characteristic $T_1$, $T_2$, and $T_2^*$ values. MR images may be "weighted" by choosing a combination of imaging parameters which highlights the effect of a particular one of these parameters. For

example, $T_1$-weighted images are formed with a short TE and a short TR to minimise transverse relaxation. Meanwhile, $T_2$-weighted images are generated using long TRs, such that most of the longitudinal magnetisation is recovered in between RF pulses, and long TEs, to allow the transverse relaxation to decay to provide $T_2$ contrast.

The clinical interpretation of weighted images is essentially qualitative - a radiologist will assess the relative brightness of the signal in a particular anatomical area and use this to draw conclusions about tissue biology. Computer algorithms may be employed to analyse weighted images but changes in imaging parameters across different dates or scanners may cause differences in image contrast. This may lead to inaccurate conclusions, particularly when evaluating longitudinal changes.

Quantitative MRI aims to directly measure the underlying physical properties of a tissue, independent of measurement conditions. The value of a voxel in a quantitative image does not result from a mixture of different contrasts, as in weighted images, but rather has a direct physical meaning behind it. This enables unbiased interpretation of tissue biology. Quantitative images are typically generated through physics-based models in which the parameter is calculated through the application of a signal model to a series of images. Examples of quantitative MRI parameters include the aforementioned relaxation times $T_1$, $T_2$, and $T_2^*$, but many more exist, such as proton density fat fraction (PDFF), quantitative susceptibility ($\chi$), and the apparent diffusion coefficient (ADC). For details on the quantitative parameters employed throughout this thesis, please see Section 2.2.4.

### 2.2.3 Breast Clinical MR Protocol

Now that we have described key concepts behind image formation in MRI, we continue our discussion from Section 2.1.4.3 to describe the technical basis of clinical breast MRI.

As we have previously described, clinical breast MRI protocols are based around dynamic contrast enhanced (DCE)-MRI, which employs the use of gadolinium-based contrast agents. Gadolinium is a highly paramagnetic element owing to its seven unpaired electrons. The presence of gadolinium induces $T_1$-shortening through

dipolar interactions between the electrons and nearby water molecules; concentrated areas of gadolinium therefore appear bright on $T_1$-weighted images.

DCE-MRI consists of $T_1$-weighted images acquired before and at several intervals after administration of the contrast agent. These images are typically fat-suppressed to avoid the adipose tissue, which appears bright in $T_1$-weighted images, obscuring any regions of enhancement. The temporal images acquired enable clinicians to examine the uptake and wash-out of the contrast agent. A plot of signal intensity against time is commonly used to characterise lesions. Tumours grow a chaotic, leaky vasculature to fuel their growth. Gadolinium chelates from the contrast agent leak into the extravascular space where they remain for a short time until they are reabsorbed into the blood. Malignant lesions therefore typically show rapid early signal enhancement, reflecting the fast leakage of contrast into the tumour environment, followed by signal washout, as contrast redistributes to the bloodstream and is removed. Benign lesions on the other hand typically exhibit a shallower initial uptake, with a subsequent plateau or a continued uptake of contrast agent.

Typically, DCE-MRI images are interpreted qualitatively. The properties of the time-intensity curves are visually classified into one of several categories by a radiologist (Figure 2.10). As per ACR BI-RADS® guidance [80], the initial phase of the curve is defined as slow/medium/fast whilst the intermediate and late phase may be classed as persistent (Type IA and IB), plateau (Type II), or washout (Type III). Quantitative metrics may be generated from the signal enhancement curve, but the reproducibility of these metrics is poor across different MRI scanners [81]. In addition to signal intensity, several other qualitative features are used to inform lesion assessment. These include the shape of the mass, the appearance of its margin, and the pattern of enhancement within the lesion.

Many clinical protocols include $T_2$-weighted imaging for identification of cysts and other structures with high water content. Non-fat-suppressed $T_1$-weighted images may also be acquired for identification of fat-containing lesions such as lipomas and fat necrosis.

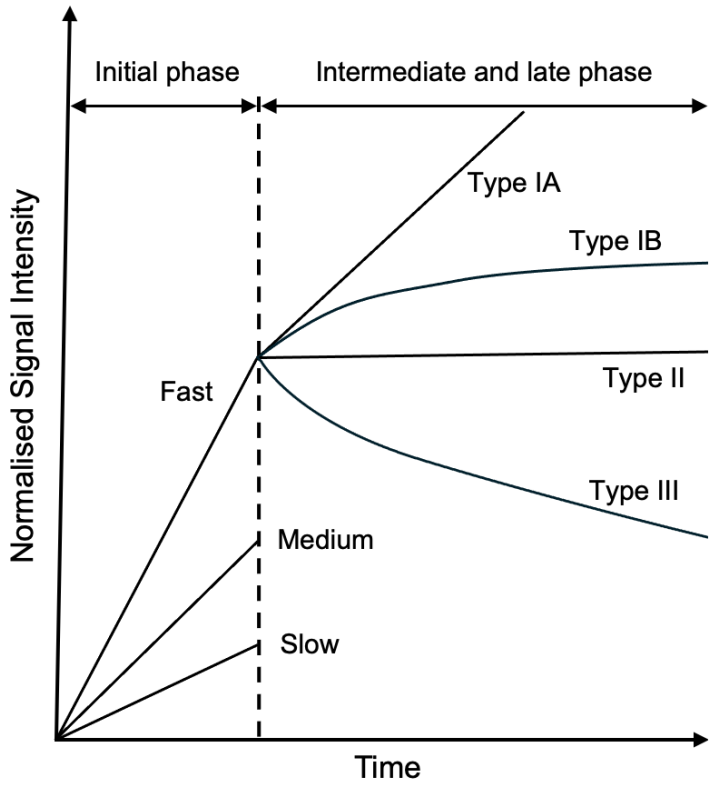


**Figure 2.10:** Illustration showing different categories of time-intensity curves in the initial post-contrast phase and the intermediate and late post-contrast phase. Figure inspired by Kuhl et al. [82] and McClymont [76].

In recent years, diffusion-weighted imaging (DWI) has begun to be employed in breast MR protocols. This technique aims to assess the random Brownian motion of water molecules in a tissue. Malignant lesions are typically hypercellular which restricts the movement of water molecules, leading to lower diffusion within malignant lesions than benign lesions. The addition of DWI has been shown to improve the specificity of breast MRI [83, 84], suggesting utility in diversifying from assessment of neovascularity alone.

Diffusion-weighted sequences apply motion-sensitizing gradients which impart variable phase on water molecules dependent upon their motion relative to the gradient. The b-value of a diffusion gradient determines its sensitivity to the motion of water molecules such that

$$S(b) = S_0 e^{-b \times \mathrm{ADC}} \tag{2.14}$$

where $S(b)$ is the signal intensity with b-value $b$, $S_0$ is the signal intensity without a diffusion gradient, and ADC is the apparent diffusion coefficient. Quantitative maps of ADC may be generated with the acquisition of at least two b-values. Typically, diffusion weighted imaging utilises EPI sequences to minimise the scan time to avoid image misregistration caused by participant motion in between subsequent acquisitions. A cut off in ADC may be used to influence breast lesion assessment, with current recommendations suggesting ADC $\lesssim$ 1.0 x $10^{-3}$ $mm^2/s$ indicates malignancy [85]. Whilst guidance on the interpretation of DWI is not currently specified in the BI-RADS® guidelines [80], it is expected to be included in the next version to reflect its increasing use in the clinic.

Abbreviated breast MRI protocols are increasingly adopted in practise. These protocols aim to shorten the overall examination time by focusing on acquisition of the most essential DCE-MRI images for diagnosis. Typically, one pre-contrast image and one-post-contrast image are acquired. Abbreviated MRI protocols are typically only a few minutes long and have been shown to yield comparative diagnostic success compared to full protocols [86, 87]. Currently, abbreviated MRI is being evaluated in an NHS framework with the FAST MRI Research Programme [88]. Ultrafast MRI is also increasingly explored, which emphasises the sampling speed of images during the initial contrast uptake phase. Ultrafast sequences may be included as part of abbreviated breast MRI protocols to capture maximal information in the shortest amount of time.

### 2.2.4 Quantitative MRI Parameters in Thesis

Here we briefly introduce the primary quantitative MRI parameters employed in this thesis.

**PDFF** Proton density fat fraction, or PDFF, is a quantitative measure of tissue fat concentration. PDFF has been extensively used in the diagnosis, staging, and management of metabolic dysfunction-associated steatotic liver disease (MASLD)

[14, 89]. PDFF also demonstrates increasing utility in characterisation of fat content in other tissues, such as the pancreas [90], bone marrow [91], and skeletal muscle [92].

PDFF is measured using chemical shift encoded (CSE)-MRI techniques, which exploit the difference in resonant frequency between protons in water molecules and protons in fat molecules (triglycerides). In these techniques, multi-echo gradient echo images are acquired. The signal in a voxel containing fat and water acquired at echo time $t_n$ may be described as

$$S_n = (\rho_W e^{i\phi_W} + \rho_F e^{i\phi_F} C_n) e^{-R_2^* t_n} e^{i(2\pi\psi t_n)} \tag{2.15}$$

where $R_2^* = \frac{1}{T_2^*}$, $\psi$ is the frequency shift due to field inhomogeneities (the "field map"), $\phi_W$ and $\phi_F$ are the phase offsets of fat and water protons at $t = 0$, $C_n = \Sigma_{(p=1)}^{P} \alpha_p e^{i2\pi f_p t_n}$ is a known spectrum of fat with P peaks, relative amplitudes $\alpha_p$ and relative frequencies $f_p$, and $\rho_W$ and $\rho_F$ are the water amplitude and fat amplitude respectively. The signal equation is solved for unknown variables $\rho_W$, $\rho_F$, $R_2^*$, $\psi$, and $\phi_0$, usually through the application of a linear least-squares algorithm across the different echo times. Techniques behind the solution of this signal equation are explored in Chapter 5. PDFF is finally calculated as

$$PDFF = 100\% \times \frac{\rho_F}{\rho_W + \rho_F} \tag{2.16}$$

In this thesis, we explore the calculation and application of PDFF in the breast, and demonstrate its potential in quantifying breast density and characterising properties of breast adipose tissue such as adipocyte size and phenotype.

**$T_2^*$** As described in Section 2.2.1.2, $T_2^*$ is the effective transverse decay time, which is reconstructed simultaneously to PDFF in the chemical-shift encoded MRI technique described above. Figure 2.11 shows example $T_2^*$ and PDFF maps of the liver. The presence of iron shortens $T_2^*$ due to its strong paramagnetic properties. $T_2^*$ may therefore be used to accurately estimate liver iron content (LIC) [16, 94]. Thus far, $T_2^*$ has primarily been used in the diagnosis of iron overload diseases, such as haemochromatosis, but may also have applications in measurement of

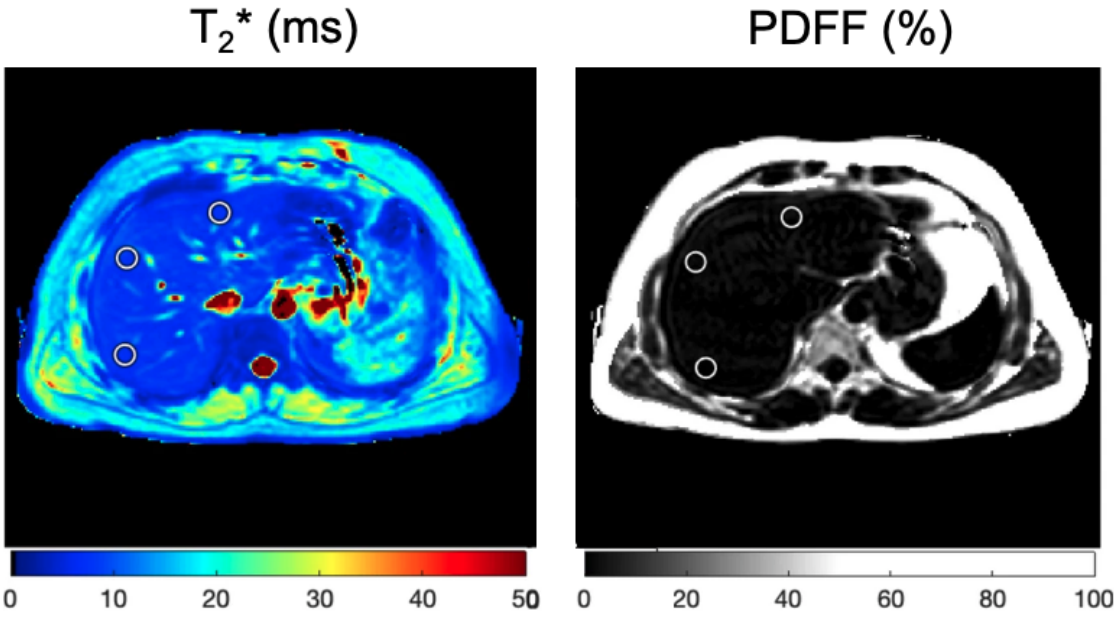


**Figure 2.11:** Example $T_2^*$ (left) and PDFF (right) maps of the liver. The colour bars correspond to the $T_2^*$ and PDFF values of each voxel. Figure adapted from Dennis et al. [93] under CC BY 4.0. [32].

iron sparing diseases, such as hepatocellular carcinoma [95]. $T_2^*$ is also affected by paramagnetic deoxyhaemoglobin within red blood cells, and is therefore dependent upon blood oxygenation and tissue vascularity [96].

Whilst this metric has not yet been extensively quantified in the breast, research suggests $T_2^*$ may be able to distinguish between invasive breast cancers and ductal carcinoma in situ [97]. The $T_2^*$ of DCIS was found to be shorter than that of invasive cancer; the biological basis behind this finding is unclear but may result from the increased presence of calcifications in DCIS. An alternative explanation may be that magnetic field inhomogeneities are induced by tissue interfaces in the fibroligamentous tissue which lies adjacent to the affected ducts of DCIS. In another study, $T_2^*$ was shown to correlate to pathological response in breast cancer after chemotherapy, which may reflect the anti-vascular effects of the treatment [98]. $T_2^*$ measured in breast tumours has been shown to be independent of DCE-MRI and DWI metrics, suggesting it may provide additional information to these methods [99].

In this thesis, we explore the use of $T_2^*$ in the characterisation of breast adipose tissue as a potential correlate for adipose tissue vascularity, and for the density

of iron-bearing mitochondria within adipocytes.

**Other Parameters** Participants' clinical scans were not available for consultation in this thesis. ADC maps were therefore used alongside standard $T_1$- and $T_2$-weighted images in Chapter 8 to guide localisation of lesions in the images in conjunction with the participants' reported medical history. Multi-shot EPI sequences were acquired as described in Section 2.3.2. ADC maps were calculated using a non-linear fitting algorithm with Perspectum Ltd. software (Perspectum Ltd., Oxford, United Kingdom).

## 2.3 Data Sources

### 2.3.1 Studies

The MR data employed throughout this thesis was derived from three sources; the IMOGEN study, the RADIUS study, and a technical development research agreement with Perspectum Ltd. The participant procedures and MR protocol employed varied slightly between these studies, but all participants received a non-contrast 1.5T breast MRI scan which included standard weighted acquisitions and acquisitions intended to generate quantitative MR metrics. Please see Section 2.3.2 for further details.

#### 2.3.1.1 IMOGEN

The IMOGEN study is a large-scale observational cohort study which aims to develop and evaluate quantitative non-contrast MRI methodologies in breast disease [100]. This study aims to recruit over one thousand women who have been referred to a secondary care breast clinic, in addition to a small cohort of healthy volunteers and women with confirmed breast cancer. All participants must be 30 years of age or older. The IMOGEN study was reviewed and given favourable opinion by the West of Scotland Research Ethics Committee (REC reference: 20/WS/0110).

Study participants attended a single visit in which they gave written informed consent and a medical history, underwent anthropometric measurements including

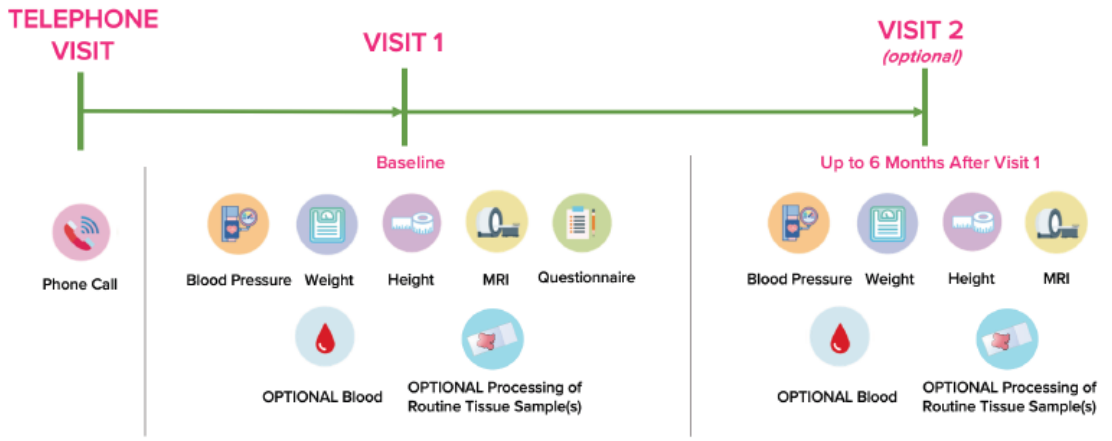


**Figure 2.12:** IMOGEN Study Flowchart. Figure reproduced from Perspectum Ltd.

height, weight, and blood pressure, and a received a non-contrast breast MRI scan (Figure 2.12). Some participants also gave blood for biochemical analysis. Furthermore, as we describe in more detail in Chapter 10, some participants were asked to consent to additional histological processing of tissue samples scheduled to be removed as part of their routine care. An optional second visit was available if needed for the purpose of clarifying findings in the baseline images.

All participants received a breast MRI scan in the standard prone position using a breast RF coil. Some participants also underwent additional MR imaging in the supine position using flexible body coils whilst wearing a rigid plastic bra to support the breasts during the scan. For further details on this bra and the supine data acquired, please see Chapter 9.

After the MRI scan, participants were given a questionnaire which asked them to describe their experience and comfort levels during the scan. For participants with suspected breast disease, the participants' subsequent clinical diagnosis was collected from their medical records or, for self-referred participants, through contacting the participant directly.

Participants for the IMOGEN study were recruited from two clinical sites and one patient identification centre (PIC), or were self-referred.


**Figure 2.13:** RADIUS Study Flowchart. Figure reproduced from Perspectum Ltd.

#### 2.3.1.2 RADIUS

The RADIUS study is a cross-sectional observational study which aims to develop and assess novel MRI techniques in their quantification of multiple organ measurements [101]. RADIUS is split into different sub-projects, with each one aiming to develop MRI techniques in a different organ or disease area. The data employed in this thesis derived from the breast RADIUS sub-project (RGP-7). The RADIUS study was reviewed and given favourable opinion from the West of Scotland Research Ethics Committee (REC reference: 21/WS/0066).

Unlike the IMOGEN study, RADIUS participants were not required to have been referred to a secondary care breast clinic. Participants recruited under RADIUS included healthy volunteers, women with confirmed breast cancer, and women with confirmed benign disease. All participants were 18 years of age or older.

Participants made up to two separate visits for the study, during which they gave informed consent, provided a medical history, and underwent basic anthropometric measurements including blood pressure, height, and weight (Figure 2.13). Spirometry and vicorder measurements were available as optional additional procedures. All participants received a non-contrast breast MRI scan. As with the IMOGEN study, all participants were imaged in the prone position, and some underwent

additional imaging in the supine position with or without a plastic bra. Participants also received an experience questionnaire after the scan.

Both the IMOGEN and RADIUS studies are sponsored by Perspectum Ltd.

#### 2.3.1.3 Technical Development

In addition to clinical investigation studies, Perspectum Ltd. also carries out scans under a technical development research agreement to develop MR methodologies for potential future applications in studies. Under this agreement, participants were imaged for development of non-contrast breast MRI technologies. Participants imaged under the technical development agreement included healthy volunteers and participants with benign breast disease. All participants gave written informed consent and underwent at least one non-contrast breast MRI scan. Participants were scanned in at least one position of prone, supine, or supine with a plastic bra.

### 2.3.2 MR Data

The data in this thesis was sourced across three sites from four different 1.5T MR systems. These included one Siemens Magnetom Aera, one Siemens Magnetom Avanto, and one Siemens Magnetom Sola (Siemens Healthineers, Erlangen, Germany), as well as one GE Voyager (GE Healthcare, Chicago, USA). The protocols across the different vendors and models were similar but varied slightly according to study restrictions and scanner capabilities. Relevant acquisitions in the *in vivo* MR protocols are described below. Please see the tables included in Appendix A for full details of acquisition values.

**Weighted Acquisitions** Where possible, after an initial three-plane localiser, all participants were scanned with a $T_1$-weighted sequence and a $T_2$-weighted sequence for the purpose of subsequent scan planning and anatomical identification. To maintain clinical relevance, these scans were pulled from the manufacturer's standard breast protocol library. On both Siemens and GE, $T_1$-weighted images were generated with a fast low angle shot (FLASH) dual-echo Dixon approach, a type of spoiled GRE imaging with a low flip angle and a strong spoiler gradient to

minimise transverse relaxation. On GE, this sequence used ultrafast gradients and a preparation pulse; this is referred to as fast spoiled gradient echo (FSPGR) by GE nomenclature [102]. The Dixon approach used on both manufacturers enables the scanner to generate in-phase, out-of-phase, water, and fat images from these acquisitions. The $T_2$-weighted images were acquired using turbo (also known as "fast") spin echo (TSE/FSE) acquisitions on both manufacturers, though the GE sequence also included a 90° flip-back pulse for faster relaxation of the longitudinal component (fast recovery FSE or frFSE).

**Multi-Echo Gradient Echo** All participants were scanned with a three-dimensional six-echo spoiled gradient echo sequence for the purpose of generating PDFF and $T_2^*$ maps with CSE-MRI. This is referred to as a "multi-echo GRE" sequence throughout this thesis for simplicity. A low flip angle was used to minimise $T_1$-weighted effects. The sequences were adapted from existing multi-echo GRE sequences commonly used in liver PDFF quantification, and are therefore hereafter referred to as "LMS IDEAL 3D" on Siemens scanners and "IDEAL-IQ" on GE scanners.

The multi-echo GRE sequences were matched closely between vendors but scanner restraints lead to slight variations in the MR parameters; please see Chapter 3 for evaluation of the impact of these differences. Both sequences acquired complex echo data; however, whilst both the magnitude and the phase raw echo data could be exported on Siemens scanners, due to manufacturer restrictions, only magnitude data was able to be exported on the GE machine. This restricted the CSE-MRI signal model which could be used in post-processing - please see Chapter 5 for further discussion on the algorithms employed to generate the PDFF and $T_2^*$ maps.

**Diffusion** Where possible, participants were scanned with an EPI sequence for quantification of ADC. Whilst all scanners employed a multi-shot EPI acquisition, the RESOLVE technique was employed on Siemens Aera and Sola scanners. This enables high resolution diffusion imaging through readout segmentation of the multi-shot EPI acquisition. All diffusion acquisitions employed b-values in accordance with current clinical guidelines [103].

## 2.4 Summary

This chapter has provided an overview of the central concepts associated with this thesis. In particular, it has described breast anatomy and breast disease, summarised important factors in assessment of breast cancer risk, and described the different imaging modalities used in the clinical assessment of breast cancer. This chapter has also provided a brief introduction to MRI physics and quantitative imaging, described the MR parameters explored in this research, and detailed the data sources employed throughout.

# 3

# Optimal Approach for Breast CSE-MRI: Influence of the Pulse Sequence

In Chapter 2 we introduced chemical shift encoded (CSE-) MRI and briefly described how this technique enables quantification of proton density fat fraction (PDFF) and $T_2^*$. CSE-MRI is dependent upon the choice of a number of algorithmic and acquisitive factors, and whilst PDFF and $T_2^*$ have demonstrated wide applicability in other organs, these metrics have not yet been extensively quantified within the breast. We therefore now set out to assess the optimal CSE-MRI method for generating breast PDFF and $T_2^*$ maps. In this chapter, we examine the effect of the choice of multi-echo GRE pulse sequence through *in silico* and *in vitro* analyses.

## Contents

## 3.1 Introduction

CSE-MRI was introduced in a seminal paper from Dixon et al. in 1984 [104]. Dixon's original approach employs two spin echoes acquired at times when the water and fat signals are in-phase and out-of-phase respectively; through the use of simultaneous equations, the signals arising from water and fat respectively may be deconstructed, and a signal fat fraction (SFF) may be calculated. Modern Dixon techniques employ either two or three echoes for fat-water separation, and have been used in conjunction with $T_1$-weighted breast acquisitions for the purposes of fat suppression [105, 106] and fibroglandular tissue quantification [107, 108].

However, these Dixon-based approaches suffer from the assumption of perfect $B_0$ homogeneity, which is difficult to achieve even with modern shimming techniques. Furthermore, as per Equation 2.15, the signal fat fraction is only equal to the proton density fat fraction (PDFF) when the effect of multiple confounding variables have been addressed, such as $T_2^*$ decay and the spectral complexity of fat.

The iterative decomposition of water and fat with echo asymmetric and least-squares (IDEAL) CSE-MRI approach was introduced by Reeder et al. in 2004 [109]. This approach demonstrated how PDFF may be determined through iterative estimation of the field map (a measure of $B_0$ homogeneity) using a multi-echo GRE acquisition. This work provided the basis for modern CSE-MRI approaches, which use multi-echo GRE sequences and correct for confounding variables through their inclusion in the signal model.

An overview of how a GRE signal may be sampled from a multi-echo acquisition is shown in Figure 3.1. The data acquired at each echo time captures a single timepoint in the GRE signal dictated by the signal model. By acquiring multiple echoes, the GRE signal curve can be estimated at each voxel; the unknown variables $\rho_W$, $\rho_F$, $R_2^*$, $\psi$ and $\phi_0$ are solved for in Equation 2.15 and thereby PDFF (Equation 2.16) and $T_2^*$ $(= 1/R_2^*)$ maps can be generated. Both the number of echoes and choice of echo times is important to ensure sufficient sampling of the GRE signal.

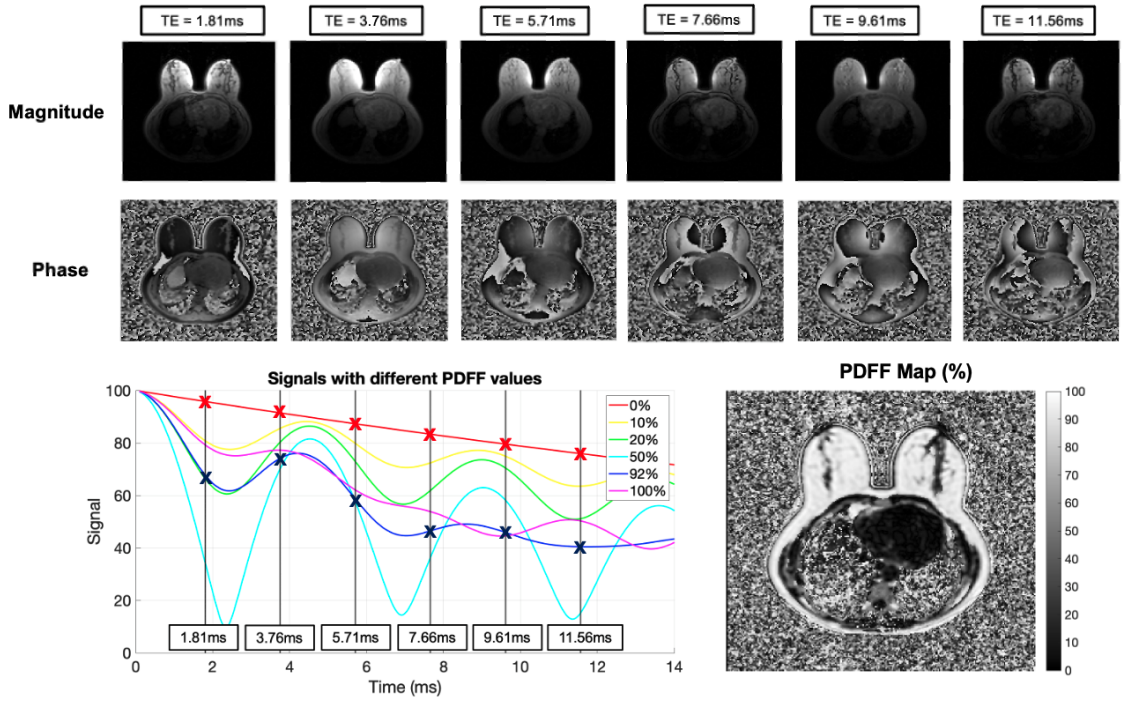


**Figure 3.1:** Overview of PDFF Map Generation. Top: Raw GRE MRI images acquired at 6 different echo times. Both magnitude and phase images are shown. Bottom Left: Simulation showing different GRE signals for a constant $T_2^*$ and varying levels of PDFF. The amplitude of the oscillation of the GRE curve varies with fat content. Black vertical lines show the GRE signal acquired at the six echo times. The red crosses show sampling of the GRE signal in an area of 0% PDFF, such as breast fibroglandular tissue, whilst the blue crosses show sampling of the GRE signal in an area of 92% PDFF, such as in breast fatty tissue [110]. Bottom Right: The PDFF map may be inferred from estimating the GRE curve at each pixel using the images acquired at each echo time.

The choices of flip angle and repetition time in the GRE acquisition must also be carefully considered. The signals arising from water and fat are modified by a bias arising from the difference in $T_1$ between the two species as follows [111]:

$$S_W = \frac{\rho_W(1 - e^{-TR/T_{1W}})\sin\alpha}{(1 - e^{-TR/T_{1W}}\cos\alpha)} \tag{3.1}$$

$$S_F = \frac{\rho_F(1 - e^{-TR/T_{1F}})\sin\alpha}{(1 - e^{-TR/T_{1F}}\cos\alpha)} \tag{3.2}$$

This $T_1$ bias effect may be reduced either through lengthening the TR or decreasing the flip angle (FA). Increasing TR extends the acquisition time which may be infeasible in clinical practise, particularly for 3D GRE acquisitions which may already last several minutes. Decreasing the FA reduces the $T_1$ bias without

increasing scan length, but this comes as the expense of SNR. For flip angles significantly lower than the Ernst angle, the signal amplitude is proportional to FA [112], such that halving the flip angle halves SNR.

As described in Section 2.3.2, the MRI data available for use in this thesis was acquired across four different 1.5T scanners from two different vendors. A 6-echo 3D SPGRE acquisition with a low flip angle was acquired across all scanners for calculation of PDFF and $T_2^*$. Due to differences in scanner capabilities, there were slight differences in the sequences across the two vendors; the Siemens sequence ("LMS IDEAL 3D") employed the following parameters $TE_1/\Delta TE/TR$ = 1.81ms/1.95ms/15ms, flip angle 5°, whilst the GE sequence ("IDEAL-IQ") employed $TE_1/\Delta TE/TR$ = 0.92ms/1.36ms/9.84ms, flip angle 6°[1].

In this section we evaluate the two multi-echo GRE sequences through simulations and phantom scans to ensure that quantification of PDFF and $T_2^*$ is invariant to, and accurate across, the different scanner models used in this thesis. This is an important step to undertake prior to imaging volunteers.

## 3.2 Methods

### 3.2.1 Simulations

A parameter space of range 0-100% PDFF and 10-100ms $T_2^*$ was generated. This parameter space was chosen according to the approximate physiological ranges of PDFF and $T_2^*$ expected to be observed at 1.5T in the human breast. Reference $T_2^*$ values within the breast have not yet been published at 1.5T, therefore a wide exploratory $T_2^*$ range was employed. This range encompassed the reference values published at 3T [97, 113] and accounted for values observed in a preliminary examination of *in vivo* breast $T_2^*$ maps at 1.5T.

To evaluate the impact of the choice of TEs, raw echo data was generated across the parameter space at the echo times employed in the GE and Siemens acquisitions[2]. The simulated echo data were fitted using a magnitude-only algorithm, MAGO

[1] Complete details of all GRE scan parameters are available in Appendix A.

[2] I gratefully acknowledge the use of the ISMRM Fat Water toolbox in this work [114].

[15], and a multi-peak fat spectrum derived from subcutaneous adipose tissue [115]. An overview of the MAGO algorithm is provided in Chapter 5; this algorithm was employed due to its use as the proprietary algorithm of Perspectum and due to its lack of reliance on phase echo data, which cannot be exported from all scanner types. Additional simulations were performed to evaluate the impact of $T_1$ bias in the GRE sequences through multiplying the simulated water and fat signals by the GRE $T_1$-weighting factors detailed in Equations 3.1 and 3.2 before processing with MAGO. $T_{1f}$ was set as 296ms and $T_{1w}$ was set as 1266ms to reflect reported $T_1$ values of breast fatty tissue and fibroglandular tissue respectively [116].

Complex Gaussian-distributed noise with an amplitude of 0.2% the maximum signal across the simulated echo data was added to the echo images. This noise level was selected to reflect approximate noise observations in in-vivo GRE data. The simulations were run 10,000 times to mimic an ROI of 100×100 voxels for each value combination of $T_2^*$ and PDFF. The difference between the calculated PDFF and $T_2^*$ values and the true PDFF and $T_2^*$ values was found at each iteration. Finally, the mean error and the standard deviation of the error across the iterations were calculated.

### 3.2.2 Phantom Scans

Four phantoms were scanned across the four scanners to assess the accuracy of PDFF and $T_2^*$ measured with the 3D GRE sequences. All phantoms were originally commissioned for commercial purposes by Perspectum Ltd. Due to phantom availability, the specific phantom scanned at each site varied, but all phantoms followed the same basic design (Figure 3.2). Please see Appendix B for further information on the phantoms employed for this work.

Each phantom consisted of a number of sealed vials within an acrylic spherical housing unit which was filled with a doped flood solution to improve local magnetic field homogeneity. Some of the phantom vials contained a known mixture of peanut oil and agar; the relative proportion of these components set the "known" PDFF value within these vials. Additionally, the agar components of some phantom vials

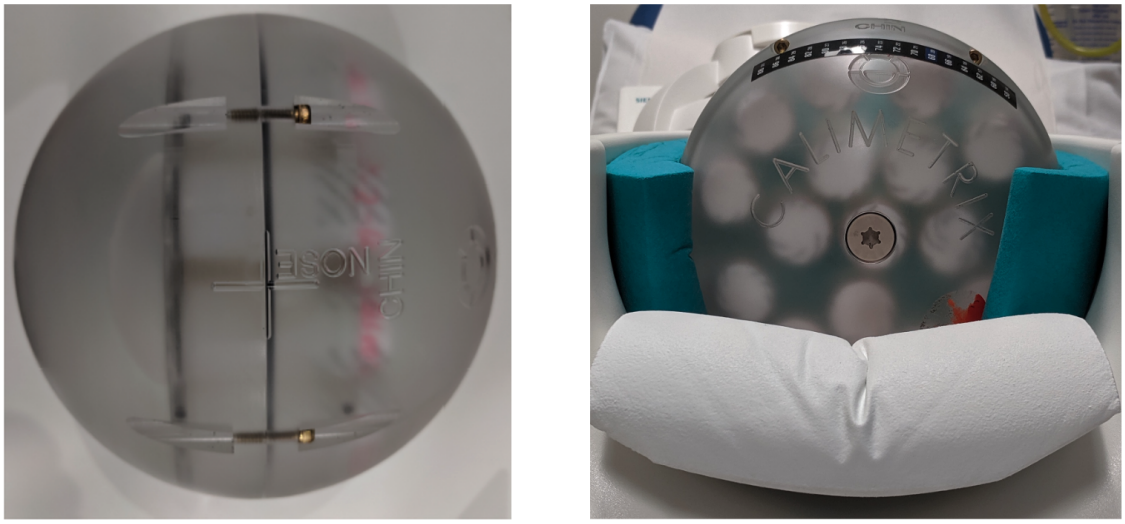


**Figure 3.2:** Example of a spherical flood phantom, showing the spherical acrylic housing, vials, and LCD thermometer strips. The "CHIN" and "NOSE" markings assist with phantom positioning inside the head coil, shown on the right. Photos reproduced from Perspectum Ltd.

without peanut oil were doped with manganese chloride to alter the $T_2^*$. Figure 3.3 shows two example phantom $T_2^*$ and PDFF maps.

Unlike $T_1$ and $T_2$, which are inherent properties of a substance, there are no theoretical relaxivity equations which govern calculation of $T_2^*$ given the known concentrations of the phantom components[3]. To ensure a consistent approach to determining a "known" $T_2^*$ value for each vial, we use the $T_2^*$ as measured with an MRI sequence which is used as the "gold standard" for $T_2^*$ measurement by Perspectum Ltd., LMS MOST [95, 117]. Reference LMS MOST $T_2^*$ values were already available for each phantom.

Phantoms were kept in a temperature-stable environment for 24 hours prior to scanning, and the phantom temperature was recorded immediately before the scan using an LCD thermometer. Phantoms were scanned using the head coil available at each scanner, and were secured with foam padding as shown in Figure 3.2.

Acquired echo images of the phantoms were fitted using MAGO and a multi-peak peanut oil spectrum corrected for a temperature of 22°C [118, 119]. Circular regions-of-interest (ROIs) with a diameter of 15mm were placed by one operator within

[3]For further details on relaxivity equations, please see Appendix C.

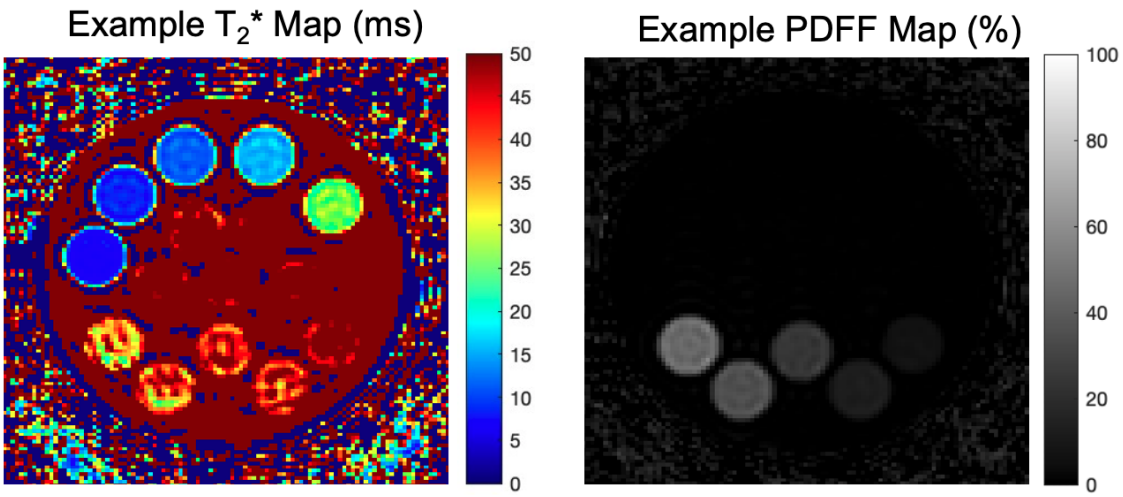


**Figure 3.3:** Example $T_2^*$ (left) and PDFF (right) maps of a spherical flood phantom. The five $T_2^*$ vials are visible at the top of the phantom and the five PDFF vials at the bottom.

the vials; the median PDFF and $T_2^*$ were then extracted and compared against the known values. The "median" operator was employed on the recommendation of Roberts et al. [120] who demonstrated that, particularly at lower SNRs, the median produces a less biased estimate of ROI-based PDFF than the mean.

## 3.3 Results

### 3.3.1 Simulations

Simulations performed using the Siemens and GE GRE parameter values are shown in Figures 3.4 and 3.5 respectively. The mean error in PDFF and $T_2^*$ throughout the parameter space for both acquisitions is low, demonstrating sufficient sampling of the GRE signal by both sets of echo times. Markers on the figures show two example combinations of $T_2^*$ and PDFF in breast fibroglandular tissue (black) and fatty tissue (yellow). The mean error in PDFF across both manufacturers at these example data points is less than 0.01%, whilst the mean error in $T_2^*$ is less than 0.03ms. We expect the majority of pixels in the breast to reflect the approximate set of values in these example data points, suggesting that minimal bias is incurred in measurement of PDFF and $T_2^*$ as a result of the choice of echo times.

The standard deviation of the error in PDFF and $T_2^*$ is greatest at a value of approximately 65% PDFF for Siemens and 55% PDFF for GE. As explored in Chapter 5, in magnitude-based CSE-MRI algorithms, typically two candidate solutions for PDFF and $T_2^*$ are found. Up until a given PDFF value, the PDFF and $T_2^*$ from the first solution will be assigned, and thereafter the second solution is used. This PDFF value is known as the "switching point"; due to the use of a multi-peak fat spectrum, this is not necessarily at 50%. The value of the switching point also varies according to the choice of echo times and field strength [15]. The highest ambiguity between the two candidate solutions lies at the switching point, such that some pixels may be incorrectly assigned to the alternative solution. The standard deviation of the error in PDFF and $T_2^*$ is therefore highest at this value of PDFF. This behaviour of incorrect solution assignment is reflected in the adjacent faint lines of underestimation and overestimation in the mean PDFF error plots.

Simulations reflecting the addition of the $T_1$ effect on both acquisitions, in addition to the choice of echo times, are shown in Figures 3.6 and 3.7. The addition of the $T_1$ bias effect results in an overestimate of PDFF across the parameter space. This overestimate is expected due to the lower $T_1$ of fat compared to water, which biases $S_f$ and $S_w$ according to Equations 3.1 and 3.2. The bias induced by the $T_1$ effect is higher across the GE simulation than the Siemens - this is owed to its slightly higher flip angle (6° versus 5°) and lower TR (9.84ms versus 15ms). The mean error in PDFF at the example fatty tissue point was 2.40% for GE and 1.39% for Siemens, whilst that at the example fibroglandular tissue data point was <0.01% across both manufacturers. The largest overestimate in PDFF throughout the parameter space was 5.15% for Siemens and 9.77% for GE; these values occurred at true PDFFs close to 50%, where the balance of the two species is most equal such that the $T_1$ bias effects are most prominent.

The error in $T_2^*$ remains relatively unaffected by the addition of the $T_1$ effect, with the mean errors at the example data points from both sequences measuring less than 0.02ms. The only notable change in the $T_2^*$ error maps is a slight alteration in

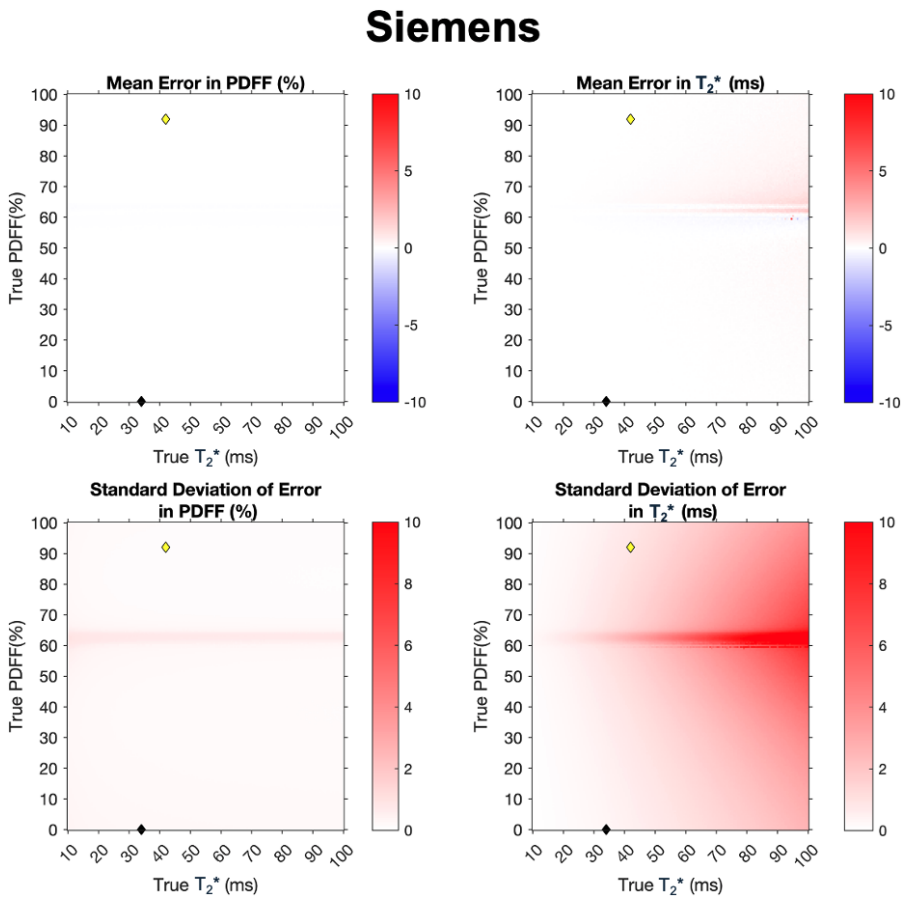


**Figure 3.4:** Simulation showing the impact of the choice of echo times in the Siemens GRE acquisition. Top: Mean error in PDFF and $T_2^*$ across the noise iterations. Bottom: The standard deviation of the error in PDFF and $T_2^*$ across the noise iterations. Two example combinations of $T_2^*$ and PDFF are shown for breast fibroglandular tissue (black diamond) and fatty tissue (yellow diamond) across the plots.

the position of the switching point, now set at a slightly lower true PDFF value to reflect the overestimation in PDFF calculation.

One *in vivo* GE GRE dataset in this thesis used marginally different TE/TR (TE = 0.90ms versus 0.92ms, TR = 9.87ms versus 9.84ms); echo spacing and flip angle were unchanged. Simulations showed at most 0.06% difference in PDFF bias and 0.5ms difference in $T_2^*$ bias across the entire parameter space, and at most 0.01% and 0.01ms differences in the example breast data points. This dataset is therefore included in future chapters, as the deviation in acquisition parameters minimally impacts quantification of PDFF and $T_2^*$.

Additional simulations were performed to assess the impact of reducing the flip

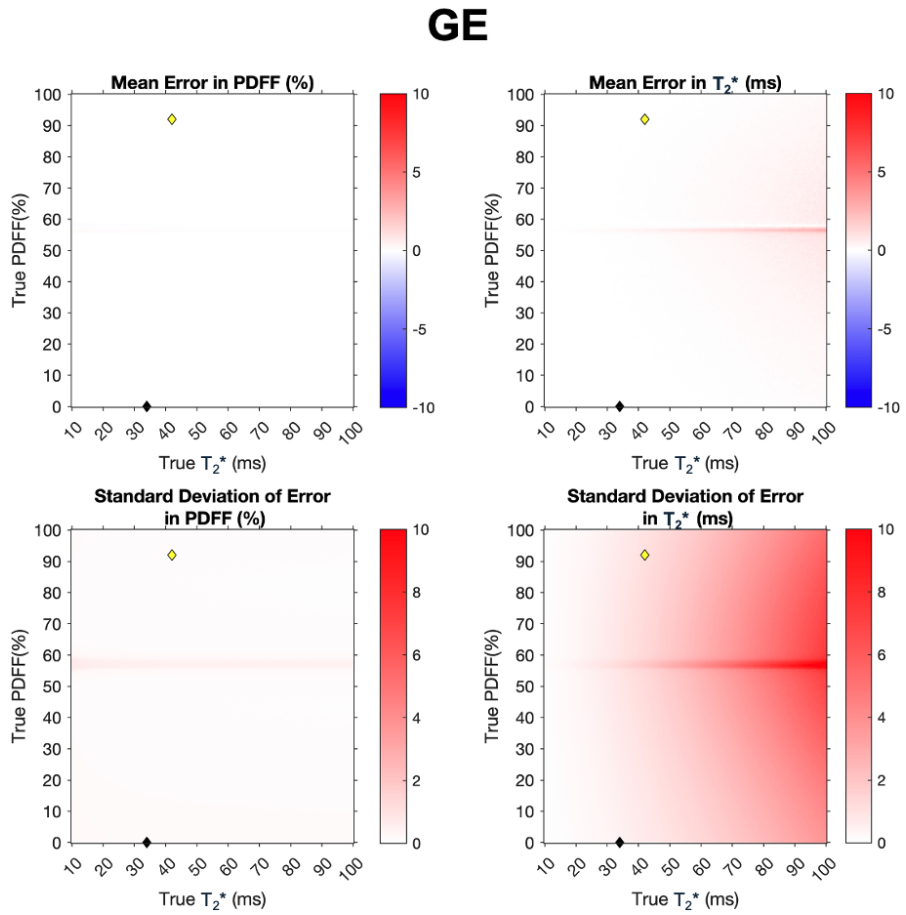


**Figure 3.5:** Simulation showing the impact of the choice of echo times in the GE GRE acquisition. Top: Mean error in PDFF and $T_2^*$ across the noise iterations. Bottom: The standard deviation of the error in PDFF and $T_2^*$ across the noise iterations. Two example combinations of $T_2^*$ and PDFF are shown for breast fibroglandular tissue (black diamond) and fatty tissue (yellow diamond) across the plots.

angle to 1° in the Siemens and GE GRE acquisitions (Figures 3.8 and 3.9). The reduction in the $T_1$ bias effect significantly reduced the error in PDFF throughout the parameter space, but the accompanying decrease in SNR lead to more unreliable quantification, with the standard deviation of the error in the fatty tissue data point increasing 6-fold for PDFF and 7-fold for $T_2^*$.

### 3.3.2 Phantom Scans

Phantom scans revealed a bug in the GE MRI system, wherein the output raw echo data appeared "squashed" compared to the scanner generated maps from the same IDEAL-IQ acquisition (Figure 3.10). This error was found to be caused

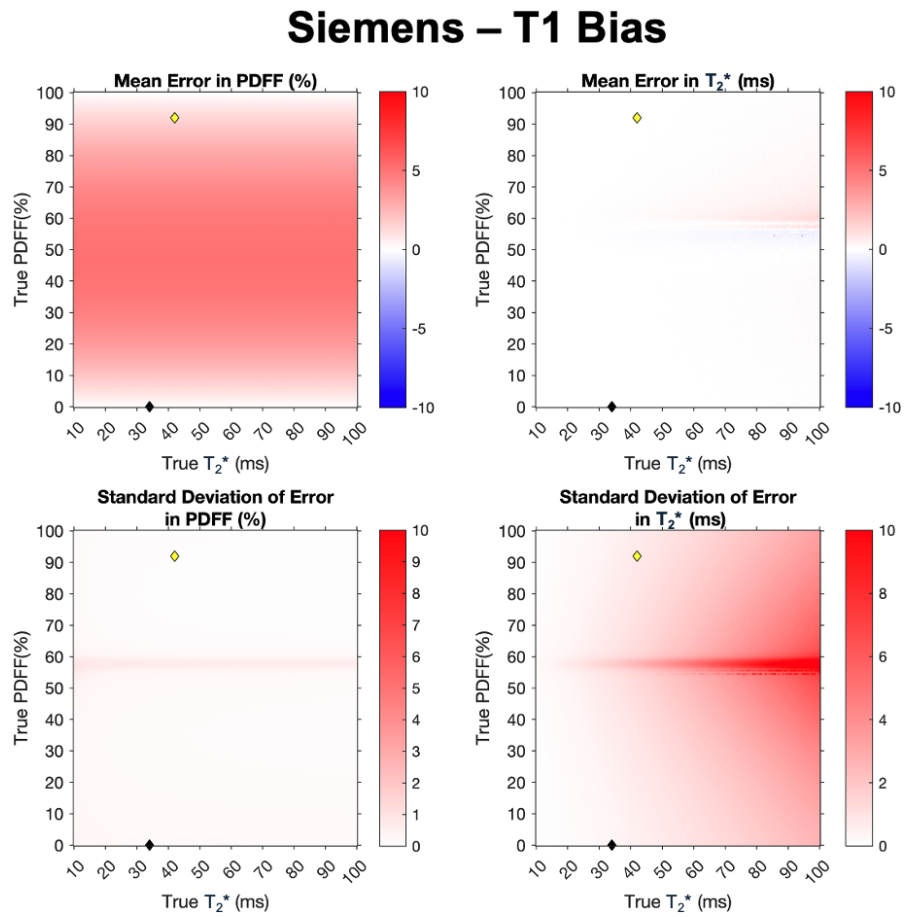


**Figure 3.6:** Simulations showing the impact of the $T_1$-weighting effect and the choice of echo times in the Siemens GRE acquisition. Top: Mean error in PDFF and $T_2^*$ across the noise iterations. Bottom: The standard deviation of the error in PDFF and $T_2^*$ across the noise iterations. Two example combinations of $T_2^*$ and PDFF are shown for breast fibroglandular tissue (black diamond) and fatty tissue (yellow diamond) across the plots.

by switching off the GradWarp option in the User CVs, which is an algorithm which corrects for gradient non-linearity [121]. GradWarp had been turned off for this scan to avoid altering the raw phase echo data. Unfortunately, as elsewhere reported [122], whilst the GradWarp option is turned off, the reconstruction for images with rectangular fields of view is incorrectly assumed to be square. The 90% FOV in the phase-encoding direction in the IDEAL-IQ scan therefore resulted in incorrect calculation of the images by the GE algorithm, such that they appear "squashed" by a factor of 0.9. This error was corrected through resampling of the echo data in MATLAB. The calculated IDEAL-IQ scanner maps (such as the in-phase, out-of-phase, fat, and water maps) were output correctly - presumably

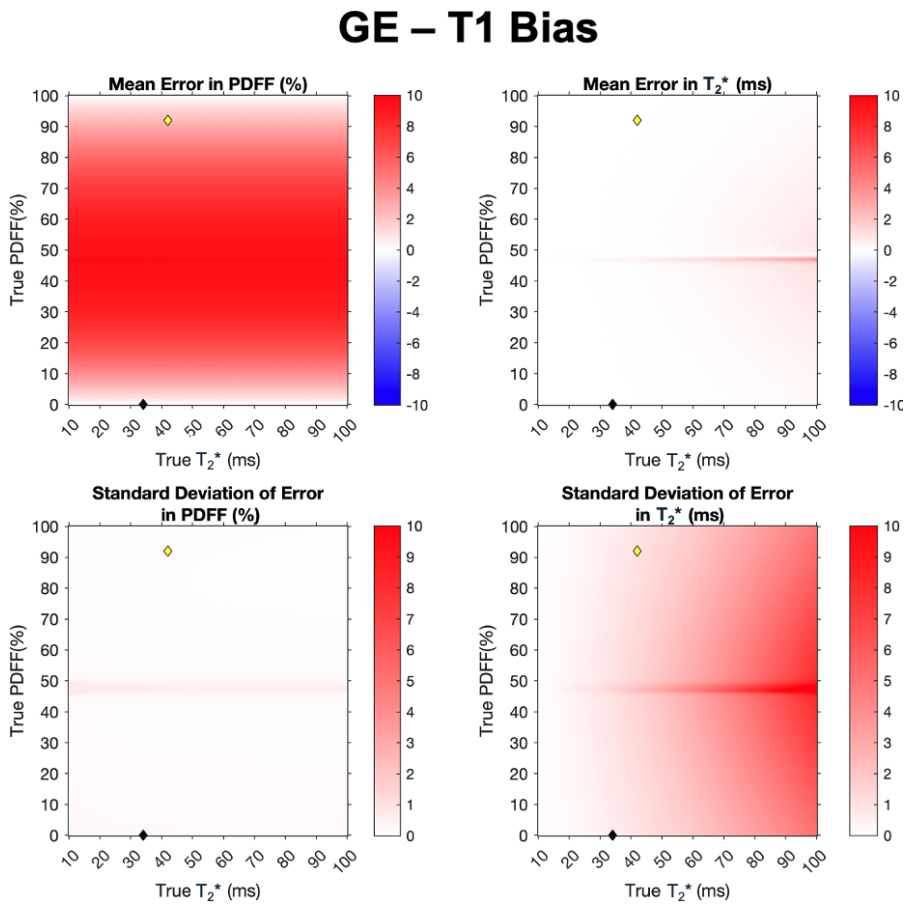


**Figure 3.7:** Simulations showing the impact of the $T_1$-weighting effect and the choice of echo times in the GE GRE acquisition. Top: Mean error in PDFF and $T_2^*$ across the noise iterations. Bottom: The standard deviation of the error in PDFF and $T_2^*$ across the noise iterations. Two example combinations of $T_2^*$ and PDFF are shown for breast fibroglandular tissue (black diamond) and fatty tissue (yellow diamond) across the plots.

due to the application of GradWarp during map calculation overriding the negative User CV option. The presence of GradWarp in the scanner generated maps was confirmed through the appearance of the background noise forming a characteristic barrel shape when windowed, which was not present in the raw echo data.

Furthermore, whilst the IDEAL-IQ raw magnitude echo data could be output from the GE system through manipulation of the User CVs, we were unsuccessful in the export of the raw phase echo data. This is a common issue across many scanners and provides further reason to employ the MAGO algorithm in this analysis.

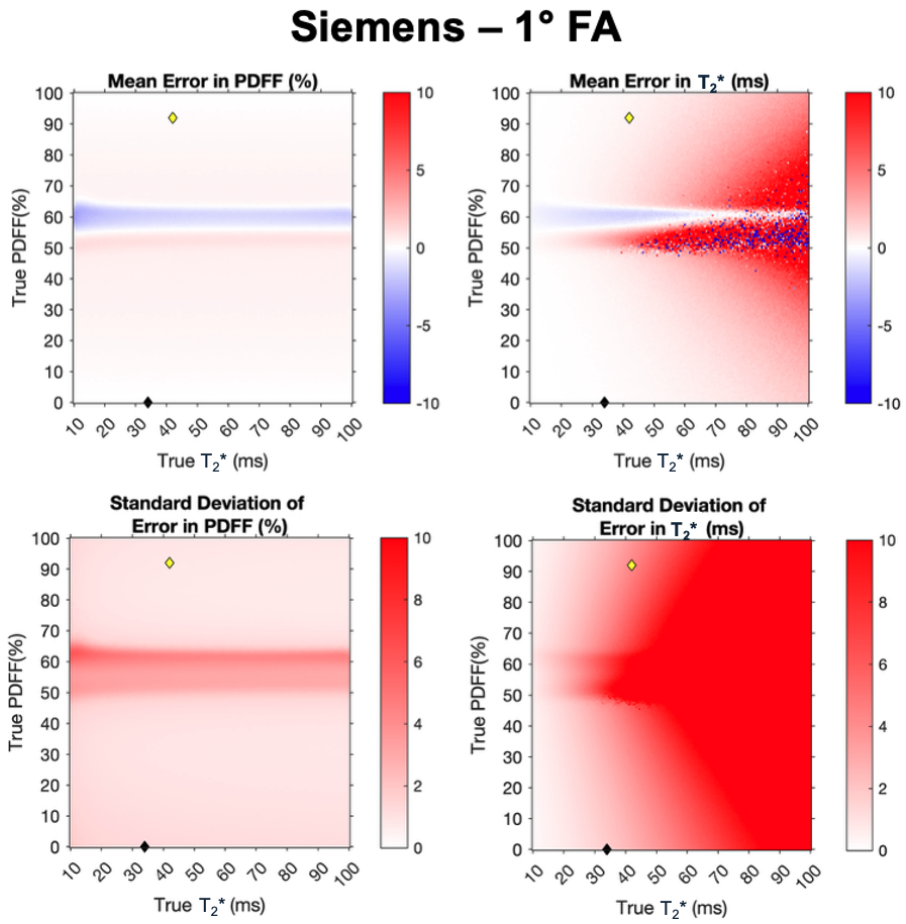


**Figure 3.8:** Simulations showing the impact of employing a 1° flip angle on the Siemens GRE acquisition. Top: Mean error in PDFF and $T_2^*$ across the noise iterations. Bottom: The standard deviation of the error in PDFF and $T_2^*$ across the noise iterations. Two example combinations of $T_2^*$ and PDFF are shown for breast fibroglandular tissue (black diamond) and fatty tissue (yellow diamond) across the plots.

#### 3.3.2.1 PDFF

Figures 3.11 and 3.12 demonstrate the agreement between the known and measured phantom PDFF values across the four scanners. Somewhat counter-intuitively, the agreement appeared to vary according to the scanner model despite the same acquisition protocol being employed across scanners of the same manufacturer. For example, whilst the Siemens Sola demonstrated excellent accuracy in PDFF calculation, with Bland-Altman analysis [123] showing a bias of 0.71% and limits of agreement of -0.2% to 1.6%, the Siemens Avanto scanner demonstrated a much larger bias of 5.99% and limits of agreements of 0.9% to 11.1%.

Further investigation revealed the cause of this discrepancy to be the choice

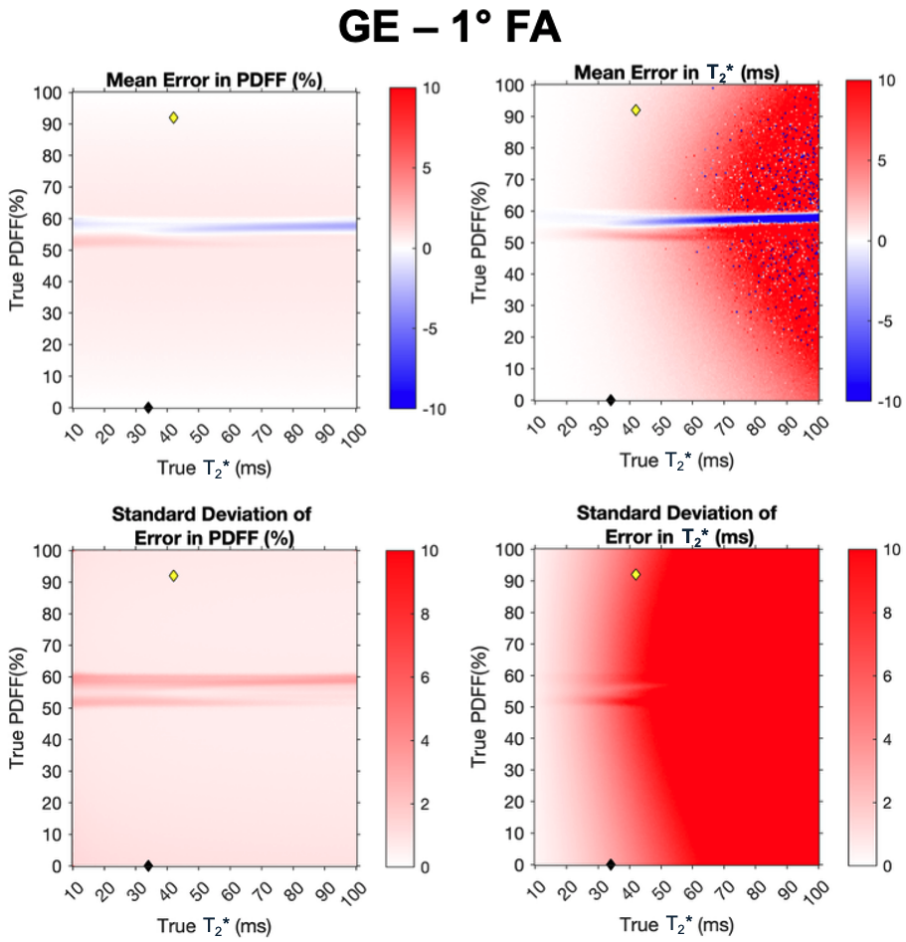


**Figure 3.9:** Simulations showing the impact of employing a 1° flip angle on the GE GRE acquisition. Top: Mean error in PDFF and $T_2^*$ across the noise iterations. Bottom: The standard deviation of the error in PDFF and $T_2^*$ across the noise iterations. Two example combinations of $T_2^*$ and PDFF are shown for breast fibroglandular tissue (black diamond) and fatty tissue (yellow diamond) across the plots.

of phantom employed in each scan. As described, owing to the availability of the commercial phantoms, phantoms from different commercial "series" were scanned at each site (Appendix B). The relevant difference here is the $T_{1f}$ and $T_{1w}$ of the phantoms. Whilst peanut oil was used in all phantoms, such that $T_{1f} \approx 300$ms at 1.5T, the $T_1$ of the agar component varied. In series A phantoms, measurements performed by Perspectum Ltd. showed that the agar measured approximately 630ms at 1.5T, whilst the $T_1$ of the agar component in series B and C lies much closer to that of pure water, measuring approximately 2200ms at 1.5T. The $T_1$ bias effect, resulting in an overestimate in PDFF, is therefore much more pronounced in phantom series B and C owing to the greater difference between $T_{1f}$ and $T_{1w}$.

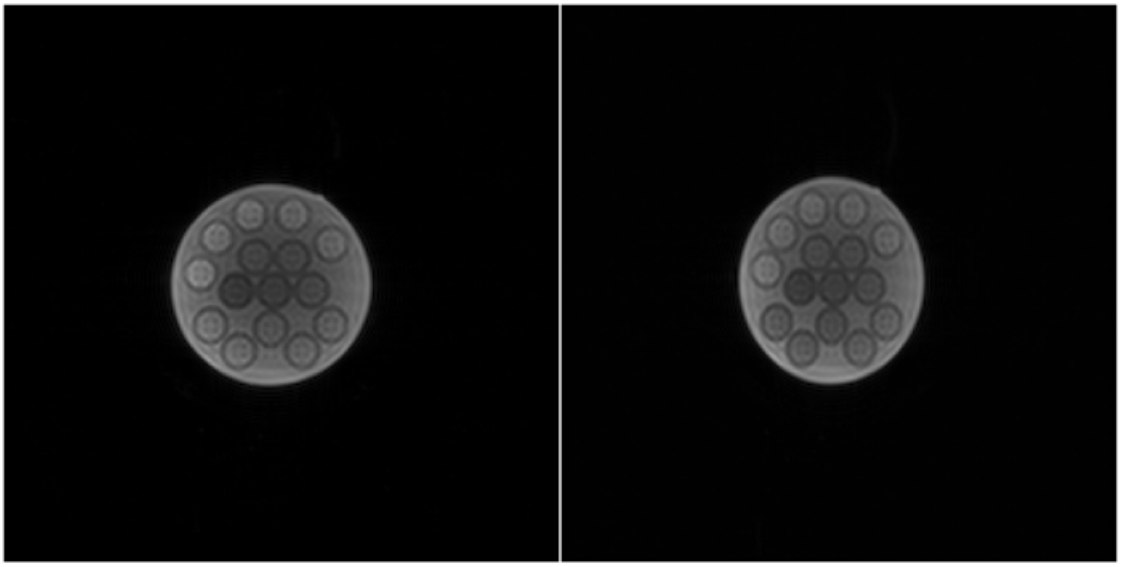

**Figure 3.10:** Demonstration of the GE FOV Reconstruction Bug. Left: In-phase scanner-generated IDEAL-IQ image. Right: Exported raw magnitude IDEAL-IQ echo data at first echo time at same slice location. The echo data on the right appears "squashed" due to incorrect reconstruction in the echo data when the GradWarp setting is off.

The Siemens Avanto and Aera scans, which demonstrate the largest bias, were performed using series B and C phantoms, whilst the GE Voyager and Siemens Sola scans were performed using the series A phantoms.

The trend of the data points within the Bland-Altman plots demonstrate a relationship which is reflective of the $T_1$ bias effect; this is particularly obvious in the Siemens Aera plot, wherein the deviation increases as PDFF increases up to a maximum and then begins to decreases, such that at the 100% PDFF vial the error is minimal.

The two 55% vials in the Aera scan were partially fat-water swapped in the PDFF image; this may be indicative of the proximity of their PDFF value to the switching point. Excluding these vials from analysis (Figure 3.13) demonstrated that the Aera performs similarly to the Avanto, which used a phantom with the same $T_{1w}$, suggesting consistent implementation of the acquisition across scanner models. One series A phantom, with the lower $T_{1w}$, was scanned on the Siemens Aera during development of an alternative acquisition with the same parameters as the LMS IDEAL 3D scan but with 3mm isotropic resolution; Figure 3.14

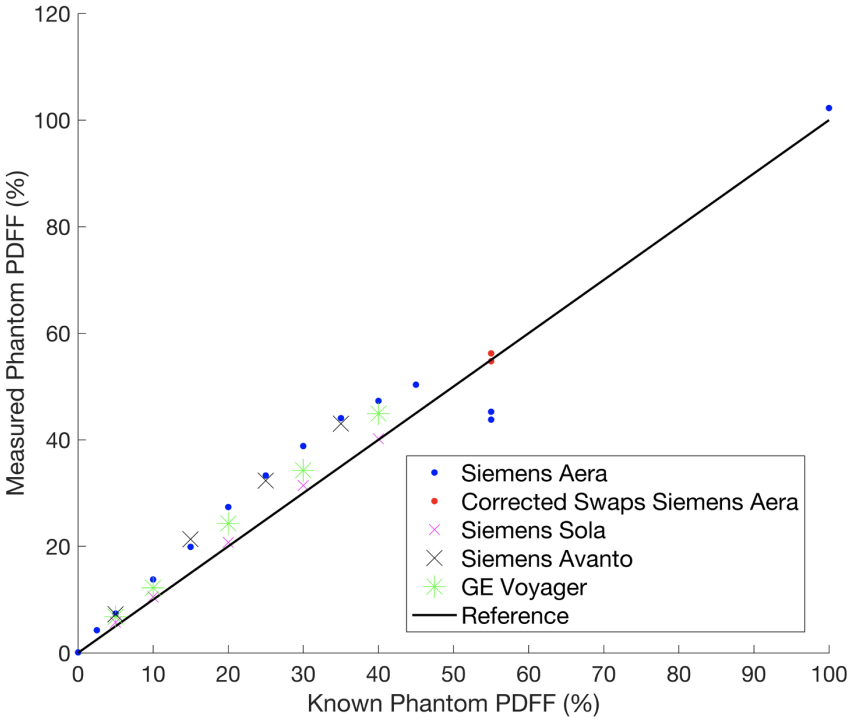


**Figure 3.11:** Overview plot shows the phantom PDFF measured using the two aforementioned 3D GRE sequences for GE and Siemens on four different scanners against the known PDFF. Here, the known PDFF refers to the PDFF specified in the manufacturing instructions. For the Siemens Aera, the corrected values of the fat-water swapped 55 percent PDFF vials are shown in red.

demonstrates the vastly reduced bias and tighter limits of agreement resulting from this change of the $T_{1w}$ of the phantom.

To reflect the simulation in Figure 3.9, an additional acquisition was performed using a 1° flip angle on the GE Voyager, which demonstrated the reduced impact of the $T_1$ bias effect caused by using a lower flip angle (bias 3.49% at 5° (Figure 3.12) versus 1.49% at 1° (Figure 3.15)).

#### 3.3.2.2 $T_2^*$

Figures 3.16 and 3.17 demonstrate the agreement between the known and measured phantom $T_2^*$ values. The accuracy of $T_2^*$ measurement across all four scanners was excellent, with all biases measuring less than 0.5ms. This reflects the appropriate choice of echo times and the robustness of $T_2^*$ to the $T_1$ bias effect demonstrated in Section 3.2.1.

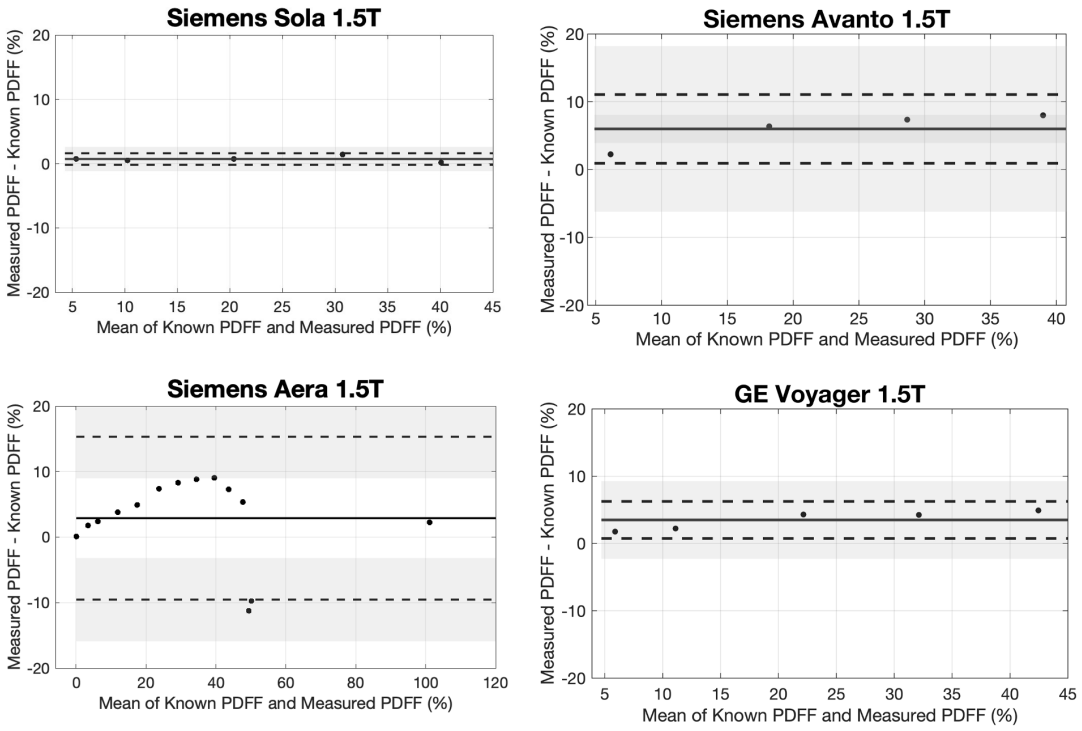


**Figure 3.12:** Bland-Altman plots display the agreement between the known PDFF and the PDFF measured across the four different scanners. As discussed, the discrepancies between the scanners may be attributed in part to the different phantoms employed in each scan.

## 3.4 Discussion

The inferiority of two- and three- point Dixon techniques compared to multi-echo confounder-corrected (CC) CSE-MRI for accurate fat fraction calculation is reported throughout literature [124–127]. In this thesis, we employed a 6-echo GRE sequence with a low flip angle to minimise $T_1$ bias effects, along with a CC-CSE-MRI algorithm which accounts for the spectral complexity of fat and $T_2^*$ decay.

The choice of echo times in both the Siemens and GE GRE acquisitions induced minimal bias in measurement of PDFF and $T_2^*$, suggesting sufficient sampling of the GRE signal. As expected, $T_2^*$ measurement was minimally impacted by $T_1$ bias, but simulations and phantom scans demonstrated the dependency of the PDFF measurement on this effect. The 3D GRE sequences employed flip angles of 5° and 6°, in line with typical values for CC-CSE-MRI [128, 129]. The intention of this choice is to limit $T_1$ bias whilst retaining sufficient SNR.

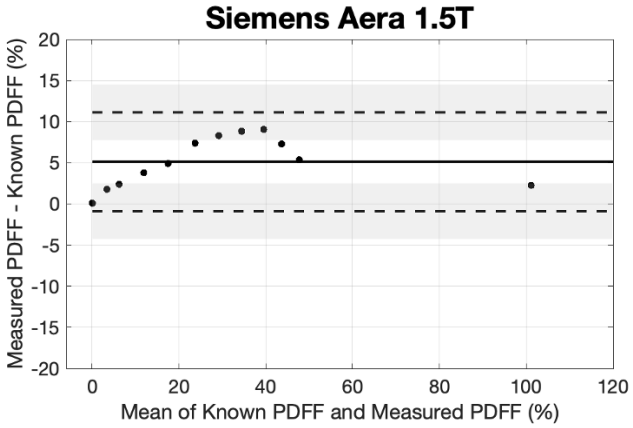


**Figure 3.13:** Bland-Altman plot comparing PDFF measured on the Siemens Aera 1.5T scanner to known PDFF excluding the two 55% PDFF vials which displayed evidence of fat-water swaps.

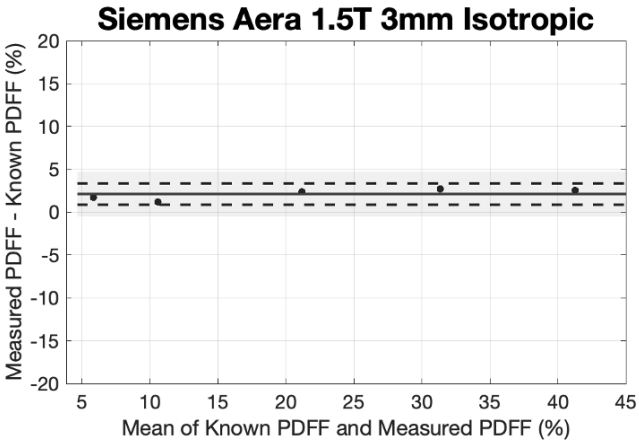


**Figure 3.14:** Bland-Altman plot comparing PDFF measured on the Siemens Aera 1.5T scanner using a Series A phantom and a 3mm isotropic resolution to known PDFF.

The difference between $T_{1w}$ and $T_{1f}$ is greater in the breast compared to the liver, such that the $T_1$ bias effect is exaggerated; this may suggest that a lower flip angle should be used compared to liver CSE-MRI acquisitions. An additional phantom scan demonstrated the improved PDFF accuracy incurred by reducing the flip angle to 1°; however, simulations demonstrated a 6- to 7-fold increase in the uncertainty of PDFF and $T_2^*$ quantification due to the accompanying substantial reduction in SNR. Whilst accuracy is important, the practical use of PDFF and $T_2^*$ must be considered. Ground truth measurements of PDFF and $T_2^*$ *in vivo* are not possible; PDFF and $T_2^*$ would instead be used as comparative biomarkers between

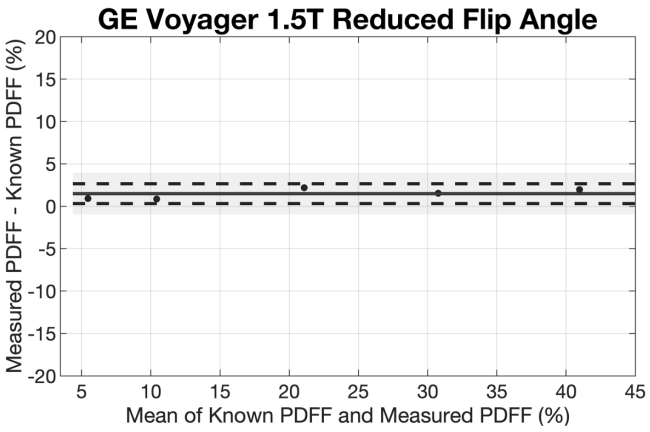


**Figure 3.15:** Bland-Altman plot comparing PDFF measured on the GE Voyager 1.5T with a reduced flip angle of 1 degree compared to the typical 6 degree.

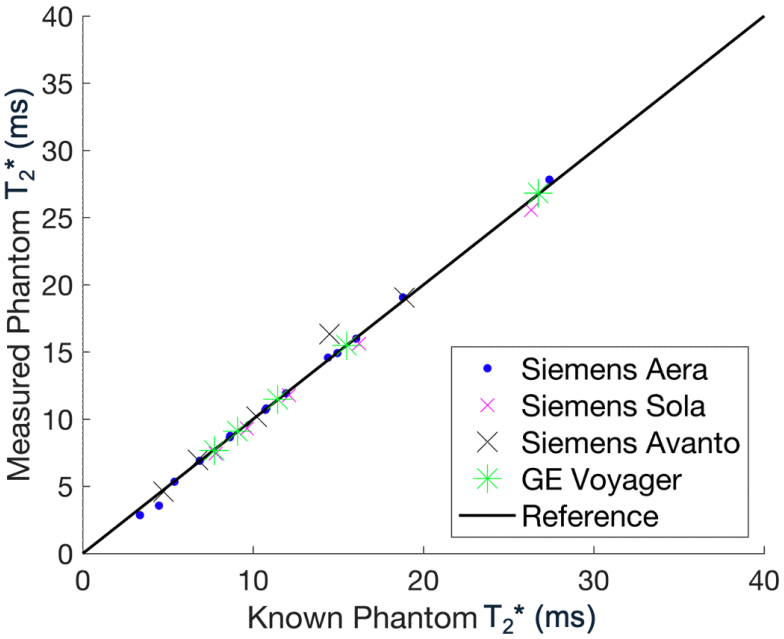


**Figure 3.16:** Overview plot shows the phantom $T_2^*$ measured using the two aforementioned 3D GRE sequences for GE and Siemens on four different scanners against the known $T_2^*$. Here, the known $T_2^*$ refers to the $T_2^*$ measured using the gold standard acquisition, LMS MOST.

cohorts and across time points. The reliability of measurement may be therefore be a more important consideration than accuracy in this context.

Simulations demonstrated that the impact of the $T_1$ bias effect on fibroglandular tissue PDFF was negligible, whilst an overestimate of approximately 2% PDFF was found in fatty tissue. Where measuring the PDFF of adipose tissue, such as in Chapters 7, PDFF values range approximately between 80% to 96%. In this

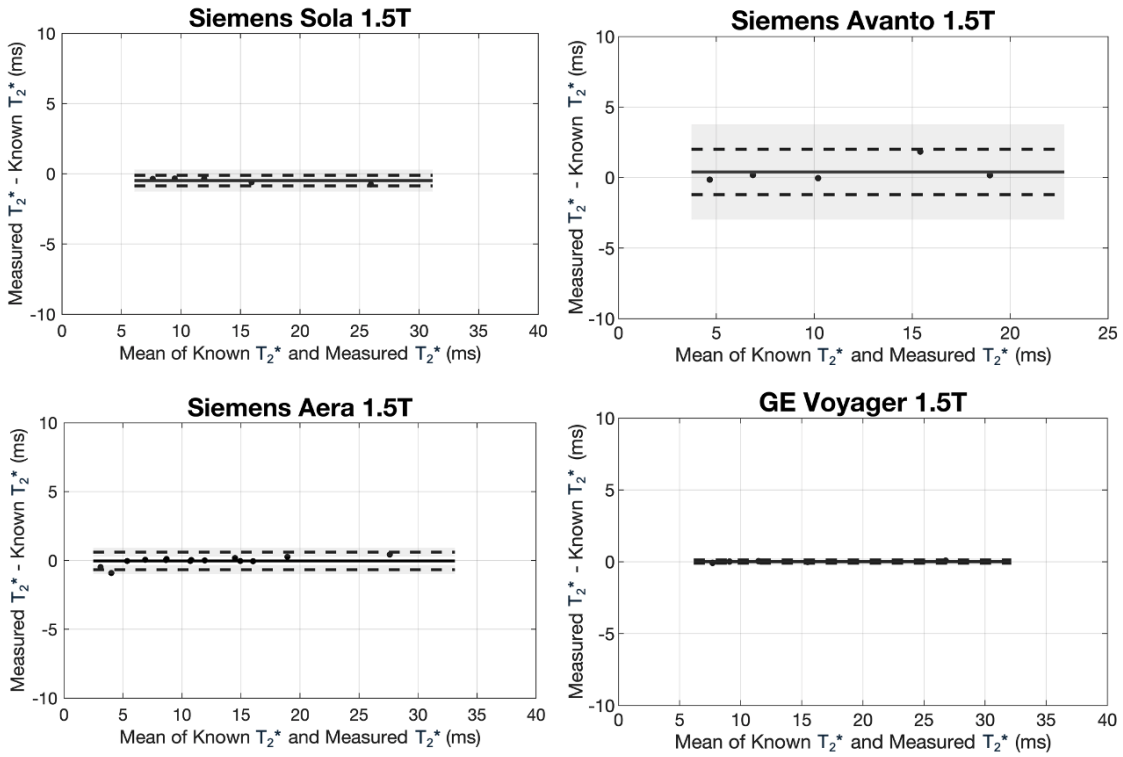


**Figure 3.17:** Bland-Altman plots display the agreement between the known $T_2^*$ and the $T_2^*$ measured across the four different scanners.

range, the overestimate of PDFF from the $T_1$ bias effect is relatively consistent, thus comparative measurement should be minimally impacted. A true difference of 16.0% PDFF across this range would measure as a difference of 13.6% on Siemens, representing a deviation of 2.38%, and as 11.8% on GE, representing a deviation of 4.2%. These deviations are comparable to the reported same-day, same-scanner repeatability of PDFF at 1.5T, which ranges between 1.1-4.4% [128]. Voxels containing mixed species, such that PDFF $\approx$ 50%, would be most impacted by the $T_1$ bias effect. For measurement of whole breast PDFF, such as in Chapter 6, this suggests that breasts with sparsely distributed fibroglandular tissue, thus which incur a greater degree of the partial effect, would be more affected by $T_1$ bias compared to those with condensed areas of fibroglandular tissue. The extent of this bias in investigated in Chapter 6.

Excellent agreement was found between the Siemens and GE acquisitions in quantification of $T_2^*$; this was reflected in both the simulations and the phantom results. PDFF was more significantly overestimated in the GE acquisition compared

to Siemens, due to the higher flip angle and reduced TR. Simulations found that the difference in PDFF measurement between the vendors was negligible in simulated fibroglandular tissue, whilst in simulated fatty tissue the difference in PDFF measurement was around 1%.

Close agreement in PDFF was found between Siemens scanner models when comparing scans performed using phantoms with the same $T_{1w}$. A key limitation of this work was the availability of consistent commercial phantoms and the high $T_{1w}$ of the series B and C phantoms, which limited the applicability of their use due to the differing impacts of the $T_1$ bias effect. This work suggested the need for a set of breast-specific phantoms which more accurately reflect the physiological properties of the breast. These are developed in Chapter 6.

The choice of GRE sequences in this work was limited to those contained within the existing study MRI protocols. Alternative future approaches could include employing a dual flip angle technique to eliminate $T_1$ bias [111], though this would double the scan time, or reducing the flip angle, pending an *in vivo* investigation into the achieved repeatability of the metrics, and bearing in mind SNR requirements for sufficient visualisation of breast structures.

## 3.5 Conclusion

Simulations and phantom scans demonstrated excellent accuracy in quantification of $T_2^*$ across the two GRE sequences. Quantification of PDFF was impacted by the $T_1$ bias effect but is minimally impacted at typical breast tissue values. Further work is needed using breast-specific phantoms to fully understand the impact of this effect.

# 4

# Optimal Approach for Breast CSE-MRI: Influence of the Fat Spectrum

In Chapter 3, we evaluated the impact of the GRE acquisition on quantification of breast $T_2^*$ and PDFF with *in silico* and *in vitro* analyses. In the next two chapters, we perform *in vivo* analyses to investigate how the method with which the GRE data is processed impacts the calculation of these metrics. These analyses are necessary to ensure that the breast $T_2^*$ and PDFF maps used hereafter are of optimal quality, prior to their application in a range of clinical purposes. Firstly, in this chapter, we assess the effect of the choice of multi-peak fat spectrum employed in the signal model.

This chapter was adapted in part from the paper Gordon et al. 2022 [110][1].

## Contents



[1]Such parts are reproduced with permission from Springer Nature

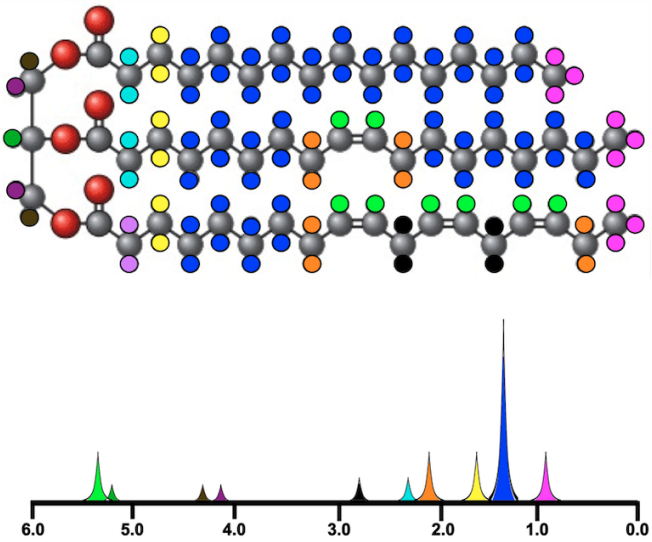


**Figure 4.1:** Visualisation of different proton environments are shown within the triglyceride chain along with their corresponding peaks in a fat spectrum. Each colour represents a different proton environment, owing to their proximity to other atoms in the triglyceride chain. For example, the dark blue circles correspond to the "methlyene" proton group, corresponding to -$CH_2$- protons, which are the most abundant and therefore result in the spectral peak with largest amplitude. Image courtesy of Allen D. Elster, MRIquestions.com.

## 4.1 Introduction

In addition to the choice of pulse sequence, quantification with CC-CSE-MRI is impacted by the choice of fat spectrum in the signal model (Equation 2.15). Whilst water has a single resonant frequency due to the identical environment of the two protons in each molecule, the protons in a triglyceride molecule will be in one of many different environments. This gives rise to a multi-peak spectrum of fat, wherein each peak corresponds to a unique proton environment. For instance, the peak with the largest relative amplitude corresponds to protons in the methylene group (-$CH_2$-), which form a large part of a triglyceride chain (Figure 4.1).

In the CSE-MRI model, the fat spectrum is denoted as $C_n = \Sigma_{(p=1)}^{P} \alpha_p e^{i2\pi f_p t_n}$, where $P$ is the number of peaks, $\alpha_p$ is the relative amplitude of each peak, and $f_p$ is the relative frequency of each peak to the water peak. Literature reports up to 10 resolvable peaks across fat spectra, but in practise many spectra have fewer due to the merging of adjacent peaks from spectral profile broadening.

In early CSE-MRI algorithms, fat was simplified as having a single resonant frequency, corresponding to that of the methylene protons. It has since been demonstrated that use of single-peak spectra leads to incomplete fat water separation and that multi-peak models are necessary for accurate quantification of PDFF and $T_2^*$ [130, 131]. A fat spectrum may be found using magnetic resonance spectroscopy (MRS) or multi-echo GRE. The use of MRS typically requires high field strengths to avoid signal broadening, whilst GRE acquisitions require a high number of echoes for complete definition of all fat peaks. Therefore, in typical CSE-MRI algorithms, the fat spectrum is assumed to be known *a priori* for the anatomy of interest.

Whilst the choice of multi-peak fat spectrum makes relatively little difference in quantification of PDFF in the liver [130], it becomes increasingly important in situations where there is higher fat content [132, 133]. A review of CSE-MRI algorithms across a broad physiological range of PDFF demonstrated a bias of up to 50ms $T_2^*$ incurred by use of different spectra at the highest simulated PDFF value [134]. We therefore hypothesise that in breast adipose tissue, where fat content is high, that the choice of fat spectrum may be important.

Triglyceride composition varies in different deposits of subcutaneous fat according to their position and functionality [135]. Breast adipose tissue is functionally specialised by its paracrine and endocrine involvement with mammary gland biology, and displays differences in both mechanical properties [136] and triglyceride content [137] compared to adipose tissue elsewhere in the body. To date, the incorporation of a breast-specific fat spectrum into CSE-MRI has not been studied. Of the groups who have examined CSE-MRI in the breast, Henze Bancroft et al. [127] assumed breast fat and subcutaneous fat to be equivalent, whilst Hisanaga et al. [138] and Borde et al. [139] employed the generic fat spectrum of the vendor. In this section, we aim to define a breast-specific fat spectrum and to examine how the performance of CSE-MRI in mammary fat varies with the choice of fat spectrum.

## 4.2 Methods

### 4.2.1 Data Acquisition

Sixty-nine female participants were scanned across the three studies described in Section 2.3. Fifty-two participants were healthy with no known breast disease or had benign breast disease (the "benign" cohort), whilst seventeen participants had been diagnosed with malignant breast disease (the "malignant" cohort). The mean age of the participants was 44 years (range 22–77 years).

Participants were imaged in the prone position on one of the four 1.5T scanners using the available bilateral breast coil at each site. The 3D axial 6-echo gradient echo scan described in Section 3.1 was acquired as part of a multi-parametric protocol described in Section 2.3.2.

### 4.2.2 Spectroscopic Analysis

Breast adipose MR spectroscopic data was derived from Freed et al. [140] [2]. The group acquired a three-dimensional sagittal 144-echo gradient-echo sequence with a low flip angle and a bandwidth of 693 Hz. In their work, a Fourier transform was applied to each voxel with initial corrections for phase and eddy currents to produce an MR spectrum. The water peak was removed from the spectra. The corrected voxel-wise data were then fitted with a 10-peak spectral model which enabled determination of the final eddy and phase current corrections. A region of interest (ROI) was drawn in the breast adipose tissue; the peak parameters from the voxel-wise fits were discarded and the final MR spectrum was determined through averaging the spectra across the ROI.

As Freed et al.'s work concentrated on determining the relative areas of five select peaks, the spectra were re-analysed to determine the relative areas of all peaks. Four spectra were analysed; these were acquired in the breast adipose tissue of a participant with no suspicious findings in MRI (designated "healthy breast fat spectrum 1"), a participant with a stable benign lesion (designated "healthy

[2]I gratefully acknowledge the provision of MR spectral data by Professor Gene Kim and Professor Pippa Storey at New York University Grossman School of Medicine.

breast fat spectrum 2"), a participant with ductal carcinoma in situ (DCIS), and a participant with known invasive ductal carcinoma (IDC).

A model was fitted to the corrected and averaged MR spectra which consisted of a constant baseline and 10 Lorentzian line profiles (Figure 4.2). Please see Appendix D for a description of the Lorentzian function and further details on the spectral model employed. The initial values of all parameters in the Lorentzian equation were kept consistent across the four spectra. The positions of the Lorentzian peaks were initially set to literature values but allowed to vary during the fit. The spectral data was fitted to the model using a non-linear least squares approach. The $R^2$ (a widely accepted goodness-of-fit measure - see Section 4.2.4), of the final fit to the spectral data was greater than 0.99 for all spectra, except for healthy breast fat spectrum 1, which had a slightly poorer $R^2$ of 0.98. Finally, the area under each peak was found through integrating the Lorentzian equation associated with each peak across the spectra between 0 and 5.6ppm. Table 4.1 reports the calculated chemical shift values and relative areas of each of the ten peaks in the four breast fat spectra.

### 4.2.3 PDFF and $T_2^*$ Map Generation

The multi-echo GRE MRI data were processed using the MAGO algorithm [15] to produce PDFF and $T_2^*$ maps. The GRE data was processed seven times, each time using a different multi-peak spectral model. The spectral models included the four ten-peak breast fat spectra derived above, a nine-peak spectrum derived from subcutaneous adipose tissue [115], a seven-peak spectrum derived from subcutaneous adipose tissue [141] and a six-peak spectrum derived from liver fat [142]. Whilst the composition of liver fat and breast adipose tissue are different, the liver fat spectrum is readily available in the clinical setting and is well described in literature, therefore it was included in this analysis to enable assessment of its applicability to breast fat in CSE-MRI. The seven-peak adipose tissue spectrum intentionally disregarded three fat peaks during analysis, and was included here for comparison.

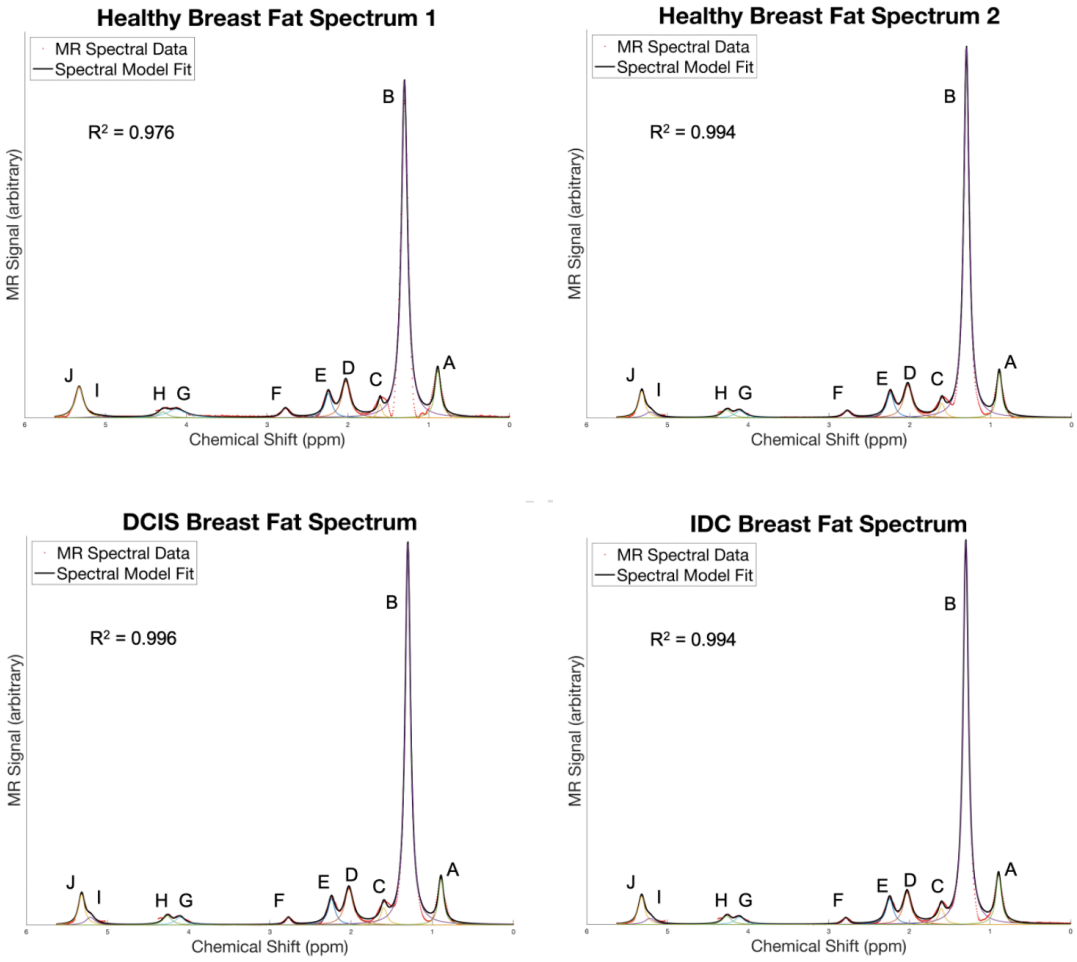


**Figure 4.2:** MR spectra in the breast adipose tissue of: Top left: a participant with no suspicious findings in MR images (designated "healthy breast fat spectrum 1"), top right: a participant with a stable focus that has been followed up for 4 years and is assumed benign (designated "healthy breast fat spectrum 2"), bottom left: a participant with ductal carcinoma in situ (DCIS), and bottom right: a participant with invasive ductal carcinoma (IDC).

### 4.2.4 Estimation of Map Quality

The performance of a CSE-MRI algorithm may be assessed through examining the goodness-of-fit (GoF) of the model estimate of the GRE signal to the acquired echo data. $R^2$ is a well-known estimate of GoF, which is defined as

$$R^2 = 1 - \frac{RSS}{TSS} \tag{4.1}$$

where $RSS$ denotes the residual sum-of-squares and $TSS$ denotes the total sum-of-squares. For acquired signal data $S_n$ with a mean $\overline{S}$, and for reconstructed

| | Healthy 1 | | Healthy 2 | |
|---|---|---|---|---|
| **Peak Label** | **Chemical Shift (ppm)** | **Relative Area (%)** | **Chemical Shift (ppm)** | **Relative Area (%)** |
| J | 5.33 | 7.00 | 5.32 | 4.98 |
| I | 5.08 | 0.73 | 5.21 | 1.77 |
| H | 4.29 | 1.61 | 4.26 | 2.37 |
| G | 4.12 | 4.67 | 4.10 | 2.22 |
| F | 2.77 | 2.10 | 2.77 | 1.56 |
| E | 2.24 | 5.15 | 2.24 | 5.79 |
| D | 2.03 | 8.87 | 2.03 | 8.66 |
| C | 1.60 | 1.60 | 1.60 | 2.57 |
| B | 1.30 | 60.44 | 1.30 | 62.93 |
| A | 0.89 | 7.84 | 0.89 | 7.15 |

| | DCIS | | IDC | |
|---|---|---|---|---|
| **Peak Label** | **Chemical Shift (ppm)** | **Relative Area (%)** | **Chemical Shift (ppm)** | **Relative Area (%)** |
| J | 5.32 | 5.27 | 5.32 | 5.25 |
| I | 5.21 | 1.98 | 5.22 | 1.73 |
| H | 4.26 | 2.30 | 4.26 | 2.25 |
| G | 4.11 | 2.18 | 4.11 | 2.12 |
| F | 2.77 | 1.17 | 2.79 | 1.12 |
| E | 2.24 | 5.41 | 2.24 | 5.80 |
| D | 2.03 | 8.93 | 2.03 | 7.67 |
| C | 1.60 | 3.23 | 1.60 | 2.98 |
| B | 1.30 | 62.27 | 1.30 | 62.57 |
| A | 0.89 | 7.26 | 0.89 | 8.52 |

**Table 4.1:** Chemical shift values and relative areas of the fitted fat peaks in the MR spectra of the breast adipose tissue of a participant with no suspicious findings in MR images (designated "healthy breast fat spectrum 1" or "healthy 1" ) and a participant with a benign lesion (designated "healthy breast fat spectrum 2" or "healthy 2").

GRE signal $\hat{S}$

$$RSS = \sum_n (S_n - \hat{S}_n) \tag{4.2}$$

$$TSS = \sum_n (S_n - \bar{S}) \tag{4.3}$$

$R^2$ is the most commonly employed metric in assessment of PDFF and $T_2^*$ map quality, and has been used to compare algorithmic performance, including the performance of different fat spectra in CSE-MRI [132]. However, the calculation of $R^2$ in non-linear regression models, such as those used in CSE-MRI algorithms, results in a dependency of this metric upon estimated parameters, in particular $T_2^*$

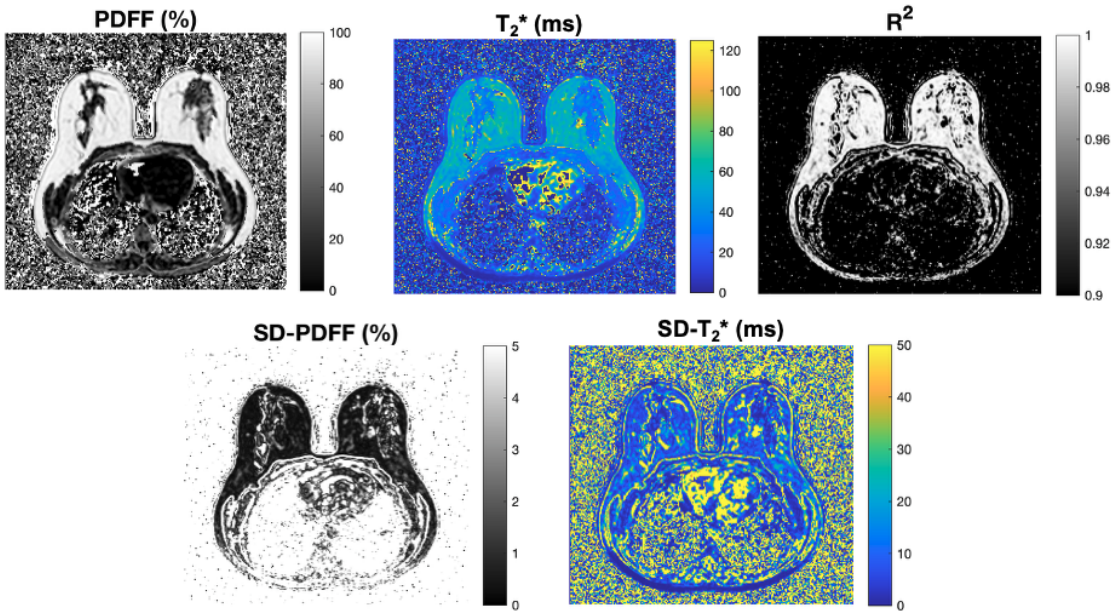


**Figure 4.3:** Example PDFF, $T_2^*$, $R^2$, SD-PDFF, and SD-$T_2^*$ maps at the central slice of the GRE acquisition for one participant. Example quantitative breast maps, shown at the central slice of a 3D GRE acquisition. Top left: Proton Density Fat Fraction (PDFF) map, with units of percentage, reflecting tissue fat content at each pixel, top centre: $T_2^*$ map, with units of milliseconds (ms), reflecting the transverse relaxation time at each pixel, top right: the $R^2$ map, showing the goodness-of-fit of the CSE-MRI signal model to the acquired data, bottom: SD-PDFF and SD-$T_2^*$ maps, reflecting the uncertainty in measurement of each of these metrics at each pixel.

[90]. Specifically, a longer $T_2^*$ necessitates a shallower GRE curve; this causes $S_n$ to be closer to $\bar{S}$, resulting in a lower TSS and thereby a lower $R^2$.

Bagur et al. therefore sought to derive parameter-independent metrics of map quality in CSE-MRI [90, 143]. They aimed to provide these metrics in intuitive units to enable easy understanding of the error associated with each quantitative map. This was achieved by computing error maps of PDFF and $R_2^*$ via the Cramér-Rao Lower Bound (CRLB), described as SD-PDFF and SD-$R_2^*$. The metrics were validated in silico and show promising results in discernment of artefactual versus physiological tissue heterogeneity *in vivo*. Please see Appendix E for further details on the calculation of SD-PDFF and SD-$R_2^*$.

We derived maps of $R^2$, SD-PDFF, and SD-$R_2^*$ alongside PDFF and $T_2^*$ (Figure 4.3). Simple error propagation was used to convert SD-$R_2^*$ to SD-$T_2^*$: where $\delta R_2^*$ is the error in $R_2^*$ measurement (here quantified using SD-$R_2^*$) and $\delta T_2^*$ is the error

in $T_2^*$ measurement (SD-$T_2^*$), we find

$$\delta T_2^* = \left| \frac{dT_2^*}{dR_2^*} \right| \delta R_2^* \tag{4.4}$$

$$\frac{dT_2^*}{dR_2^*} = \frac{-1}{(R_2^*)^2} \tag{4.5}$$

$$\text{SD-}T_2^* = \delta T_2^* = \left| \frac{-1}{(R_2^*)^2} \right| \delta R_2^* = \frac{T_2^*}{R_2^*} \delta R_2^* = \frac{T_2^*}{R_2^*} \text{SD-}R_2^* \tag{4.6}$$

### 4.2.5 Generation of Whole Breast Masks

A morphology-based approach was used to generate a body mask. Initial masks were computed separately in the water and fat images using an Otsu threshold [144]. This method selects the intensity threshold that best separates a bimodal intensity distribution by minimising the within-class variance. The two masks were morphologically opened using a spherical structuring element and then combined into one mask with a logical OR operation. Morphological closing was then applied to the combined mask using another spherical structuring element. An additional image erosion step was used to remove the skin.

Minor variations in this method were performed for Siemens and GE data owing to slight differences in the image intensity profiles of the acquisitions. For Siemens data, the Otsu threshold was computed using the square-root transform of the fat and water image intensities. This was performed to help include faint posterior pixels in the body mask and to reduce the impact of outlier pixels. In GE, a wider distribution of image intensities was observed, suggesting noisier data, and thus the Otsu threshold was computed without the square root transform. In Siemens, the spherical structuring element had a radius of 3 pixels for both opening and closing, whilst in GE the spherical structuring element used for the morphological opening operation was smaller, with a radius of 1 pixel. This ensured that clusters of background noise were not erroneously included in the mask.

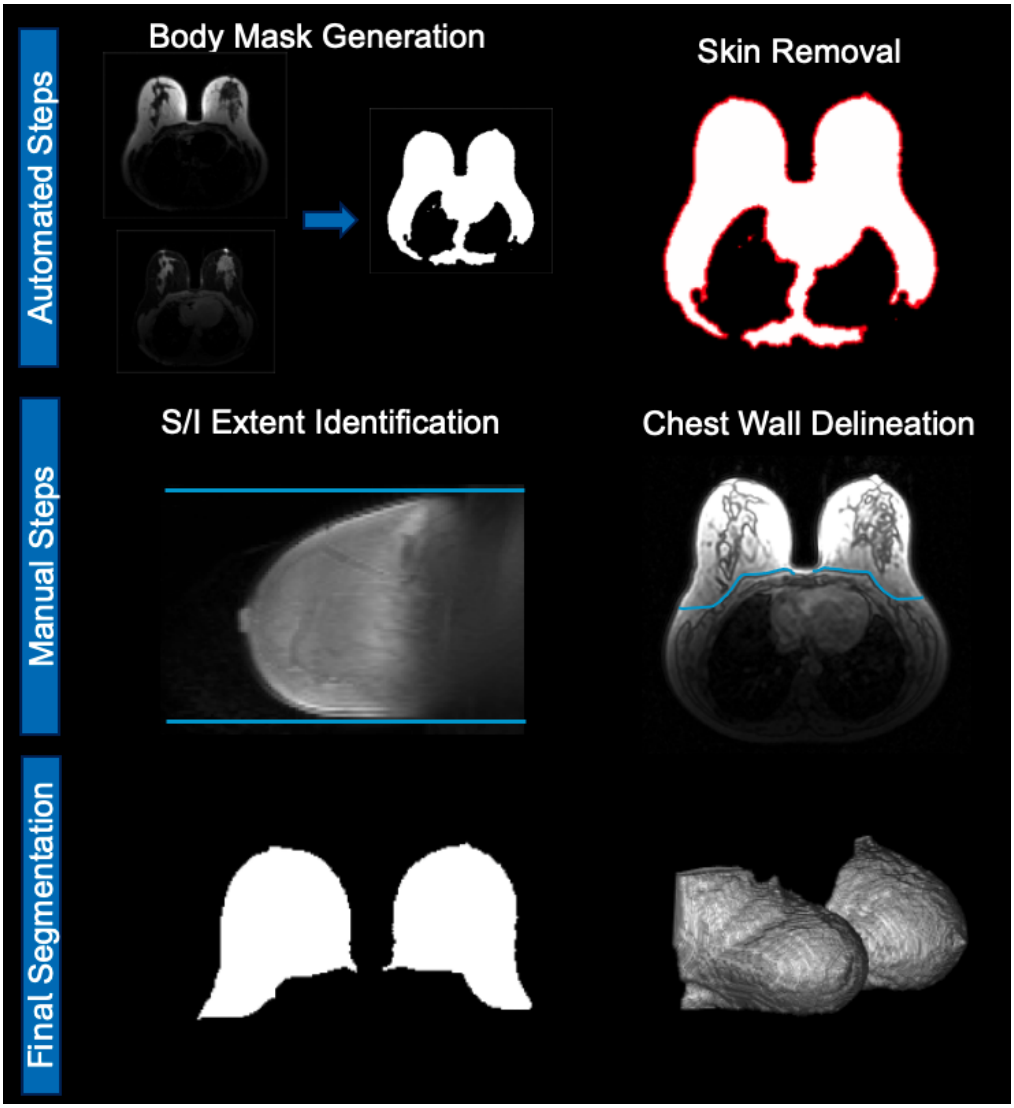


**Figure 4.4:** Breast mask segmentation technique for an example dataset including: automated calculation of a body mask using a morphological approach, automated removal of skin through image erosion, manual identification of the superior/inferior extent of the breast and manual chest wall delineation. Figure adapted from Gordon et al. [145].

To segment the breasts from the body, the chest wall was manually delineated on the central slice of the first echo magnitude image. The superior/inferior extent of the breast was defined using the maximum intensity projection of these echo images in the sagittal plane (Figure 4.4).

### 4.2.6 Segmentation of Adipose Tissue from Fibrous Tissue

To separate fibrous tissue from adipose tissue, the monogenic signal was used as described in Ralli et al. [146] using a log-Gabor filter. Five filters were used with wavelengths 2, 3, 4, 5 and 6 pixels and a $\sigma/f_0$ ratio of 0.5 was employed. The phase symmetry was computed for the first echo image, which provided the highest contrast between fibrous and fatty tissue.

Phase symmetry is computed from the responses of the even (log-Gabor) and odd (Riesz-transformed log-Gabor) filters. Phase symmetry measures the extent to which the even filter response dominates the odd response, and thus quantifies the extent to which a given voxel contains a symmetric feature. It was hypothesised that thin pieces of fibrous tissue surrounded by adipose tissue would have high phase symmetry values. An Otsu threshold was applied to the calculated phase symmetry map to provide a mask which identified thin strands of fibroglandular tissue (Figure 4.6).

This process readily identified thin segments of fibroglandular tissue but could not detect larger homogeneous fibroglandular tissue clumps. Therefore, an additional step was employed. A histogram was plotted of all PDFF values in a breast mask and a multi-modal Gaussian model was fitted to a kernel-smoothed estimate of the histogram using a non-linear least squares approach (Figure 4.5). To limit outlier influence, the histogram was limited between -40% and 140%. The three peaks fitted were hypothesised to correspond to fibroglandular tissue, adipose tissue, and mixed voxels. A threshold to exclude remaining areas of fibrous tissue was found by calculating the three sigma lower bound for the fat peak; when this value was inappropriate, such as when peak fitting to the histogram was poor, the threshold was manually selected through examination of the histogram.

### 4.2.7 Statistical Tests

The median PDFF, $T_2^*$, $R^2$, SD-PDFF, and SD-$T_2^*$ were calculated across the segmented adipose tissue of each participant. The variation in each of these parameters across the different fat spectra were evaluated using the Wilcoxon signed

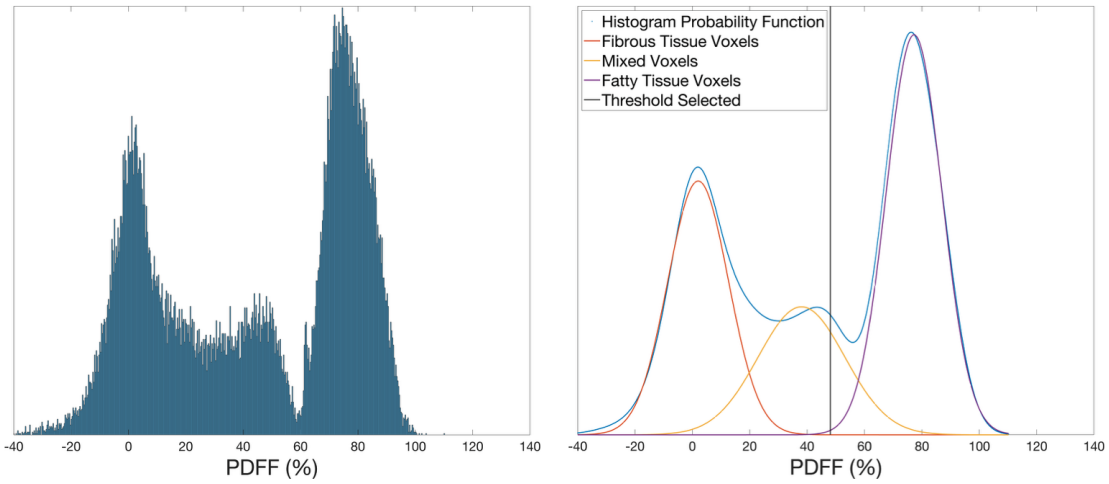


**Figure 4.5:** Left: Example histogram of all PDFF values across a mask of the breasts. Right: Multi-modal Gaussian fitting to the probability density function of the histogram of PDFF values, showing identification of the threshold value.

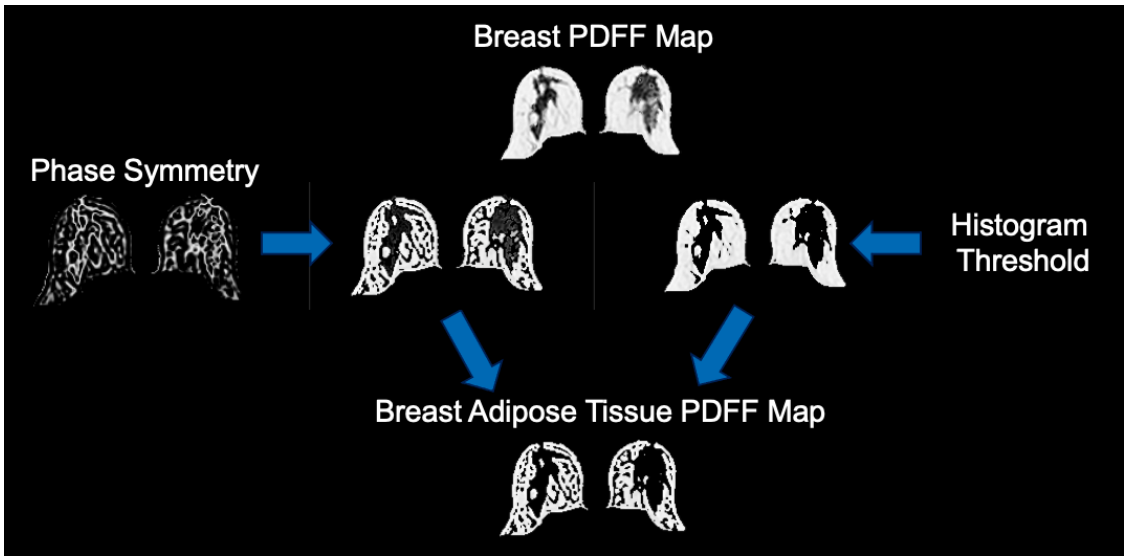


**Figure 4.6:** Overview of segmentation technique to separate fibrous and fatty tissue, including calculation of phase symmetry map and histogram analysis.

rank test with Bonferroni correction for the pairwise fat spectra comparisons, and Friedman's test.

## 4.3 Results

Friedman's test demonstrated significant differences between adipose tissue PDFF calculated with the seven different fat spectra ($p < 1e\text{-}33$) (Figure 4.7). PDFF was significantly different in pairwise comparisons between each breast spectrum

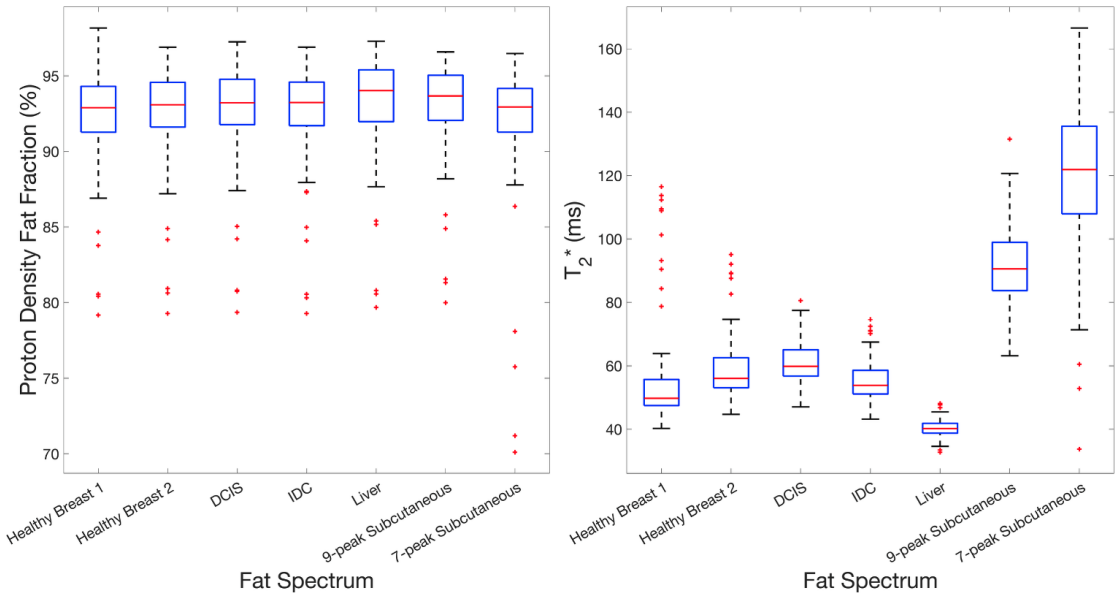


**Figure 4.7:** Left: Box plot showing the median PDFF of breast adipose tissue calculated using different fat spectra. Right: Box plot showing the median $T_2^*$ of breast adipose tissue calculated using different fat spectra. Left to right: healthy breast fat spectrum 1, healthy breast fat spectrum 2, breast fat spectrum from participant with IDC, breast fat spectrum from participant with DCIS, liver fat spectrum, nine-peak subcutaneous fat spectrum, seven-peak subcutaneous fat spectrum.

and the nine-peak subcutaneous spectrum ($p < 0.01$ across all comparisons); as an implementation of this spectrum has already been used in breast CSE-MRI [127], this result is of particular interest. Similarly, PDFF was significantly different between each breast fat spectrum and the liver fat spectrum ($p < 0.01$ across all comparisons). Whilst this does not indicate inherent performance, it does indicate the statistically significant effect that the choice of fat spectrum can have. However, despite these statistically significant differences, the largest difference in median PDFF found between all spectra was 1.1%. This is comparable to the reported same-day, same-scanner repeatability of PDFF at 1.5T, which ranges between 1.1-4.4% [128].

$T_2^*$ calculated across the different spectra varied significantly (Friedman's test, $p < 1e\text{-}74$), with a maximum difference in median $T_2^*$ of 81.7ms. Whilst no definitive ground truth of breast adipose tissue $T_2^*$ exists, one study reported a reference $T_2$ of 53.3±2.1ms at 1.5T [116], suggesting that $T_2^*$ measurements should be lower than this. This casts doubts upon the validity of the measurements made using the nine-peak and seven-peak subcutaneous spectra.

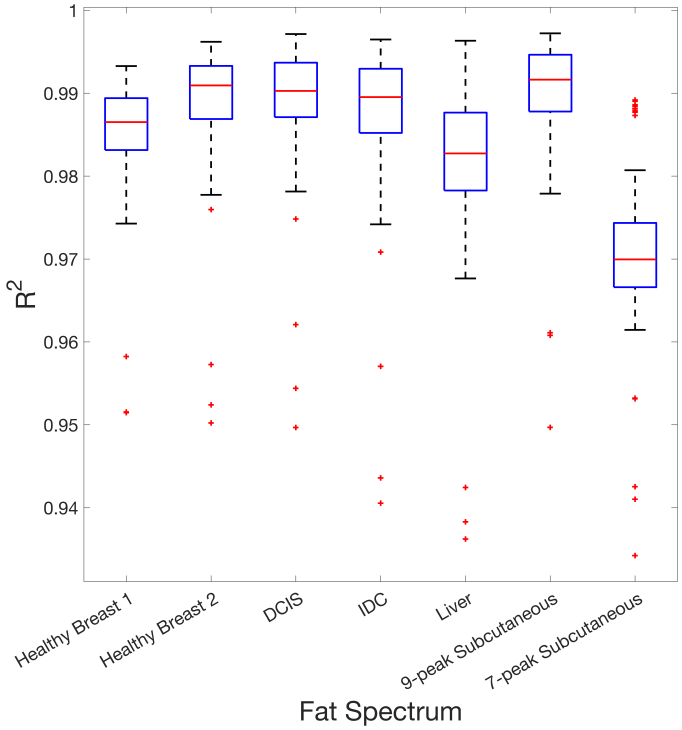


**Figure 4.8:** Box plot showing variation in the median $R^2$ found in breast adipose tissue using different fat spectra in the CSE-MRI algorithm. Left to right: healthy breast fat spectrum 1, healthy breast fat spectrum 2, breast fat spectrum from participant with IDC, breast fat spectrum from participant with DCIS, liver fat spectrum, nine-peak subcutaneous fat spectrum, seven-peak subcutaneous fat spectrum.

Analysis of $R^2$, SD-PDFF, and SD-$T_2^*$ revealed distinct differences in the GoF of the maps generated with the different spectra. Friedman's test demonstrated a significant difference in $R^2$ across the seven spectra ($p < 1e\text{-}62$) (Figure 4.8). The seven-peak subcutaneous fat spectrum had significantly lower $R^2$ than all other spectra ($p < 1e\text{-}11$ across all comparisons). This may be due in part to the higher $T_2^*$ measured using this spectrum, but the significantly elevated SD-PDFF and SD-$T_2^*$ confirm its poor performance in breast CSE-MRI (Figure 4.9). The liver fat spectrum demonstrated significantly reduced $R^2$ compared to the breast fat and nine-peak subcutaneous fat spectra ($p < 1e\text{-}3$ for all comparisons). The low $T_2^*$ measured using this spectrum suggests its $R^2$ may even be artificially increased. Literature suggests an $R^2$ threshold of 0.97 to define the analysability of PDFF maps [147]; by this criterion, less than 5% of data would be excluded using any of the breast spectra or the nine-peak subcutaneous fat spectrum, whilst less than

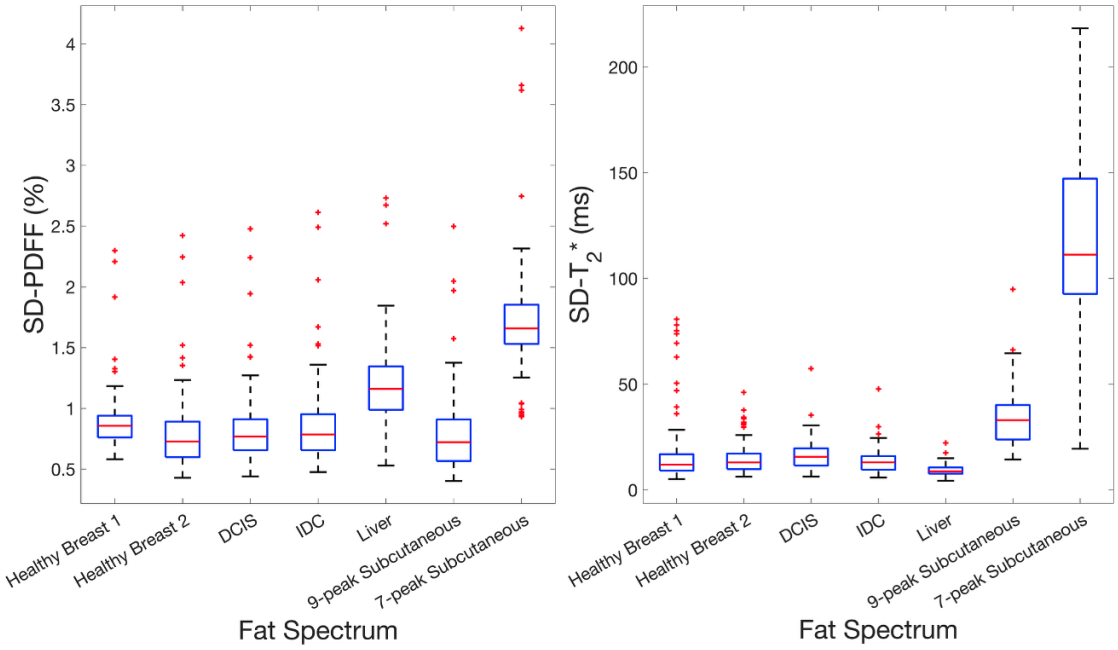


**Figure 4.9:** Left: Box plot showing variation in the median SD-PDFF found in breast adipose tissue using different fat spectra in the CSE-MRI algorithm. Right: Box plot showing variation in the median SD-$T_2^*$ found in breast adipose tissue using different fat spectra in the CSE-MRI algorithm. Left to right: healthy breast fat spectrum 1, healthy breast fat spectrum 2, breast fat spectrum from participant with IDC, breast fat spectrum from participant with DCIS, liver fat spectrum, nine-peak subcutaneous fat spectrum, seven-peak subcutaneous fat spectrum.

8% of data would be excluded using the liver spectrum.

The four spectra derived from breast adipose tissue performed similarly across the GoF metrics. However, the first healthy breast fat spectrum showed slightly poorer performance with reduced $R^2$ and elevated SD-PDFF compared to the other breast spectra. This may be attributed to the poorer fit of the 10-peak spectral model to the MRS data found in Section 4.2.2.

Analysing data derived from the benign cohort data separately to that of the malignant cohort did not affect the relative performance of the median SD-PDFF and SD-$T_2^*$ between the breast fat spectra (Figure 4.10). A change in the spectrum associated with the highest median $R^2$ was observed; this was found to be the DCIS spectrum in the malignant cohort, and the second healthy breast fat spectrum in the benign cohort. However, the $R^2$ distributions of these two spectra were not significantly different in either cohort (benign cohort: p = 0.65,

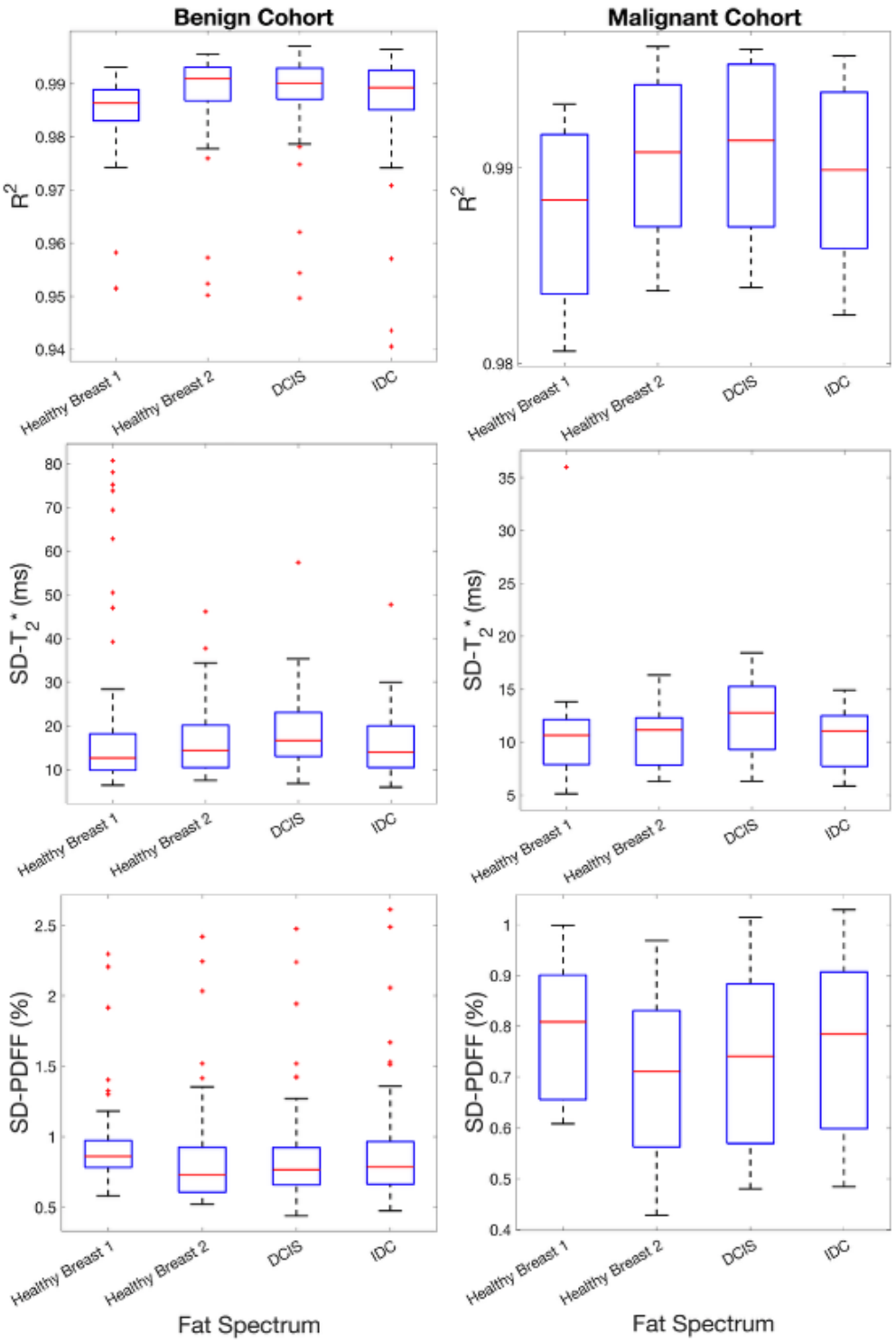


**Figure 4.10:** Box plots showing analyses split according to the disease status of the participants. Left: $R^2$, SD-$T_2^*$, and SD-PDFF analyses for the cohort of participants with benign disease only. Right: $R^2$, SD-$T_2^*$, and SD-PDFF analyses for the cohort of participants with malignant disease only. Left to right: healthy breast fat spectrum 1, healthy breast fat spectrum 2, breast fat spectrum from participant with IDC, breast fat spectrum from participant with DCIS.

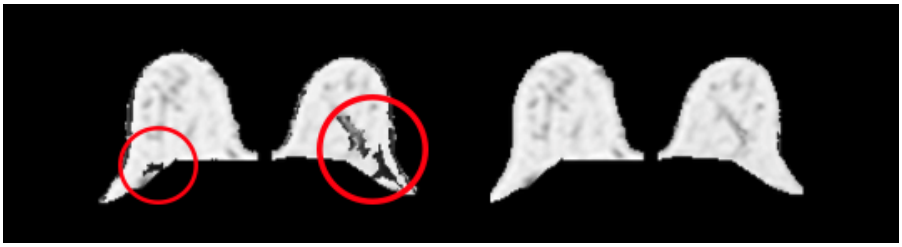

**Figure 4.11:** Example slice of a PDFF map showing region of poor fit the using nine-peak subcutaneous fat spectrum (left) compared to using the healthy breast fat spectrum 2 (right).

malignant cohort: $p = 0.43$).

Through manual review of the PDFF maps, areas of fat-water swaps resulting in artificially lowered PDFF were observed (Figure 4.11). As these areas would be segmented out during the thresholding step of adipose tissue segmentation, such areas of poor fitting are not reflected in Figure 4.7.

The adipose tissue masks generated with the liver fat spectrum were manually adjusted in ITK-SNAP [148] to ensure that any areas of poorly fitted adipose tissue would still be included. For each case, the same manually-corrected mask was applied to each of the seven PDFF maps generated with the different fat spectra. The fraction of swapped adipose tissue pixels was calculated by finding the number of pixels included in the updated adipose tissue mask with PDFF $< 20\%$.

Applying the same masks to the different PDFF maps highlighted the poor performance of the nine-peak subcutaneous fat spectrum, which was associated with the second highest fraction of swapped pixels (Figure 4.12). The swapped pixel fraction using this spectrum was significantly higher than that found using the each of the four breast fat spectra ($p <$ 1e-7 for all pairwise comparisons). The seven-peak subcutaneous fat spectrum performed particularly poorly; a median of 66% of pixels were fat-water swapped. The fraction of failed pixels was smallest in the PDFF maps generated with the liver fat spectrum, though this result may be biased due to the use of the mask generated with the liver fat spectrum as the basis for the manually-corrected maps. The four breast fat spectra showed similar performance to one another, with less than a 1% difference in the median percentage of swapped pixels observed.

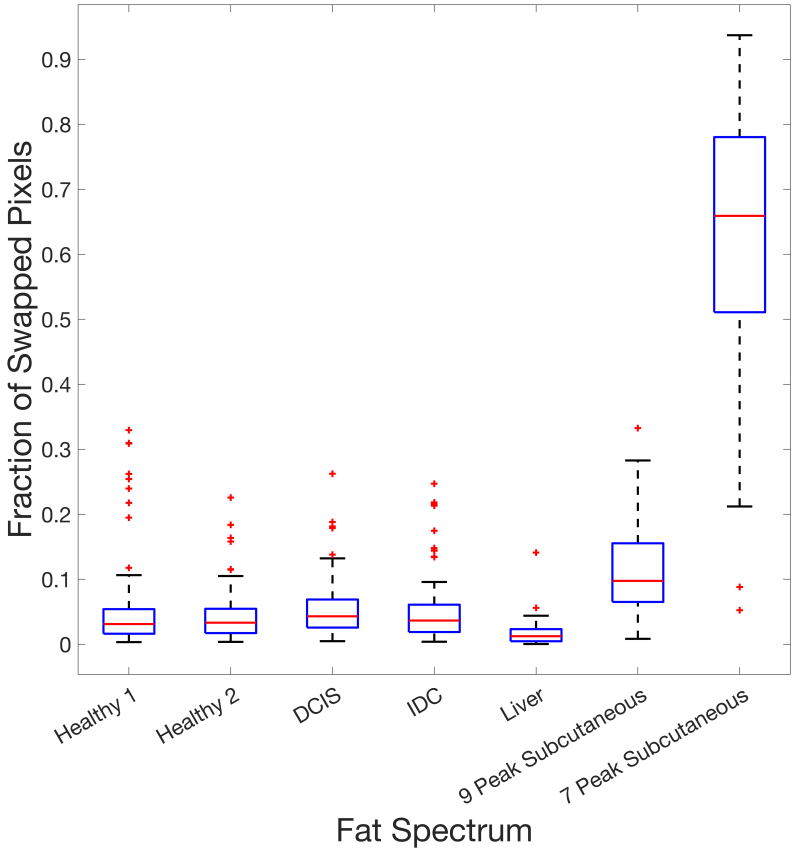


**Figure 4.12:** Box plot showing variation in the fraction of fat water swapped pixels in breast adipose tissue PDFF maps using different fat spectra in the CSE-MRI algorithm. Left to right: healthy breast fat spectrum 1, healthy breast fat spectrum 2, breast fat spectrum from participant with IDC, breast fat spectrum from participant with DCIS, liver fat spectrum, nine-peak subcutaneous fat spectrum, seven-peak subcutaneous fat spectrum.

## 4.4 Discussion

*In vivo* analysis demonstrated that the choice of fat spectrum is important in the calculation of breast adipose tissue PDFF and $T_2^*$. Whilst the difference in median adipose PDFF was comparatively low across the spectra, analysis of GoF metrics and the number of fat-water swapped pixels demonstrated a distinct difference in the quality of PDFF and $T_2^*$ maps. In clinical and pharmaceutical settings alike, map quality is critical to ensure consistent ROI placement and to avoid unnecessary re-acquisition of data.

Phase symmetry maps enabled identification of thinner strands of fibroglandular tissue (FGT) but did not identify larger FGT areas such as those often observed

in dense breasts. Whilst the use of multi-modal Gaussian fitting of histograms to provide a threshold for the exclusion of larger areas of FGT was successful, the manual intervention step performed when the fit failed was subjective. Future work could explore other methods which do not dispose of spatial information, for example the use of phase asymmetry (rather than phase symmetry), to identify and exclude larger areas of homogeneous tissue.

Whilst the nine-peak subcutaneous fat spectrum showed the best $R^2$ performance when masks were individually calculated, application of the same mask across the PDFF maps demonstrated the increased prevalence of regions of fat-water swaps when using this spectrum. This suggests that an alternative fat spectrum should be used in breast adipose PDFF calculation to ensure accurate quantification throughout the whole breast.

The particularly poor performance of the seven-peak subcutaneous fat spectra demonstrates the necessity of including all available peaks in a spectral model in CSE-MRI. The comparably improved performance of the six-peak liver fat spectrum demonstrates that it is not necessarily the number of resolvable peaks which is of importance, but rather that no fat peaks in the spectral data should be excluded in CSE-MRI. The low median SD-$T_2^*$ of the liver fat spectrum and the agreement of the calculated median $T_2^*$ with the published reference range for breast $T_2$ suggests potential utility of this spectrum in measuring breast $T_2^*$, but its poor $R^2$ and SD-PDFF performance suggests it may not be the optimal spectrum for implementation in breast CSE-MRI.

The four breast fat spectra performed well across GoF metrics, provided median $T_2^*$ measurements approximately consistent with a reported $T_2$ reference range, and resulted in low fractions of fat-water swapped pixels. The second healthy breast fat spectrum demonstrated the highest median $R^2$ and lowest median SD-PDFF of the breast spectra, and resulted in a lower median fraction of fat-water swapped pixels than the IDC and DCIS spectra. We therefore choose to implement this spectrum in breast CSE-MRI analysis for the remainder of this thesis.

The consistent relative performance of the breast fat spectra when analyses were split according to participant disease status provides confidence in CSE-MRI of the breast, as this does not suggest the need to implement a fat spectrum particular to a participant's disease state. The only observed difference was a change in the spectrum associated with the highest median $R^2$, with a spectrum derived from healthy breast fat performing better in the benign cohort and a spectrum derived from a participant with DCIS performing better in the malignant cohort; whilst the difference between the $R^2$ distributions was not significant in either cohort, future work could explore whether the $R^2$ of the fit of CSE-MRI data to a particular spectral model might help to discern fat composition and thereby disease status. It should also be noted that differences in the method of spectral analysis, such as the modelled peak shape, initialisations, and the range over which integration is performed may give rise to slight variabilities in the calculated relative areas and chemical shift values for a given spectra. Future work could also assess whether changes in spectral analysis still yield the results observed in this chapter.

There are several limitations associated with this study. Firstly, the segmentation of whole-breast adipose tissue is currently semi-automatic, requiring user intervention to delineate the chest wall and identify the extent of the breast in the superior-inferior direction. An improved method could use machine learning to identify these anatomical markers [149], or adopt additional image analysis methodologies, such as gradient analysis of an active contouring model applied to the sagittal MIP to automate the superior-inferior delineation. Secondly, ground truth measurement of fat content is impossible without histological data, therefore we are unable to determine which spectrum provided the most accurate measure of PDFF. Instead, we compare the difference in PDFF measurements arising from the use of different spectra against the reported repeatability of PDFF [128]. Whilst the reported repeatability of PDFF in this paper was calculated with inclusion of measurements at high fat contents up to 100%, the repeatability was determined *in vitro*. An additional *in vivo* study may prove beneficial to account for practical differences between phantom and participant scanning, such as participant motion, and the

greater susceptibility of phantoms to temperature effects [150]. Thirdly, when the same adipose tissue mask was applied to PDFF maps generated with different spectra for the analysis shown in Figure 4.12, the mask chosen to amend with manual corrections was that calculated from the PDFF map processed with the liver fat spectrum. To avoid bias which may be incurred by applying an adipose tissue mask calculated using a particular fat spectrum, an improved method would apply a mask calculated from a separate MR sequence and co-register back to the CSE-MRI maps.

## 4.5 Conclusion

To our knowledge, this work is the first to implement a breast-specific fat spectrum into calculation of PDFF and the first to assess the effect of the choice of fat spectrum in breast CSE-MRI. Spectral data derived from breast adipose tissue were analysed using a 10-peak spectral model; the peak positions and relative areas are reported here such that these spectra may be implemented into future CSE-MRI methodologies. Analysis of $R^2$, SD-PDFF, SD-$T_2^*$, and the fraction of fat-water swapped pixels demonstrated that spectra derived from subcutaneous fat and liver fat showed poorer performance in breast CSE-MRI compared to breast-specific fat spectra. To ensure optimal map quality, we choose to implement a spectrum derived from healthy breast fat into the remaining *in vivo* CSE-MRI analysis in this thesis.

# 5

# Optimal Approach for Breast CSE-MRI: Influence of the Fitting Algorithm

In Chapter 4, we completed the first stage of our investigation into defining the optimal CSE-MRI method for breast GRE data by considering the choice of fat spectrum in the signal model. In this chapter, we complete this investigation through evaluating the impact of the post-processing algorithm with which the GRE data is fitted to the signal model.

## Contents

## 5.1 Introduction

In Chapter 2, we noted that the signal acquired at echo time $t_n$ in a particular voxel containing fat and water may be described as

$$S_n = (\rho_W e^{i\phi_W} + \rho_F e^{i\phi_F} C_n) e^{-R_2^* t_n} e^{i(2\pi\psi t_n)} \tag{2.15}$$

where $R_2^* = \frac{1}{T_2^*}$, $\psi$ is the $B_0$ field inhomogeneity or "field map", $\phi_W$ and $\phi_F$ are the phase offsets of fat and water protons at $t = 0$, $C_n = \Sigma_{(p=1)}^{P} \alpha_p e^{i2\pi f_p t_n}$ is the known fat spectrum, and $\rho_W$ and $\rho_F$ are the water magnitude and fat magnitude respectively. Calculation of PDFF ($= 100\% \times \frac{\rho_F}{\rho_W + \rho_F}$) and $T_2^*$ at each voxel require the solution of this equation for the six unknown variables ($\rho_W$, $\rho_F$, $R_2^*$, $\psi$, $\phi_W$, $\phi_F$). Though $\rho_W$, $\rho_F$, and $R_2^*$ are independent of the particular voxel, $\psi$, $\phi_W$, and $\phi_F$ are generally expected to vary smoothly throughout the map.

The large number of variables poses a difficult problem, requiring acquisition of multiple echoes and a search across a six-dimensional parameter space for the optimal fit of acquired data to the signal model. This problem may be simplified by employing certain assumptions or "constraints" [151].

One commonly-employed constraint assumes that the water and fat protons share the same initial phase offset such that $\phi_W = \phi_F = \phi_0$; this is referred to as the "phase-constrained" signal model. This assumption is physically reasonable for GRE acquisitions and demonstrates improved noise performance or a reduction in the number of echoes required [152].

The phase-constrained signal model may then be written as

$$S_n = (\rho_W + \rho_F C_n) e^{-R_2^* t_n} e^{i(2\pi\psi t_n + \phi_0)} \tag{5.1}$$

To find the optimal fit of acquired MRI data to this signal model and to thereby determine the unknown variables required to produce PDFF and $T_2^*$ maps, a "fitting algorithm" is employed. These algorithms are typically based upon minimisation of the least squares' difference between the signal data and the signal model, however, many variations exist. In this chapter, we endeavour to find the optimal "fitting

algorithm" with which to process breast GRE data. We therefore now describe the key concepts behind different fitting algorithms.

CSE-MRI fitting algorithms may be classified as complex-based or magnitude-based according to whether or not the algorithm uses the acquired phase images. Complex-based algorithms endeavour to solve Equation 5.1 using the complex-valued MRI signal and therefore require estimation of the field map, $\psi$; this is a non-trivial optimisation problem with multiple candidate solutions [109, 153]. Convergence to the wrong solution may lead to misidentification of the dominant species, leading to fat-water swaps (Section 2.2.1.10).

To mitigate this problem and encourage selection of the correct candidate solution, many complex-based CSE-MRI algorithms employ an additional constraint through the assumption of field map smoothness [154, 155]. However, the assumption of field map smoothness is not always valid, particularly in areas of varying magnetic susceptibility. Complex-based algorithms are also sensitive to errors in phase images, such as those arising from eddy currents caused by changing magnetic field gradients.

Magnitude-based algorithms pose an alternative approach to calculation of PDFF and $T_2^*$ which does not rely on phase data. Considering only the magnitude component of the signal in Equation 5.1 we find

$$|S_n| = |\rho_W + \rho_F C_n| e^{-R_2^* t_n} \tag{5.2}$$

Notably, the $e^{i(2\pi\psi t_n + \phi_0)}$ term vanishes due to its unit magnitude. Magnitude-based fitting algorithms therefore require determination of just three variables $(\rho_W, \rho_F, T_2^*)$, and do not require the assumption of field map smoothness. Magnitude-based fitting algorithms are particularly useful in settings where standardisation across a number of scanners is important, as phase information cannot reliably be exported from all vendors (Section 2.3.2).

Concerns have been raised about the so-called fat-water ambiguity observed in magnitude-based methods, which reflect the inability of these algorithms to determine the dominant species in a voxel. This arises from the similarity of the signal magnitude in a voxel with PDFF $= X$ and a voxel with PDFF $= 100\% - X$.

Incorrect identification of the dominant species may lead to fat-water swap artefacts. The discarding of acquired phase information by magnitude-based algorithms also reduces the effective SNR.

"Hybrid" fitting algorithms [156] seek to employ the benefits of both complex- and magnitude-based approaches. Such algorithms are initialised with a complex-based solution and then employ a magnitude-based refinement step to minimise the sensitivity of the solution to phase errors. However, hybrid approaches are still inherently based upon field map estimation and require acquisition of complex data.

Previous works evaluating CSE-MRI fitting algorithms have largely focused on their application in the liver and other comparatively homogenous regions [114, 157, 158]. The breast is a highly heterogenous organ, with fibroglandular tissue distributed throughout the fatty tissue, resulting in the presence of many tissue interfaces. Breast fibroglandular tissue itself consists of many components such as ducts, lobules, and collagenous connective tissues; this is thought to induce magnetic field inhomogeneities within the FGT [159]. The structure of the breast may therefore reduce confidence in the assumption of field map smoothness and therefore may affect the optimal choice of fitting algorithm.

The achievable SNR may also differ between breast and liver GRE acquisitions owing to the use of different RF coils and the different proximity of the organs to the coil surface; this may also affect the optimal choice of CSE-MRI fitting algorithm due to the differential impact of discarding phase information.

In this chapter, we evaluate different CSE-MRI fitting algorithms for generation of breast-specific PDFF and $T_2^*$ maps. We assess the quality of maps generated using a variety of magnitude-based and hybrid fitting algorithms, and use this to infer the algorithm with which the breast GRE data should be processed in the remainder of this thesis.

## 5.2 Methods

The choice of fitting algorithm is dependent upon the availability of phase GRE data. As described in Section 2.3.2, whilst complex echo data was available for

Siemens GRE acquisitions, only magnitude data was output from GE scanners. In this chapter, we therefore split the analyses by scanner vendor, owing to the incompatibility of GE echo data with complex and hybrid-based techniques.

Participants across both vendors were imaged in the standard prone position on a 1.5T scanner using the available bilateral breast coil at each site. The 3D axial 6-echo gradient echo scan described in Section 3.1 was acquired.

### 5.2.1 Siemens

Fifty-nine women were scanned on Siemens scanners across the three studies described in Section 2.3. Forty-three women had no known breast disease or benign breast disease, whilst sixteen women had been diagnosed with malignant breast disease. The mean age of the participants was 44 years (range 22–78 years).

Three fitting algorithms were applied to the Siemens data. The healthy breast fat spectrum derived in Chapter 4 was incorporated into the signal model. The approaches employed included one magnitude-based algorithm, one magnitude-based algorithm with a complex-based refinement step, and one hybrid-based algorithm initialised with complex data. We describe these algorithms in further detail below.

#### 5.2.1.1 MAGO - Magnitude-Based

MAGO ("MAGnitude-Only") is a magnitude-based CSE-MRI fitting algorithm developed by Bagur et al. [15] which uses multi-point optimisation and a multi-peak fat spectrum to resolve the aforementioned fat-water ambiguity which is inherent to magnitude-based algorithms. At each voxel, MAGO finds two candidate solutions using the multi-point search method, one of which is water-dominant and the other of which is fat-dominant. The solution with the lowest fitting residual to the acquired data is deemed as the "chosen" set of parameters at each voxel.

MAGO has demonstrated excellent accuracy and reproducibility across phantoms and liver datasets [15] and is used by Perspectum Ltd. in commercial offerings for quantification of liver fat and iron. MAGO was used as the fitting algorithm of

choice in Chapters 3 and 4 due its lack of reliance on phase echo data, which could not be output by the GE scanner, and its commercial applicability.

#### 5.2.1.2 MAGO with Field Map Smoothing (MAGO-FMS) - Magnitude-Based with Complex Refinement

An extension to the MAGO algorithm was recently proposed by Bagur et al. [90]. Where complex data is available, the group propose a method which estimates the field map following use of the MAGO algorithm. The "chosen" MAGO solution is used to guide an estimation of the field map with the complex data. The estimated field map is then compared against another estimate of the field map, which is found using the "alternative" MAGO solution. A refined field map is found through voxel-wise selection of the candidate field map value which lies closest to a smoothed version of the original field map estimate. This refinement step also yields adjusted MAGO PDFF and $T_2^*$ maps, as the entire parameter set is implemented in any voxels which are swapped to the "alternative" MAGO solution.

#### 5.2.1.3 Graph Cut with Magnitude-Based Refinement (GC-MBR) - Hybrid

The last of the three algorithms examined employed a "hybrid"-based approach to calculation of PDFF and $T_2^*$. Firstly, a complex-based estimate of PDFF and $T_2^*$ was found using the graph-cut-based algorithm described by Hernando et al. [155]. Rather than estimate PDFF and $T_2^*$ individually at each voxel, this algorithm is based upon minimisation of a cost function across all voxels. The cost function includes a data fidelity term, which accounts for the residuals between the measured signal and the signal model, and an adaptive spatial smoothness term, which encourages field map smoothness whilst preventing over-smoothing of the data in regions where the field map is not expected to be smooth, such as at tissue interfaces. The method uses a graph-cut algorithm to update the voxels simultaneously for different candidate field maps to reduce the likelihood of local errors.

The complex-based graph cut solution was then refined using the magnitude-based refinement step described by Yu et al. [156]. Briefly, an iterative algorithm

which compares the magnitude of the acquired signal data to the magnitude of the signal generated with a candidate solution is initialised using a complex-based solution, such as that found using the graph cuts. The error in the candidate fat and water terms is estimated and the candidate solution is updated. This updated solution is then compared again to the acquired data - this process continues until the iteration converges.

### 5.2.2 GE

Ten women were scanned on a GE Signa Voyager scanner across the IMOGEN and RADIUS studies (Section 2.3). Nine women had no known breast disease or benign breast disease, whilst one woman had been diagnosed with malignant breast disease. The mean age of the participants was 45 years (range 28–63 years).

The MAGO algorithm was applied to the raw GE echo data using the healthy breast fat spectrum derived in Chapter 4. Whilst only magnitude raw echo data was available, the PDFF and $T_2^*$ maps generated by the proprietary algorithm of the vendor, IDEAL-IQ [160], were also output by the scanner.

Details of the particular algorithm and fat spectrum employed by the IDEAL-IQ approach are unavailable, though it is known to be based upon the IDEAL algorithm [109] (Section 3.1), which employs complex-based estimation of the field map to find PDFF and $T_2^*$. IDEAL-IQ is noted to employ a multi-peak fat spectrum, and to correct for phase error [161, 162], suggesting inclusion of a possible magnitude-based refinement step. For the GE data, where raw phase data was unavailable, we compared the MAGO-generated PDFF and $T_2^*$ maps to those output by the scanner using the proprietary IDEAL-IQ algorithm.

### 5.2.3 Analysis

Estimation of SD-PDFF and SD-$T_2^*$ maps via the Cramér-Rao Lower Bound is not appropriate for the MAGO-FMS and GC-MBR fitting algorithms. Appendix E describes the calculation of the CRLB, which is based upon estimation of the Fischer Information Matrix. Generation of the FIM relies upon a single, well-defined

likelihood function from which we can infer the most likely value of unobserved parameters ($\rho_W, \rho_F, R_2^*$,...) given an observed CSE-MRI signal. This is a reasonable assumption for the MAGO algorithm. However, the MAGO-FMS and GC-MBR algorithms both apply additional refinement steps after estimation of an initial solution to the signal equation, such that parameter estimation cannot be described by a singular fixed function. The performance of these algorithms must therefore be assessed empirically. The analysis in this chapter consequently focuses on the fraction of fat-water swapped pixels as the primary metric of the quality of the CSE-MRI maps.

For each dataset, the manually-corrected adipose tissue mask generated in Chapter 4 was applied to the PDFF maps resulting from each solution. As performed in Chapter 4, the number of fat-water swapped adipose tissue pixels was defined as the number of pixels measuring <20% PDFF lying within this "ground truth" adipose tissue mask.

Breast adipose tissue masks were also determined individually for the maps generated by each algorithm using the method described in Chapter 4, such that no fat-water swapped pixels would be included in these masks. The median PDFF and $T_2^*$ values across these masks were calculated and compared across the algorithms.

## 5.3 Results

### 5.3.1 Siemens

The median PDFF and $T_2^*$ observed in the breast adipose tissue was similar across the three fitting algorithms employed in the Siemens analysis (Figure 5.1), with a difference of less than 0.3% in the median adipose PDFF and less than 1ms in the median adipose $T_2^*$.

However, the proportion of fat-water swapped pixels incurred by use of each algorithm varied significantly (Figure 5.2). The hybrid fitting algorithm (GC-MBR) produced the lowest median incidence of swaps; this was reflected in visual assessment of map quality (Figure 5.3). With this algorithm, the median proportion of swapped adipose tissue pixels was just 0.2%. Comparatively, the incidence of

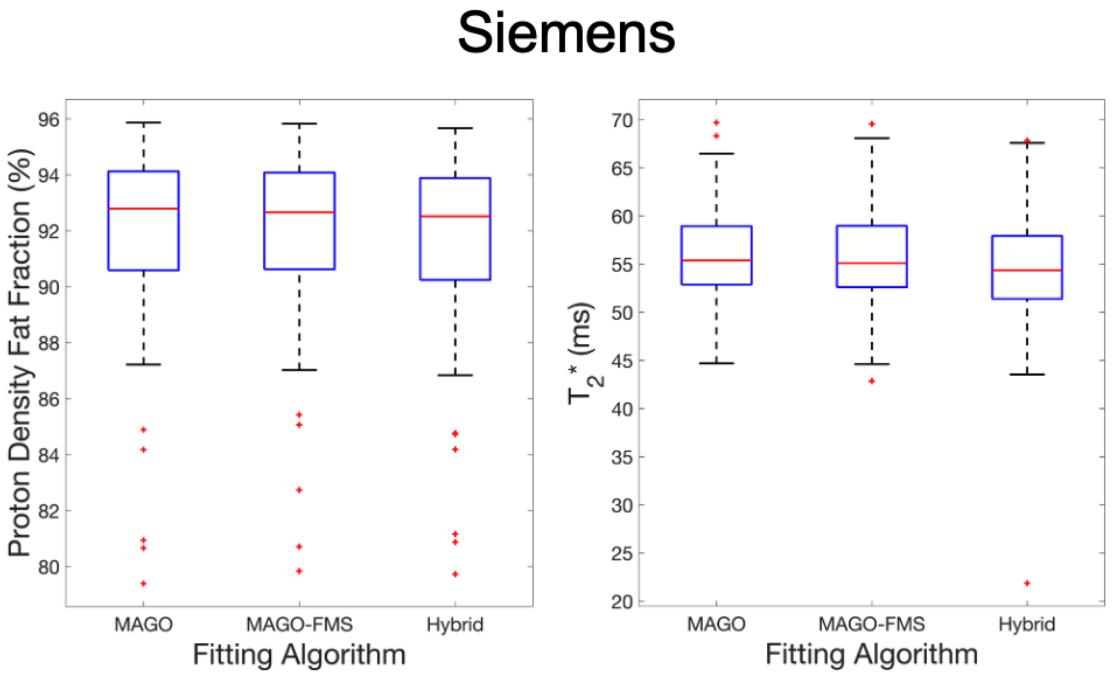


**Figure 5.1:** Box plots visualising the difference in median adipose tissue PDFF and $T_2^*$ across the three fitting algorithms employed in the Siemens GRE analysis. The median PDFF and $T_2^*$ varies minimally across the algorithms.

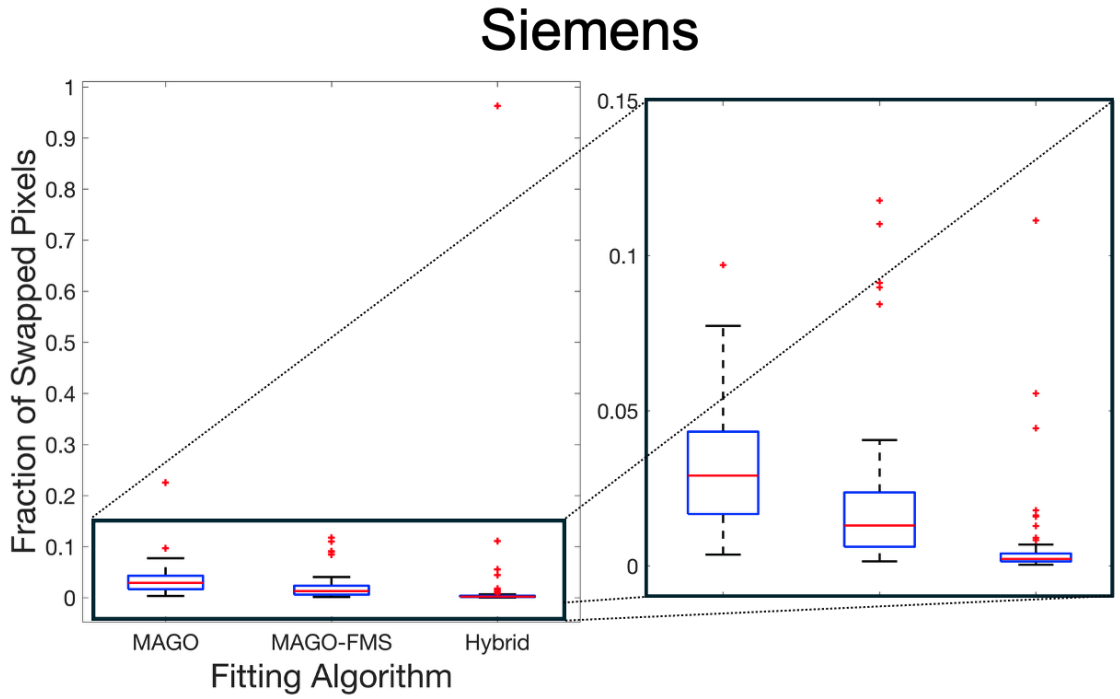


**Figure 5.2:** Box plot demonstrating the fraction of fat-water swapped adipose tissue pixels in the PDFF maps produced by each algorithm examined with the Siemens GRE data. Though one outlier datapoint is observed with 96% swapped pixels, the hybrid algorithm produces the lowest median fraction of swapped pixels compared to the MAGO and MAGO-FMS algorithms.

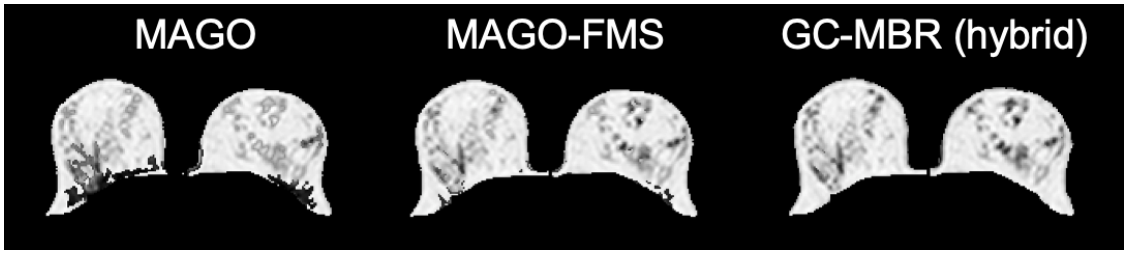


**Figure 5.3:** Example slice from the PDFF maps for a poor quality dataset processed using the MAGO algorithm, the MAGO algorithm with field map smoothing (MAGO-FMS), and the hybrid algorithm (GC-MBR). For both cases, extensive areas of fat-water swapped pixels are observed in the PDFF map processed with the MAGO algorithm. The MAGO-FMS algorithm produces fewer swaps, whilst no swapped pixels are observed in the map produced by the hybrid algorithm.

swapped pixels was approximately six times higher in the MAGO-FMS maps (1.3%) and thirteen times greater in the MAGO maps (2.9%).

Though the hybrid algorithm generally performed excellently, in one dataset, a complete fat-water swap was observed throughout the entirety of the hybrid PDFF map. This effect accounts for the outlier data point observed with ∼96% of swapped pixels. Notably, Borde et al. [139] employed a hybrid-based algorithm (mDixon Quant) in quantification of breast PDFF, and discarded 18% of the data due to fat-water swaps encountered throughout the entire dataset, which were attributed to failure in the phase error correction step. For the hybrid algorithm employed in this work (GC-MBR), only 1.7% of data was impacted by this effect. Borde et al. attribute the failure in phase error correction to the bipolar gradients employed in their GRE acquisition. The improved performance of the hybrid algorithm in this work could arise from the use of a monopolar readout gradient, or could be attributed to employing a breast-specific fat spectrum.

### 5.3.2 GE

The "ground truth" adipose tissue segmentation could not be applied to the IDEAL-IQ maps, owing to a slight mis-registration between the raw echo data and the scanner-generated maps, after correction for the GE GradWarp bug described in Section 3.3.2. The adipose tissue masks generated from the IDEAL-IQ acquisition were therefore visually inspected against the IDEAL-IQ PDFF maps, with the

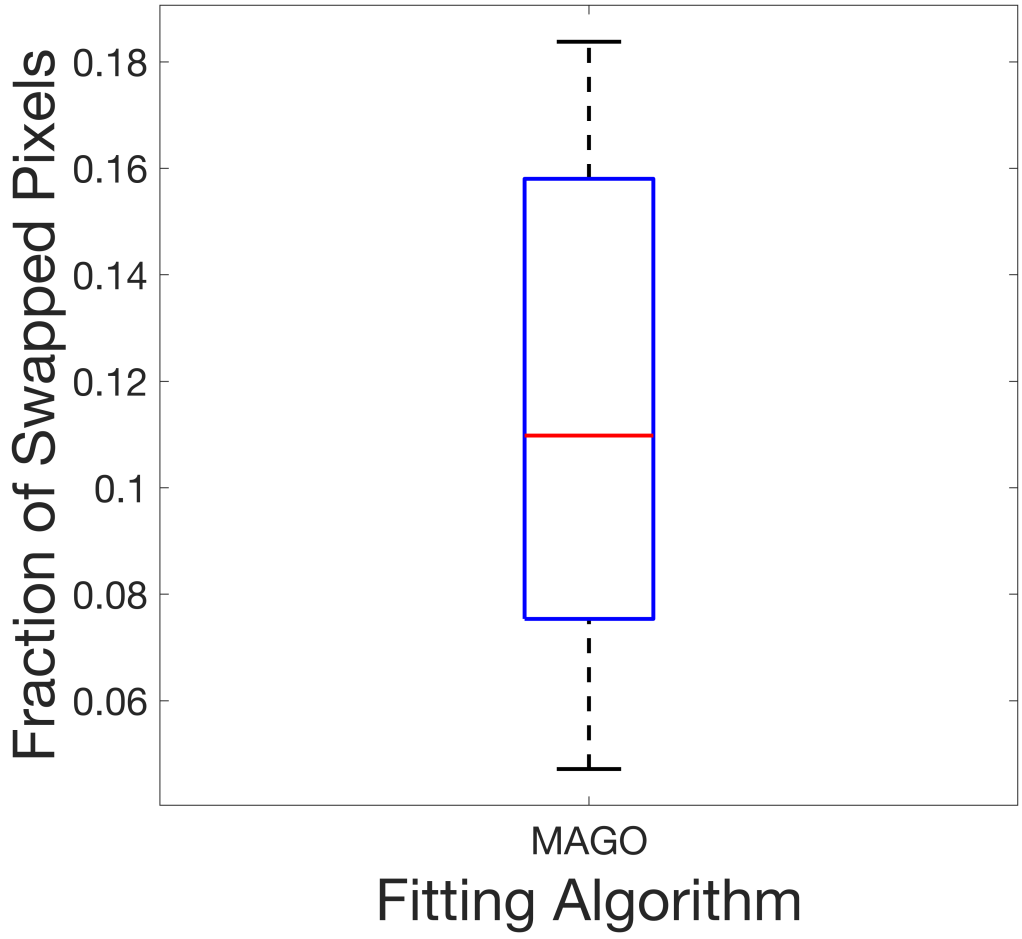


**Figure 5.4:** Box plot demonstrating the fraction of fat-water swapped adipose tissue pixels in the PDFF maps produced by the MAGO algorithm as applied to the GE GRE data. No fat-water swapped pixels were observed in the GE IDEAL-IQ acquisition.

intention of correcting the masks to include any fat-water swapped adipose tissue pixels which may have been excluded by use of the thresholding step during mask generation (Section 4.2.6). However, no fat-water swapped breast adipose tissue pixels were observed.

On the contrary, the incidence of fat-water swaps was high in the MAGO-generated GE PDFF maps (Figure 5.4), with a median proportion of 11.0% of adipose tissue pixels affected. This is approximately four times greater than the the incidence of swaps observed in the Siemens MAGO PDFF maps. This result could be attributed to a difference in SNR observed between the vendors - though a slightly higher flip angle was utilised in the GE GRE acquisition, an 8-channel breast coil was employed, which may incur poorer SNR performance than the 18-channel

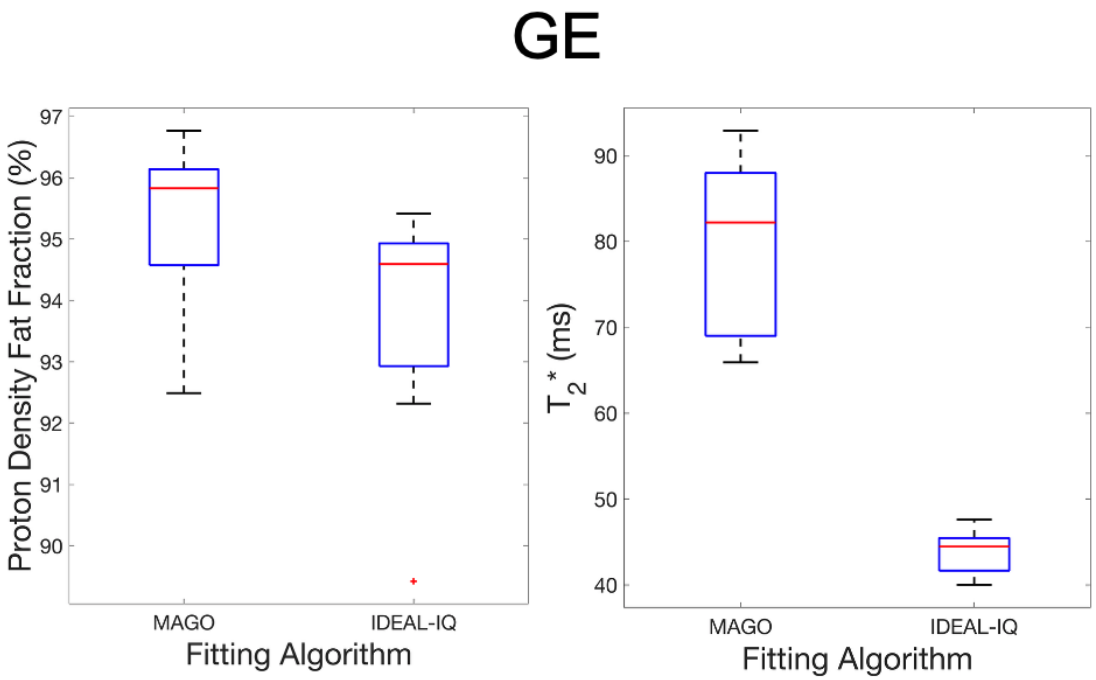


**Figure 5.5:** Box plots visualising the difference in median adipose tissue PDFF and $T_2^*$ across the two algorithms employed in the GE GRE analysis. The median PDFF and $T_2^*$ varies across the algorithms; this may be attributable in part to the "noise floor" effect.

breast coil used in the majority (93%) of Siemens acquisitions.

The median breast adipose tissue PDFF and $T_2^*$ varied between the IDEAL-IQ and MAGO-generated maps (Figure 5.5). A moderate difference of 1.2% was observed in the median adipose tissue PDFF, whilst a large difference of 38ms was observed in the median $T_2^*$. Whilst comparative analysis of GoF metrics such as $R^2$, SD-PDFF, and SD-$T_2^*$ was not possible, and whilst no *in vivo* ground truth measurements of PDFF or $T_2^*$ exist, the adipose tissue $T_2^*$ values observed with IDEAL-IQ lie closer to those observed in the Siemens data across all fitting algorithms (Figure 5.1), and are more consistent with other adipose tissue $T_2^*$ values reported at 1.5T [163]. The overestimation in $T_2^*$ by the MAGO algorithm could be attributable to the noise floor effect [164, 165], in which the Rician noise distribution of magnitude data overestimates the MR signal at low SNR. The signal is therefore prevented from decaying to zero at later echo times; instead, it approaches a positive noise floor. This causes an overestimation in the measured $T_2^*$, as a fitting algorithm will assume the acquired signal to be decaying more slowly than it truly is. The

GE magnitude data may be particularly impacted by this effect due to the reduced number of channels in the breast coil employed which is associated with lower SNR.

## 5.4 Discussion

Quantitative analysis suggests that, where phase data is available, a hybrid fitting algorithm provides better quality breast PDFF maps over a magnitude-based algorithm either with or without a complex refinement step. This may be caused by the increase in effective SNR resulting from initialising the hybrid algorithm with complex data. The assumption of field map smoothness is often employed in complex-based algorithms, which can lead to quantification errors in areas where this assumption is not valid. The adaptive smoothness term in the complex-based graph cut algorithm step of the hybrid algorithm employed in this work accounts for the irregularity of the field maps acquired in the breasts, where tissue interfaces are common.

Phase echo data was not available for GE GRE data, therefore the aforementioned hybrid algorithm could not be employed. Instead, we evaluated the scanner-generated IDEAL-IQ PDFF and $T_2^*$ maps against those generated with MAGO. The absence of fat-water-swapped pixels observed in the IDEAL-IQ maps suggests that this algorithm provides preferable quantification of breast PDFF and $T_2^*$ over MAGO. Like the Siemens analysis, this result may also derive from an effective increase in SNR due to the incorporation of phase data in the IDEAL-IQ algorithm. However, using scanner-generated maps limits user flexibility; for example, it is not possible to incorporate a breast-specific spectrum, or to interrogate the underlying signal fit. Nevertheless, for the purpose of this thesis, the quality of the PDFF and $T_2^*$ maps is crucial - particularly for applications such as breast density quantification (Chapter 6), where accurate quantification of PDFF across the entire breast is essential.

All algorithms examined in this work employed a mono-exponential decay accounting for a single $T_2^*$ value shared by the fat and water species. In practise, the $T_2^*$ of these species may not be identical; the incorporation of single common $T_2^*$ value in Equation 2.15 reflects an additional assumption which has been made

in the signal model. However, dual-$T_2^*$ models demonstrate poor noise performance [166], and are rarely employed in practise.

The key limitation of this work is the small number of CSE-MRI fitting algorithms examined. Including additional algorithms in this analysis could help to determine if further gains in performance are possible. Daudé et al. examined a variety of CSE-MRI fitting algorithms in the sacral and supraclavicular regions of the body, where large $B_0$ inhomogeneities were observed [134]. An algorithm based upon IDEAL with additional constraints implemented [151] performed well; this approach could translate well to the breast, where significant field inhomogeneities are expected, and the IDEAL-IQ algorithm has already been demonstrated to perform well. Additionally, the GOOSE algorithm has been shown to produce a good quality breast PDFF map [167] which contained fewer areas of fat-water swaps than other algorithms. Further work could also examine the performance of machine-learning-based algorithms in CSE-MRI; convolutional neural networks (CNNs) are increasingly used for this purpose, with field map regularisation enforced via a loss function.

In this work, we have shown the importance of including phase information in breast CSE-MRI, and demonstrated the utility of a hybrid approach initialised with a graph cut algorithm, which yields swaps in only 0.2% of adipose tissue pixels. Given that some of these cases may reflect user error in the definition of the "ground truth" adipose tissue masks, the proportion of swaps may be even lower. Therefore, whilst many variations of CSE-MRI algorithms exist, this work has demonstrated the excellent quality produced by the hybrid GC-MBR and IDEAL-IQ algorithms and their sufficiency for use in this thesis. Future work should also compare breast CSE-MRI algorithms at 3T, where differences in SNR and the potential presence of bipolar readout gradients could influence these results.

## 5.5 Conclusion

Quantitative evaluation of PDFF map quality suggests that hybrid fitting algorithms initialised with complex data outperform magnitude-based approaches in breast

CSE-MRI. In this thesis, we will employ a hybrid-based fitting algorithm initialised with a graph-cut algorithm (GC-MBR), alongside a breast-specific fat spectrum, in the analysis of Siemens GRE data. For GE data, where phase echo data is not available, we will employ the PDFF and $T_2^*$ maps generated by the proprietary algorithm of the vendor, IDEAL-IQ.

# 6

# Quantitative Breast Density Calculation with Proton Density Fat Fraction

Over the last three chapters, we determined the optimal approach for generation of breast PDFF and $T_2^*$ maps, having considered the effect of the GRE acquisition, fat spectrum, and fitting method in the CSE-MRI algorithm. We now consider our first application of breast PDFF maps - namely, their utility in providing a quantitative, non-ionising calculation of volumetric breast density.

This chapter was adapted in part from Gordon et al. [145], Gordon et al. [168], and Gordon et al. [169].

## Contents

| BI-RADS® Category | Description |
|---|---|
| A | The breasts are almost entirely fatty. |
| B | There are scattered areas of fibroglandular density. |
| C | The breasts are heterogeneously dense, which may obscure small masses. |
| D | The breasts are extremely dense, which lowers the sensitivity of mammography. |

**Table 6.1:** The breast composition categories defined by the ACR BI-RADS® Atlas version 5 (2013) [30]. For further information, please see www.acr.org/Quality-Safety/Resources/BIRADS.

## 6.1 Introduction

Mammographic breast density is a measure of the relative proportion of fibroglandular to fatty tissue in the breast, which is a strong, well-established risk factor for breast cancer [9, 39, 170] and a confounder for the sensitivity of mammography [8]. In Section 2.1.3.1, we outlined quantitative and qualitative methodologies employed in assessment of breast density. Notably, in clinical practise, a four-category classification defined by the Breast Imaging-Reporting and Data System (BI-RADS®) (Table 6.1) is employed. The BI-RADS® classification relies on a radiologist's judgement to classify images based on visual assessment alone, and has been shown to have substantial inter- and intra- operator variability [10, 171–174]. This variability remains regardless of the experience of the radiologist [175], and differences have been demonstrated in the classifications assigned by UK versus US radiologists [176]. As discussed in Section 2.1.3.1, quantitative, automated approaches to calculation of breast density with mammography eliminate operator variability, but are inherently limited due to the two-dimensional nature of the imaging modality and the necessity of the application of ionising radiation.

MRI offers an inherently three-dimensional, non-ionising solution to measurement of volumetric breast density. Quantitative MRI-based techniques are typically based on voxel classification, in which each voxel in the MRI image is categorised as either containing solely fibroglandular tissue or solely fatty tissue. Breast density may

then be determined through calculation of the proportion of the number of voxels identified as fibroglandular tissue to the total number of voxels within the breasts.

As described in previous chapters, PDFF is a robust, quantitative measure of tissue fat concentration. This biomarker has recently been proposed as a technique for calculation of volumetric breast density which does not rely on the binary classification of voxels [127, 139]. The fundamental basis for the calculation is that fibroglandular tissue contains no fat and therefore is associated with a PDFF of 0%, whilst adipose tissue has high fat content and is therefore associated with a high PDFF value. By taking the mean PDFF across the whole breast, and accounting for the known adipose tissue PDFF, we can infer the relative proportion of fibroglandular tissue in the breast. This approach to calculation of breast density does not require voxels containing a mixture of both tissue types to be classified as either fatty tissue or fibroglandular tissue; this could reduce the error in MRI-based breast density quantification arising from the partial volume effect.

Two studies have examined PDFF in the calculation of breast density thus far. Borde et al. [139] showed promise in the clinical translation of this biomarker, observing a negative correlation between whole-breast PDFF and BI-RADS® density categories. Meanwhile, Henze Bancroft et al. [127] found good reproducibility across MR acquisition parameters in the volume of fibroglandular tissue derived from proton density water fraction (PDWF) maps.

Studies have not yet incorporated a breast-specific fat spectrum in PDFF-derived breast density, and the clinical performance of this biomarker has not been examined at 1.5T. Studies have also not yet accounted for the variation in breast adipose tissue PDFF observed between subjects, and instead assume a constant value for all participants. The performance of PDFF has also not yet been compared to traditional quantitative MRI algorithms for breast density assessment. For example, the hypothesised superior robustness of PDFF-based density calculations to the partial volume effect has not yet actually been demonstrated; for this, direct comparison against voxel-classification-based MRI algorithms is required.

This chapter will assess whether a PDFF-derived breast density calculation which accounts for the specific composition of breast fat can distinguish between clinically meaningful categorisations at 1.5T and whether this biomarker shows improved performance against traditional MRI-based techniques.

Firstly, in Section 6.2, we describe the development of specialised phantoms and use these to compare the accuracy of PDFF against classification-based density algorithms. Subsequently, in Section 6.3, we examine *in vivo* data to compare PDFF-derived breast density to radiologist-assigned BI-RADS® scores, and assess the impact of accounting for the specific PDFF of participants' breast adipose tissue. We also examine the impact of accounting for the distribution of fibroglandular tissue through calculation of textural features in the PDFF maps.

## 6.2 *In Vitro* Evaluation Against Classification-Based Algorithms

### 6.2.1 Introduction

Voxel-classification-based approaches for calculating breast density often rely on interactive thresholding of $T_1$-weighted images [177–180]. In these approaches, a user selects a cut-off value in the image intensity to distinguish between the fatty and fibroglandular tissue types. Manual tissue segmentation by expert readers is commonly used as a ground truth estimate of breast density, but is rarely performed in practise due to its time-consuming nature [181].

Algorithms based on fuzzy c-means (FCM) clustering offer a semi-automated approach to the segmentation of fibroglandular and fatty tissue. Firstly, a user selects the number of clusters and initialises each one with an image intensity value. The algorithm calculates a membership matrix (known as a "partition matrix") which indicates how likely each pixel is to belong to each cluster. Each pixel is then assigned to belong to the cluster with the highest membership value. The user then must determine the tissue type captured by each cluster through visual comparison to the original $T_1$-weighted image. FCM clustering (FCMC) has been shown to reduce operator variability compared to global thresholding [182], and the

addition of a bias field correction step further improves accuracy [183]. However, significant user input into FCMC algorithms is required and the density calculation is fundamentally limited by the partial volume effect.

Ground truth measurement of volumetric breast density is not possible without access to *ex vivo* whole breast samples. We therefore developed a series of five specialised phantoms and used these to compare the accuracy of PDFF against FCM clustering of $T_1$-weighted images in breast density calculation.

## 6.2.2 Methods

### 6.2.2.1 Phantom Development

The phantoms consisted of plastic containers filled with known volumes of peanut oil, representative of breast fatty tissue, and agar, representative of breast fibroglandular tissue (Figure 6.1). By varying the relative proportion of agar to oil, each phantom was designed to have a known volumetric breast density. The agar component was cut into different sized blocks; this was intended to vary the levels of the partial volume effect induced by each phantom. For a cube with sides $n \times n \times n$, the surface area to volume ratio is $\frac{6}{n}$; smaller pieces of agar therefore had a higher surface area to volume ratio and were expected to be more affected by the partial volume effect. The largest agar piece was a single continuous block, representative of breasts with a concentrated area of fibroglandular tissue, whilst the smallest pieces of agar were cut into cubes measuring 0.5cm $\times$ 0.5cm $\times$ 0.5cm, to represent more scattered breast structures (Figure 6.2).

The design of these phantoms was based upon the phantoms described in Henze Bancroft et al. [127]. They created three phantoms, each containing a different relative proportion of agar and different sized agar pieces. We based our phantoms upon this design but included more phantoms in the series, such that we could examine density and tissue structure as independent variables. Henze Bancroft et al. doped the agar component of the phantoms to have a similar $T_1$ to breast fibroglandular tissue using copper sulphate ($CuSO_4$). We expanded upon this work by doping the agar component to produce both a similar $T_1$ and $T_2$ to

| | Phantom 1 | Phantom 2 | Phantom 3 | Phantom 4 | Phantom 5 |
|---|---|---|---|---|---|
| True Density | 15% | 5% | 25% | 15% | 15% |
| Block Size | 1.0cm x 1.0cm x 1.0cm | 1.0cm x 1.0cm x 1.0cm | 1.0cm x 1.0cm x 1.0cm | 0.5cm x 0.5cm x 0.5cm | 6.0cm x 5.7cm x 2.0cm |
| Photo |  | | | | |
| $T_1$-weighted Image | 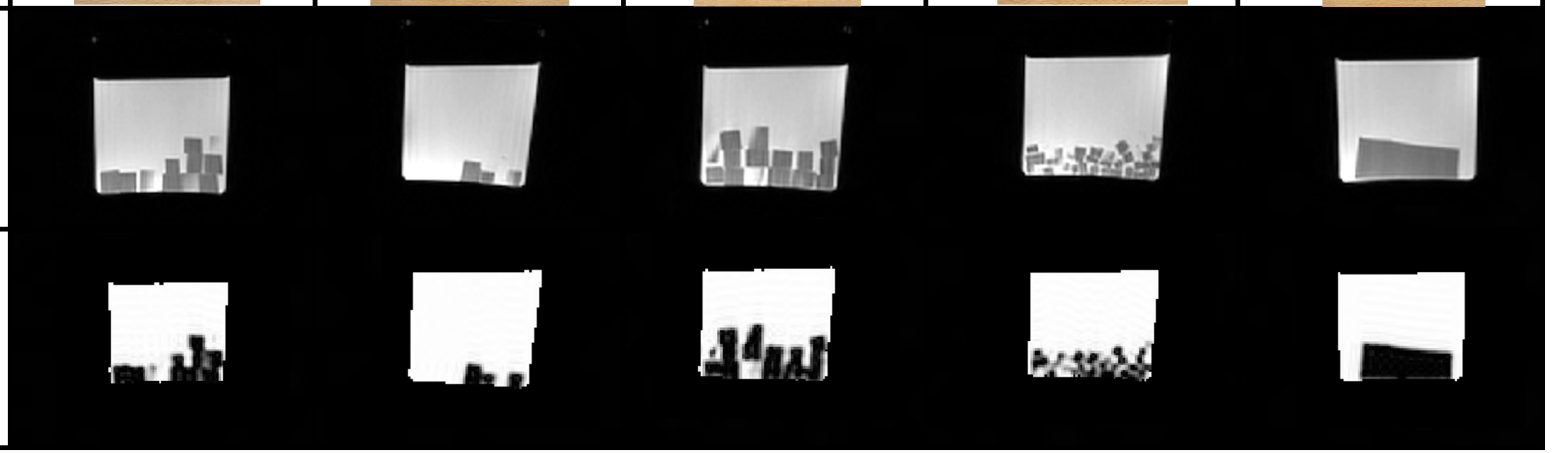 | | | | |
| PDFF Map | | | | | |

**Figure 6.1:** Overview of the developed breast density phantoms. The five phantom contain known volumes of agar and peanut oil. The size of the agar pieces varies between each phantom to represent different levels of partial voluming, ranging from a continuous block of agar (Phantom 5) to 0.5cm x 0.5cm x 0.5cm cubes (Phantom 4). For each phantom, a single slice of the $T_1$-weighted image and a single masked slice of the PDFF map is shown.

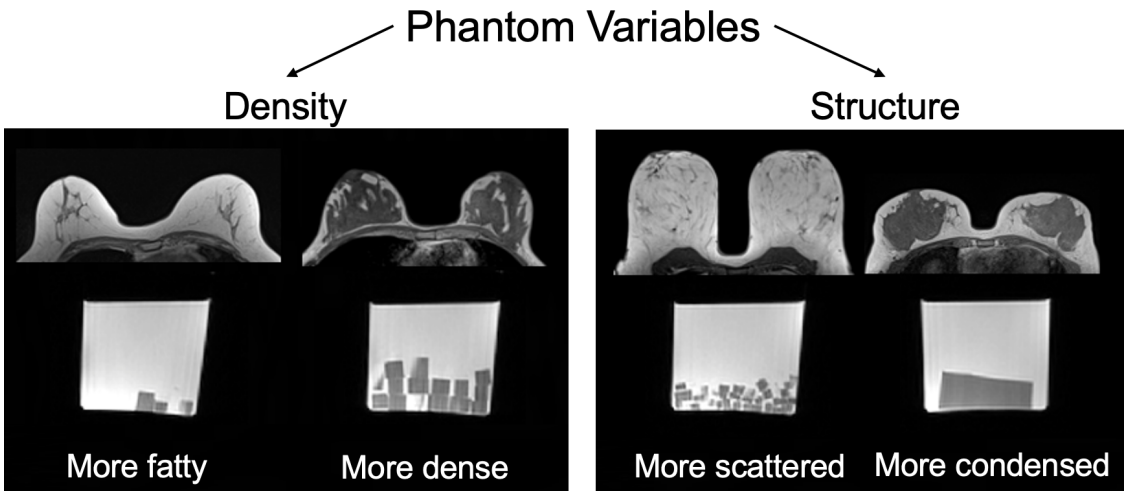


**Figure 6.2:** Overview of the two variables in phantom design - the known density of the phantoms and the structure of the fibroglandular tissue component within the phantom, varied by the size of the agar block. The left hand side image shows $T_1$-weighted images of two phantoms with the same block size but different known densities, whilst the right hand side image shows two phantoms with the same known density but different block sizes. $T_1$-weighted *in vivo* images of volunteers with different breast densities and structures are shown for comparison.

breast fibroglandular tissue. These are reported in literature to be measured as 1266±82ms and 58±10ms at 1.5T respectively [116]. We used nickel chloride ($NiCl_2$) as the dopant for this purpose at a concentration of 0.73mM in a 3% agar solution. These concentrations were determined through examination of phantom relaxivity equations (see Appendix C). Sodium benzoate at a concentration of 3mM was also included in the agar solution to act as a preservative.

#### 6.2.2.2 Image Acquisition

Phantoms were scanned on a 1.5T GE Signa Voyager scanner using an 8-channel breast coil. The phantoms each rested in one opening of the breast coil, and were secured in position using foam padding.

A 3D $T_1$-weighted FSPGR Dixon sequence (LAVA Flex) with an in-plane reconstructed resolution of 0.78 × 0.78mm$^2$ was performed - further sequence parameters are given in Section A.1. Additionally, a 3D 6-echo gradient-echo scan (IDEAL-IQ) was acquired with an in-plane resolution of 1.71 × 1.71mm$^2$ for generation of PDFF maps - please see Section A.3 for further details.

Acquisitions deemed by Perspectum Ltd. to be the "gold-standard" for measurement of $T_1$ and $T_2$ were also performed to evaluate the achieved relaxation times of the agar component. A turbo spin echo inversion recovery sequence (TSE-IR) with 7 inversion times was acquired for estimation of $T_1$ whilst a multi-contrast spin echo acquisition with 8 echoes was used to measure $T_2$. These scans were performed on Phantoms 1 and 5 as the agar component for Phantom 5 was made in a different batch, though to the same specification, as the agar component for Phantoms 1-4.

#### 6.2.2.3 Analysis Methods

PDFF maps were generated using the proprietary algorithm of the vendor (IDEAL-IQ, GE Healthcare), which accounts for $T_2^*$ decay and a multi-peak fat spectrum.

$T_1$ and $T_2$ maps were generated using in-house Perspectum software based upon fitting an inversion recovery curve and a signal decay curve respectively (Equations 2.7 and 2.9). ROIs were positioned within the agar and the median $T_1$ and $T_2$ were calculated. The $T_1$ of the agar component was measured to be 1158ms in Phantom 1 and 1175ms in Phantom 5. Whilst these values lie just outside the standard deviation of the $T_1$ of fibroglandular tissue at 1.5T (1266±88ms), they lie within 9% of the median value. This deviation is consistent with the criteria used to accept phantoms in Perspectum, which allows for a 12% deviation from the target $T_1$ using the TSE-IR measurement employed in this work. The $T_2$ of the agar component was measured to be 56ms in Phantom 1, and 59ms in Phantom 5, both lying within the standard deviation of the $T_2$ of breast fibroglandular tissue at 1.5T (58±10ms) and within 4% of the average fibroglandular tissue $T_2$ [116].

Whole phantom masks were generated for PDFF maps and the $T_1$-weighted Dixon images using the automated approach described previously in Section 4.2.5, which is based upon the application of morphological operations to the generated water and fat images (Figure 6.3).

Three FCMC algorithms were applied to the $T_1$-weighted images (Figure 6.4). This included FCMC without any bias field correction (BFC), with simultaneous

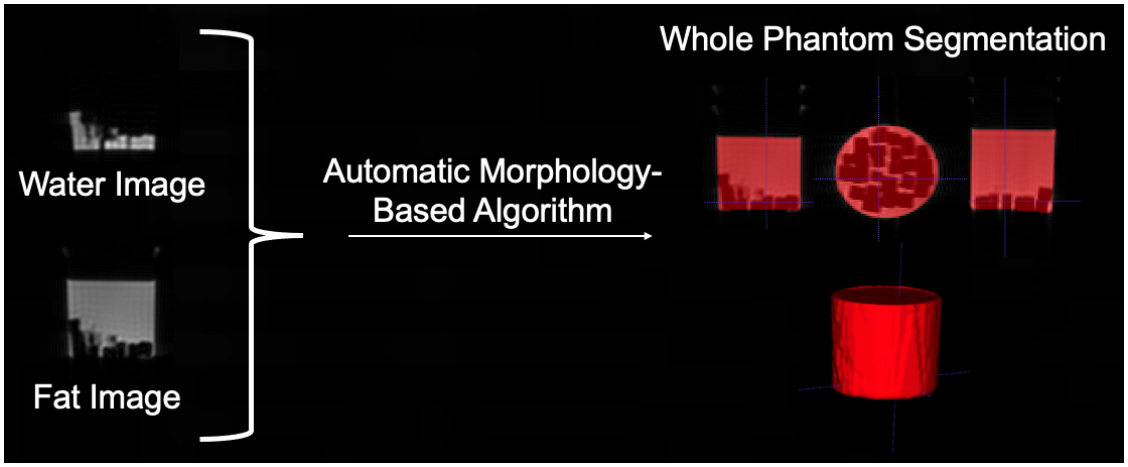


**Figure 6.3:** Example images showing the generation of a whole phantom segmentation. Calculated water and fat images, which may be produced by both the $T_1$-weighted Dixon acquisition and the CSE-MRI acquisition, are combined under morphological operations to produce a segmentation of the whole phantom. The resulting whole phantom segmentation is shown in red. In the top right hand row, the segmentation is shown overlayed on the fat image in the axial, coronal, and sagittal views, whilst below, the three dimensional segmentation is shown.

correction of the bias field [184, 185][1], and with a type of bias field correction known as N4 [186], which uses histogram sharpening and a B-spline model to estimate and correct the bias field. Areas of the partial volume effect were observed around the phantom edge in the $T_1$-weighted images, so an additional image erosion step was included in generation of the phantom masks for the $T_1$-weighted images.

The FCMC algorithms were set to identify three clusters in the $T_1$-weighted images (oil, agar, and background) and were initialised using user-placed ROIs. The user then classified the component identified by each cluster. Density was calculated as

$$\text{Density } (\%) = 100\% \times \frac{N_{\text{Agar}}}{N_{\text{Agar}} + N_{\text{Oil}}} \tag{6.1}$$

where $N_{\text{Agar}}$ and $N_{\text{Oil}}$ are the number of voxels in each cluster within the phantom mask.

For determination of PDFF-derived breast density, we firstly consider the PDFF of a single voxel, $r$. Where the proportion of fibroglandular tissue in the voxel is

[1]We gratefully acknowledge the use of the Bias Field Corrected Fuzzy C-Means toolbox by Dirk-Jan Kroon [185].

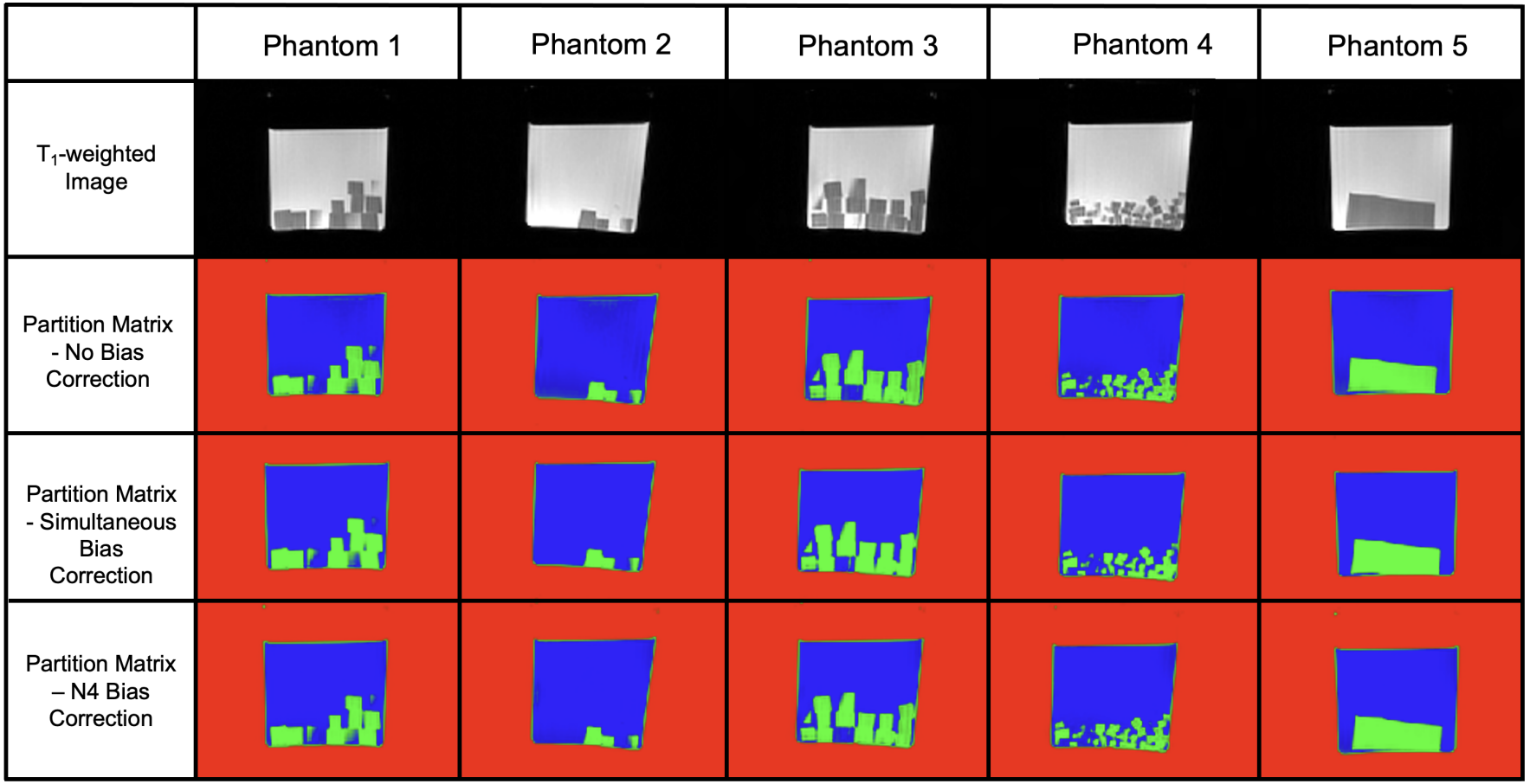


**Figure 6.4:** Central slices of the 3D $T_1$-weighted images and calculated partition matrices for each phantom using FCMC with three different bias field correction techniques. The partition matrices reflect the likelihood of each pixel belonging to one of three clusters and are shown here in an RGB colourmap, such that the colour of each pixel corresponds with the likelihood of the pixel belonging to each cluster. Red corresponds to the cluster initiated in the background, blue corresponds to the cluster initiated in oil, and green corresponds to the clustered initiated in the agar. Regions of the partial volume effect can be observed around the phantom edge, where pixels incorrectly show increased likelihood of belonging to the agar cluster.

$\rho(r)$, the PDFF of that voxel will be measured as

$$PDFF(r) = PDFF_{\text{Fibroglandular}}\rho(r) + PDFF_{\text{Adipose}}(1 - \rho(r)) \tag{6.2}$$

where $PDFF_{\text{Fibroglandular}}$ is the known PDFF of the fibroglandular tissue and $PDFF_{\text{Adipose}}$ is the known PDFF of the adipose tissue. Re-arranging for $\rho(r)$, we find the proportion of fibroglandular tissue in each voxel is [127]

$$\rho(r) = \frac{PDFF_{\text{Adipose}} - PDFF(r)}{PDFF_{\text{Adipose}} - PDFF_{\text{Fibroglandular}}} \tag{6.3}$$

Breast density can be calculated as

$$\text{Density } (\%) = 100\% \times \frac{\int\limits_{ROI} \rho(r)dV}{\int\limits_{ROI} dV} \tag{6.4}$$

where $dV$ denotes that the integration should be performed over the volume of the whole breast segmentation, $ROI$. Assuming constant voxel size,

$$\text{Density } (\%) = 100\% \times \frac{\sum\limits_{r=1}^{N} \rho(r)}{N} \tag{6.5}$$

where $N$ is the number of voxels in the segmentation. Substituting for 6.3, we find

$$\text{Density } (\%) = 100\% \times \frac{\sum\limits_{r=1}^{N} \frac{PDFF_{\text{Adipose}} - PDFF(r)}{PDFF_{\text{Adipose}} - PDFF_{\text{Fibroglandular}}}}{N} \tag{6.6}$$

Assuming constant $PDFF_{\text{Fibroglandular}}$ and $PDFF_{\text{Adipose}}$ across the voxels, breast density may be calculated as

$$\text{Density } (\%) = 100\% \times \frac{PDFF_{\text{Adipose}} - \frac{\sum\limits_{r=1}^{N} PDFF(r)}{N}}{PDFF_{\text{Adipose}} - PDFF_{\text{Fibroglandular}}} \tag{6.7}$$

where $\frac{\sum\limits_{r=1}^{N} PDFF(r)}{N}$ is the mean PDFF across the whole breast segmentation.

In the phantoms, $PDFF_{\text{Fibroglandular}} = PDFF_{\text{Agar}} = 0\%$ whilst $PDFF_{\text{Adipose}} = PDFF_{\text{PeanutOil}} = 100\%$, therefore

$$\text{Density } (\%) = 100\% - \frac{\sum_{r=1}^{N} PDFF(r)}{N} \tag{6.8}$$

Bland-Altman analysis [123] [2] was used to compare density measured with the different algorithms against ground truth values. In addition to the 95% limits of agreement (LoA), bias, and half-width of the LoA (HWLoA) commonly reported in Bland-Altman analysis, here we also report the mean absolute deviation (MAD) of the data from ground truth for optimal comparison to relevant literature.

To provide an initial assessment of the variability of $T_1$-weighted FCMC algorithms, $T_1$-weighted images of one healthy volunteer were analysed using FCMC with N4-BFC. The volunteer was imaged on a GE Signa Voyager 1.5T scanner using the $T_1$-weighted sequence employed throughout this thesis, which is described in full in Table A.1. A mask of the whole of both breasts was found using the approach described in Section 4.2.5. A paper by Clendenen et al. [188] provided the basis for the *in vivo* FCMC methodology. For greatest consistency with the approach described in this work, the skin erosion step which was employed in previous calculation of whole breast masks in this thesis was not performed, and the breast mask was applied to the $T_1$-weighted images prior to application of the FCMC algorithm. Seven clusters were employed, with three initialised in the fibroglandular tissue, two in the fatty tissue, one in the skin, and one in the image background. To initialise each cluster, one user placed an ROI with radius 1.6mm in the tissue of interest; the mean signal within the ROI was used to initialise this cluster in the FCMC algorithm.

### 6.2.3 Results

Bland-Altman analysis demonstrated the significant over-estimation of phantom density by $T_1$-weighted FCMC algorithms due to regions of the partial volume effect (PVE) around the phantom edge (Figure 6.5). Applying an additional image erosion step to phantom masks of the $T_1$-weighted images to intentionally exclude this region

[2] We gratefully acknowledge use of the Bland-Altman toolbox by Rik [187].

improved this bias. PDFF demonstrated excellent accuracy in density measurement (bias = 0.09%, 95% limits of agreement (LoA) = -0.85-1.03%, half-width of the LoA (HWLoA) = 0.94%, mean absolute deviation (MAD) = 0.35%). When comparing PDFF against the $T_1$-weighted FCMC algorithms with the additional image erosion step, PDFF demonstrated tighter agreement compared to $T_1$-weighted FCMC without BFC (bias = 0.21%, LoA = -1.08-1.51%, HWLoA = 1.30%, MAD = 0.55%) and with simultaneous BFC (bias = -0.33% LoA = 3.70-3.04%, HWLoA = 3.37%, MAD = 1.05%). $T_1$-weighted FCMC with N4-BFC and the additional image erosion step showed comparable agreement to PDFF but had a slightly higher bias (bias = 0.45%, LoA = -0.48-1.38%, HWLoA = 0.93%, MAD = 0.56%).

PDFF showed the least dependence of all algorithms upon the surface area to volume ratio of the agar component (Figure 6.6), which correlates with the level of the partial volume effect within the phantom.

The calculated breast density of one volunteer varied considerably (26.3%-33.0%) depending on user classification of one voxel cluster (Figure 6.7). Qualitative assessment suggests that neither segmentation captures the fibroglandular tissue structure completely accurately. In particular, thinner areas of fibroglandular tissue were poorly identified, and the algorithm struggled to distinguish between fibroglandular tissue and skin.

### 6.2.4 Discussion

*In vitro* analysis of specialised breast density phantoms demonstrated the improved accuracy of PDFF-derived breast density over algorithms based on fuzzy c-means clustering of $T_1$-weighted images. The accuracy of breast density quantification is particularly important for patient risk stratification, where breast density measurements must closely reflect the true tissue composition to support clinical decision-making. Accurate breast density measurements are also vital when assessing longitudinal changes to the breast structure, such as examining the involution of the breast post-menopause or assessing the effect of chemotherapy on healthy breast tissue. Previous studies employed specially-developed phantoms to measure the accuracy of

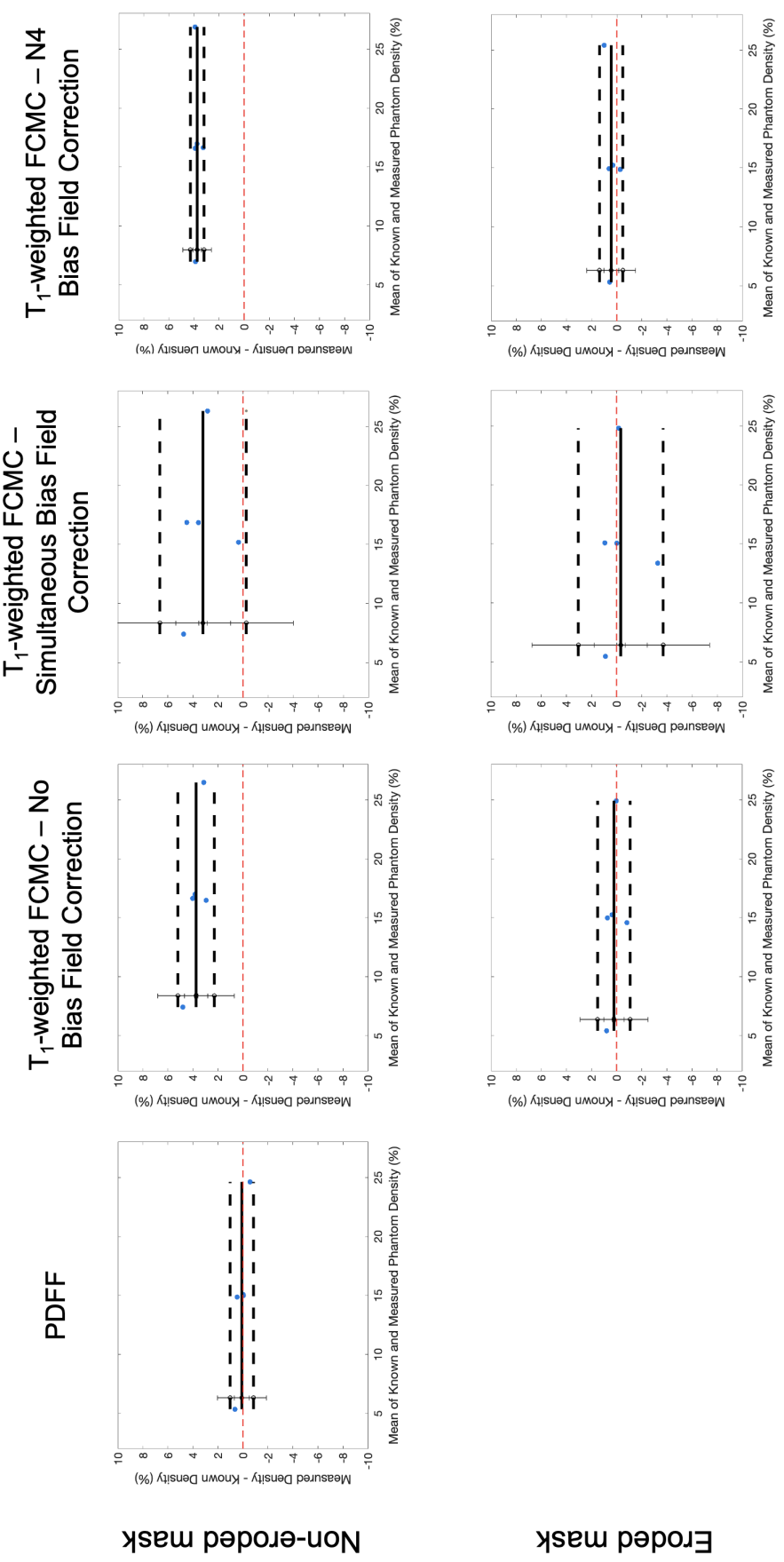


**Figure 6.5:** Bland-Altman plots showing agreement between known phantom density and phantom density measured with four density calculation algorithms. These include PDFF and fuzzy c-means clustering of $T_1$-weighted images without bias field correction, with simultaneous bias field correction, and with N4 bias field correction. Results are shown when the phantom masks in the $T_1$-weighted images do and do not include an additional image erosion step to remove regions of the partial volume effect observed around the phantom edge.

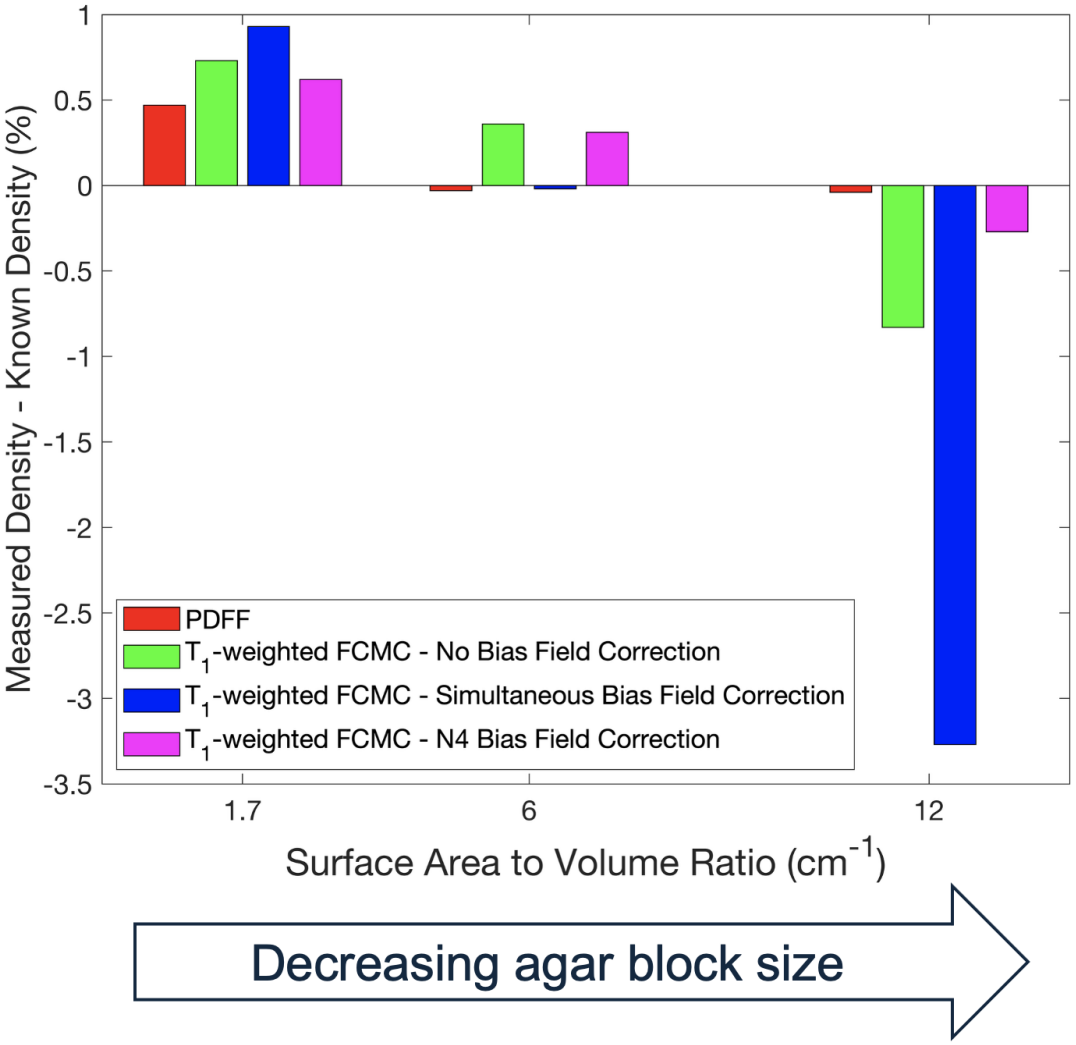


**Figure 6.6:** Grouped bar charts showing the dependence of each density calculation algorithm on the surface area:volume ratio of the agar components, which is an indication of the level of the partial volume effect. Density calculation with PDFF is more insensitive to the partial volume effect than the $T_1$-weighted FCMC algorithms.

automated mammographic techniques for volumetric breast density measurement, reporting MAD values between 1.1-3.4% [189, 190]. In this work, the MAD of PDFF-derived density was 0.4%, suggesting MRI-PDFF may also offer improved accuracy over volumetric density calculations obtained with mammography.

Independently altering the phantom variables enabled us to conclude that PDFF is less sensitive to the partial volume effect than $T_1$-weighted FCMC algorithms, which rely on voxel classification. As described in Chapter 3, calculation of PDFF is still affected somewhat by the partial volume effect as voxels containing mixed

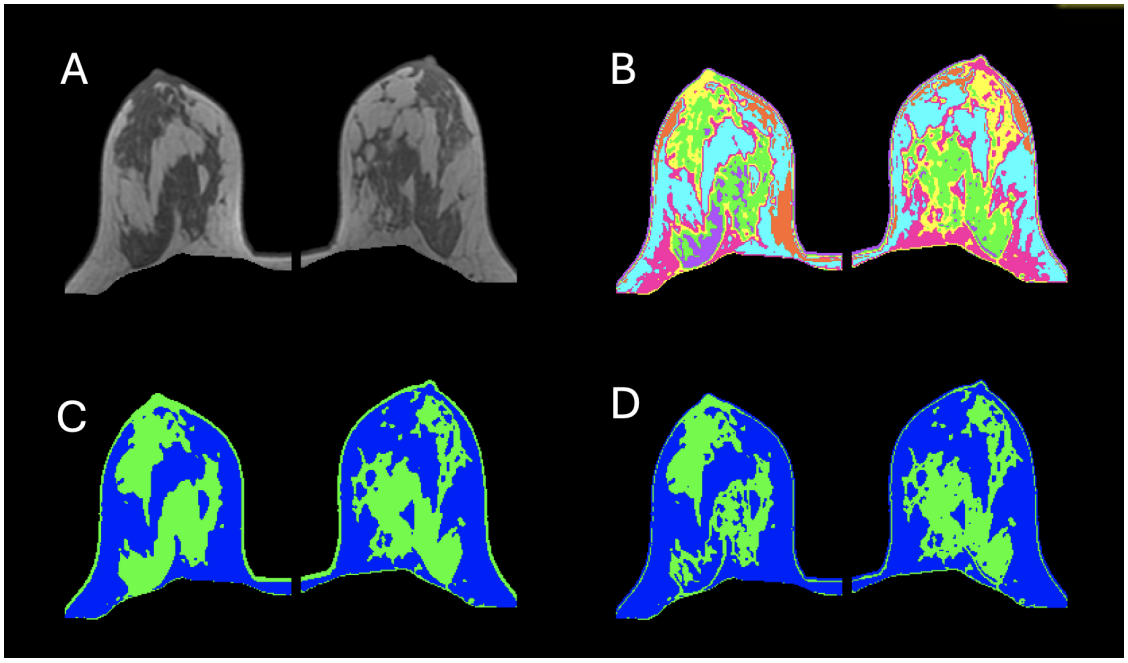


**Figure 6.7:** Overview of an example *in vivo* dataset processed with an N4 bias-corrected fuzzy c-means clustering algorithm to calculate breast density. A: $T_1$-weighted image which has been corrected for the bias field using the N4 algorithm prior to application of the FCMC algorithm. B: The seven clusters identified by the FCMC algorithm, with each cluster shown in a different colour. C,D: Two different segmentations of the fibroglandular tissue, found through user classification of the seven identified clusters. Depending on whether the user identifies a particular cluster as FGT, the density estimate varies significantly, with neither segmentation capturing the exact FGT structure. Notably, in both choices, some of the skin is misidentified as FGT.

species are most subject to the $T_1$ bias effect, causing a larger overestimate in PDFF and thereby a larger underestimate in density estimation. This is reflected in the slight trend shown in Figure 6.6, where the difference between the measured and known density becomes increasingly negative as the agar block size decreases. The degree of this trend is significantly less than those observed using the $T_1$-weighted FCMC algorithms.

Fuzzy c-means clustering of $T_1$-weighted images is highly dependent upon the bias field correction algorithm and relies on users' judgement during algorithm initialisation and cluster categorisation. Clendenen et al. [188] reported moderate inter- and intra- operator variability of breast density calculated with FCMC, with coefficients of variation (CoVs) of 2.1% and 6.1% respectively. However, the group noted that the total number of clusters and the number of clusters to measure

fibroglandular tissue were fixed for all operators, so the reported variability is lower than that expected in practise. The operator-independence of PDFF in calculation of breast density could free radiologists' time and reduce measurement variability, whilst its insensitivity to structural composition and scan parameters [127] suggest it could be a widely-implementable clinical biomarker.

A key limitation of this work is the early-stage, prototype nature of the phantoms. Commercially-available plastic containers were used to house the peanut oil and agar, and were chosen due to their low cost and wide availability. These containers are not completely waterproof and over time and continued use, small amounts of oil may leak from the phantom, changing the known density. However, even a leakage of 5ml of oil, a considerable spill, would change the density by less than 0.2% for a phantom with 15% density. During transit, oil may also be displaced within the phantom to temporarily coat the sides and the underside of the phantom lid. This oil may not be included in the density measurement, which could affect comparison of measurements to the ground truth. Another limitation of these phantoms is that the network of FGT they represent is shaped differently to that in the breast. However, this was necessary to be able to accurately control the surface area to volume ratio of the components. An additional limitation of this work lies in that we have only compared the accuracy of PDFF against $T_1$-weighted FCMC algorithms on one scanner. Future work will use the phantoms in a cross-vendor study to evaluate the performance of these algorithms across a wider range of scanners and to assess the comparative reproducibility of the density measurements.

### 6.2.5 Conclusion

PDFF provides a more accurate and robust density calculation than fuzzy clustering of $T_1$-weighted images, with reduced sensitivity to the partial volume effect and the bias field.

## 6.3 *In Vivo* Comparison Against BI-RADS® Categorisations

### 6.3.1 Introduction

The limited inter- and intra- operator agreement of assigning a BI-RADS® breast density category (Table 6.1) is well documented throughout the literature [10, 172–176]. However, despite this variability, BI-RADS® density classifications are firmly embedded in clinical practise. For a novel breast density assessment method to be integrated into the clinic, close agreement with BI-RADS® categorisations must be demonstrated.

Guidelines often employ a dichotomous classification between "fatty" (BI-RADS® categories A & B) and "dense" (BI-RADS® categories C & D) breasts to influence clinical decision-making [191–193]. For example, in some countries, supplemental screening with ultrasound has been introduced for women with "dense" breasts [194, 195], whilst in the USA the FDA requires women with "dense" breasts to be informed of their breast density after undergoing mammography [196].

As we demonstrated in the previous section, PDFF provides a promising solution to measurement of breast density which is more accurate than other quantitative MRI-based methodologies. In this Section, we will examine the clinical applicability of PDFF through comparison of PDFF-derived density to the radiologist-assigned BI-RADS® density categorisation.

At the beginning of this chapter, we described that Borde et al. [139] demonstrated a significant negative correlation between whole breast PDFF and the BI-RADS® categorisation, suggesting promise in the clinical applicability of this biomarker. However, this analysis was performed only at a field strength of 3T, and the approach with which PDFF maps were generated was susceptible to phase errors which lead to the exclusion of 18% of acquired datasets. A breast-specific fat spectrum has not yet been incorporated into calculation of PDFF-derived breast density, which we showed in Chapter 3 to result in improved map quality. It should

also be noted that Borde et al. did not directly calculate breast density, instead using whole breast PDFF as a correlate inverse measurement of breast density.

Whilst Henze Bancroft et al. [127] did derive volumetric breast density from the PDFF maps, neither paper accounted for the variation in breast adipose PDFF across participants. As we described in Chapter 2, and as addressed in literature [197, 198], the PDFF of adipose tissue is thought to vary according to vascularity and adipocyte size, and may even provide a measure of breast fat "quality". Assuming the PDFF of breast adipose tissue to be constant across participants could influence the accuracy of PDFF-derived breast density calculations; for example, if a participant's true breast adipose PDFF were higher than the constant breast adipose PDFF value assumed in the density calculation in Equation 6.7, the participant's breast density would be underestimated. Furthermore, the ability of PDFF to distinguish between the commonly-used dichotomous categorisation of breasts as "fatty" or "dense" has not yet been assessed.

In this work, we will examine the correlation of PDFF-derived breast density to clinically meaningful density categorisations at 1.5T and assess the impact of correcting density calculations for the specific PDFF of participants' breast adipose tissue. We also examine the effect of including spatial information regarding the distribution of fibroglandular tissue in the breast on alignment with the qualitatively-defined BI-RADS® density classifications (Table 6.1).

### 6.3.2 Methods

Forty-seven female participants were scanned in the prone position across the three studies described in Section 2.3. Thirty-eight of the participants were imaged on a Siemens Magnetom Aera 1.5T scanner whilst nine participants were imaged on a GE Signa Voyager 1.5T scanner. The 3D 6-echo gradient echo scan described in Section A.3 was acquired for generation of PDFF maps. Additionally, the standard $T_1$-weighted and $T_2$-weighted 3D acquisitions described in Sections A.1 and A.2 were acquired.

**Figure 6.8:** Central slice of 3D PDFF map, showing example placement of the four circular ROIs with radius 4mm within the breast adipose tissue. These ROIs were used to determine the measured $PDFF_{\text{Adipose}}$ for each individual, which was input into the density calculation.

Both magnitude and phase raw echo GRE data was available for the Siemens acquisition. Therefore, in accordance with the conclusion of Chapter 5, a hybrid fitting method [156] initialised with a graph cut algorithm and complex data [155] was used to generate three-dimensional breast PDFF maps. A healthy breast fat spectrum was incorporated into the signal model, in agreement with the conclusion of Chapter 4.

As described in Section 3.3.2, the raw GRE data output by the GE scanner only contained magnitude information, therefore raw complex GRE data could not be accessed. For two GE data cases, no raw GRE data was exported, only scanner-generated maps were available. For consistency across the GE images, in this work, the scanner-generated PDFF maps were employed, which were generated offline using the hybrid fitting algorithm of the vendor ("IDEAL-IQ").

Voxels in the PDFF maps were constrained to values between 0-100% and whole breast masks were generated using the approach described in Section 4.2.5. This approach is based upon generation of a body mask using an automated morphology-based algorithm, which was combined with an automated step for skin exclusion and manual delineation of the chest wall and the superior/inferior extent of the breasts. Whilst in previous chapters, the manual delineations were carried out on the raw echo images, for the GE data, the delineations were performed on the scanner output fat images, as echo data was not available for all cases. For each dataset, the mean PDFF across the whole breast segmentation was calculated.

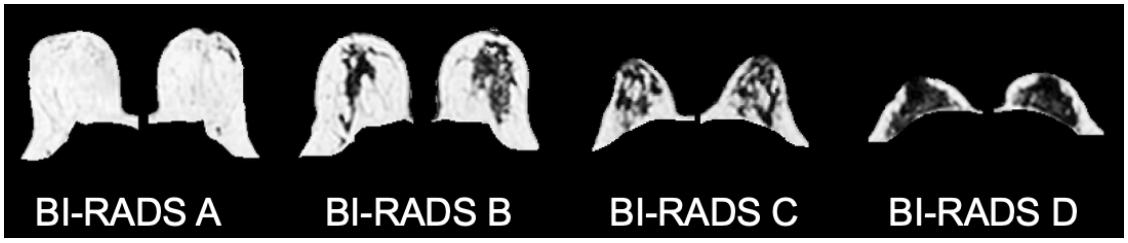


**Figure 6.9:** Examples of the central slices of three-dimensional PDFF maps of datasets classified as each BI-RADS® density category by a radiologist.

PDFF-derived breast density was calculated according to Equation 6.7. We employed two approaches to use of this equation. In the first approach, $PDFF_{\text{Fibroglandular}}$ was set to 0% and a constant value of $PDFF_{\text{Adipose}} = 91.6\%$ [110] was employed across all participants. In the second approach, $PDFF_{\text{Adipose}}$ was determined for each individual through measurement of the median PDFF across four ROIs with radius 4mm which were placed by one user in areas of breast adipose tissue in positions which avoided inclusion of fibroglandular tissue and vasculature on the central slice of the PDFF map (Figure 6.8).

One radiologist with 2 years' experience assigned BI-RADS® density categories (Table 6.1) (Figure 6.9) through examination of the three-dimensional $T_1$-weighted and $T_2$-weighted images. The difference in PDFF-derived breast density between the assigned BI-RADS® categories was evaluated using the Wilcoxon rank sum test for pairwise category comparisons and the Kruskal-Wallis test; the Spearman correlation coefficient was also computed. Receiver operating characteristic (ROC) curves were generated and the area under the curve (AUC) was calculated to assess the performance of PDFF-derived density in distinguishing between fatty (A & B) and dense (C & D) breasts.

To provide a spatial measures of tissue distribution in the breasts, the grey level co-occurrence matrix (GLCM) of each three-dimensional PDFF map was calculated [3]. GLCMs are a statistical method used to quantify textural features by measuring how often pairs of voxel intensities occur at a given direction to one another. The probability of a voxel with intensity $i$ lying adjacent to a voxel with intensity $j$ may

[3]We gratefully acknowledge the use of the 3D-Gray-Level-Co-Occurrence-Matrix toolbox by sxg [199].

be expressed as $P_{i,j}$. A variety of textural features, known as Haralick features [200], may be quantified from GLCMs. We firstly calculated the homogeneity feature of the GLCM, which measures the degree of local similarity in image intensities. Mathematically, the homogeneity of a GLCM is defined as

$$\text{Homogeneity} = \sum_{i=0}^{N-1} \sum_{j=0}^{N-1} \frac{P_{i,j}}{1 + |i - j|} \tag{6.9}$$

such that higher weights are assigned to co-occurences of voxels with similar intensities ($i \approx j$), which in this case correspond to similar PDFF values. We also calculated the contrast feature of the GLCM, which quantifies local variations in image intensity. Mathematically, contrast is defined as

$$\text{Contrast} = \sum_{i=0}^{N-1} \sum_{j=0}^{N-1} (i - j)^2 \, P_{i,j} \tag{6.10}$$

such that higher contrast will be observed where adjacent pixels have very different PDFF values.

To calculate the GLCMs, the 3D PDFF maps were resampled to have isotropic voxel resolution. Image intensities defined by the PDFF values were split into 64 bins which were capped between 0-100%. Symmetric (direction-agnostic) GLCMs were used, such that $P_{ij}$=$P_{ji}$, to ensure consistency with standards for medical image analysis and to remain agnostic to image orientation. GLCMs were calculated in 13 different voxel directions, corresponding to all non-redundant voxel adjacency orientations in 3D. The calculated homogeneity and contrast values were compared to the BI-RADS® categorisations through ROC analysis, and were assessed both as stand-alone metrics, and as supplementary biomarkers to PDFF-derived breast density.

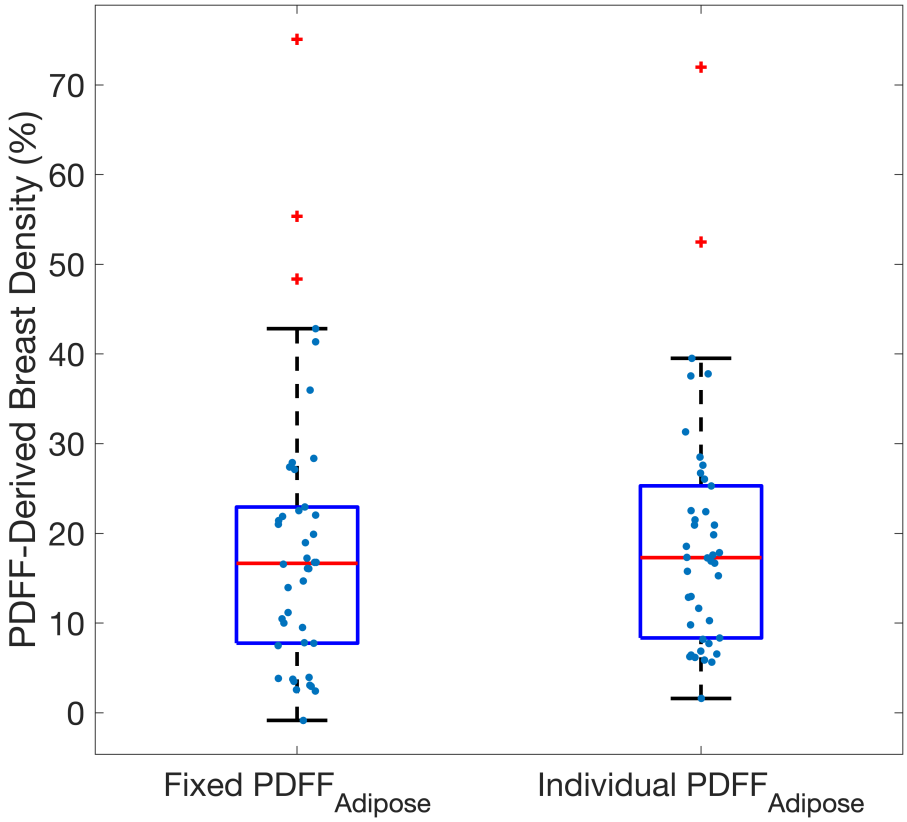


**Figure 6.10:** Box plot showing the difference in PDFF-derived breast density across the cohort when a fixed, constant value for adipose tissue PDFF is employed in Equation 6.7 versus when adipose tissue PDFF is calculated individually for each participant through placement of ROIs in the breast fat. The red crosses show outlier data points excluded automatically from the box plot analysis, whilst the blue circular markers each correspond to one dataset included in the box plot analysis.

### 6.3.3 Results

Four datasets which did not provide complete coverage of the superior/inferior extent of the breast were excluded from analysis. Additionally, one data set was excluded due to a fat-water swap observed throughout the entire PDFF map. The mean age of the participants included in the analysis was 39 years (range 22–77 years).

PDFF-derived breast density calculated with a fixed $PDFF_{\text{Adipose}}$ was not statistically significantly different to that calculated using the measured $PDFF_{\text{Adipose}}$ of each individual (Wilcoxon signed rank test, p = 0.07) (Figure 6.10). However, Bland-Altman analysis demonstrated poor agreement between the two methods, with limits of agreement ranging between -6.5–5.8% (Figure 6.11). The Bland-Altman plot demonstrated a strong positive correlation between the difference

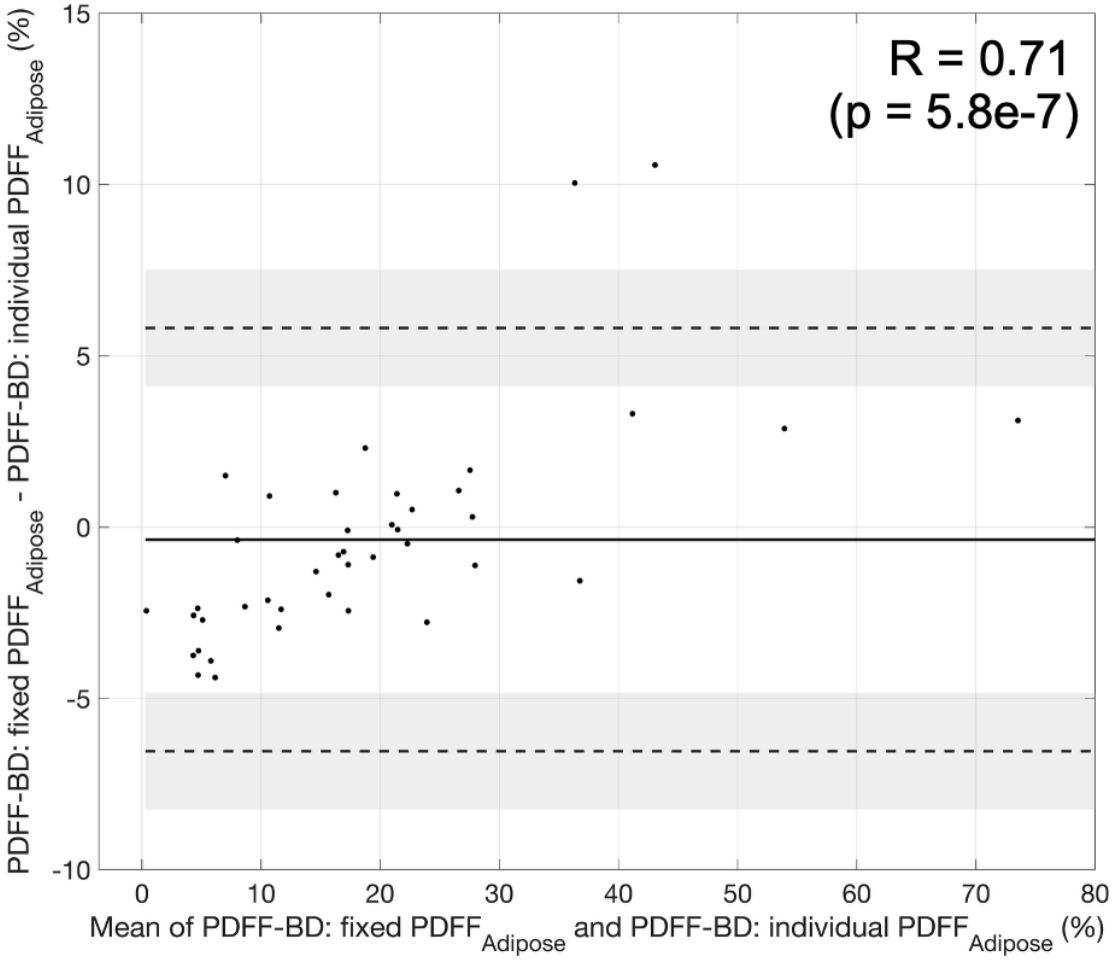


**Figure 6.11:** Bland-Altman plot showing the agreement of PDFF-derived breast density across the cohort when a fixed, constant value for adipose tissue PDFF is employed in Equation 6.7 versus when adipose tissue PDFF is calculated individually for each participant through placement of ROIs in the breast fat. A strong positive correlation between the mean breast density and the difference between breast density calculated with a fixed versus individual $PDFF_{\text{Adipose}}$ is evident (R = 0.71, p = 5.8e-7, Spearman's correlation coefficient.)

between the breast density calculated using the two methods and the average breast density (R = 0.71, p = 5.8e-7, Spearman's correlation coefficient). To investigate this result, scatter plots of calculated density were plotted against the measured $PDFF_{\text{Adipose}}$ (Figure 6.12). A strong negative correlation was observed between breast density and $PDFF_{\text{Adipose}}$, regardless of which approach to calculation of breast density was employed, but the correlation was slightly stronger using the fixed $PDFF_{\text{Adipose}}$ approach (fixed $PDFF_{\text{Adipose}}$ approach: R = -0.72, p = 2.5e-7, individual $PDFF_{\text{Adipose}}$ approach: R = -0.63, p = 1.5e-5). This result indicates that

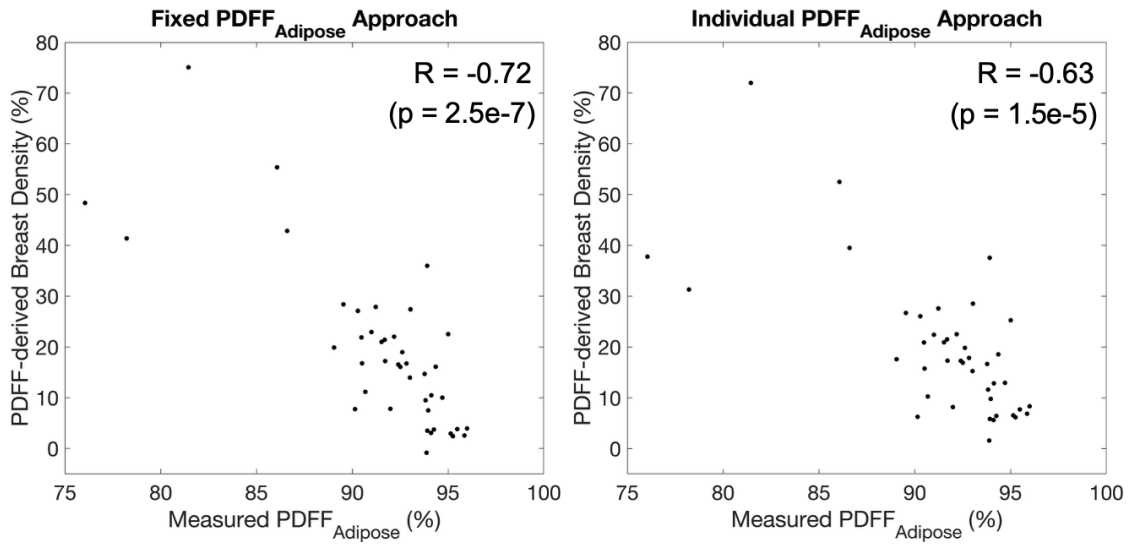


**Figure 6.12:** Scatter plots demonstrating the relationship between $PDFF_{\text{Adipose}}$ and PDFF-derived breast density. Plots are shown for both a PDFF-derived breast density calculation which employs a fixed value for $PDFF_{\text{Adipose}}$ and a PDFF-derived breast density calculation which accounts for the measured $PDFF_{\text{Adipose}}$ of each individual participant. A strong negative correlation is observed in both plots (fixed $PDFF_{\text{Adipose}}$ approach: R = -0.72, p = 2.5e-7, individual $PDFF_{\text{Adipose}}$ approach: R = -0.63, p = 1.5e-5), which is consistent with literature that finds that higher adipose PDFF is typically associated with higher BMI which is associated with lower breast density.

the fixed-value approach could underestimate density when the true $PDFF_{\text{Adipose}}$ exceeds the fixed value, and overestimate density where the true $PDFF_{\text{Adipose}}$ value is lower. Notably, one dataset yielded a negative breast density of -0.9% when the fixed-value approach was employed, due to the mean PDFF across the breasts measuring higher than the fixed $PDFF_{\text{Adipose}}$ value employed. Using the specific $PDFF_{\text{Adipose}}$ of the participant yielded a physiologically-reasonable breast density value of 1.6%. It should be noted that the observed correlation between breast density and adipose PDFF (regardless of method) is consistent with trends described in literature; a higher BMI is associated with lower breast density [201], but may also be associated with higher adipose PDFF due to adipocyte hypertrophy and rarefaction of capillaries [197], as explored in Chapter 7.

Receiver operating curve (ROC) analysis demonstrated very good agreement of PDFF-derived breast density with the dichotomous categorisation of breasts as "fatty" or "dense" (Figure 6.13). The AUC slightly improved when PDFF-derived

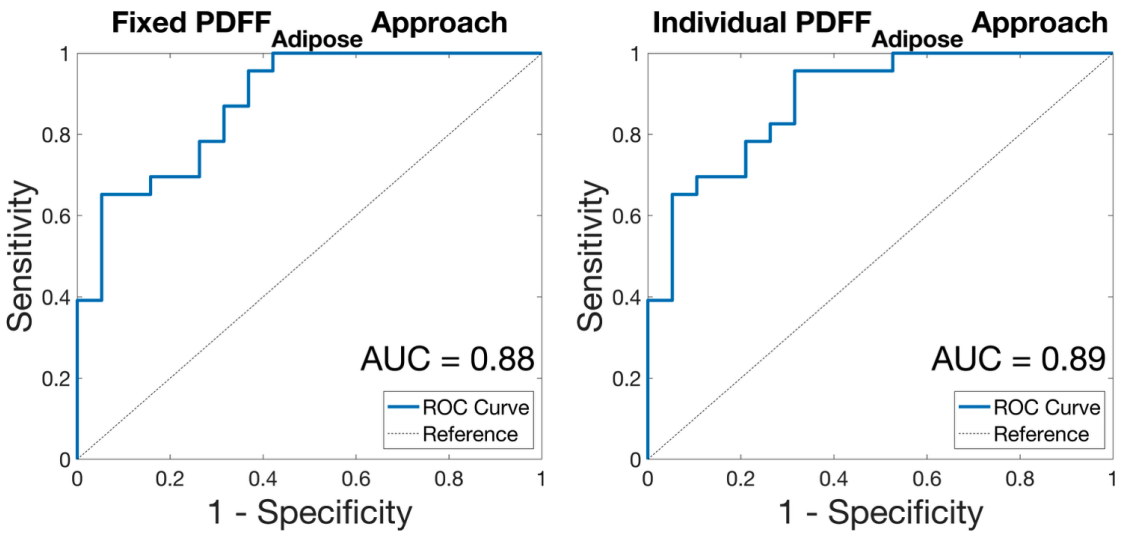


**Figure 6.13:** Two receiver operating characteristic (ROC) curves showing the performance of PDFF-derived density in distinguishing between "fatty" and "dense" breasts. One ROC curve shows the performance of the algorithm which employs a fixed $PDFF_{\text{Adipose}}$ value whilst the other shows the performance of the algorithm which accounts for the measured $PDFF_{\text{Adipose}}$ of each individual. The area under the curve (AUC) demonstrates very good performance for both calculations of PDFF-derived breast density (AUC = 0.88 and 0.89 respectively), with the individual $PDFF_{\text{Adipose}}$ approach performing slightly better than the fixed $PDFF_{\text{Adipose}}$ approach.

breast density was calculated using the individually-calculated $PDFF_{\text{Adipose}}$ values (AUC = 0.89) compared to using a fixed, constant value of $PDFF_{\text{Adipose}}$ (AUC = 0.88). Whilst there is no ground truth measurement of breast density with which it is possible to measure accuracy, this result suggests that accounting for the unique $PDFF_{\text{Adipose}}$ of the individual may be preferable for optimal agreement of PDFF-derived breast density with clinical categorisations. For this reason, and to ensure unphysical density measurements are not obtained, we therefore employ this technique throughout the remainder of the results.

A strong positive association between the BI-RADS® category and PDFF-derived density was found (R = 0.76, p = 4.6e-9). PDFF-derived breast density was significantly different in pairwise comparisons between BI-RADS® categories B, C, and D (Figure 6.14). A significant difference was not found between categories A and B breasts. This may be attributable in part to low participant numbers, with only four participants having been assigned to BI-RADS® category A. Kruskal-Wallis

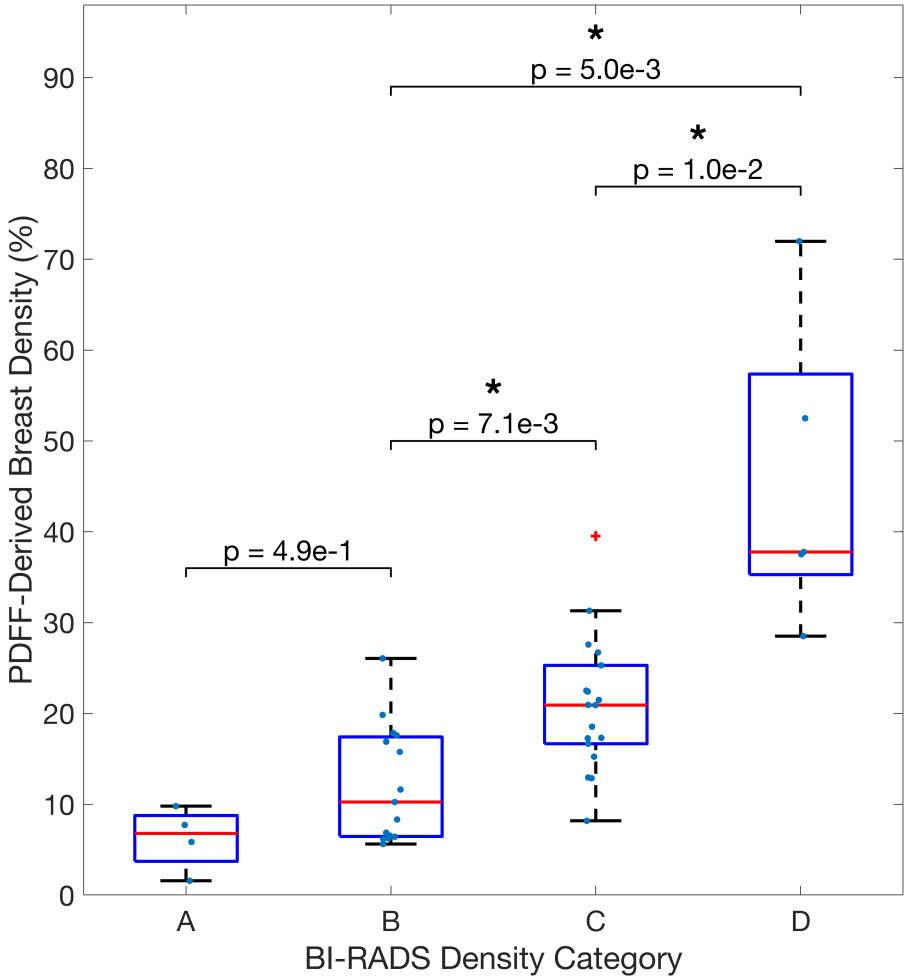


**Figure 6.14:** Box plot demonstrating the distribution of PDFF-derived breast density for each BI-RADS® category. The $*$ marker denotes a significant difference in PDFF-derived density between pairwise BI-RADS® categories. The red cross shows an outlier data point excluded automatically from the box plot analysis, whilst the blue circular markers each correspond to one dataset included in the box plot analysis.

analysis showed distinct separation across the four groups (p = 2.2e-5).

PDFF-derived breast density was significantly different between fatty and dense breasts (p = 1.9e-5, Wilcoxon rank sum test) (Figure 6.15), in line with the strong discriminatory performance (AUC = 0.89) demonstrated previously. The optimal PDFF-derived density value for discrimination between fatty and dense breasts in the ROC analysis was 12.9%.

The GLCM-derived homogeneity metric demonstrated good discriminatory ability between fatty and dense breasts (AUC = 0.83) (Figure 6.16). However, combining homogeneity and PDFF-derived density did not improve performance;

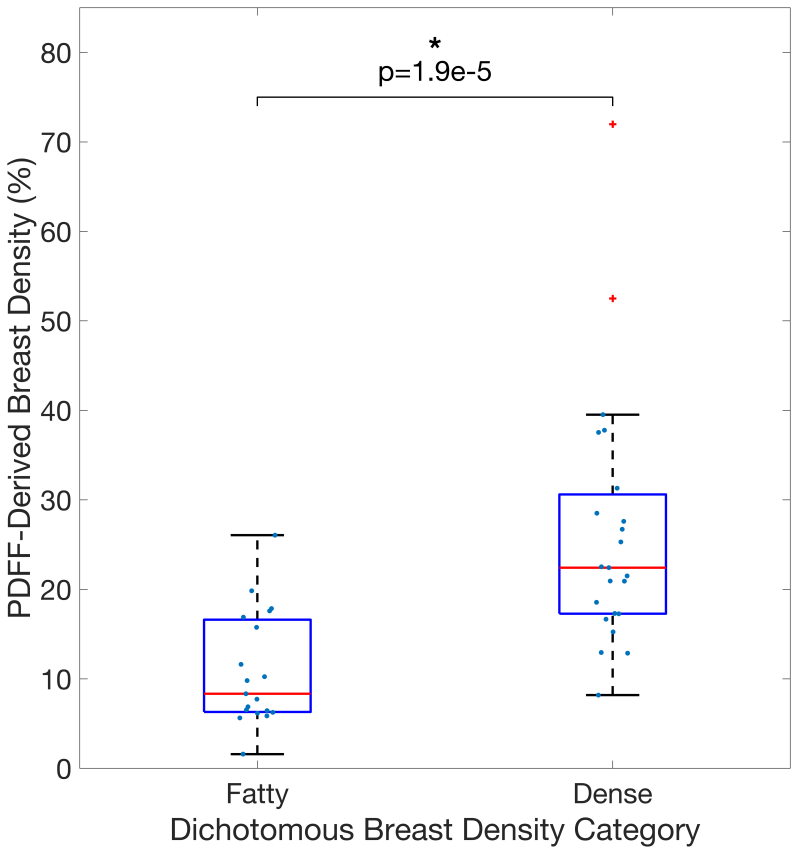


**Figure 6.15:** Box plot demonstrating the distribution of PDFF-derived breast density for the dichotomous density categories of "fatty" and "dense". The $*$ marker denotes a significant difference in PDFF-derived density between the categories. The red cross shows an outlier data point excluded automatically from the box plot analysis, whilst the blue circular markers each correspond to one dataset included in the the box plot analysis.

the AUC of the combined model remained at 0.89, the same as PDFF-derived density alone. The contrast GLCM metric demonstrated excellent discrimination between the dichotomous density categories (AUC = 0.91). Combining PDFF-derived density with GLCM-contrast increased the AUC to 0.92, outperforming either metric alone.

Distinguishing between BI-RADS® category B and C breasts has been noted to be particularly difficult [173]. Further ROC analysis demonstrated the added value of GLCM-contrast in distinguishing between these two BI-RADS® categories; when combined with PDFF-derived breast density, the AUC increased to 0.87, compared to 0.82 for PDFF-derived density alone (Figure 6.17).

Separating the Siemens and GE analyses demonstrated similar performance of PDFF-derived breast density across scanner vendors, with the Siemens and

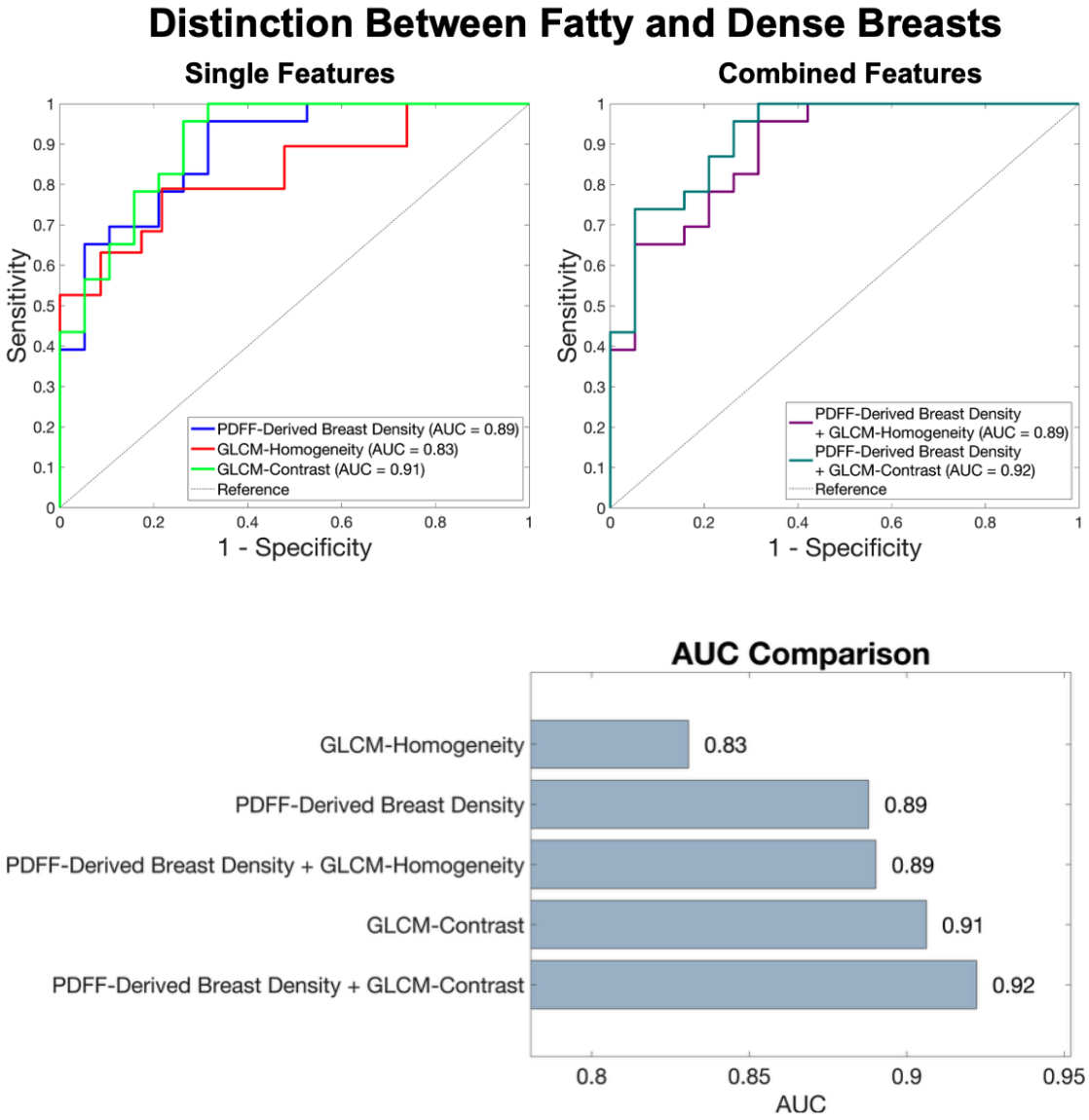


**Figure 6.16:** Receiver operating characteristic (ROC) curves showing the performance of PDFF-derived density, GLCM-homogeneity and GLCM-contrast in distinguishing between "fatty" and "dense" breasts. The performance of these metrics as single (top left) and combined (top right) features is shown, and the resulting AUCs are summarised (bottom).

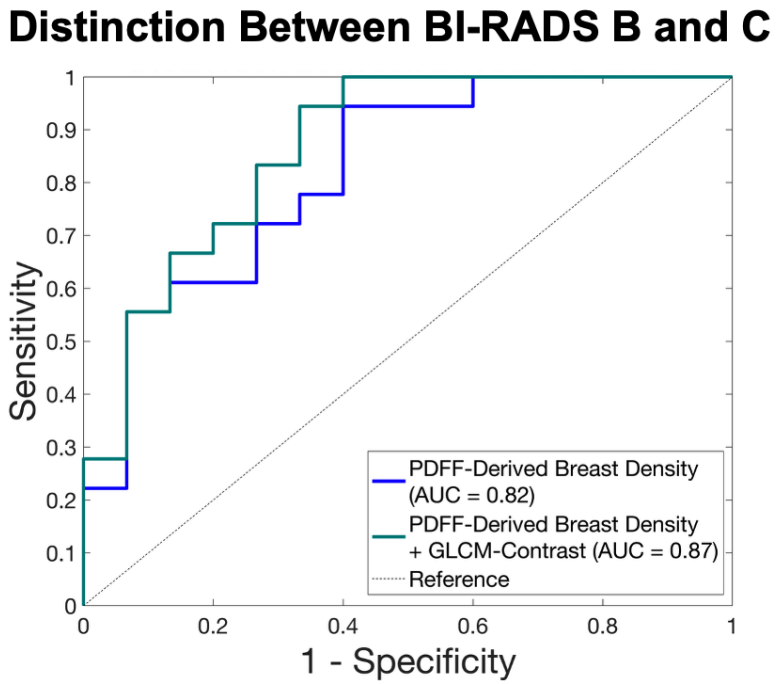


**Figure 6.17:** Receiver operating characteristic (ROC) curves showing the performance of PDFF-derived density, and PDFF-derived breast density in a combined model with GLCM-contrast in distinguishing between BI-RADS® category B and C breasts.

GE analysis both yielding an AUC of 0.90 (Figure 6.18). However, only nine datasets were acquired with the GE scanner, which does not provide confidence in the GE AUC measurement. The AUCs measured using each scanner individually were slightly higher than that of the combined analysis (AUC = 0.89): this is expected due to differences in the post-processing algorithm employed for each vendor. Bootstrapping analysis was performed using 2000 iterations to quantify the confidence intervals associated with this analysis, which demonstrated that the AUC values calculated using Siemens data (CI 0.78-0.98) and GE data (CI 0.57-1.00) were not significantly different from one another or from the combined analysis (CI 0.77-0.97). Though greater participant numbers are required, particularly on the GE scanner, these results suggest similar ROC performance across the two vendors, which provides confidence in PDFF-derived breast density.

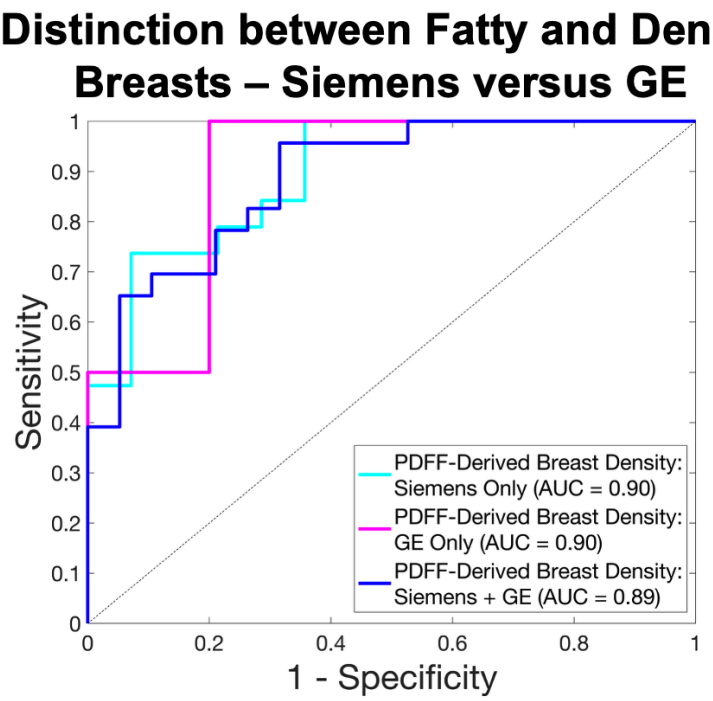


**Figure 6.18:** Receiver operating characteristic (ROC) curves showing the performance of PDFF-derived density in distinguishing between fatty and dense breasts, considering the data acquired on Siemens and GE separately and together.

### 6.3.4 Discussion

The significant difference of PDFF-derived density between BI-RADS® categories at 1.5T is promising for the clinical deployment of this biomarker. ROC analysis demonstrated that PDFF-derived density enables distinction between "fatty" and "dense" breasts, suggesting that the metric could integrate easily with clinical practise and therefore be used to influence clinical decision-making.

Combining the contrast GLCM-derived texture metric with PDFF-derived density demonstrated improved discriminatory ability over either metric alone, suggesting that accounting for spatial information in the images is important for agreement with the clinical categorisation. The radiologist used the 5th and latest edition of the BI-RADS® Atlas [30] to define density categories in this work (Table 6.1). This edition of the Atlas re-defined the BI-RADS® density categories by eliminating the approximate quartile ranges of percentage fibroglandular tissue which the previous edition included alongside the qualitative descriptions [202]. This change was implemented to emphasise that the distribution of dense tissue

affects the likelihood that a tumour could be missed in mammographical screening. For example, breasts with fibroglandular tissue clustered in one area would be at higher risk of lesion obscuration than breasts with the same percentage density but a more even tissue distribution. It should be noted that a significant difference in density classification was found when clinicians employed the updated versus previous guidelines [203], suggesting that an emphasis on textural features translated to real world impact.

The utility of PDFF to quantify breast density has only recently been proposed. Water-fat separation techniques have previously been used to calculate breast density using Dixon-based approaches [188, 204, 205], but produce a signal-weighted fat fraction value which is dependent upon the imaging parameters employed. To counteract $T_1$ and $T_2$ bias effects, some papers employ an additional calibration step [204, 205]. As described in Section 3.1, calculation of PDFF is confounder-corrected, accounting for $T_2^*$ decay and a multi-peak fat spectrum; this biomarker has been demonstrated as a robust, accurate measure of tissue fat concentration [128, 158] which does not require calibration.

As described previously, Borde et al. [139] used a complex fitting algorithm to compare PDFF to BI-RADS® categorisations. In their work, 18% of datasets were excluded due to failing fat quantification. Considering the Siemens analysis in this work, for which both magnitude and phase data was available, only 3% of datasets were excluded for this reason. Using a hybrid fitting algorithm with a breast-specific fat spectrum may therefore improve the quality of breast PDFF maps, which is consistent with the results of Chapters 4 and 5.

There are several limitations of this work. Firstly, mammographic data, the most common imaging modality with which BI-RADS® categorisations are made, was not available for use in this research. Therefore, the radiologist defined the BI-RADS® category on the basis of standard $T_1$-weighted and $T_2$-weighted MRI images, using the BI-RADS® guidance for density categorisation in MRI images. Whilst the categorisation descriptions are the same across both modalities, ideally future work would repeat this analysis through comparison to mammography-derived

BI-RADS® scores for optimal comparison to clinical practise. Another limitation is the semi-automated nature of the breast mask generation procedure, which requires user intervention to delineate the chest wall and the superior/inferior extent of the breast. Future implementations of PDFF-derived breast density should employ fully automated whole breast segmentation techniques. Four small ROIs were used for measurement of $PDFF_{\text{Adipose}}$ in each dataset. This adipose segmentation technique was employed to ensure that no fibroglandular tissue was included in calculation of $PDFF_{\text{Adipose}}$, which could have biased the density calculation. However, as a result, only a small amount of breast fat was sampled. Future work could include segmentation of all breast adipose tissue to define $PDFF_{\text{Adipose}}$, such as that described in Chapter 4. Lastly, low participant numbers were observed in the most extreme density classifications, with just four and five participants assigned to BI-RADS® categories A and D respectively. These participant numbers reflect the approximate population distribution of density categorisations, with approximately 10% of women categorised into each of these two groups [30]. Future work would assess PDFF-derived breast density across a larger cohort to reduce the confidence intervals on the AUC analysis and to sample a greater number of participants at the extremities of the density spectrum.

### 6.3.5 Conclusion

PDFF-derived breast density enables distinction between fatty and dense breasts, suggesting that this biomarker could be used to influence patients' clinical pathways and would integrate well into clinical practise. Accounting for the specific PDFF of the participants' breast adipose tissue showed a slight improvement in discriminatory performance between fatty and dense breasts compared to using a fixed adipose PDFF value, and ensured that unphysical density values were not obtained. Combining PDFF-derived breast density with a GLCM-derived contrast metric improved classification ability compared to either metric alone, suggesting utility in accounting for the distribution of dense tissue in the breast, which is emphasised by the latest BI-RADS® guidance [30].

## 6.4 Conclusion

Through phantom and *in vivo* analyses, we have demonstrated that PDFF-derived breast density is a highly accurate biomarker which is able to distinguish between clinical breast density categorisations. Generation of PDFF maps from a short, non-contrast acquisition could reduce operator variability in breast density assessment and enable accurate longitudinal monitoring of breast density without repeated exposure to ionising radiation.

# 7

# PDFF and $T_2^*$ to Assess Adipose Tissue Quality for Breast Cancer Risk

In Chapter 6, we demonstrated the utility of PDFF in providing accurate quantification of volumetric breast density. In this chapter, we consider a second application of CSE-MRI in the assessment of breast cancer risk by exploring the potential of PDFF and $T_2^*$ in measurement of the quality of breast adipose tissue.

This chapter was based in part on Gordon et al. [206].

## Contents



## 7.1 Introduction

In Chapter 2, we described the increasing recognition of obesity and the metabolic syndrome as significant predictive factors in breast cancer [17, 25–28]. The expansion of fat cells during weight gain ("adipocyte hypertrophy") is thought to drive this relationship (Figure 7.1). Hypertrophic adipose tissue adopts a state of chronic inflammation, demonstrating increased macrophage infiltration, the release of circulating inflammatory cytokines such as interleukin-6 (IL-6) and tumour


**Figure 7.1:** Illustration of adipocyte hypertrophy, showing the expansion of the lipid droplet within each fat cell under weight gain.

necrosis factor alpha (TNF-$\alpha$), decreased production of adiponectin, and increased production of leptin [17, 26, 59, 61]. This provides a favourable environment for carcinogenesis. Expression of the enzyme aromatase is also increased in hypertrophic adipocytes [25, 61]; this increases oestrogen production, which is a key driver of hormone-receptor positive breast cancer.

BMI is typically used as a simplified indicator of obesity in breast cancer risk prediction models. However, adipose tissue inflammation has been reported in individuals with a normal BMI ("metabolically obese normal weight people") [207]. Conversely, some people with high BMI demonstrate normal metabolic health ("metabolically healthy obese people") [208]. Studies have demonstrated that the level of adipose tissue inflammation - characterised by the presence of crown-like structures (CLS), dead adipocytes surrounded by macrophages - is a risk factor for breast cancer independent of BMI [209], and recent work suggests that BMI may underestimate the influence of obesity upon breast cancer risk [210]. The adequacy of BMI in breast cancer risk assessment is therefore under scrutiny, and the need for more direct measurements of adipose tissue composition is highlighted.

Direct measurement of adipose tissue quality is largely performed histologically, requiring biopsy or surgical tissue excision to assess fat cell size and the presence of crown-like structures. Alternative, non-invasive imaging techniques are increasingly explored. CT demonstrates reduced attenuation in hypertrophic adipose tissue [211, 212] but requires the application of ionising radiation. MR spectroscopy detects changes in the fatty acid composition, morphology, and hydration of hypertrophic adipocytes [213–215], but may rely on representative sampling of

smaller regions of breast adipose tissue, and the resolution of spectral peaks at lower field strengths may prove difficult.

In this chapter, we consider the potential of CSE-MRI in the assessment of hypertrophic breast adipose tissue. Adipocyte hypertrophy increases the relative proportion of fat to water within the fat cells [216] as they expand with excess lipids; increased breast adipose tissue PDFF may therefore reflect a greater adipocyte size. Hypertrophic adipose tissue is also associated with a rarefaction of capillaries [217, 218]; an increase in breast adipose tissue $T_2^*$ may therefore also be associated with poorer fat quality.

The work in this chapter provides early assessment of these hypotheses and describes the future work required for use of these markers in assessment of breast cancer risk.

## 7.2 Methods

### 7.2.1 Data Acquisition

Fifty-two female participants were scanned across the three studies described in Section 2.3. All participants were healthy with no known breast disease or had benign breast disease. The mean age of the participants was 39 years (range 22–77 years).

Participants were imaged in the prone position on a 1.5T scanner using the available bilateral breast coil at each site. The 3D axial 6-echo gradient echo scan described in Section 3.1 was acquired. PDFF and $T_2^*$ maps were generated using the fitting algorithms which were concluded to give optimal CSE-MRI map quality in Chapter 5. For the forty-three datasets acquired on Siemens scanners, the hybrid GC-MBR algorithm was used, along with the healthy breast fat spectrum derived in Chapter 4. For the nine datasets acquired on GE, the scanner-generated IDEAL-IQ maps were employed.

### 7.2.2 Image Analysis

One participant was excluded from analysis due to fat-water swaps present throughout the dataset. The mean age of the analysed participants was 39 years (range 22–77 years).

Breast adipose tissue was segmented according to the methodology described in Section 4.2.6. For comparative purposes, four circular ROIs with radius 4mm were also placed in the breast adipose tissue in the central slice of the CSE-MRI maps, as described in Section 6.3.2. The median PDFF and $T_2^*$ across the whole adipose tissue segmentation, and across the ROIs, were computed.

Imaging-derived markers were compared against participants' BMI and age. For thirty participants, BMI was derived from height and weight measured empirically as part of the IMOGEN and RADIUS studies. For the remaining twenty-two participants, BMI was derived from self-reported height and weight values.

The Spearman correlation coefficient was computed to assess the relationships between breast adipose tissue PDFF and $T_2^*$ with BMI. The correlations were assessed with and without correction for the participants' age using partial correlation analysis. The shape of the observed correlations were explored using the curve fitting toolbox in MATLAB; the $R^2$ of the data fit to four functions were compared.

## 7.3 Results

The median PDFF across the breast adipose tissue segmentation correlated strongly with BMI (R = 0.63, p = 8.7e-7). The strength of this correlation slightly increased with correction for participant age (R = 0.70, p = 1.2e-8). Repeating this analysis with user-placed ROIs yielded consistent results with those observed using the whole breast adipose tissue segmentation (R = 0.63, p = 6.8e-7 without age correction, R = 0.69, p = 3.4e-8 with age correction) (Table 7.1).

Figure 7.2shows the linear regression of the median breast adipose tissue PDFF, calculated across the segmentation, on BMI, yielding an $R^2$ of 0.34. The PDFF of breast adipose tissue demonstrates a plateau at higher BMI values. Three

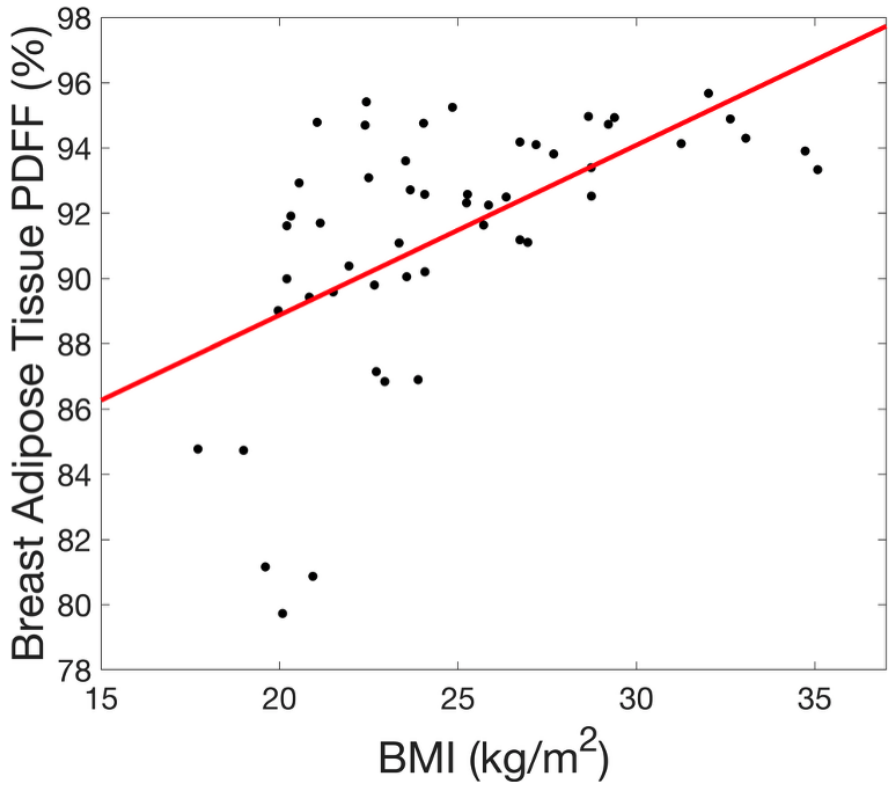


**Figure 7.2:** Scatter plot demonstrating the relationship between BMI and the median breast adipose tissue PDFF calculated across a segmentation of the breast adipose tissue. A strong, positive correlation is observed, with a plateau of adipose tissue PDFF at higher BMI values. The linear regression fit to this data is overlaid in red.

additional functions were therefore fitted to this data (Figure 7.3). A logistic function ($y = \frac{a}{1+e^{-b(x-x_0)}}$) yielded the best $R^2$ (= 0.43) compared to a hyberbolic saturation function ($y = \frac{ax}{b+x}$), $R^2 = 0.39$) and an exponential saturation function ($y = a(1 - e^{-bx})$, $R^2 = 0.41$). The optimal fit of the data to the logistic function was described by $y = \frac{94.5}{1+e^{-0.25(x-9.8)}}$, consistent with a plateau at 94.5% PDFF.

The median breast adipose tissue $T_2^*$ demonstrated a negligible correlation with BMI (Figure 7.4). This result was consistently observed across both the adipose tissue segmentation (R = 0.16, p = 0.25) and the user-placed ROIs (R = 0.14, p = 0.32). Correction for participant age had minimal impact upon the correlation strength (segmentation: R = 0.15, p = 0.29, ROIs: R = 0.13, p = 0.38). Correlations remained statistically insignificant when analyses across the whole adipose segmentation were separated according to scanner vendor (without age correction: GE only: R = 0.32, p = 0.40, Siemens only: R = 0.15, p = 0.34, with

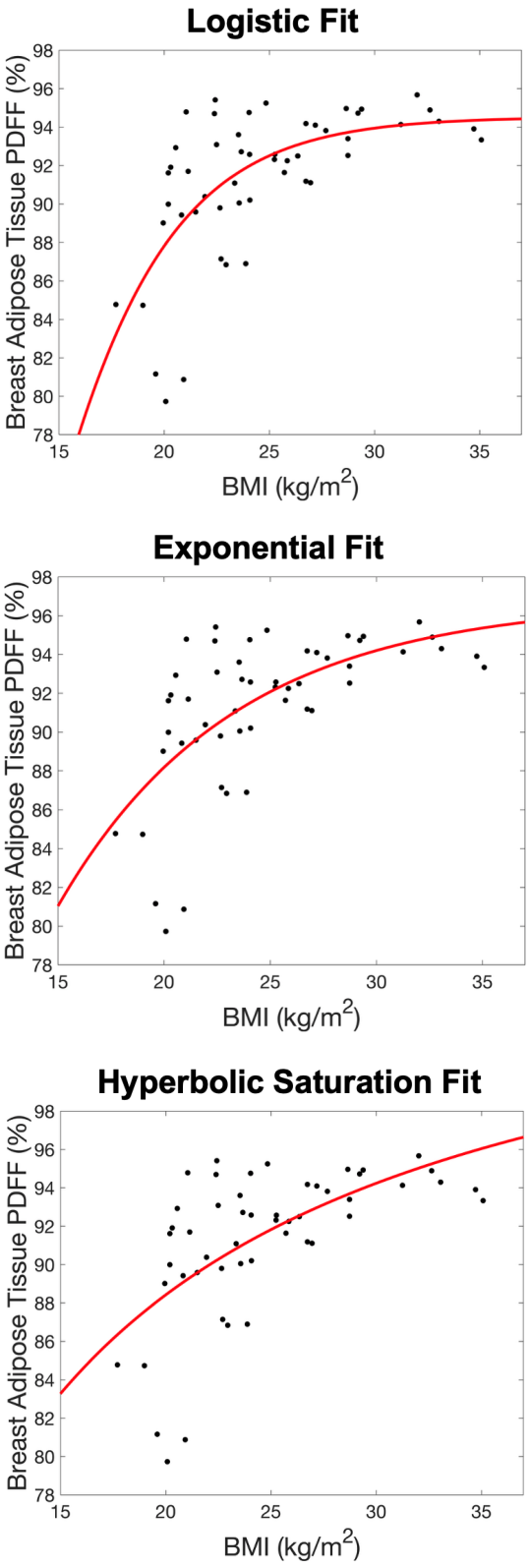


**Figure 7.3:** Three scatter plots show the relationship between the median breast adipose tissue PDFF calculated across the breast adipose tissue segmentation, and BMI. The fits of a logistic (top), exponential (middle), and hyperbolic saturation (bottom) function to the data are overlaid in red.

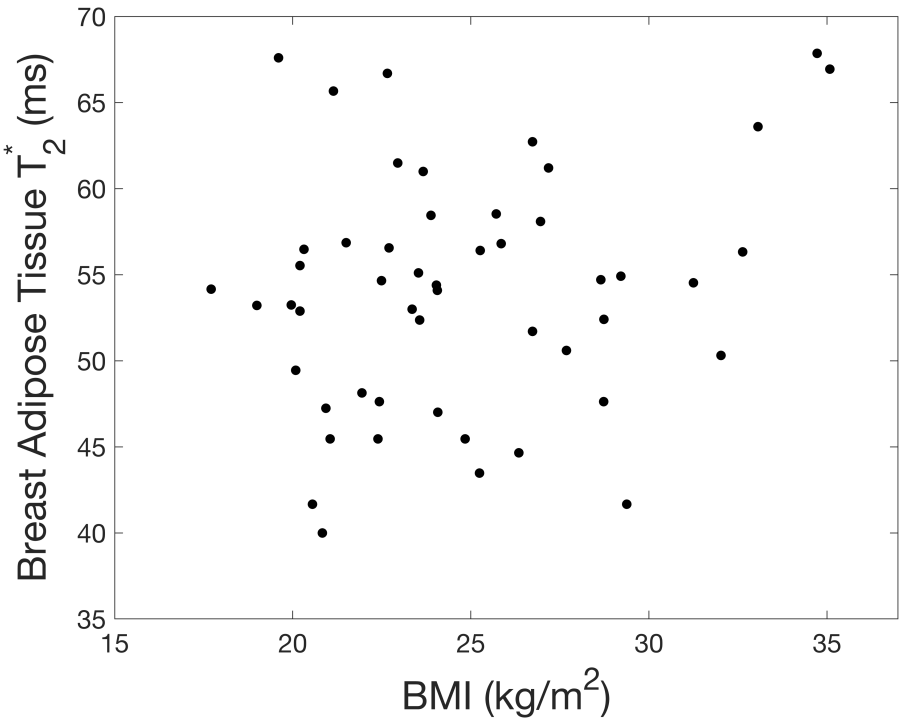


**Figure 7.4:** Scatter plot demonstrating the relationship between BMI and the median breast adipose tissue $T_2^*$ calculated across a segmentation of the breast adipose tissue. No correlation between the metrics is observed.

| | **PDFF vs BMI** | | **$T_2^*$ vs BMI** | |
|---|---|---|---|---|
| | Segmentation | ROIs | Segmentation | ROIs |
| Without age correction | 0.63* | 0.63* | 0.16 | 0.14 |
| With age correction | 0.70* | 0.69* | 0.15 | 0.13 |

**Table 7.1:** Comparison of the Spearman correlation coefficients between BMI and breast adipose tissue PDFF and $T_2^*$, shown with and without correction for participant age. The coefficients are shown when the median PDFF and $T_2^*$ values are computed across a segmentation of all breast adipose tissue, and when they are computed across four user-placed ROIs within breast adipose tissue in the central slice of the CSE-MRI maps. Values marked with * indicate $p < 0.05$.

age correction: GE only: R = 0.51, p = 0.20, Siemens only: R = 0.16, p = 0.33).

No correlation was observed between the breast adipose tissue $T_2^*$ and PDFF calculated across the adipose tissue segmentation (R = -0.17, p = 0.22) (Figure 7.5).

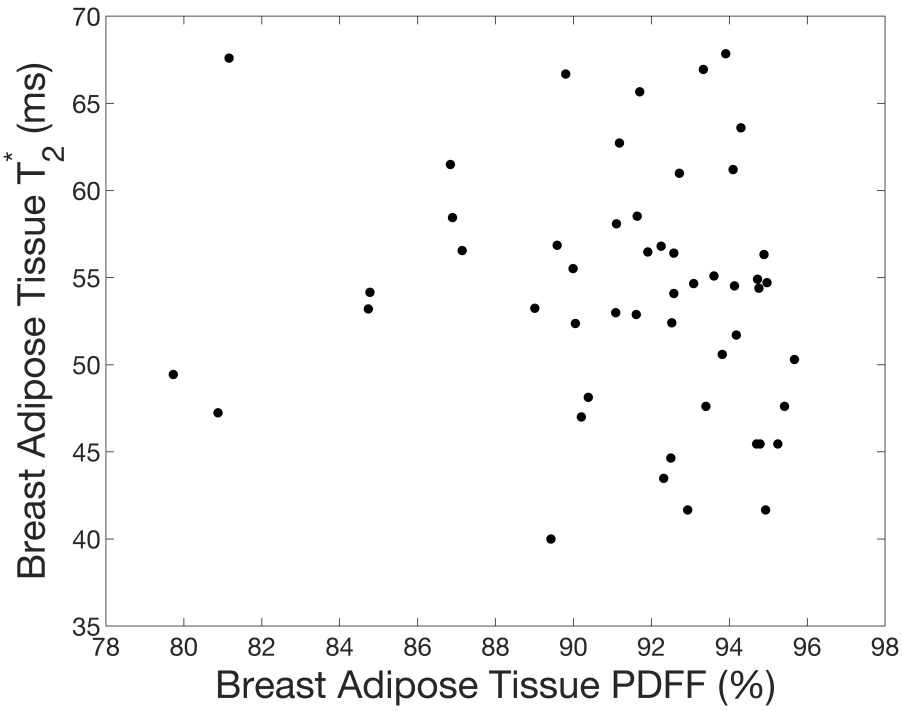


**Figure 7.5:** Scatter plot demonstrating the relationship between the median breast adipose tissue PDFF and the median breast adipose tissue $T_2^*$ calculated across a segmentation of the breast adipose tissue. No correlation between the metrics is observed.

## 7.4 Discussion

The strong, positive correlation between BMI and breast adipose tissue PDFF may reflect an increase in adipocyte hypertrophy at higher BMI values. This finding reflects results observed in gluteal fat, where positive correlations were noted between obesity markers and gluteal adipose tissue PDFF [197].

The consistency of the ROI- and segmentation-based analyses in this chapter suggests that the observed relationship between BMI and $PDFF_{\text{Adipose}}$ is unlikely to result from failure in the breast adipose tissue segmentation. Breast density is typically higher at lower BMI values [201]; it could therefore be suggested that the adipose segmentation may be more susceptible to the inclusion of FGT and the partial volume effect at lower BMI values, thereby artificially lowering $PDFF_{\text{Adipose}}$. However, the agreement of the ROI- and segmentation- based analyses suggests that this is not the case, indicating a physiological cause behind the correlation. The observed plateau of $PDFF_{\text{Adipose}}$ at higher BMI could reflect a maximum

adipocyte volume, above which fat is stored ectopically in other tissues [219, 220]. The optimal fit of a logistic function to the data suggests that this plateau occurs at approximately $PDFF_{\text{Adipose}} = 94.5\%$.

Adipocyte hypertrophy is typically accompanied by the infiltration of water-rich macrophages. We suggest that the increase in proportional fat content resulting from the expansion of the fat cell under adipocyte hypertrophy may outweigh the effect of the increased water content arising from greater macrophage presence, leading to an overall increase in $PDFF_{\text{Adipose}}$.

Notably, a previous investigation could not find a significant correlation between fat cell size and adipose tissue PDFF in mice [198]. However, the study employed a 3-echo GRE acquisition which may be more susceptible to noise which could reduce the sensitivity of the PDFF measurements. Furthermore, murine and human adipose tissue demonstrate biological differences [218], and the variation in murine adipocyte size is smaller than that in human adipocytes [221]. Regardless, the increase in proportional fat content reflected by $PDFF_{\text{Adipose}}$ at higher BMI values could reflect physiological characteristics other than increased fat cell size, such as the reduced vascular density associated with hypertrophic adipose tissue [217, 218].

A recent study suggested that the fatty acid composition (FAC) of breast adipose tissue can be measured from a multi-echo GRE acquisition with a deep-learning approach [222]. In principle, both PDFF and FAC could be quantified from the same multi-echo GRE acquisition - these could act as complimentary biomarkers in measurement of hypertrophic adipose tissue.

Magnetic susceptibility differences between fat and water lead to $T_2^*$ shortening where the mix of the two species is greatest [223]; therefore, as fat content approaches 100%, we might expect longer $T_2^*$ values. This suggests that as BMI, and the associated fat content of the adipose tissue, increases, $T_2^*$ should increase accordingly. This relationship would be strengthened by the reduced vascular density associated with hypertrophic adipose tissue. Whilst adipose tissue $T_2^*$ has indeed demonstrated positive correlations with fat content in gluteal, supraclavicular, and perirenal adipose tissue [197, 224], in this chapter, breast adipose tissue $T_2^*$ demonstrated a

negligible correlation with both BMI and breast adipose PDFF. This difference may result from physiological variations in the adipose tissue depots; the heterogeneous distribution of FGT amongst adipose tissue in the breast results in the presence of many tissue boundaries and non-uniform environments, inducing local variations in magnetic susceptibility. This may obscure the expected relationship between $T_2^*$ and adipose tissue PDFF.

Unfortunately, histological data was not available for comparison in this work. As we describe in Chapter 10, significant work to acquire histological data was undertaken, but unfortunately this has not yet been received at the time of writing.

In the absence of histology, we cannot definitively determine the mechanisms behind the results observed in this chapter. However, this work has demonstrated the potential of adipose tissue PDFF to reflect tissue characteristics associated with breast cancer risk, and provides caution in the measurement of breast adipose $T_2^*$ for this purpose, where differences in breast physiology compared to other adipose tissue depots may prevent the applicability of this metric. Future work should compare breast adipose tissue PDFF to cancer incidence and focus on its measurement in a postmenopausal population, where the link between obesity and breast cancer risk is strongest. Ultimately, PDFF could enable direct assessment of breast adipose tissue quality alongside simultaneous, accurate quantification of breast density, thereby optimising the assessment of breast cancer risk.

## 7.5 Conclusion

PDFF may be able to reflect characteristics of breast adipose tissue which are associated with breast cancer risk, although comparison to histological data and epidemiological validation is needed. Initial evaluation suggests that breast adipose tissue $T_2^*$ may not provide accurate measurement of these tissue properties.

# 8

# Peritumoural Breast Adipose Tissue Characterisation with PDFF and $T_2^*$

The applications of PDFF and $T_2^*$ examined thus far in this thesis have focused on their utility as markers of breast cancer risk. In this chapter, we apply these biomarkers to pathological data to explore their value in lesion characterisation and the assessment of disease severity through characterisation of the perilesional adipose tissue.

This chapter was based in part on Gordon et al. [110][1].

## Contents



## 8.1 Introduction

The complexity of the adipose organ and its close association with cancer are increasingly well-recognised. Histological studies not only reveal the obesity-related structural alterations to adipocytes outlined in the previous chapter, but also demonstrate functional and phenotypical differences in adipocytes located adjacent

[1]Such parts are reproduced with permission from Springer Nature.

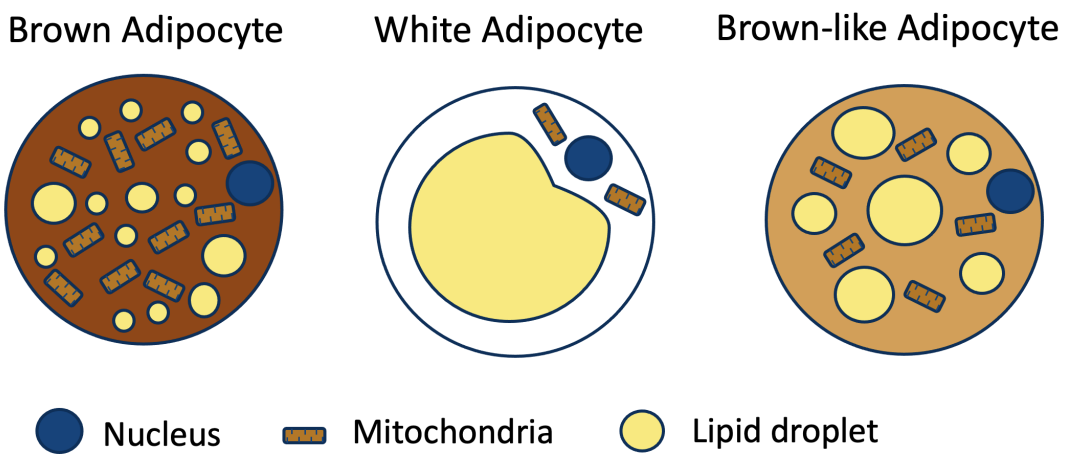


**Figure 8.1:** Illustration of brown, white, and brown-like ("beige") adipocyte types. White adipocytes, primarily used for energy storage, contain a single, large lipid droplet and have few mitochondria. Brown adipocytes, primarily used for thermogenesis, contain multiple, smaller lipid droplets, and have a high mitochondrial density. The properties of brown-like, or "beige", adipocytes lie between those of the two other cell types. Figure inspired by Guertin et al. [226]

to invasive cancer [58, 59]. These altered fat cells are referred to as cancer-associated adipocytes (CAAs).

CAAs in proximity to breast cancer exhibit an increased expression of proteases, adipokines, and pro-inflammatory cytokines, which encourages aggressive tumour behaviour [58, 225]. In addition, CAAs undergo delipidation, that is, the depletion of their intracellular lipid contents, which are subsequently used by adjacent cancer cells to further support tumour proliferation [60, 61].

CAAs adjacent to breast cancer also demonstrate brown-like adipocyte characteristics. Human adipose tissue (AT) may be broadly classified into two subtypes: white adipose tissue (WAT) and brown adipose tissue (BAT) (Figure 8.1). WAT is predominantly used for energy storage; its composite adipocytes contain a single large lipid droplet and a small number of mitochondria. BAT, however, is primarily used to convert energy into heat through uncoupled respiration. This functionality is enabled through the expression of uncoupling protein 1 (UCP-1). Structurally, BAT adipocytes are characterised by the presence of multiple, small lipid droplets, and a high mitochondrial content. White adipocytes may differentiate into brown-like ("beige") adipocytes in a process referred to as "browning" (Figure 8.2). These


**Figure 8.2:** Illustration showing the differentiation of a white adipocyte into a brown-like ("beige") adipocyte, in the process referred to as "browning".

beige adipocytes are defined within WAT by the presence of multiple, smaller lipid droplets, a higher mitochondrial density, and the expression of the UCP-1 protein. *Ex vivo* and *in vitro* studies demonstrate that CAAs in proximity to breast cancer display an upregulation of these brown-like characteristics [18, 227]. Beige adipocytes are believed to promote breast cancer progression [228]; though uncertainty remains as to the pathway of this relationship, it is believed that adipocyte browning contributes to the hypermetabolic state of breast cancer. One theory suggests that beige adipocytes may demonstrate the ability to secrete soluble factors which encourage angiogenesis; this may contribute to tumour progression alongside the depletion of their lipid stores [228, 229].

A recent study indicates that adipocyte browning and delipidation may not only be induced by secretions from cancer cells, but also by paracrine signalling from other adipocytes, suggesting a "domino effect" in the activation of CAAs [60]. These findings indicate that the characterisation of adipocytes in close proximity to breast cancer may have use in disease prognosis, as well as in lesion classification.

We hypothesise that the MR biomarkers PDFF and $T_2^*$ may enable non-invasive characterisation of the perilesional adipose tissue. Specifically, we hypothesise that a reduction in perilesional adipose PDFF could reflect the delipidation of CAAs and the smaller, multilocular lipid droplets associated with beige adipose tissue. We further hypothesise that a reduction in perilesional adipose $T_2^*$ may reflect the higher density of iron-rich mitochondria within the brown-like cancer-associated adipocytes.

These hypotheses are consistent with reports showing clear PDFF and $T_2^*$ differences between established depots of white and brown adipose tissue [230, 231].

Thus far, only one group has examined the PDFF of peritumoral breast adipose tissue. The group demonstrated that a lower PDFF measurement in adipose tissue adjacent to invasive breast cancer was associated with lymph node metastasis [138], and with poorer recurrence-free survival rates [232]. These results indicate the utility of peritumoral adipose PDFF as a prognostic marker. However, the $T_2^*$ of perilesional breast adipose tissue has not yet been examined, and the ability of these markers to distinguish between benign and malignant lesions remains to be explored.

In this chapter, we examine PDFF and $T_2^*$ in the characterisation of cancer-associated adipocytes through quantification of these metrics in the perilesional adipose tissue of participants with malignant and benign breast disease.

## 8.2 Methods

### 8.2.1 Image Acquisition

Participants included in this analysis received a clinical diagnosis of malignant or benign breast disease, and had at least one breast lesion which lay adjacent to breast adipose tissue. Ten participants had histologically-confirmed malignant breast disease; this included nine participants with invasive ductal carcinoma (IDC) and one participant with ductal carcinoma in situ (DCIS). Three participants had received a diagnosis of benign breast cysts.

One lesion from each participant was analysed, with the exception of one participant who had four observable cysts lying adjacent to adipose tissue, all of which were included in this work. Participants with confirmed breast cancer underwent biopsy as part of their clinical care; the median date of the biopsy was 27 days prior to the MRI scan (range 12–49 days).

The thirteen participants (median age 58 years, range 41–74 years) were imaged in the prone position on a 1.5T scanner across the three studies described in Section 2.3. The 3D 6-echo gradient echo scan described in Section A.3 was acquired for generation of PDFF and $T_2^*$ maps alongside the $T_1$-weighted and

$T_2$-weighted 3D acquisitions described in Sections A.1 and A.2. Additionally, the multi-shot EPI acquisition described in Section A.4 was acquired for generation of apparent diffusion coefficient (ADC) maps. No contrast agent was administered throughout the MRI exam.

### 8.2.2 Image Analysis

PDFF and $T_2^*$ maps were generated using the fitting algorithms determined to provide optimal CSE-MRI map quality in Chapter 5. Eleven datasets (nine malignant, two benign) were acquired on Siemens scanners and had both magnitude and phase echo data available; the maps for these cases were therefore generated using the hybrid GC-MBR algorithm along with a healthy breast fat spectrum (Chapter 4). The scanner-generated IDEAL-IQ maps were employed for the remaining two datasets acquired on GE machines. ADC maps were generated from the multi-shot EPI acquisitions using a non-linear fitting algorithm within Perspectum Ltd. software (Liver*MultiScan* Discover™).

Lesions were identified in the PDFF and $T_2^*$ maps through comparison of participants' medical history against the $T_1$- and $T_2$-weighted images. ADC maps were also used to guide lesion localisation, in which reduced ADC was used as an indication of malignancy (Section 2.2.3). For each lesion, a single slice of the 3D PDFF and $T_2^*$ maps was selected for analysis, which was chosen to best encompass the lesion and its neighbouring adipose tissue.

Due to constraints in recruiting participants with clinically-confirmed breast cancer, five of the ten participants with malignant disease had a surgical breast clip in place at the time of the MRI scan. In these cases, clip-induced susceptibility artefacts did not fully obscure the lesion and at least one slice of the GRE acquisition was acquired at a position where the lesion could be visualised without artefact in the $T_1$-weighted and $T_2$-weighted images. Datasets in which clip-induced susceptibility artefacts precluded lesion identification were excluded prior to the selection of the thirteen participants analysed in this work.

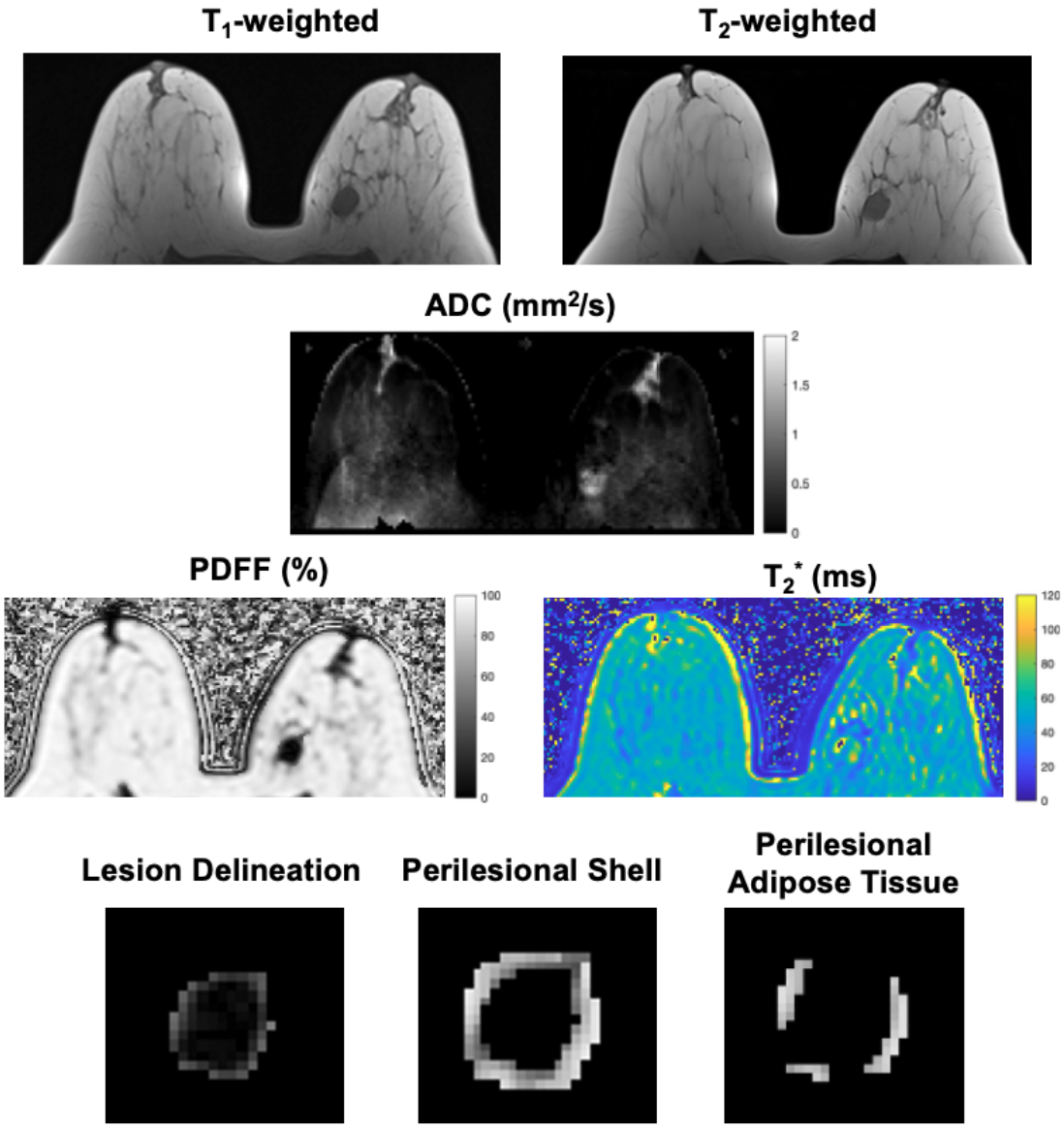


**Figure 8.3:** Overview of the acquired images, calculated quantitative maps, and segmentation of the perilesional adipose tissue for a participant with a lesion of invasive ductal carcinoma (IDC). Top: $T_1$- and $T_2$- weighted images acquired at the lesion location. The lesion can be visualised in the inner region of the image-right breast, where it is isointense to FGT in both images. Middle: Single slices of the ADC, PDFF, and $T_2^*$ maps acquired at the lesion location. Bottom: Overview of the definition of the perilesional adipose segmentation algorithm. The manual delineation of the lesion on the PDFF map (left) is dilated by a spherical structuring element to generate a perilesional shell (middle) which is then corrected to exclude evident regions of FGT and vasculature to produce the final perilesional adipose tissue segmentation (right).

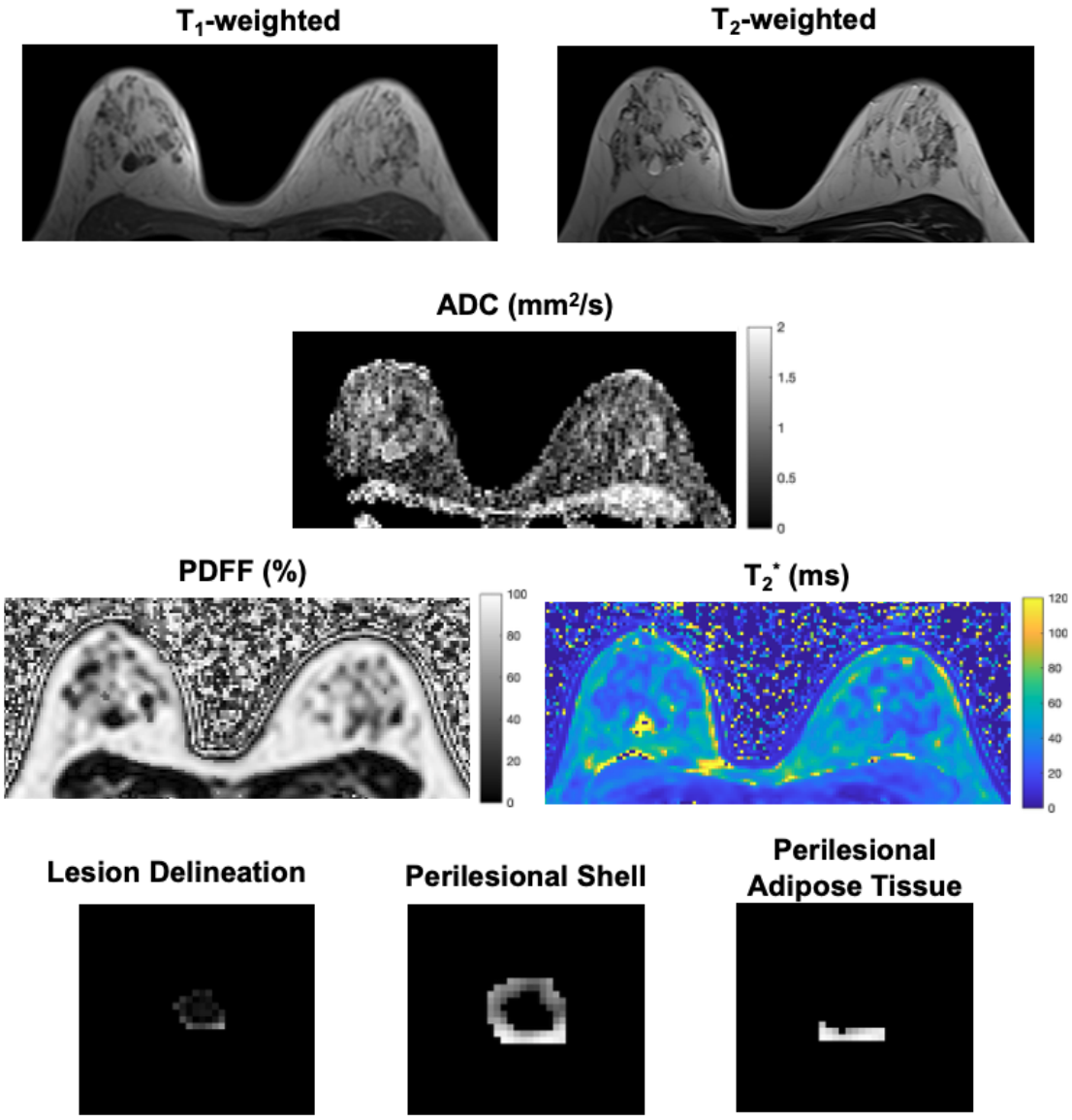


**Figure 8.4:** Overview of the acquired images, calculated quantitative maps, and segmentation of the perilesional adipose tissue for a participant with a breast cyst. Top: $T_1$- and $T_2$- weighted images acquired at the lesion location. The lesion can be visualised in the inferior region of the image-left breast, where it is hypointense to FGT in the $T_1$-weighted image and hyperintense to FGT in the $T_2$-weighted image. Middle: Single slices of the ADC, PDFF, and $T_2^*$ maps acquired at the lesion location. Bottom: Overview of the definition of the perilesional adipose segmentation algorithm. The manual delineation of the lesion on the PDFF map (left) is dilated by a spherical structuring element to generate a perilesional shell (middle) which is then corrected to exclude evident regions of FGT and vasculature to produce the final perilesional adipose tissue segmentation (right).

Lesions were manually delineated by one user on the selected slice of the PDFF map, using the $T_1$-weighted, $T_2$-weighted and ADC images as reference. To produce a mask of perilesional adipose tissue, the lesion mask was dilated using a disk structuring element with a radius of three pixels. The dilated mask was subtracted from the lesion mask to yield a three-pixel-thick shell surrounding the lesion. This thickness corresponds to a distance of 5.2mm and was selected based on literature which suggests CAAs may be limited to lie within 5mm of the tumour edge [233]. The shell was manually corrected to exclude regions of evident FGT and vasculature.

The median $T_2^*$ and PDFF across the masks of perilesional adipose tissue were calculated (hereafter "$T_{2\ \mathrm{AT-Peri}}^*$" and "$PDFF_{\mathrm{AT-Peri}}$"). For each lesion, $T_{2\ \mathrm{AT-Peri}}^*$ and $PDFF_{\mathrm{AT-Peri}}$ were compared against i) the participant's whole breast adipose tissue medians as found across a segmentation of all breast adipose tissue (Section 4.2.6) and ii) the medians across four 4mm ROIs placed in the participant's normal breast adipose tissue (Section 6.3.2). Differences between the perilesional and reference values were compared across disease types using the Wilcoxon rank sum test. Additionally, for each lesion, the Mahalanobis distance ("$D_M$") was computed between the centroids of the perilesional and reference adipose tissue pixels in the bivariate PDFF-$T_2^*$ space. This metric provides a unitless measure of multivariate separation which accounts for unit and scaling differences between the metrics, with larger $D_M$ reflecting a greater degree of separation. Please see Appendix F for definition of the Mahalanobis distance.

Lastly, receiver operator characteristic (ROC) curves were plotted to assess the performance of the difference between perilesional and reference PDFF, the difference between perilesional and reference $T_2^*$, and the Mahalanobis distance, in distinguishing between malignant and benign lesions. The segmentation of all breast adipose tissue was used to define the reference adipose tissue for this analysis. Bootstrapping analysis was performed with 2000 iterations to provide confidence intervals of the resulting area under the curve (AUC) values.

## 8.3 Results

Malignant lesions demonstrated a reduction in perilesional adipose tissue PDFF compared to reference adipose tissue PDFF, with a median difference of -5.2% or -6.4%, depending on the definition of the reference PDFF value (Table 8.1). Benign lesions demonstrated a more moderate difference in PDFF between the adipose tissue depots (-1.0% or -1.4%). The Wilcoxon rank sum test demonstrated that the difference between perilesional and reference AT was significantly different between benign and malignant lesions; this result was consistent using either definition of the reference adipose tissue.

| | **Median Difference in PDFF (IQR) (%)** | |
|---|---|---|
| | $PDFF_{\mathrm{AT-Peri}} - PDFF_{\mathrm{AT-All}}$ | $PDFF_{\mathrm{AT-Peri}} - PDFF_{\mathrm{AT-ROI}}$ |
| Benign | $-1.0\,(-1.7$ to $-0.3)$ | $-1.4\,(-1.8$ to $-0.2)$ |
| Malignant | $-5.2\,(-7.8$ to $-3.8)$ | $-6.4\,(-9.9$ to $-4.5)$ |
| $p$ | $5.0 \times 10^{-4}$* | $2.4 \times 10^{-4}$* |

**Table 8.1:** Table showing the median (IQR) difference between the perilesional adipose tissue PDFF ($PDFF_{\mathrm{AT-Peri}}$) and a reference adipose tissue PDFF for malignant and benign breast lesions. The reference value is defined as either the PDFF across a segmentation of all breast adipose tissue ($PDFF_{\mathrm{AT-All}}$), or the PDFF across four ROIs placed in normal breast adipose tissue ($PDFF_{\mathrm{AT-ROI}}$). $p$ indicates the significance of the difference between malignant and benign groups (Wilcoxon rank sum test), with * indicating $p < 0.05$.

Whilst the median difference in $T_2^*$ between perilesional and reference AT was more negative in malignant compared to benign lesions, this result was not statistically significant for either definition of the reference adipose tissue (Table 8.2).

The Mahalanobis distance ($D_M$) between perilesional and reference adipose tissue in the PDFF-$T_2^*$ space was significantly greater for malignant lesions than benign lesions (Table 8.3); this result was consistent using either reference adipose tissue definition.

ROC analysis demonstrated the excellent performance of the difference between perilesional and reference AT PDFF in distinguishing between malignant and benign lesions (AUC = 0.98, 95% confidence interval 0.90-1.00) (Figure 8.5). The

| | **Median Difference in $T_2^*$ (IQR) (ms)** | |
|---|---|---|
| | $T_{2\ \mathrm{AT-Peri}}^* - T_{2\ \mathrm{AT-All}}^*$ | $T_{2\ \mathrm{AT-Peri}}^* - T_{2\ \mathrm{AT-ROI}}^*$ |
| Benign | 7.6 (−1.6 to 12.3) | 3.7 (−4.2 to 9.6) |
| Malignant | −1.6 (−7.3 to 5.7) | −1.0 (−7.7 to 5.1) |
| $p$ | 0.37 | 0.56 |

**Table 8.2:** Table showing the median (IQR) difference between the perilesional adipose tissue $T_2^*$ ($T_{2\ \mathrm{AT-Peri}}^*$) and a reference adipose tissue $T_2^*$ for malignant and benign breast lesions. The reference value is defined as either the $T_2^*$ across a segmentation of all breast adipose tissue ($T_{2\ \mathrm{AT-All}}^*$), or the PDFF across four ROIs placed in normal breast adipose tissue ($T_{2\ \mathrm{AT-ROI}}^*$). $p$ indicates the significance of the difference between malignant and benign groups (Wilcoxon rank sum test), with * indicating $p < 0.05$.

| | **Median $D_M$ (IQR)** | |
|---|---|---|
| | $D_{M(\mathrm{AT-Peri:AT-All})}$ | $D_{M(\mathrm{AT-Peri:AT-ROI})}$ |
| Benign | 0.75 (0.53 to 0.92) | 1.01 (0.58 to 1.11) |
| Malignant | 2.19 (1.30 to 5.1) | 1.86 (1.36 to 2.1) |
| $p$ | $1.7 \times 10^{-3}$* | $7.5 \times 10^{-3}$* |

**Table 8.3:** Table showing the median (IQR) Mahalanobis distance ($D_M$) in the PDFF-$T_2^*$ space between the perilesional adipose tissue and a reference adipose tissue for malignant and benign breast lesions. Pixels in the reference adipose tissue are defined as either those across a segmentation of all breast adipose tissue, yielding Mahalanobis distance $D_{M(\mathrm{AT-Peri:AT-All})}$, or those across four ROIs placed in normal breast adipose tissue, yielding Mahalanbois distance $D_{M(\mathrm{AT-Peri:AT-ROI})}$. $p$ indicates the significance of the difference between malignant and benign groups (Wilcoxon rank sum test), with * indicating $p < 0.05$.

Mahalanobis distance also demonstrated excellent performance (AUC = 0.95, 95% confidence interval 0.82-1.00). However, the difference in $T_2^*$ between the two adipose tissue depots showed poor discriminatory ability (AUC = 0.65, 95% confidence interval 0.30-0.95).

The single lesion of DCIS demonstrated a smaller reduction in perilesional AT PDFF compared to the nine lesions of IDC - in fact, the DCIS result lay outside of the full range of IDC PDFF values, regardless of the choice of reference AT (Table 8.4). $D_M$ was also reduced for the DCIS measurement compared to the median IDC value (Table 8.6). The DCIS $D_M$ lay outside the full range of IDC values for one, but not both, definitions of the reference AT. Surprisingly, the

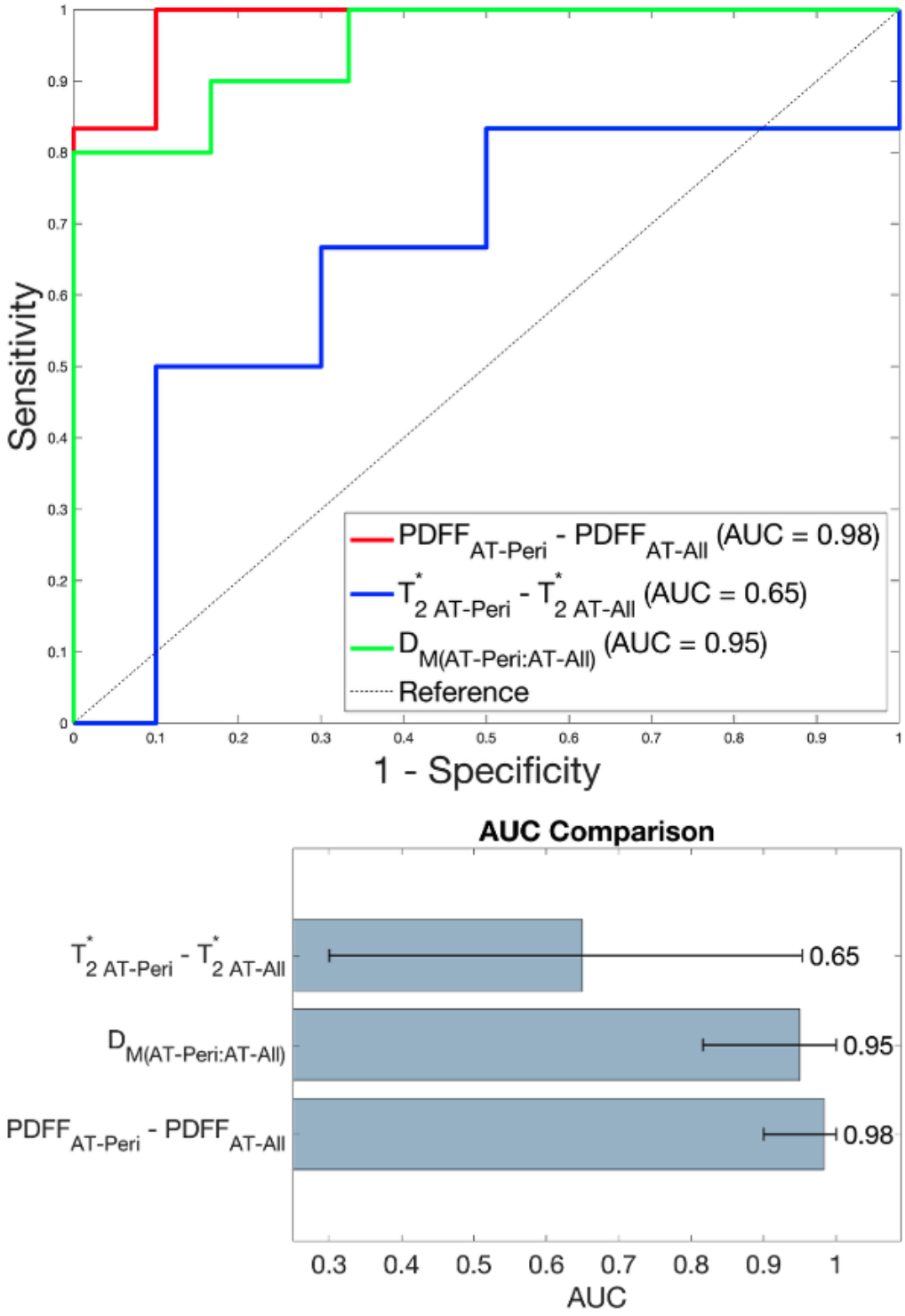


**Figure 8.5:** Receiver Operator Characteristic (ROC) curves demonstrating the performance of three biomarkers in distinguishing between benign and malignant lesions. This includes the difference between perilesional and reference adipose tissue PDFF, the difference between perilesional and reference adipose tissue $T_2^*$, and the Mahalanobis Distance. The reference adipose tissue is here defined as a segmentation across all the breast adipose tissue of each participant.

difference in $T_2^*$ observed around DCIS was more negative than the median $T_2^*$ difference around IDC. However, the DCIS result lay well within the range of values observed across the IDC lesions (Table 8.5).

| | **Median Difference in PDFF (Full Range) (%)** | |
|---|---|---|
| | $PDFF_{\text{AT−Peri}} - PDFF_{\text{AT−All}}$ | $PDFF_{\text{AT−Peri}} - PDFF_{\text{AT−ROI}}$ |
| DCIS (n = 1) | −1.8 | −3.2 |
| IDC (n = 9) | −6.0 (−15.9 to − 3.1) | −7.0 (−16.9 to − 3.3) |

**Table 8.4:** Table showing the median (full range) difference between the perilesional adipose tissue PDFF ($PDFF_{\text{AT−Peri}}$) and a reference adipose tissue PDFF for IDC lesions, compared to a single lesion of DCIS. The reference value is defined as either the PDFF across a segmentation of all breast adipose tissue ($PDFF_{\text{AT−All}}$), or the PDFF across four ROIs placed in normal breast adipose tissue ($PDFF_{\text{AT−ROI}}$).

| | **Median Difference in $T_2^*$ (Full Range) (ms)** | |
|---|---|---|
| | $T_{2\ \text{AT−Peri}}^* - T_{2\ \text{AT−All}}^*$ | $T_{2\ \text{AT−Peri}}^* - T_{2\ \text{AT−ROI}}^*$ |
| DCIS (n = 1) | −7.3 | −7.7 |
| IDC (n = 9) | −0.9 (−13.0 to 33.3) | −1.0 (−10.5 to 32.1) |

**Table 8.5:** Table showing the median (full range) difference between the perilesional adipose tissue $T_2^*$ ($T_{2\ \text{AT−Peri}}^*$) and a reference adipose tissue $T_2^*$ for IDC lesions, compared to a single lesion of DCIS. The reference value is defined as either the $T_2^*$ across a segmentation of all breast adipose tissue ($T_{2\ \text{AT−All}}^*$), or the $T_2^*$ across four ROIs placed in normal breast adipose tissue ($T_{2\ \text{AT−ROI}}^*$).

| | **Median $D_M$ (Full Range)** | |
|---|---|---|
| | $D_{M(\text{AT−Peri:AT−All})}$ | $D_{M(\text{AT−Peri:AT−ROI})}$ |
| DCIS (n = 1) | 0.92 | 1.63 |
| IDC (n = 9) | 2.37 (0.99 to 5.39) | 1.92 (0.87 to 3.72) |

**Table 8.6:** Table showing the median (full range) Mahalanobis distance ($D_M$) in the PDFF-$T_2^*$ space between the perilesional adipose tissue and a reference adipose tissue for IDC lesions, compared to a single lesion of DCIS. Pixels in the reference adipose tissue are defined as either those across a segmentation of all breast adipose tissue, yielding Mahalanobis distance $D_{M(\text{AT−Peri:AT−All})}$, or those across four ROIs placed in normal breast adipose tissue, yielding Mahalanbois distance $D_{M(\text{AT−Peri:AT−ROI})}$.

## 8.4 Discussion

The decrease in the PDFF of peritumoural compared to reference adipose tissue indicates that PDFF may be reflective of physiological changes in cancer-adjacent mammary fat. The statistically-significant greater reduction in PDFF around malignant compared to benign lesions implies that the decrease in peritumoural PDFF may reflect differences in physiological adipose tissue properties rather than inaccuracies in lesion segmentation.

The PDFF reduction was greater in proximity to invasive cancer than in a single case of *in situ* disease; this could indicate that the magnitude of the PDFF reduction may reflect the pathological severity. Hisanaga et al. observed that a greater reduction in perilesional adipose tissue PDFF was associated with lymph node metastasis [138]. Lymph node status was not available for our data, but the greater reduction in PDFF around invasive compared to *in situ* disease may be consistent with the hypothesis that greater reductions in PDFF are associated with more severe disease.

Although characterisation of CAAs typically focuses on invasive cancer due to direct tumour-adipocyte interactions at the invasive front, a reduction in adipocyte size has also been described adjacent to DCIS [234]. Correspondingly, we observed a greater decrease in PDFF around the single case of DCIS compared to benign lesions, suggesting that PDFF could reflect the decreased adipocyte size close to DCIS. However, as this observation is based on a single case, additional cases of non-invasive cancer are needed to confirm this observation.

The weak ROC performance of $T_2^*$ suggests that this biomarker could be insensitive to differences in the properties of peritumoural breast adipose tissue. $T_2^*$ is highly influenced by local magnetic field inhomogeneities; susceptibility at the adipose-tumour interface could therefore dominate $T_2^*$ measurement and overwhelm contributions from increased tissue vascularity and the increased mitochondrial density of adipocytes. However, the confidence intervals on the AUC measurement were high, and, though statistical significance was not reached, the median perilesional $T_2^*$ did reflect expected physiological trends. This may suggest that $T_2^*$

could reflect changes to peritumoral adipose tissue, but that insufficient datasets were acquired in this analysis to demonstrate this. Regardless of whether $T_2^*$ may reflect changes in peritumoural adipose tissue, this biomarker has been shown to be markedly different within lesions of DCIS and IDC, and to correlate with the histological grade of the disease [97]. As $T_2^*$ is simultaneously generated alongside PDFF in the CSE-MRI algorithm, this biomarker could be a complementary metric to PDFF in lesion characterisation.

The Mahalanobis distance demonstrated excellent discrimination between benign and malignant lesions. However, its performance did not exceed that of PDFF alone; coupled with the limited utility of $T_2^*$, this suggests that most of the metric's discriminatory ability arises from PDFF. Calculation of the Mahalnobis distance also benefits from large numbers of datapoints, which are inherently limited when examining a small region of perilesional adipose tissue. Furthermore, unlike PDFF, which directly reflects tissue fat content, the Mahalanobis distance lacks physiological applicability, and its use suppresses spatial information from the image. This suggests that PDFF is the preferable choice of biomarker for this application.

In the absence of histological data, the biological mechanism underlying the PDFF reduction around malignant lesions remains uncertain. The results could reflect the delipidation and browning of cancer-associated adipocytes, but peritumoral oedema may similarly manifest as a reduction in perilesional PDFF. Additionally, despite excluding obvious blood vessels from the perilesional ROI, angiogenesis may also contribute to a reduction in perilesional adipose tissue PDFF. These mechanisms are not exclusive, and could all theoretically contribute to the observed results. Regardless of mechanism, PDFF could provide a novel biomarker for cancer which does not depend on contrast agents.

The perilesional ROI examined in this work encompassed adipocytes lying immediately adjacent to the lesion edge out to a radial distance of 5mm. This choice of ROI was motivated by the finding that at a distance of >5mm from the tumour edge, adipose tissue is morphologically homogenous [233]. This aligns with the definition of CAAs as adipocytes lying in the first few layers at the invasive

front, lying approximately <2mm from the tumour edge [234, 235]. However, a recent paper reports activation of a lipolytic gene in breast adipocytes up to 4cm from the tumour, implying phenotypic changes beyond the immediate invasive front [236]. This supports the interpretation that the reductions in peritumoural PDFF measured 5mm from the tumour edge by Hisanaga et al. and Tani et al. [138, 232], reflect differences in adipocyte properties, rather than simply peritumoural oedema. In the same paper [236], a technique based on dual-energy mammography [237] was employed to quantify lipid content in three concentric peritumoural rings up to 6mm from the tumour edge. A progressive reduction in lipid content was observed as rings neared the tumour edge, which was consistent with an observed reduction in fat cell size; this provides confidence in the ability of imaging-derived quantitative fat content to characterise peritumoural adipose tissue. Future work could examine the gradual change of PDFF along radial lines from the lesion to distant adipose tissue; this could inform automated exclusion of FGT from the perilesional shell, and even track the extent of the effected adipose tissue.

There are several limitations associated with this work. First is the limited number of cases available to date for inclusion in this work. Small sample sizes restrict statistical power and limit the robustness of ROC-based performance estimates. As a result, the findings of this chapter should be considered as preliminary rather than as a definitive validation of the biomarkers explored. Larger datasets will be required to confirm the observed results and to more reliably assess the biomarkers' discriminatory ability; this chapter establishes an analytical framework for conducting such analyses in future studies. Secondly, clinical diagnostic images were not available. Lesions were therefore identified by matching their described location to $T_1$- and $T_2$-weighted images and ADC maps, which may be an imperfect process. Thirdly, lesions were manually delineated directly on the PDFF maps using the $T_1$- and $T_2$- weighted images and the ADC maps as reference. Future work should delineate the lesions on a separate acquisition and perform image registration to the PDFF and $T_2^*$ maps to minimise bias. Fourthly, all six benign lesions analysed in this work were cysts. Whilst $D_M$ and PDFF

distinguished between cancer and cysts with excellent performance, this distinction is rarely clinically challenging due to the lesions' distinct appearances. Nonetheless, these results indicate the ability of these biomarkers to reflect differences in adipose tissue properties around malignant and benign disease, which is the focus of this work. Future work should repeat this analysis across a broader spectrum of disease. Lastly, biopsy-induced effects and clip-induced susceptibility artefacts may affect the PDFF and $T_2^*$ of cancer adjacent adipose tissue. Whilst the time between biopsy and pre-operative breast MRI has been shown not to affect the accuracy of the scan [238], guidance suggests that contrast-enhanced mammography should be performed at least 2 weeks after biopsy [239]; in this work, biopsies were completed a median of 27 days prior to the MRI scan, suggesting that most biopsy-induced effects should have dissipated. Clip-induced susceptibility artefacts were avoided in slice selection in this work to mitigate their impact. Nonetheless, future work should include assessment of fat adjacent to needle-naive tumours.

Assessment of perilesional breast adipose tissue with quantitative MRI may have pharmaceutical applications. Expanding research implicating cancer-associated adipocytes in tumour progression points to their potential application as a therapeutic target; several pathways linked to CAAs are already being evaluated for this purpose [240, 241]. Pending a histological investigation and validation across a larger cohort, the reduction in perilesional PDFF could ultimately be used to measure the response of CAAs to treatment. In addition to fuelling tumour progression, CAAs are also associated with the proliferation of a radioresistant phenotype in breast tumours [242]. Characterisation of CAAs could thereby also be used to predict the response of disease to radiotherapy. Notably, the browning and delipidation of peritumoural adipose tissue has also been observed in renal cancer [243], and CAAs are key to the progression of ovarian cancer [244]; the applications of peritumoural PDFF may therefore not only be limited to the breast.

## 8.5 Conclusion

PDFF may be able to reflect physiological differences in cancer-adjacent adipose tissue associated with tumour progression and treatment resistance. Current indications suggest $T_2^*$ may not be able to reflect these physiological changes. The difference in PDFF between perilesional and reference adipose tissue, and the Malahnobis distance in the PDFF-$T_2^*$ space demonstrated excellent discriminatory ability between benign and malignant lesions, though more datasets are needed. Breast adipose tissue PDFF could ultimately be used to inform disease characterisation and to infer treatment response, pending histological confirmation of the biological mechanism behind the results observed.

# 9

# The "MR Bra": A Support Device for Supine Breast Imaging

In the previous chapters, we demonstrated the utility of several non-contrast, quantitative MRI biomarkers in the diagnosis and risk assessment of breast cancer. Development of a clinical breast MRI protocol which does not rely on injection of contrast agent could greatly improve the participant experience of breast MRI. We now examine another approach through which the participant experience may be improved. In this chapter, we describe the development of the MR Bra, a specialised support device to enable breast MRI to be performed in the supine position.

This chapter was adapted in part from Gordon et al. [245].

## Contents

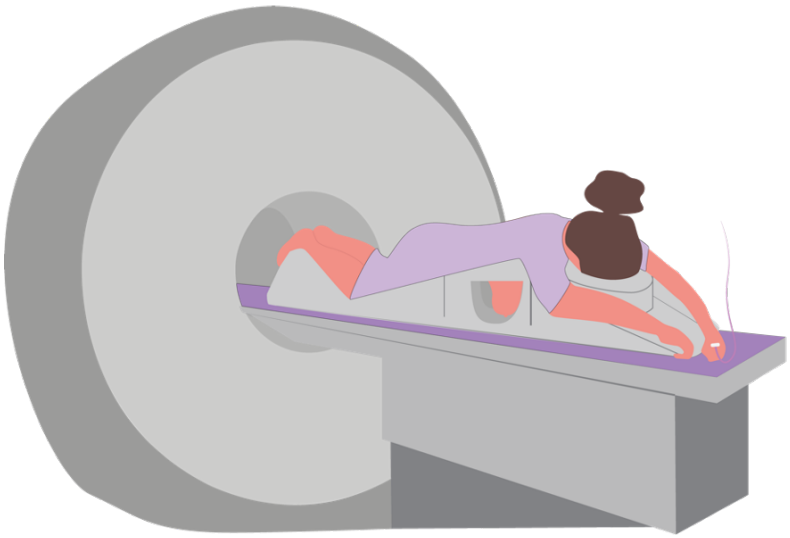

**Figure 9.1:** Illustration of the prone position employed for breast MRI, showing the breasts hanging into the breast-specific RF coil. Image by Haley Fig.

## 9.1 Introduction

Conventional breast MRI is performed in the prone position with patients' breasts hanging down into a breast-specific RF coil (Figure 9.1). This position minimises respiratory motion and elongates the breast tissue from the chest wall by distorting the breast shape under gravity, enabling the breast structure to be clearly viewed and optimising the detection of abnormalities [246, 247]. The prone position is uncomfortable for many women and inaccessible for those with significant mobility issues [13]. Moreover, breast-specific coils are only available at roughly a third of clinical sites, and their purchase may cost up to $120,000 [248]; this limits the accessibility of breast MRI.

Performing breast MRI in the supine position could improve patient comfort whilst enabling better image registration to other modalities, such as ultrasound [249–252]. Importantly, the supine position is employed for MR imaging of nearly all other anatomical regions. Enabling breast imaging in the same position could thereby also facilitate the discovery of opportunistic findings indicative of breast cancer. However, concerns remain regarding visualisation of the fine structure of

**Figure 9.2:** Photographs showing two examples of flexible body coils ("flex" coils), which could be used for supine breast imaging as shown here. Images from Perspectum Ltd.

the breast as the breast tissues are compressed under the effect of gravity. Flexible body ("flex") coils, which are typically used for abdominal imaging, may be used in supine breast MRI (Figure 9.2), but the necessary placement of this coil on the patient's chest causes additional breast compression. Their use in clinical MRI protocols could result in an uneven flow of contrast owing to compression of the breast parenchyma; this could affect wash-out curves and therefore potentially hinder diagnosis [253]. Additionally, the lack of tissue separation achieved in the supine position may obscure the detection of anomalies during radiologist review. Furthermore, the application of pressure to an RF coil can distort the transmit field; this can lead to imaging artefacts in the form of areas of high signal intensity [253, 254] which may further impede image interpretation.

The feasibility of performing diagnostic breast MRI in the supine position has been demonstrated by Fausto et al. [255]. In this study, foam pads were used to minimise compression of the breast tissue beneath the weight of the RF coil. However, the group noted the difficulty of their approach in participants with large breasts which extend beyond the front edge of the thorax in the supine position. Siegler et al. implemented a semi-rigid custom coil for supine breast MRI but this was limited in its coverage of the breast [247]. Recent development of novel vest-like coils for supine breast imaging show excellent results [256, 257] but clinical implementation necessitates sites to purchase an expensive new coil, which are currently limited to 3T and are each specific to only one scanner manufacturer.

To address this clinical need and overcome the above limitations, we developed a support device (the "MR Bra") for supine breast imaging, which is designed for use with the readily-available flexible body coils. The intention of the MR Bra is to support the breasts to prevent them from falling into the armpits, to elongate the structure of the breast in the supine position, and to prevent compression of the breasts from the weight of the coil placed on top of the chest. Through use of the MR Bra, we aim to improve patient comfort whilst maintaining acceptable image quality and sufficient breast extension to enable radiologists to interpret images successfully. Implementation of the MR Bra could ultimately improve the accessibility of breast MRI, as no specialised coils would be required for its use.

This chapter reports the performance of four prototypes of the MR Bra. We assess the SNR achieved against conventional prone imaging, compare quantitative biomarkers calculated in each position, and provide a preliminary assessment of employing negative pressure. We also report feedback from participants and clinicians to evaluate patient comfort and the feasibility of implementing this support device in clinical practise.

## 9.2 Methods

### 9.2.1 Design

We here describe the design of the four prototypes of the MR Bra. Intellectual property relating to the MR Bra is owned and managed by Perspectum Ltd., and the MR Bra is a registered design with the UK Intellectual Property Office (registration number 6413500).

#### 9.2.1.1 Prototypes 1 and 2

The first two prototypes of the MR Bra were developed in-house by Perspectum Ltd. Prototype 1 consisted of cups designed by Alan Blunt, a qualified engineer, using Autodesk Inventor [258]. Cups were 3D-printed in hard plastic (Figure 9.3) and fastened together using an elasticated fabric band which was changed between scans. Three sizes were developed to account for different breast volumes.

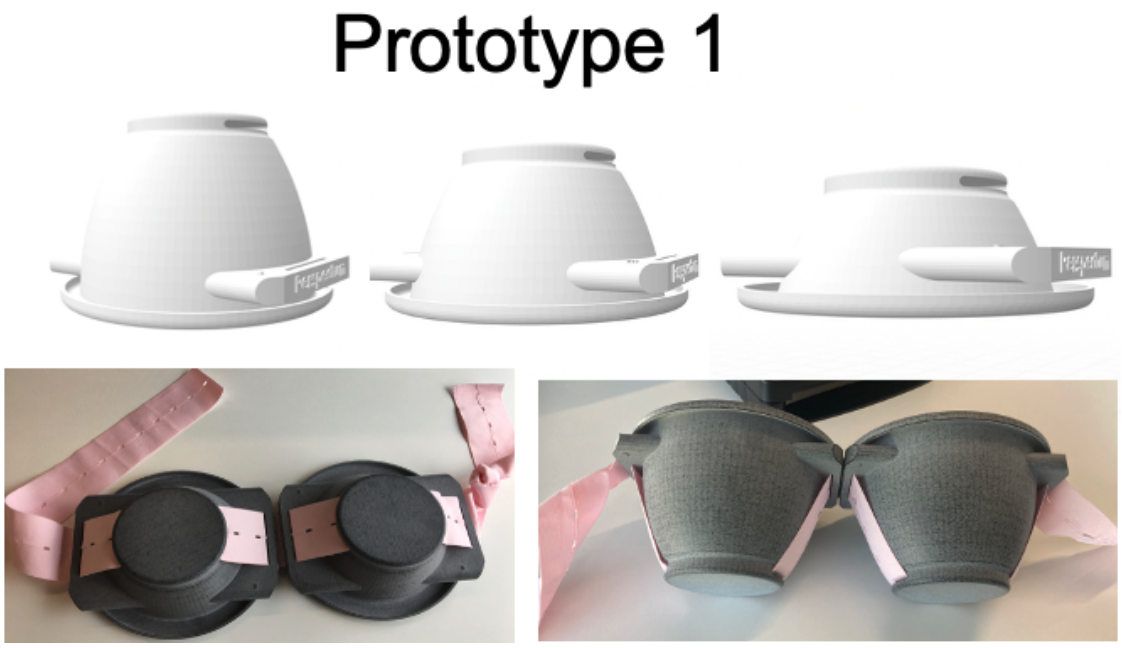


**Figure 9.3:** Design and photographs of the first prototype of a support device for supine imaging (the "MR Bra"). This model was designed in-house at Perspectum Ltd. by Alan Blunt, a qualified engineer, using Autodesk Inventor [258], 3D-printed in hard plastic and attached using elasticated fabric bands. Three sizes of this prototype were developed to account for different breast sizes. Images from Perspectum Ltd.

Prototype 2 employed commercially-available plastic structures as cups and incorporated a mechanism for applying negative pressure to draw the breasts away from the chest wall and elongate the breast tissue (Figure 9.4).

#### 9.2.1.2 Prototypes 3 and 4

An NIHR i4i FAST grant was awarded to Perspectum Ltd. to develop and evaluate further prototypes of the MR Bra[1]. This resulted in a further two prototypes of the MR Bra which were designed by Perspectum Ltd. in collaboration with Pulseteq Ltd., and manufactured by PulseTeq Ltd.

Prototype 3 consisted of 3D-printed hard plastic cups trimmed with a soft plastic gasket (Figure 9.5). The cups were hemispherical in shape and a duckbill valve enabled application of negative pressure. The valve allowed different vacuum

[1]This project was funded by the National Institute for Health and Care Research (NIHR) under its Invention for Innovation (i4i) Programme (Grant Reference Number NIHR205925). The views expressed are those of the author(s) and not necessarily those of the NIHR or the Department of Health and Social Care.


**Figure 9.4:** Photograph of Prototype 2 of the MR Bra. This support device was made in-house at Perspectum Ltd. from commercially-available plastic cups and included the ability to apply negative pressure. Image from Perspectum Ltd.

pumps to be applied; a handheld bulb pump is shown in Figure 9.5 and was used for initial evaluation of this model. The cups were connected with a plastic hinge to allow for separation of the cups when required, for example for participants who may have undergone single mastectomy.

Prototype 4 was developed following initial user feedback on Prototype 3. The cups in Prototype 4 were shaped to include greater lateral coverage of the breasts and a thicker gasket made from polyurethane resin was used to improve patient comfort (Figure 9.6). The cups were connected with an elasticated hinge. An umbrella valve was installed which, as in Prototype 3, was compatible with different vacuum pumps. A handheld electric battery pump was used for evaluation of this model (Figure 9.7).

#### 9.2.1.3 Participant Use

The MR Bra is intended to be worn and fitted by the participant prior to the MRI scan. Where there is the option to apply negative pressure, the participant applies this themselves such that it is in their control (Figure 9.7). Participants lie in the supine position with the available flexible body coil resting on top of the MR Bra (Figure 9.8). To ensure optimal hygiene, fabric straps are changed between

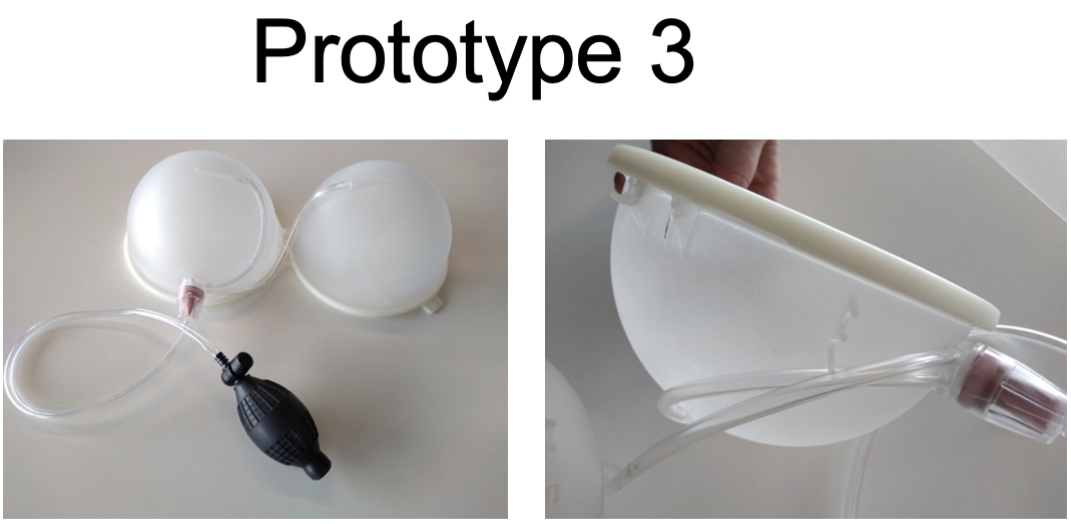


**Figure 9.5:** Photographs of Prototype 3 of the MR Bra, a 3D-printed support device with the option to apply negative pressure through a hand-operated pump. This prototype was the first of two developed with the support of an NIHR i4i FAST grant awarded to Perspectum Ltd. and manufactured by PulseTeq Ltd. Images from Perspectum Ltd.

participants and cups are cleaned with anti-bacterial wipes.

### 9.2.2 Fitting Sessions

During development of the third and fourth prototypes of the MR Bra, we invited healthy volunteers from Perspectum Ltd. to try on the MR Bra and to feedback on its comfort and ease of fit. Fitting sessions were performed for eight volunteers with Prototype 3 and with thirteen volunteers with Prototype 4. Volunteers were asked to complete a short questionnaire after their fitting session in which participants were asked to rate their comfort on a scale of 1–10.

### 9.2.3 Image Acquisition

#### 9.2.3.1 Prototypes 1 and 2

To evaluate the first prototype of the MR Bra, sixteen healthy women (mean age 37 years, range 31-58 years) gave informed consent under the IMOGEN study (Section 2.3.1.1) and were imaged on a Siemens MAGNETOM Aera 1.5T scanner. Participants were firstly imaged in the prone position using an 18-channel breast

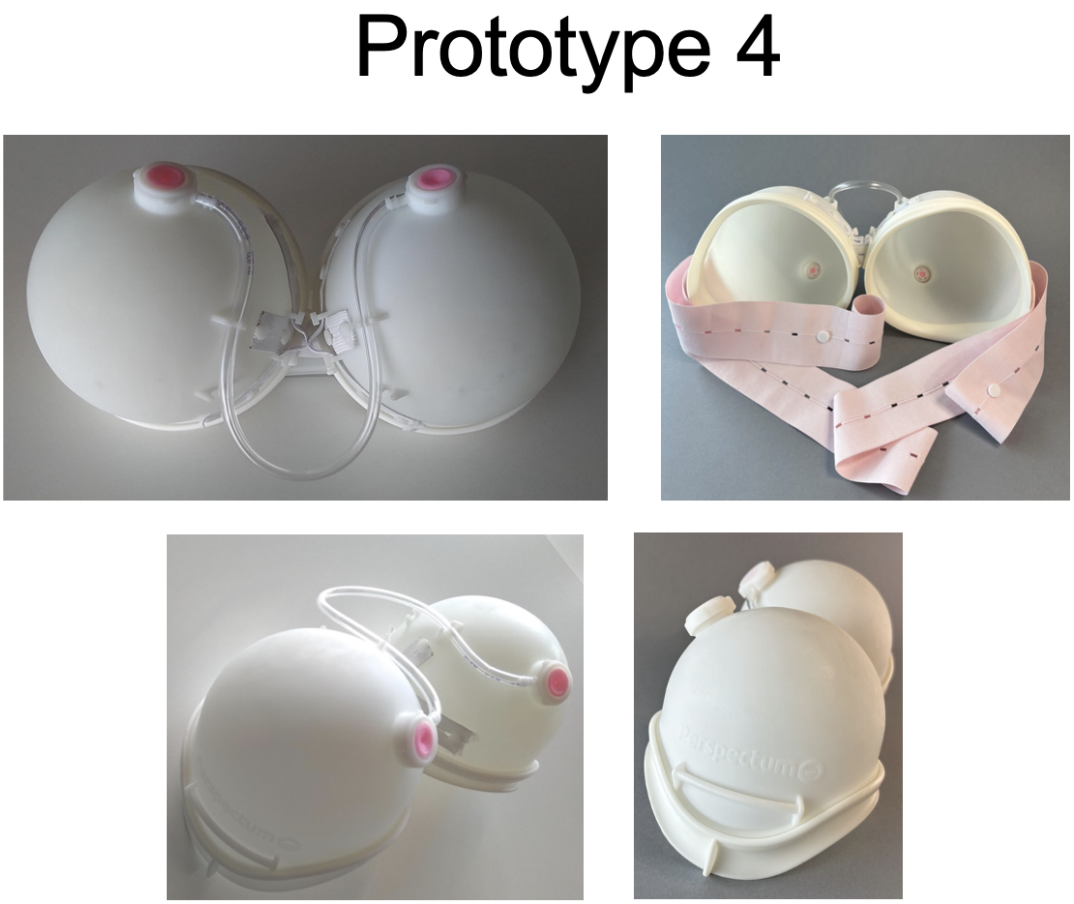


**Figure 9.6:** Photographs of Prototype 4 of the MR Bra, the second of two prototypes developed with the support of an NIHR i4i FAST grant. The predominant difference between Prototypes 3 and 4 is the greater lateral coverage of the breasts and the thicker gasket in Prototype 4. Images from Perspectum Ltd.

coil (Siemens Healthineers). Participants were then imaged in the supine position with a 6-channel flexible body coil (Siemens Healthineers) whilst wearing Prototype 1 of the MR Bra (Figure 9.8 (left)). The most appropriate size of MR Bra was found according to ease of fit of the model and participant comfort. A 3D axial $T_1$-weighted Dixon scan was performed as described in Section 2.3.2. Participants completed an optional short free-text questionnaire to feedback on their experience of the scan in each position.

One healthy participant underwent additional imaging with the flex coil in the supine position. The participant was firstly imaged without a support device

**Figure 9.7:** Photograph of a participant wearing the fourth prototype of MR Bra, applying negative pressure using an electric battery pump. The application of negative pressure is performed by the participant, such that it is in their control. Image from Perspectum Ltd.

**Figure 9.8:** Photographs of participant positioning whilst wearing the MR Bra. The MR Bra is fitted by the participant prior to the scan. The participant then lies on the scanner bed in the supine position and the RF coil is placed on top of the bra. Left: Prototype 1 of the MR Bra with the Siemens flexible body coil. Right: Prototype 4 of the MR Bra with the GE flexible body coil ("AIR Coil"). Images from Perspectum Ltd.

and then with the second prototype device before and after the application of negative pressure.

#### 9.2.3.2 Prototype 4

To assess the performance of the fourth version of the MR bra, eight healthy participants gave informed consent under the RADIUS study (Section 2.3.1.2) and were imaged on a GE SIGNA Voyager 1.5T scanner. Participants were firstly imaged in the standard prone position with an 8-channel breast coil (GE Healthcare), and then in the supine position wearing the MR Bra beneath a flexible 16-channel

flexible body coil ("AIR Coil" [259]) (Figure 9.8 (right)). The spine coil was also switched on. A multi-parametric protocol was acquired, including 3D axial $T_1$-weighted Dixon images, $T_2$-weighted images, and multi-echo GRE images for use in CSE-MRI (Section 2.3.2). One participant underwent additional imaging in the supine position without a support device for comparative purposes.

Participants completed a questionnaire to feedback on the comparative comfort of each position. The majority of questions employed a Likert Scale to enable quantitative analysis of the participant experience.

## 9.2.4 Analysis

### 9.2.4.1 Prototypes 1 and 2

Proof of concept of the MR Bra was evaluated through SNR calculation and qualitative assessment of the images acquired using Prototypes 1 and 2. SNR was quantified using the method described in Section 2.2.1.9 at a central slice of the fat image from the $T_1$-weighted Dixon acquisition; one ROI was placed within the breast fat and one was placed outside of the breast in background noise[2]. Two radiologists qualitatively reviewed images of the participant who underwent additional imaging.

### 9.2.4.2 Prototype 4

Prototype 4 was used to provide a more conclusive analysis of the performance of the MR Bra.

Two experienced radiologists assigned BI-RADS density scores to the prone and supine MRI datasets acquired. The 3D $T_1$-weighted and $T_2$-weighted images were provided and the radiologists were blinded to which datasets were acquired from the same participant in the prone and supine positions.

Quantitative breast density was also evaluated in each position using the PDFF-derived approach described in Chapter 6. PDFF maps were generated using the 3D axial 6-echo GRE sequence described in Section 3.1 and the proprietary algorithm of the vendor (IDEAL-IQ, GE Healthcare). The PDFF of fibroglandular tissue

[2]We gratefully acknowledge Dr. Amy Herlihy for placing these ROIs.

was assumed to be 0% and the PDFF of breast adipose tissue was assumed to be 91.6% [110]. Whole breast segmentations were performed by one operator using a semi-automated technique which included a three-dimensional region growing algorithm within ITK-SNAP [148] and manual adjustments[3].

In contrast to Chapter 6, the PDFF-derived breast density measurements in this work were not corrected for each participant's specific breast adipose tissue PDFF. This decision was made to avoid potential confounding effects arising from a potential difference in breast adipose tissue PDFF between the positions which could influence the density measurements.

The PDFF of the breast adipose tissue was measured in each position due to its potential utility as a biomarker of cancer risk and severity (Chapters 7 and 8). Four circular ROIs with a radius of 4mm were placed in the breast fat in the central slice of the PDFF maps, as in Chapter 6 (Figure 6.8). The ROIs were positioned to avoid inclusion of fibroglandular tissue and vasculature. The PDFF of breast adipose tissue was found by taking the median PDFF value across the ROIs.

SNR was measured across the seven participants for whom $T_1$-weighted images were acquired in both positions. The approach described in Section 9.2.4.1 was employed, however four ROIs were placed in the breast adipose tissue and four were placed in the background noise to improve sampling of the data.

After assigning the BI-RADS® density scores, one experienced radiologist was unblinded to which $T_1$- and $T_2$-weighted datasets corresponded to the same participant imaged in each position. They were also provided with an additional set of images wherein one participant underwent imaging in the supine position without a support device. The radiologist was then asked to complete a questionnaire regarding the comparative image quality achieved in each position, and the potential clinical utility of the MR Bra. Additionally, two radiographers were shown the MR Bra and asked to complete a short questionnaire regarding its feasibility in clinical practise.

[3]We gratefully acknowledge Dr. Amy Herlihy for completing these segmentations.

| Breast Imaging Modality | Median SNR (IQR) (n = 16) |
|---|---|
| Prone - breast coil | 188.5 (162.4 to 211.6) |
| Supine - flex coil with MR Bra Prototype 1 | 101.3 (90.9 to 128.9) |

**Table 9.1:** Table showing the median SNR across sixteen healthy participants imaged in the prone position with the breast coil and the supine position using the flex coil and Prototype 1 of the MR Bra.

## 9.3 Results

### 9.3.1 Prototypes 1 and 2

#### 9.3.1.1 SNR

The median SNR across the sixteen healthy participants was significantly lower supine wearing Prototype 1 of the MR Bra compared to prone using the breast coil (Wilcoxon signed rank test, p = 4.4e-4) (Table 9.1). However, the MR Bra produced SNR values which are comparable to those obtained in the prone position in another 1.5T study in which the images were deemed sufficient for diagnostic interpretation [255].

Whilst fifteen participants were imaged in the supine position using the flex RF coil only, one participant was imaged with the spine RF coil switched on in addition to the flex coil. The spine coil is based inside the scanner bed; as expected, the images of this participant showed improved posterior signal intensity (Figure 9.9 (right)). However, the SNR measured in the breasts of this participant was not significantly different compared to that measured in the fifteen participants for which the spine coil was switched off (Wilcoxon rank sum test, p = 0.88).

Areas of high signal intensity or "hot spots" were observed in the prone images (Figure 9.9 (left)), which may correspond to areas of the body which are in direct contact with the breast coil.

Images of an additional participant who was imaged in the supine position without a support device demonstrated breast compression from the weight of the coil (Figure 9.10). The scan without a support device produced higher SNR than use of Prototypes 1 and 2 of the MR Bra (Table 9.2). However, the spine coil was switched on for the scan without a support device, and was switched

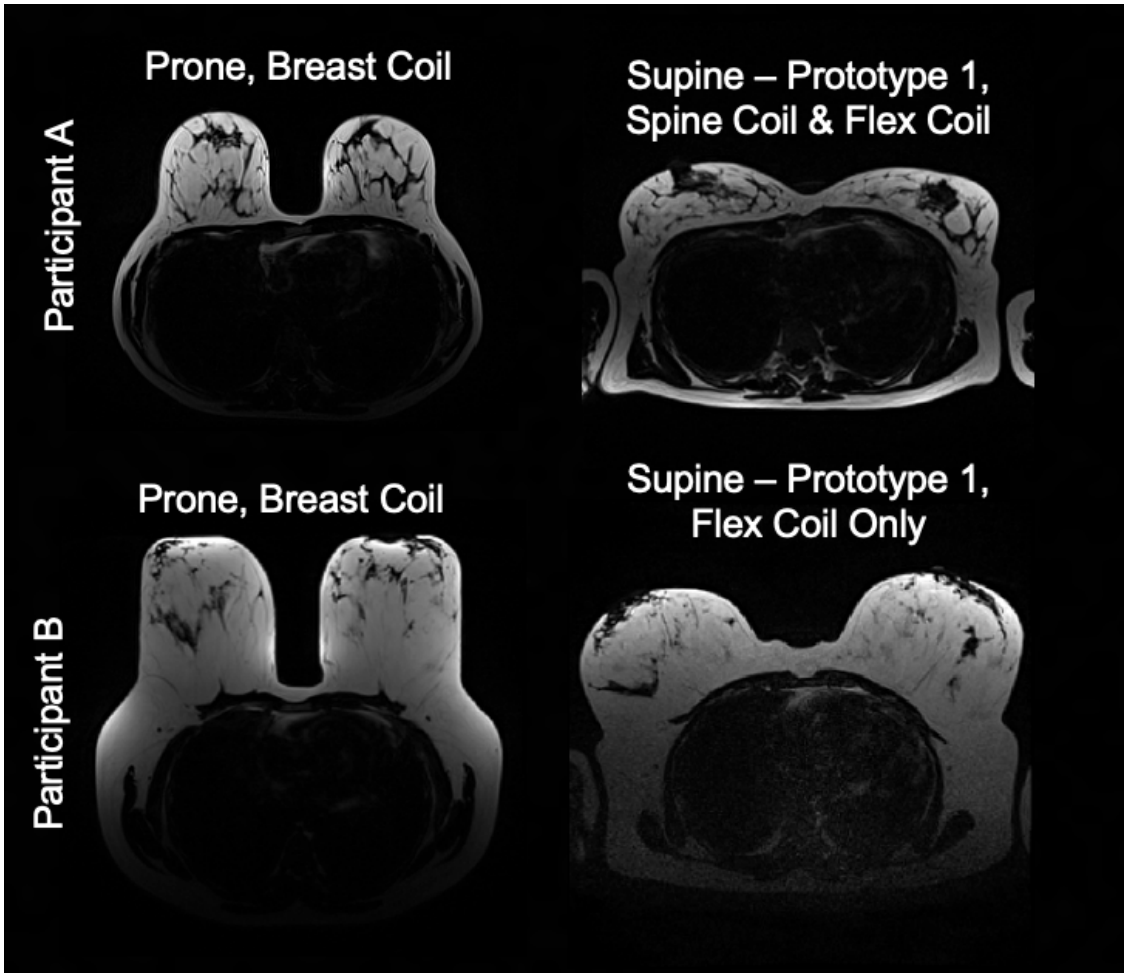


**Figure 9.9:** Central slices of the fat image from $T_1$-weighted Dixon acquisitions are shown for two participants imaged in the prone and supine positions (described here as "Participant A" (top row) and "Participant B" (bottom row). Participant A was imaged in the supine position using the flex RF coil and the spine RF coil, whilst participant B was imaged in the supine position using the flex RF coil only. As expected, the supine image of participant B shows poorer signal intensity in the posterior body. Prone images of each participant are included for comparative purposes. Signal "hot spots" can be seen in the prone images, which may correspond to areas of the body which are in direct contact with the breast coil.

off for those acquired using the MR Bra. Whilst our previous work suggests use of the spine coil does not affect measurement of SNR in the breast, a greater number of participants should be imaged without a support device before this finding should be taken as definitive.

Application of negative pressure to Prototype 2 of the MR Bra affected SNR minimally (Table 9.2). Prototype 2 demonstrated substantially reduced SNR compared to Prototype 1; this could be attributed to the singular size of Prototype

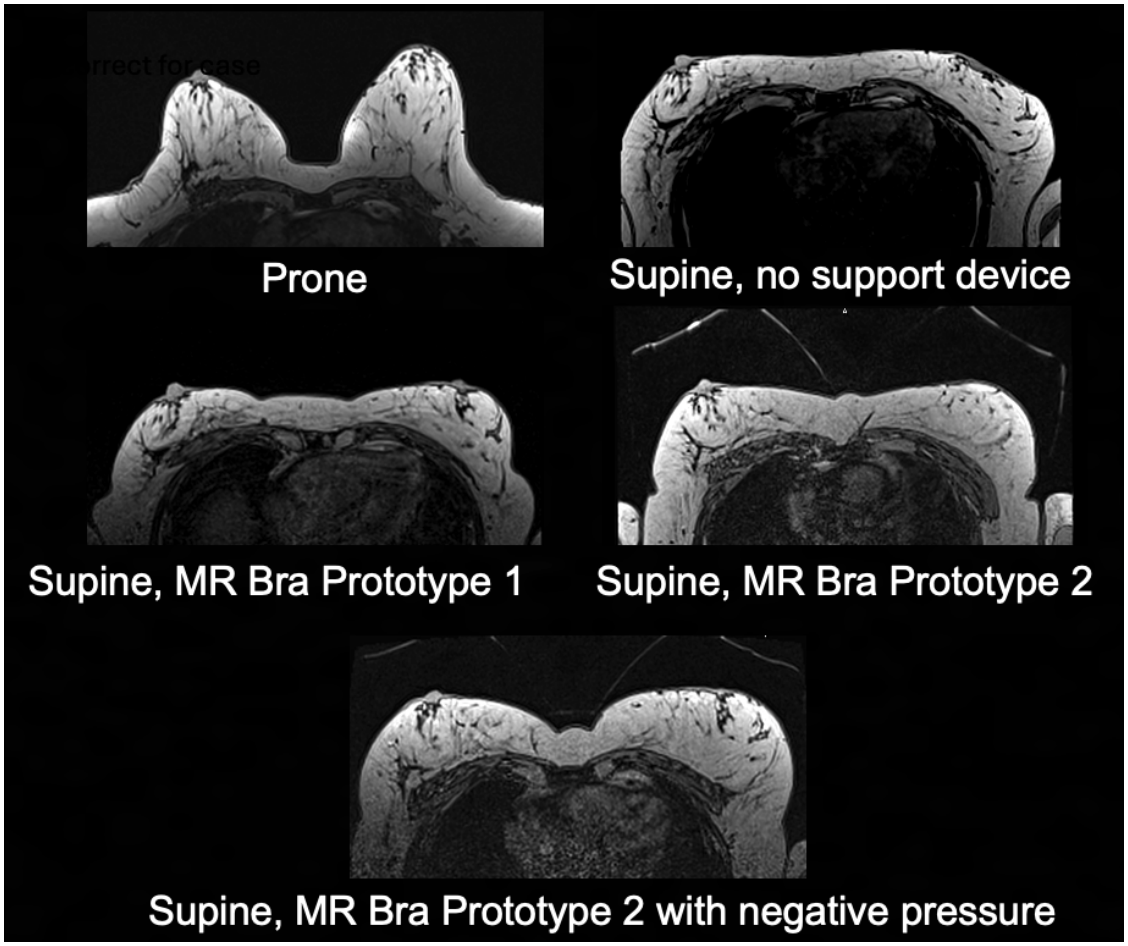


**Figure 9.10:** $T_1$-weighted out-of-phase images showing the same participant imaged at the same anatomical location with different positioning and wearing different prototypes of the MR Bra. This includes the standard prone position, supine without a support device, supine with Prototype 1 of the MR Bra, and supine with Prototype 2 of the MR Bra before and after the application of negative pressure.

2 which had a large cup depth, such that the flex coil resting atop the MR Bra is further away from the breast tissue.

#### 9.3.1.2 Qualitative Image Assessment

Two radiologists provided positive feedback on visualisation of fine structure with the MR Bra. The radiologists indicated a preference for the elongated breast shape induced by application of negative pressure.

| Breast Imaging Modality | SNR (n = 1) |
|---|---|
| Supine - flex coil and spine coil, no support device | 131.9 |
| Supine - flex coil with MR Bra Prototype 1 | 119.0 |
| Supine - flex coil with MR Bra Prototype 2 | 52.6 |
| Supine - flex coil with MR Bra Prototype 2 and negative pressure | 55.3 |

**Table 9.2:** Table showing the SNR of one participant imaged in the supine position with the flex coil without a support device, with the flex coil and Prototype 1 of the MR Bra, and with the flex coil and Prototype 2 of the MR Bra before and after the application of negative pressure.

#### 9.3.1.3 Participant Comfort

Several participants identified areas of discomfort during prone scanning. Participant tolerance of supine scanning with the MR Bra was generally good, with participants describing the position as "comfortable" and "more private". Nine participants provided comparative qualitative feedback on the comfort of the scans; of those, 89% preferred supine imaging with the Prototype 1 of the MR Bra compared to traditional prone imaging using the breast coil.

### 9.3.2 Prototypes 3 and 4 - Fitting Sessions

The mean comfort score provided by participants during fitting sessions of Prototypes 3 and 4 improved between the models; the mean reported score was 6.2 using Prototype 3 and 7.8 using Prototype 4. The comfort scores were not significantly different between the prototypes (Wilcoxon rank sum test, $p = 0.10$), however this could be affected by low participant numbers, with only seven participants having undertaken a fitting session with Prototype 3. The plastic hinge connecting the two cups in Prototype 3 failed during the fitting sessions, which encouraged the development of the elasticated hinge in Prototype 4.

### 9.3.3 Prototype 4

#### 9.3.3.1 SNR

In agreement with the results observed using Prototype 1, the median SNR across seven healthy participants was significantly lower in the supine position wearing Prototype 4 of the MR Bra compared to prone using the breast coil (Wilcoxon signed

| Breast Imaging Modality | Median SNR (IQR) (n = 7) |
|---|---|
| Prone - breast coil | 132.9 (117.1 to 144.1) |
| Supine - flex coil with MR Bra Prototype 4 | 73.1 (66.8 to 87.0) |

**Table 9.3:** Table showing the median SNR across seven healthy participants imaged in the prone position with the breast coil and the supine position using the flex coil and Prototype 4 of the MR Bra.

rank test, p = 0.015) (Table 9.3). The median SNR using Prototype 4 was 55% of that found in the traditional prone position; this is similar to the results of Table 9.1 in which the SNR using Prototype 1 was 54% of that in the prone position. However, once again, the SNR values acquired in the supine position were comparable to images acquired in the prone position in the other 1.5T study [255]. This group reported a median prone SNR of 87.91 with an interquartile range of 65.6–131.8; here we find a median supine SNR of 73.1 with an interquartile range of 66.8–87.0.

#### 9.3.3.2 BI-RADS Density Score

Two radiologists assigned the same BI-RADS density score (A–D) between prone and supine images to six out of eight and seven out of eight participants, respectively. Where different scores were provided, the prone and supine scores were only one category different (such as B versus C) or a borderline category was provided in one position but not the other (such as B versus B/C).

#### 9.3.3.3 Quantitative Density

Two datasets in which the IDEAL-IQ acquisition did not provide full coverage of the superior/inferior extent of both breasts were excluded from this analysis. Additionally, one dataset was excluded due to incorrect use of a saturation band in the IDEAL-IQ acquisition which caused an area of signal drop out within the breasts.

Bland-Altman analysis [123] showed close agreement between breast density measured in the supine position using the MR Bra and the prone position (Figure 9.11). The bias was measured to be -0.6% with the 95% limits of agreement lying between -2.3% to 1.2%. This corresponds to a half-width of the 95% limits of agreement (HWLoA) of 1.8%.

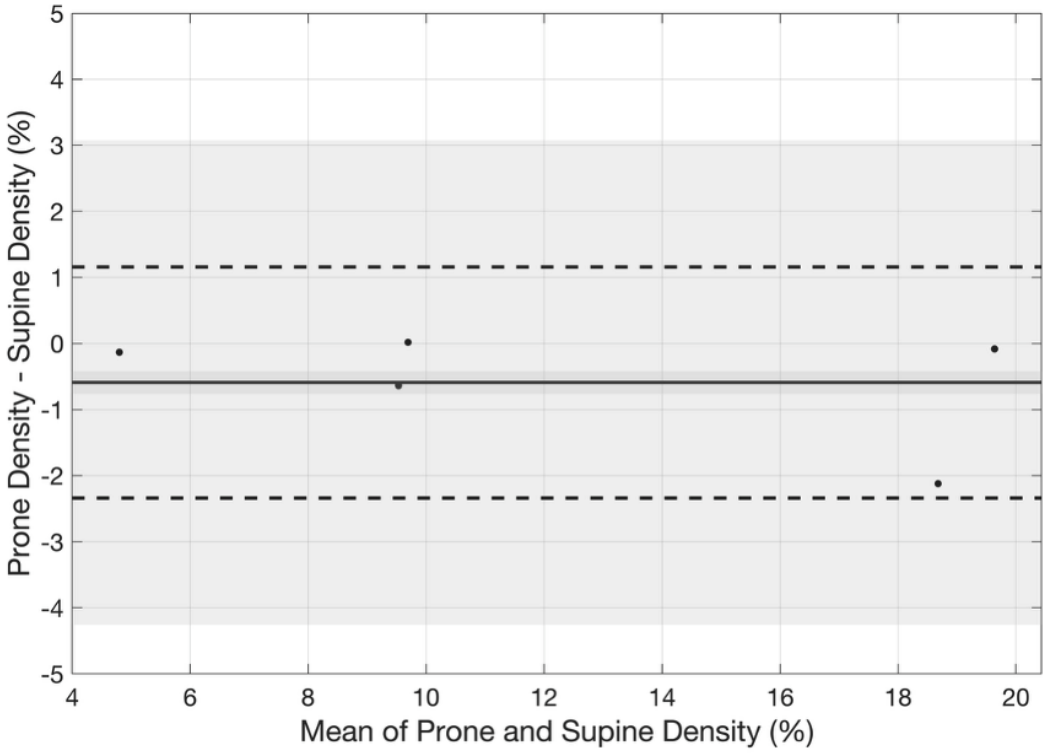


**Figure 9.11:** Bland-Altman plot showing the difference between quantitative breast density measured in the prone position and the supine position wearing Prototype 4 of the MR Bra. The black continuous line shows the overall bias in the data whilst the black dashed lines reflect the 95% limits of agreement. The grey background shows the confidence interval of the 95% limits of agreement.

In this study, data to assess the repeatability of breast density calculated in the prone position was not available for comparison against these values. However, literature suggests that this level of variation in breast density is acceptable. Firstly, Henze Bancroft et al. [127] assessed the repeatability of the volume of fibroglandular tissue measured using 6-echo CC-CSE-MRI in the prone position. They found a repeatability coefficient (RC) of 10.3cm$^3$; dividing this value by the mean measured breast volume of 1542cm$^3$, this repeatability coefficient corresponds to a 0.6% change in breast density. Whilst this result suggests poorer agreement of the prone-supine density measurement, with HWLoA of 1.8%, compared to prone-prone density measurement, Henze Bancroft et al. found an RC of 51.7cm$^3$ between two prone measurements taken at different field strengths, corresponding to a 3.4% change in breast density. Therefore, the variation in breast density measurement between

the prone position and the supine position with the MR Bra is less than that which arises due to a change in field strength.

Secondly, the repeatability coefficient of a voxel-classification-based approach to breast density with MRI was reported to be 15% [260]. In part, this value was attributed to variation in positioning of the participants in the prone position, and to tissue compression against the breast coil.

Lastly, a clinically significant change in mammographic breast density is typically considered to be around 5%, which is over two times greater than the HWLoA associated with changing positions between prone and supine positions with the MR Bra. Mullooly et al. [261] categorised a change in mammographic breast density <5% over 2 years as minimal. Chen et al. categorised the reduction in breast density for patients receiving tamoxifen into three groups; a change in breast density <5%, a change between 5 and 10%, and a change >10% [262]. Cuzick et al. [263] found no significant reduction in breast cancer risk for participants who experienced <10% reduction in breast density.

#### 9.3.3.4 PDFF of Breast Adipose Tissue

Bland-Altman analysis showed a minimal bias of -0.2% between the PDFF of breast adipose tissue measured in the prone position and that measured in the supine position using the MR Bra (Figure 9.12). The 95% limits of agreement lay between -2.6% to 2.2%, corresponding to a HWLoA of 2.4%.

For comparison, the ROI-based analysis was performed again by the same operator on the same central slice of the prone PDFF maps. Figure 9.13 shows the agreement between the two measurements of median PDFF calculated in the prone position. The bias was 0.9% with LoA -1.0% to 2.7%, corresponding to an RC of 1.9%.

The RC of the prone-prone analysis is similar to the HWLoA of the prone-supine analysis, and the bias incurred by changing participant position was found to be less than that incurred by repeating the ROI-based analysis twice in the same prone PDFF map. We therefore conclude that imaging participants in the supine

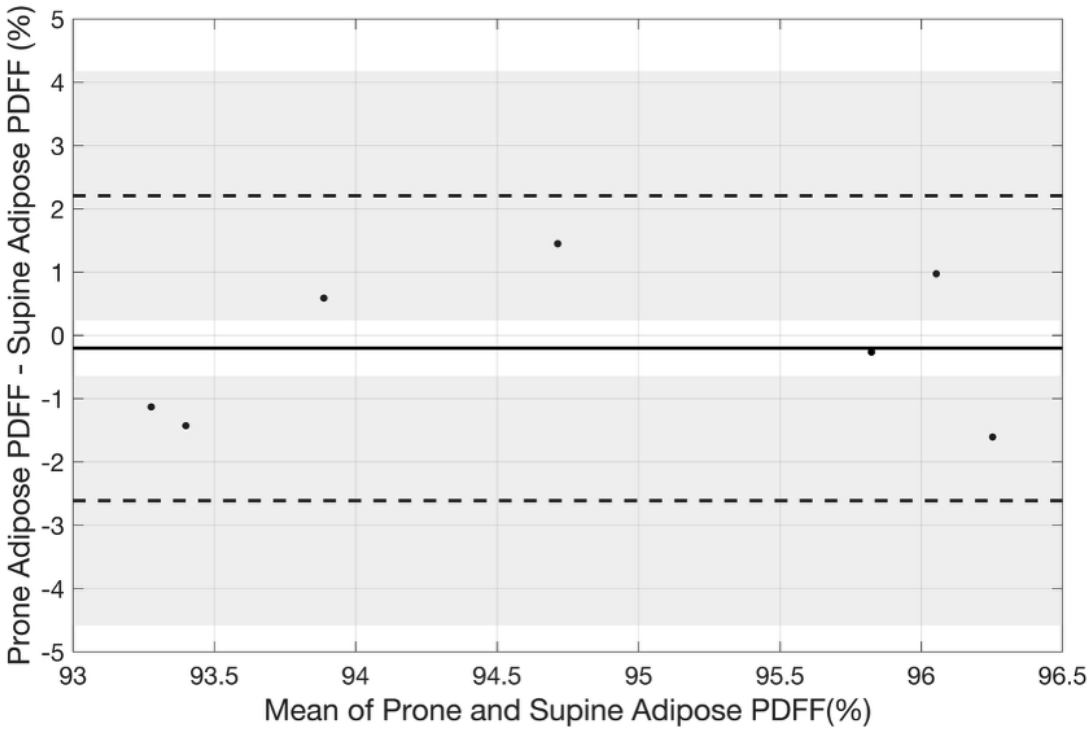


**Figure 9.12:** Bland-Altman plot showing the difference between the PDFF of breast adipose tissue measured in the prone position and the supine position wearing Prototype 4 of the MR Bra. The black continuous line shows the overall bias in the data whilst the black dashed lines reflect the 95% limits of agreement. The grey background shows the confidence interval of the 95% limits of agreement.

position with the MR Bra has minimal effect on measurement of this biomarker compared to the traditional prone position.

Employing a segmentation-based analysis to calculate the median PDFF across all breast adipose tissue, as performed in Chapter 4, may improve the repeatability of this metric compared to relying on placement of ROIs.

#### 9.3.3.5 Radiologist and Radiographer Review

The radiologist who provided feedback via questionnaire agreed that the image quality of the supine images acquired with the MR Bra were sufficient for interpretability. They noted the presence of "a small amount of artefact involving the axillary tail on each patient", but thought this would be "unlikely to be detrimental to interpretation." They agreed that the shape of the breasts in the supine position with the MR Bra was adequate for interpretability and that the

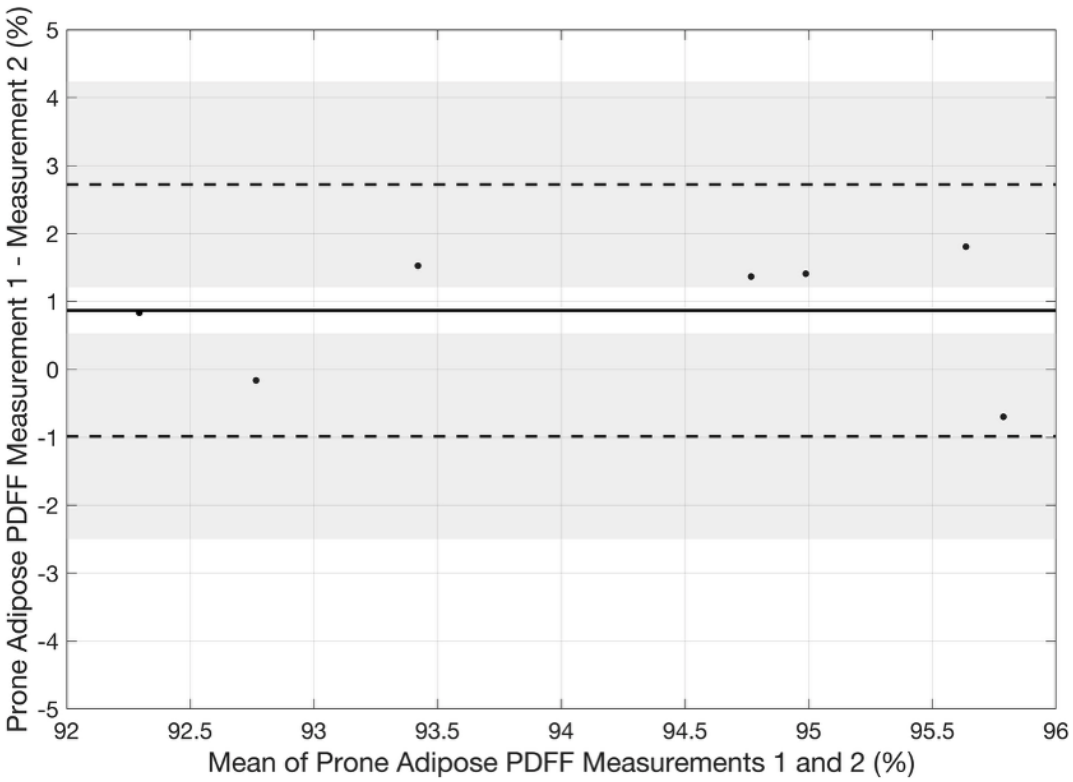


**Figure 9.13:** Bland-Altman plot showing the difference between the PDFF of breast adipose tissue measured twice in the images acquired in the prone position to provide a measure of repeatability of the metric. The black continuous line shows the overall bias in the data whilst the black dashed lines reflect the 95% limits of agreement. The grey background shows the confidence interval of the 95% limits of agreement.

axillae were seen adequately in this position.

The radiologist neither agreed nor disagreed that, with enough training, they could adequately interpret supine images taken using the MR Bra. They confirmed that post-contrast imaging of patients with known pathology would be required to decide whether image interpretation is affected, and whether small enhancing foci would be more difficult to interpret.

The radiologist strongly agreed that supine images taken using the MR Bra improved the breast shape for interpretability compared to supine images taken without the MR Bra (Figure 9.14). They also strongly agreed the supine images taken using the MR Bra were overall better compared to those without.

The radiologist raised concerns regarding the suitability of the MR Bra for use in MR-guided biopsies. They commented that, in their place of work, MRIs

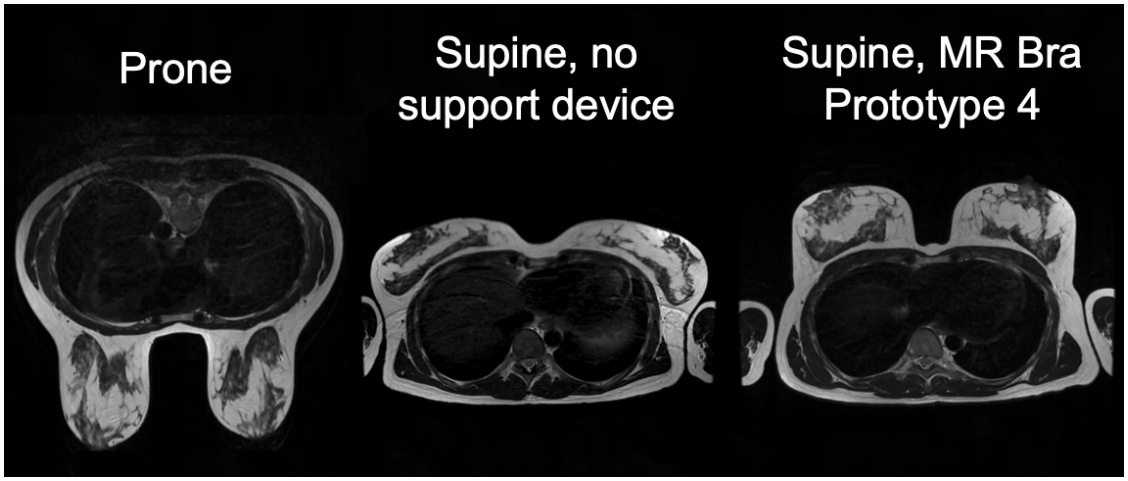


**Figure 9.14:** $T_2$-weighted images of the same patient imaged in three different positions: the standard prone position using the breast coil, the supine position using the flex coil without a support device, and the supine position using the flex coil with Prototype 4 of the MR Bra. These images were acquired at approximately the same location within the breasts, and demonstrate the difference in breast shape achieved with each position.

were only performed with a view to performing an MRI-guided biopsy if necessary, and that the planning for this biopsy would be made on the initial standard diagnostic MRI. However, they noted that different clinics perform vastly different numbers of MRI-guided biopsies.

Two radiographers also completed a short questionnaire regarding the clinical utility of the MR Bra. Both radiographers agreed that being able to perform breast MRI in the supine position would be beneficial for imaging staff, with one commenting that "the standard breast coil is heavy and awkward to set up, involving re-arranging the whole table". Both radiographers and the radiologist agreed or strongly agreed that being able to perform breast MRI in the supine position would be beneficial for patients.

However, one radiographer noted that there could be potential delays incurred if fitting the Bra proved difficult for some participants. It was also noted that centering the participant on the scanner bed is easy in the prone position as the radiographer is able to see the breasts and can adjust the patient accordingly; when the flex coil rests on top the MR Bra, visualisation of the central point of the breast may be more difficult.

#### 9.3.3.6 Participant Experience

Seven participants completed a questionnaire for both prone and supine scans. Six participants (86%) rated the overall experience of the supine scan using the Prototype 4 of the MR Bra higher than that of the scan performed in the prone position. The remaining participant provided the same rating for both scans. All participants provided a better physical comfort rating for the supine scan compared to the prone scan and rated their emotional state in the supine position as better than or equal to their emotional state in the prone position. All participants were more likely to recommend the supine scan with the MR Bra than the scan performed in the traditional prone position.

## 9.4 Discussion

Initiatives to enable breast MRI to be performed in the supine position are increasingly undertaken. Methodologies have been developed to reduce the effect of respiratory motion in this position [254, 264], whilst Obermann et al. have developed a method to reduce the number of slices a radiologist would need to review through reconstruction of axial and coronal images into a "panoramic view" [256]. Incorporating these methods into our analysis may further improve the clinical utility and the image quality achieved using the MR Bra.

To the best of our knowledge, the MR Bra is one of only two support devices developed for supine breast MRI. The other is a flexible, fabric breast support made from a knitted material which was employed in the work of Meullenet et al. [254]. The group report that volunteers who wore the support demonstrated a breast shape closer to that achieved in the prone position, which facilitated comparison to prone MRI. However, use of fabric supports in a clinical setting may prove an issue for reasons of hygiene; the MR Bra is designed to avoid cross-contamination between subjects through use of wipeable plastic cups.

In this work, initial evaluation of Prototypes 1 and 2 of the MR Bra encouraged the continued development of this device. In addition to the work presented in

this chapter, Herlihy et al. found good agreement of quantitative breast density measured using Prototype 1 to that measured in the prone position [265]; this provided further confidence in the concept of the MR Bra. Radiologist review of Prototype 2 suggested that application of negative pressure may provide preferable tissue visualisation which is more comparable to traditional prone imaging; this catalysed the inclusion of this mechanism in subsequent prototypes.

The encouraging participant feedback on Prototype 4 and the improved comparative comfort score achieved in fitting sessions compared to Prototype 3 suggested that modifications made between these models were successful, and that Prototype 4 should be used in future work.

The close agreement of breast density and breast adipose PDFF in the different positions suggests that implementation of the MR Bra could support continuity between standard prone measurements and those acquired using this device. Positive feedback on image quality achieved in the supine position with the MR Bra, along with the acquisition of acceptable SNR values, suggests that the impact of respiratory and cardiac artefacts were minimal and provides encouragement for the continued evaluation of the Bra.

Feedback from one radiologist and two radiographers suggested that whilst there is potential clinical utility of the MR Bra, the use case of the MR Bra must be evaluated carefully. Whilst the MR Bra is not appropriate for use in MR-guided biopsy, the MR Bra has potential for implementation into several other clinical and pharmaceutical settings, particularly in those which do not have a breast RF coil available. For example, we have demonstrated the utility of the MR Bra in measurement of quantitative and categorical breast density. Although a larger study population should be examined, this result suggests the potential for implementation of the MR Bra in whole-body MRI "health checks". As with the majority of MRI scans, these assessments are performed in the supine position. Reporting breast density without moving a participant to the prone position could inform women of their breast cancer risk with minimal impact on appointment duration. The MR Bra may also have utility in pharmaceutical applications where a change in breast

density is of interest; breast density measurement in the supine position could enable more seamless integration with imaging protocols for other organs such as the brain, liver, kidney, spleen, and pancreas. However, a greater number of participants should be imaged supine without a support device to ensure the necessity of the MR Bra for density measurement in this position. Furthermore, additional sizes of the latest prototype should be developed to ensure inclusivity of the design.

The main limitation of this work is the absence of participants with known breast disease imaged with a clinical DCE-MRI protocol. The lack of contrast-enhanced data is attributed to the nature of the studies employed in this thesis which ultimately aim to develop a non-contrast breast MRI protocol. To assess whether clinical implementation of the MR Bra in a diagnostic protocol is feasible, a dedicated study should be conducted to examine the MR Bra's effect on lesion identification and diagnosis. Future studies could also compare the typical length of time to fit the MR Bra versus that of fitting the breast coil.

Another limitation of this work is that although the SNR measured using Prototypes 1 and 4 was comparable to that measured in the prone position in another 1.5T study, comparison of absolute SNR values is not definitive as SNR varies significantly according to the acquisition parameters. Requirements from ACR for accreditation of an imaging centre to perform breast MRI require that "adequate" SNR should be obtained and that images should be "not too grainy" [266]. The positive feedback received from the radiologist on the image quality achieved in the supine position suggests that these criteria were met.

## 9.5 Conclusion

The MR Bra enables comfortable supine breast imaging using readily-available flexible body coils whilst maintaining acceptable SNR. Quantitative imaging metrics showed close agreement in the prone and supine positions and feedback from radiologists and radiographers encourage the continued evaluation of the Bra. The MR Bra could prove a low-cost, easily-implementable solution for supine breast MRI, particularly at sites without a dedicated breast coil, and may be especially

beneficial for mobility-impaired patients for whom traditional positioning is not possible. Future work should consider the impact of the MR Bra upon lesion identification and assess comfort across an older and more diverse population.

# 10 Summary and Future Work

## Contents



## 10.1 Summary

The increasing incidence of breast cancer, particularly amongst younger women, necessitates improvements in breast imaging. Whilst MRI offers increased sensitivity over mammography and ultrasound, its clinical implementation relies upon the injection of contrast agent, the use of the uncomfortable prone position, and upon qualitative image interpretation. In this thesis, I explored the ability of two non-contrast, quantitative biomarkers derived from chemical-shift-encoded MRI to characterise tissue properties in the breast, and considered their application in the measurement of breast density, the assessment of adipose tissue quality, and the categorisation of disease. Additionally, I provided an evaluation of the MR Bra, a support device designed to enable comfortable supine breast imaging without the need for a specialised RF coil. These aims served the ultimate goal of improving the participant experience of breast MRI and reducing variability in image interpretation.

The thesis began by defining the optimal approach to confounder-corrected chemical-shift-encoded MRI of the breast. In **Chapter 3**, I quantified the impact of $T_1$ bias in the calculation of breast PDFF maps and demonstrated the suitability of the two GRE acquisitions employed throughout the thesis. In **Chapter 4**, I detailed the first implementation of a breast-specific fat spectrum in CSE-MRI, and demonstrated the improved breast map quality achieved using such a spectrum over those derived from liver and subcutaneous fat. Lastly, in **Chapter 5**, I demonstrated the necessity of including phase data in the breast CSE-MRI fitting algorithm, and determined that a hybrid fitting algorithm based on a graph cut algorithm and the IDEAL-IQ algorithm delivered optimal breast map quality over magnitude-based techniques. These three chapters were used to determine the method of generating PDFF and $T_2^*$ maps throughout the remainder of the thesis, and serve to guide the implementation of breast CSE-MRI in future applications.

The remaining chapters aimed to investigate the applications of breast CSE-MRI. In **Chapter 6**, I described the development of five specialised breast density phantoms, which were the first to treat breast density and breast structure as independent variables in phantom design, and the first to target both $T_1$ and $T_2$ in the development of the fibroglandular-tissue-mimicking component. With these phantoms, I demonstrated that breast density calculation derived from PDFF maps was more accurate, and less sensitive to the partial volume effect, than fuzzy c-means clustering of $T_1$-weighted images. I also demonstrated the agreement of PDFF-derived breast density with BI-RADS categorisations, and encouraged the incorporation of GLCM-derived spatial features into density assessment. This work indicates PDFF as an optimal choice for breast density measurement and provides confidence in its direct clinical applicability.

In **Chapter 7** I demonstrated that PDFF may be able to reflect the characteristics of hypertrophic adipose tissue and as such could provide direct quantification of mammary fat "quality". I also noted potential limitations in the ability of $T_2^*$ to reflect these features. This chapter lays the groundwork for epidemiological

studies to evaluate breast adipose PDFF as a measure of breast cancer risk and to compare its predictive value against BMI.

In **Chapter 8**, I quantified PDFF and $T_2^*$ in perilesional breast adipose tissue and demonstrated that PDFF may capture the presence of cancer-associated adipocytes. I also found that perilesional adipose tissue PDFF was able to distinguish between benign and malignant breast lesions, though additional datasets are needed to confirm this finding. Consistent with Chapter 7, I found that $T_2^*$ may not reliably reflect breast adipose tissue characteristics. This chapter provides a foundation for future histological interrogation of these biomarkers and establishes a framework for their assessment across larger cohorts.

In **Chapter 9**, I reported an initial evaluation of the MR Bra based upon SNR, quantitative imaging metrics, and feedback from participants, radiographers, and radiologists. I demonstrated that the MR Bra enabled comfortable supine breast imaging, minimally impacted the quantification of breast density and adipose tissue PDFF compared to traditional prone imaging, and achieved acceptable SNR values. These findings provide a key step in the validation of the MR Bra prior to initiating a dedicated DCE-MRI study to examine its impact on lesion assessment.

Overall, this thesis has demonstrated the extensive applicability of PDFF in the breast. From a single, non-contrast, two-minute acquisition, this biomarker could enable accurate quantification of breast density, direct measurement of breast adipose tissue quality, and contribute to disease characterisation and prognostic assessment. This sequence could be added to existing breast MRI protocols, or incorporated into whole-body MRI "health checks". In the latter context, maintaining supine positioning throughout the scan would minimise workflow interruptions; for this, the MR Bra could provide a practical solution.

## 10.2 Future Work

I propose two further projects as a result of the findings in this thesis.

### 10.2.1 Project 1: Breast Adipose Tissue PDFF and PDFF-Derived Breast Density for the Assessment of Breast Cancer Risk in the UK-Biobank Project

The UK Biobank project is a large-scale biomedical database which aims to support research into the prevention and diagnosis of a wide range of diseases [267]. The project includes the world's largest human imaging study, having recently achieved a milestone in recruitment of 100,000 volunteers. Breast-specific images are not acquired as part of UK Biobank, therefore, evaluation of breast imaging features with this dataset has not previously been possible. However, the UK Biobank imaging protocol includes a neck-to-knee MRI Dixon scan, from which water-only and fat-only images are calculated. I propose to use these images to measure PDFF-derived breast density and breast adipose tissue PDFF across the $\sim$ 50,000 female participants, and to evaluate their associations with breast cancer risk through comparing them against the NHS-linked longitudinal data acquired. Specifically, we could assess the correlation of the metrics to breast cancer incidence over time. For breast adipose tissue PDFF, we could compare its association with breast cancer incidence against that of BMI. For PDFF-derived breast density, as repeat imaging is available, we could evaluate not only its predictive ability as a one-off measurement, but also evaluate whether assessing the change in breast density over time is a better predictor of breast cancer incidence across the cohort.

Notably, the UK Biobank Dixon acquisition employs a dual-echo approach, therefore the fat fraction maps produced do not account for the confounders addressed throughout this thesis, such as the spectral complexity of fat, the $T_1$-bias effect, or $T_2^*$ decay. The fat fraction maps therefore do not reflect true proton density fat fraction (PDFF), but rather signal fat fraction (SFF). Regardless, methods to infer true PDFF from dual-echo Dixon acquisitions have begun development [268–270]. The large scale analyses proposed in this work would also require full automation of a whole breast segmentation protocol which enables consistent breast delineation in the supine position. Once these considerations are addressed, UK Biobank would enable validation of breast adipose tissue PDFF and PDFF-derived

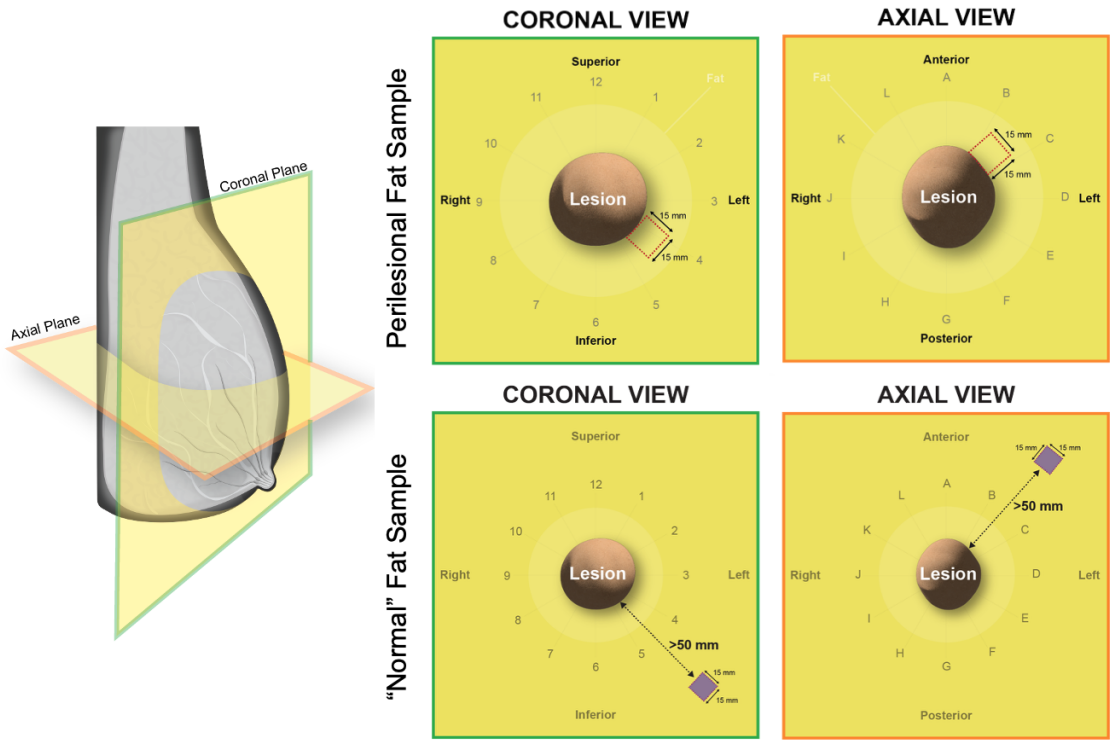


**Figure 10.1:** Illustration of the selection of a perilesional (top - yellow with red dashed outline) and a "normal" (bottom - purple with red dashed outline) breast adipose tissue sample in the IMOGEN study. Two-dimensional projections are shown to illustrate how to location of the fat sample relative to the lesion may be described. For example, the perilesional fat sample, visualised a red dashed lines, may be described as at the 4 o'clock position in the coronal view and between angles B and C in the axial view. Images by Haley Fig as part of the IMOGEN Sample Management Manual version 2.0 (Perspectum Ltd.).

density as markers of breast cancer risk, and interrogation of a range of hypotheses with these metrics, owing to the study's rich phenotypic and genetic data.

### 10.2.2 Project 2: Histological Investigation of Breast Adipose Tissue PDFF and $T_2^*$

The work of Chapters 7 and 8 indicated that PDFF may be able to reflect adipocyte hypertrophy in obese adipose tissue, and cancer-associated adipocytes in proximity to malignant lesions. However, in the absence of histological data, we cannot definitively determine the biological causes behind the results observed. This project would compare MRI metrics against matched histological images of breast adipose tissue to interrogate these hypotheses.

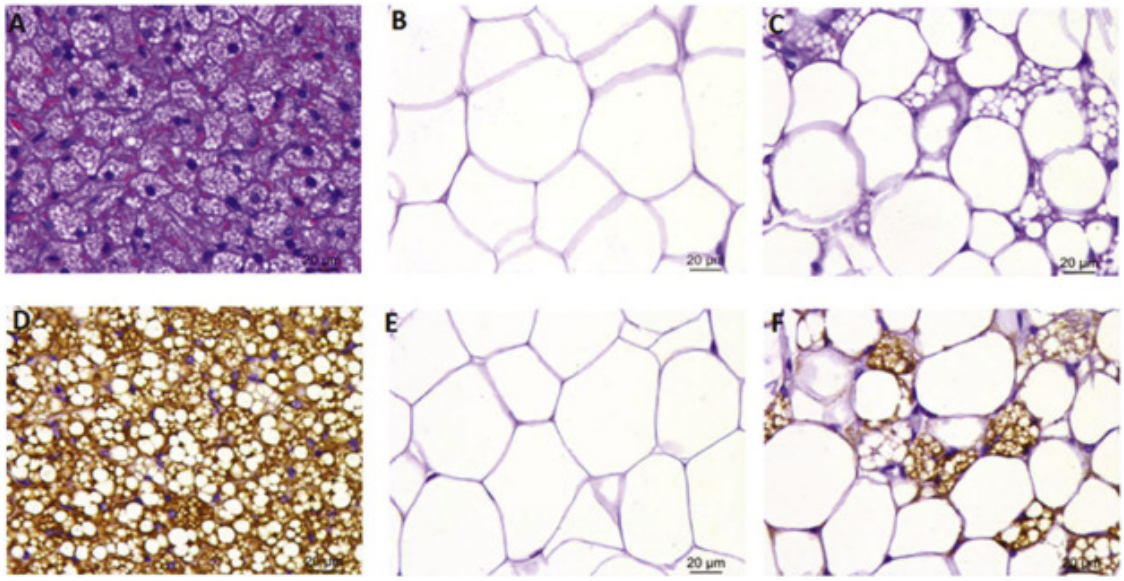


**Figure 10.2:** Histological images showing rat adipose tissue stained with H&E (A, B, C) and UCP-1 (D, E, F). Deposits of brown adipose tissue (A, D), white adipose tissue (B, E), and white adipose tissue showing brown-like features (C,F) are shown. Figure reproduced from Danysz et al. [271] with permission from Elsevier.

An amendment to the IMOGEN study (Section 2.3) was submitted in January 2024 to enable additional histological processing of the adipose tissue samples of participants scheduled to have mammary fat removed as part of their routine care. Participants' MRI scans are arranged prior to their scheduled surgical procedure, examples of which could include mastectomy, mammoplasty, and wide local excision. Where possible, perilesional and "normal" fat samples will be processed, and the location of the samples will be noted (Figure 10.1). The tissue samples will be stained with haematoxcilyn and eosin (H&E), the standard stain for visualising cell morphology, and immunohistochemistry (IHC) staining will be performed for the expression of UCP-1 (Figure 10.1). Slides will be digitised to generate whole slide images for comparison to MR biomarkers.

Significant work was carried out through the course of the DPhil to enable this project, including activation of a new clinical site and the development of a histological processing protocol. Unfortunately, at the time of writing, though MRI data are available, we have not yet received the accompanying histological data. We expect to receive this in the coming months. Upon its receipt, ground

truth measurements of adipocyte hypertrophy and peritumoural delipidation will be obtained through measurement of fat cell size on the H&E slides, and adipocyte browning will be quantified through measurement of the UCP-1 staining intensity.

We hope that these analyses will provide biological insights into the behaviour of adipose tissue PDFF and $T_2^*$, and, if positive results are obtained, provide confidence in the ability of PDFF to directly reflect adipocyte properties. Such validation could support pharmaceutical applications, wherein non-invasive assessment of adipocyte hypertrophy and CAA behaviour may be advantageous.

## 10.3 Closing Remarks

A growing body of research into self-compression mammography and abbreviated MRI indicates the field's increasing recognition of the importance of participants' comfort in breast imaging. This sentiment has been reflected by the willingness of volunteers and collaborators to engage with the research presented in this thesis; I am greatly indebted to them for their participation.

This thesis demonstrates the potential of just one non-contrast, quantitative MRI methodology to improve the risk assessment and diagnosis of breast cancer. Though contrast agent use is likely to remain a part of clinical practise for some time, I hope that this work demonstrates the added information which can be obtained through non-invasive measurement of breast tissue characteristics, and in particular indicates the utility of measuring the adipose organ. I hope that this work encourages the continued exploration of non-contrast MRI biomarkers such that, in time, we may achieve a multi-parametric MRI protocol which negates administration of contrast agent. Recent developments in deep learning suggest that this goal may be achievable sooner than anticipated [272].

I look forward to the upcoming histological investigation of the biomarkers explored in this thesis and to the advances to come in this important field.

# Appendices

# A

# MR Sequence Parameters

## Contents



The following tables show the details of the MR acquisitions employed throughout this thesis across the four different scanners.

## A.1 $T_1$-Weighted Acquisition

| MR Parameter | Siemens Aera | Siemens Avanto | Siemens Sola | GE Voyager |
|---|---|---|---|---|
| Sequence Name | t1 fl3d tra Dixon | | | Breast LAVA Flex |
| Sequence Type | 3D FLASH | | | 3D FSPGR |
| $TE_1$ (ms) | 2.39 | | | 2.08 |
| $\Delta$TE (ms) | 2.38 | 2.39 | 2.38 | 2.08 |
| TR (ms) | 6.49 | 7.28 | 6.5 | 6.00 |
| N°Echoes | 2 | | | |
| Flip Angle (°) | 10 | | | |
| Bandwidth | 870 Hz/pixel | | | 250 kHz total |
| FOV ($mm^2$) | $400 \times 400$ | | | |
| Acq Matrix Size | $274 \times 288$ | | | $288 \times 288$ |
| Acq Resolution ($mm^2$) | $1.46 \times 1.39$ | | | $1.39 \times 1.39$ |
| Rec Resolution ($mm^2$) | $1.39 \times 1.39$ | | | $0.78 \times 0.78$ |
| Rec Slice Thickness (mm) | 1.5 | | | 0.8 |
| Slice Resolution | 60% | | | N/A |
| Typical N°Acq Slices | 120 | | | |
| Typical Scan Time | 1min35s | 1min30s | 1min35s | 2min24s |

**Table A.1:** MR parameters employed in the $T_1$-weighted acquisition.

## A.2 $T_2$-Weighted Acquisition

| MR Parameter | Siemens Aera | Siemens Avanto | Siemens Sola | GE Voyager |
|---|---|---|---|---|
| Sequence Name | t2 tse tra | | | Ax T2 frFSE |
| Sequence Type | 2D FSE | | | 2D frFSE |
| TE (ms) | 67.0 | 70.0 | 67.0 | 102.0 |
| TR (ms) | 6070.0 | | | 5828.0 |
| Flip Angle (°) | 170 | | | 160 |
| Bandwidth | 228 Hz/pixel | | | 71.42 kHz total |
| FOV ($mm^2$) | 380 × 380 | | | |
| Acq Matrix Size | 448 × 336 | | | 416 × 352 |
| Acq Resolution ($mm^2$) | 0.85 × 1.13 | | | 0.91 × 1.08 |
| Rec Resolution ($mm^2$) | 0.85 × 0.85 | | | 0.74 × 0.74 |
| Slice Thickness (mm) | 4 | | | |
| Slice Gap (mm) | 1 | | | |
| Typical N°Acq Slices | 42 | | | 40 |
| Typical Scan Time | 4min10s | 4min10s | 4min10s | 4min22s |

**Table A.2:** MR parameters employed in $T_2$-weighted acquisition.

## A.3 Multi-Echo GRE Acquisition

| **MR Parameter** | **Siemens Aera** | **Siemens Avanto** | **Siemens Sola** | **GE Voyager** |
|---|---|---|---|---|
| Sequence Name | LMS IDEAL 3D | | | IDEAL IQ |
| Sequence Type | 3D GRE | | | |
| N°Echoes | 6 | | | |
| $TE_1$ (ms) | 1.81 | | | 0.92 |
| $\Delta$TE (ms) | 1.95 | | | 1.36 |
| TR (ms) | 15 | | | 9.84 |
| Flip Angle (°) | 5 | | | 6 |
| Bandwidth | 1560Hz/pixel | | 1090Hz/pixel | 222kHz Total |
| FOV ($mm^2$) | $440 \times 399$ | | | $440 \times 396$ |
| Acq Matrix Size | $128 \times 116$ | $128 \times 116$ | $128 \times 116$ | $128 \times 128$ |
| Acq Resolution ($mm^2$) | $3.44 \times 3.44$ | | | |
| Rec Resolution ($mm^2$) | $1.72 \times 1.72$ | | | |
| Slice Thickness (mm) | 2 | | | |
| Typical N°Acq Slices | 80 | | | |
| Typical Scan Time | 2min19s | 2min21s | 2min19s | 3min3s |

**Table A.3:** MR parameters employed in the multi-echo GRE acquisition.

## A.4 Diffusion-Weighted Acquisition

| MR Parameter | Siemens Aera | Siemens Sola | Siemens Avanto | GE Voyager |
|---|---|---|---|---|
| Sequence Name | RESOLVE tra SPAIR | | ep2d tra SPAIR | Ax DWI 3:1 B-0-800 |
| Sequence Type | 2D Multi-Shot RS[1] EPI | | 2D Single-Shot EPI | |
| N°b-values | 2 | | | 3 |
| B-values | 50, 800 | | | 0, 50, 800 |
| N°Echoes | 2 | | 1 | |
| $TE_1$ | 56.0 | | 76.0 | 60.2 |
| $\Delta TE$ | 21.0 | | N/A | N/A |
| TR | 8330 | | | 7570 |
| Flip Angle | 180 | | 90 | |
| Bandwidth | 920 Hz/pixel | | 1532 Hz/pixel | 500kHz Total |
| FOV | 380 × 133 | | 400 × 163 | 380 × 380 |
| Acq Matrix Size | 194 × 68 | | 192 × 78 | 194 × 194 |
| Acq Resolution | 1.96 × 1.96 | | 2.08 × 2.08 | 1.96 × 1.96 |
| Rec Resolution | 1.96 × 1.96 | | 2.08 × 2.08 | 1.48 × 1.48 |
| Slice Thickness | 3.00 | | | |
| Slice Gap | 0.75 | | | 1.00 |
| Typical N°Acq Slices | 44 | | 50 | 43 |
| Typical Scan Time | 6min40s | | 3min44s | 2min1s |

**Table A.4:** MR parameters employed in the DWI acquisition.

[1]RS = Readout-Segmented

# B

# Commercial Phantom Details

Chapter 3 details the use of several phantoms to assess the performance of the 3D GRE sequences in quantification of PDFF and $T_2^*$. We here give further details of these phantoms, which were originally commissioned for commercial purposes, and are maintained by Perspectum Ltd.

The phantoms used in Chapter 3 may be categorized into three series - hereafter described as series A, B, and C. Phantoms belonging to each series were made according to the same manufacturing specification from the same manufacturer. The exception to this is the series C phantoms, which were made to differing specifications, as each of the phantoms contain 14 vials of only one type (PDFF or $T_2^*$). The primary purpose of the phantoms is to assess the performance of the Liver*MultiScan* software [273], therefore the PDFF and $T_2^*$ values employed reflect the physiological range of these metrics within liver.

As described in Chapter 3, all phantoms consisted of individual vials housed within a flood-filled acrylic shell. $T_2^*$ vials contained agar doped with maganese chloride, whilst PDFF vials contained an emulsion of agar and peanut oil. All vials contained small amounts of sodium benzoate for preservation purposes, except for the 100% PDFF vial in phantom C-1, which contained solely peanut oil.

Phantoms in series A were manufactured by Calimetrix Ltd. (Wisconsin, United States of America). Series A phantoms contain 15 vials in total, including 5 PDFF vials, 5 $T_2^*$ vials, and 5 $T_1$ vials [1]. The water component of the PDFF vials was targeted to have a $T_1$ to mimic that of liver tissue. Measurements of

[1] $T_1$ vials are excluded from analysis in this thesis.

the water $T_1$ value by Perspectum Ltd. indicate this to be approximately 630ms at 1.5T. The PDFF vials spanned a range of 5.0% to 40% PDFF, and the $T_2^*$ vials spanned a range of 7.6ms to 27.1ms.

Phantoms in series B were manufactured by Leeds Test Objects Ltd. (York, United Kingdom). These phantoms contain 14 vials in total, including 4 PDFF vials, 5 $T_2^*$ vials, and 5 $T_1$ vials. The water component of the PDFF vials was not specified to have a set $T_1$ value; measurements performed by Perspectum show the water $T_1$ of the phantom PDFF vials measured approximately 2200ms at 1.5T. Sodium chloride was added to the vials to simulate the salinity of human tissues. The PDFF vials spanned a range of 5.0% to 35.0% and the $T_2^*$ vials spanned a range of 4.7ms to 18.9ms.

Phantoms in series C were also manufactured by Leeds Test Objects Ltd. Phantom C-1 contained 14 PDFF vials whilst phantom C-2 contained 14 $T_2^*$ vials. The PDFF ranged between 0.0% to 100.0% whilst the $T_2^*$ spanned 5.7ms to 34.5ms. As with the series B phantoms, sodium chloride was added to all vials except the 100% PDFF vial, which contained solely peanut oil. As with series B phantoms, the water component of the PDFF vials was not specified to have a set $T_1$ value; measurements by Perspectum Ltd. also indicate a water $T_1$ of approximately 2200ms at 1.5T.

# C

# Relaxivity Equations

Relaxivity is a physical property which defines how an MR relaxation time changes with the concentration of a particular species. Diamagnetic species do not contain unpaired electrons and therefore have minimal impact upon proton spin relaxation. By contrast, the concentration of paramagnetic species significantly affects MR relaxation times, as their unpaired electrons generate strong, fluctuating magnetic fields which interact with proton spins via dipolar coupling. The $T_1$ relaxivity, known as $r_1$, of a paramagnetic species is defined as

$$\frac{1}{\Delta T_1} = r_1 C \tag{C.1}$$

where C is the concentration of the species, and $\Delta T_1$ is the induced change in $T_1$. Similarly, the $T_2$ relaxivity, known as $r_2$, is defined as

$$\frac{1}{\Delta T_2} = r_2 C \tag{C.2}$$

For a material containing multiple paramagnetic species, the relaxation rate ($\frac{1}{T_1}$ or $\frac{1}{T_2}$) of the composite material is determined by the sum of the effects of each species [274], such that

$$\frac{1}{T_1} = \frac{1}{T_{1,0}} + \sum_{i}^{N} r_{1,i} C_i \tag{C.3}$$

$$\frac{1}{T_2} = \frac{1}{T_{2,0}} + \sum_{i}^{N} r_{2,i} C_i \tag{C.4}$$

where $C_i$, $r_{1,i}$, and $r_{2,i}$ denote the concentration and relaxivities of the $i$th paramagnetic species and $\frac{1}{T_{1,0}}$ and $\frac{1}{T_{2,0}}$ denote the baseline relaxation rates, which include the effect of water and any additional diamagnetic species. These equations are valid under the assumption that there is no interaction between the paramagnetic species, with each species independently interacting with the water protons.

Relaxivity equations can be used to guide phantom design by enabling calculation of the concentration of each species needed to produce a desired $T_1$ and/or $T_2$. In Chapter 6, we used phantom relaxivity equations to estimate the concentrations of nickel chloride ($NiCl_2$) and agar to be used in the fibroglandular-tissue-mimicking component of the custom breast density phantoms. In this context, the relaxation rates of the composite material is [275]

$$\frac{1}{T_1} = \frac{1}{T_{1,Water}} + r_{1,\text{Agar}} C_{\text{Agar}} + r_{1,\text{NiCl}_2} C_{\text{NiCl}_2} \tag{C.5}$$

$$\frac{1}{T_2} = \frac{1}{T_{2,Water}} + r_{2,\text{Agar}} C_{\text{Agar}} + r_{2,\text{NiCl}_2} C_{\text{NiCl}_2} \tag{C.6}$$

It should be noted that the relaxivity of a species is dependent upon field strength and temperature. Furthermore, in practise, the relaxivity of one species may be influenced by the presence of other species. For example, the relaxivity of agar is known to vary according to the concentration of nickel chloride. In our work, we used values of $r_{1,\text{Agar}}$ and $r_{2,\text{Agar}}$ which were reported at 1.5T at a concentration of 0.5mM $NiCl_2$ [276], close to the concentration of nickel chloride which was used in generation of these phantoms. We used reported relaxivity values of nickel chloride at 1.5T [276], and the known approximate $T_1$ and $T_2$ of pure water at 1.5T [277].

Due to slight differences in chemical species, the influence of other species on a species' relaxivity, and differences in determination of ground truth $T_1$ and $T_2$, phantom relaxivity equations may not always predict relaxation times exactly, even in the absence of human error during the manufacturing process. However, they provide a useful starting point from which to begin phantom design. These concentrations may then be adjusted through comparison of the theoretical $T_1$ and $T_2$ values to obtained $T_1$ and $T_2$ values to achieve the desired relaxation times. This

iterative process was performed during design of the breast density phantoms, and led to the use of a final concentration of 0.63mM nickel chloride, and 3% agar.

It should be noted that the $T_2^*$ of a substance cannot be determined through theoretical relaxivity equations as it is not an inherent property of a substance, and varies according to local field inhomogeneities. It should also be noted that the preservative sodium benzoate was used in generation of the breast density phantoms. However, this species is typically assumed to have a negligible effect on $T_1$ and $T_2$ due to it being diamagnetic and was therefore excluded from phantom relaxivity calculations.

# D

# The Lorentzian Function

The Lorentzian function characterises the profile of a single peak and is defined by the equation

$$L(x) = \frac{1}{\pi} \times \frac{\frac{\gamma}{2}}{(x - x_0)^2 + \left(\frac{\gamma}{2}\right)^2} \tag{D.1}$$

where $x_0$ is the centre position of the peak and $\gamma$ is the full width of the peak at half the peak's maximum amplitude (FWHM). The Lorentzian function is normalised such that $\int_{-\infty}^{\infty} L(x)dx = 1$. For a peak with area $A$, the Lorentzian function becomes

$$L(x) = \frac{A}{\pi} \times \frac{\frac{\gamma}{2}}{(x - x_0)^2 + \left(\frac{\gamma}{2}\right)^2} \tag{D.2}$$

or, more simply,

$$L(x) = \frac{a}{(x - b)^2 + c} \tag{D.3}$$

where $a = \frac{A\gamma}{2\pi}$, $b = x_0$, and $c = (\frac{\gamma}{2})^2$.

Lorentzian functions are commonly used to describe the shape of spectral data. To determine the relative areas of the nine fat peaks in the spectral data in Chapter 4, the data was fitted to the following model

$$y(x) = y_0 + L_1(x) + L_2(x) + ... + L_9(x) = y_0 + \sum_{n=1}^{n=9} \frac{a_n}{(x - b_n)^2 + c_n} \tag{D.4}$$

where $y_0$ reflects a constant baseline given by the minimum value of the spectral data, and $a_n$, $b_n$, and $c_n$ reflect the twenty-seven parameters allowed to vary in the fit.

# E

# The Cramér-Rao Lower Bound

In Chapter 4, we employed the parameters SD-PDFF and SD-$T_2^*$ [90, 143] to quantify the quality of CSE-MRI maps. SD-PDFF and SD-$T_2^*$ have an advantage over the traditional $R^2$ goodness-of-fit (GoF) metric in CSE-MRI due to the dependency of $R^2$ upon $T_2^*$.

SD-PDFF and SD-$T_2^*$ are derived from estimation of the Cramér-Rao Lower Bound (CRLB). Whilst the full derivation of these GoF metrics may be found in Bagur et al. [90, 143], we here provide an overview of the main principles involved in calculation of SD-PDFF and SD-$T_2^*$, with a particular focus on the CRLB.

The Cramér-Rao Lower Bound (CRLB) is a goodness-of-fit metric which provides a theoretical lower bound for the variance of an unbiased estimator. The CRLB is therefore mathematically defined as

$$\mathbf{C}_{\hat{\theta}} \geq CRLB \tag{E.1}$$

where $\mathbf{C}_{\hat{\theta}}$ denotes the co-variance matrix of the unbiased estimator $\hat{\theta}$ with model parameters $[\theta_1, \theta_2, ...\theta_N]$, such that $C_{ij}$ is the co-variance of $\theta_i$ with $\theta_j$ and $C_{ii}$ is simply the variance of $\theta_i$. The CRLB may also be considered as the highest possible precision of a measurement given the acquired data [278].

The CRLB is computed as

$$CRLB = \frac{1}{\mathbf{I}(\hat{\theta})^{-1}} \tag{E.2}$$

where $\mathbf{I}(\theta)$ denotes the Fisher Information Matrix (FIM). For Gaussian-distributed noise, the Fisher Information Matrix may be given as

$$\mathbf{I}(\hat{\theta})_{i,j} = \frac{1}{\sigma^2}\sum_{n=1}^{N}\frac{\partial s_n}{\partial \theta_i}\frac{\partial s_n}{\partial \theta_j} = \frac{1}{\sigma^2}\mathbf{J}^{\dagger}\mathbf{J} \tag{E.3}$$

where $s_n$ is the signal predicted by the signal model at the $n^{th}$ echo time, and $\sigma^2$ is the noise variance in the observed data. The Jacobian matrix is defined as

$$\mathbf{J} = \begin{bmatrix} \frac{\partial s}{\partial \theta_1} & \frac{\partial s}{\partial \theta_2} & \cdots & \frac{\partial s}{\partial \theta_K} \end{bmatrix}$$

and † denotes its Hermitian transformation.

The Jacobian matrix (and its corresponding Hermitian transformation) may be computed analytically for a given signal model. However, calculation of the FIM also requires definition of $\sigma$, which is the standard deviation of the noise in the acquired data. Whilst $\sigma$ may be defined through a theoretical SNR value, in practise, direct estimation is preferable.

In their calculation of SD-PDFF and SD-$T_2^*$ via the CRLB, Bagur et al. [90, 143] employ the Kellman method for estimation of $\sigma$ [279]. In this approach, $\sigma$ is calculated after estimation of the parameters in the signal model, and is based upon the magnitude of the residuals of the data fit, such that

$$\sigma = \frac{\text{MAD}}{0.6745} \tag{E.4}$$

where MAD is the median absolute deviation of the fitting residuals once the number of degrees of freedom in the signal model have been accounted for.

The number of degrees of freedom (denoted $p$) is dependent upon the CSE-MRI signal model used. For a magnitude-only, phase-constrained signal model, $p = 3$ ($\rho_w$, $\rho_f$, $R_2^*$). For a complex-based, phase-constrained model, $p = 5$ ($\rho_w$, $\rho_f$, $R_2^*$, $\psi$, $\phi_0$), whilst for a complex-based model not constrained by phase, $p = 6$ ($\rho_w$, $\rho_f$, $R_2^*$, $\psi$, $\phi_W$, $\phi_F$). Calculation of MAD with the Kellman estimation discards the $(p-1)$ residuals with the lowest magnitude, such that only the parameter with the greatest residual is considered.

SD-PDFF and SD-$T_2^*$ are finally computed via calculation of the CRLB with Equation E.2 using the analytically-defined measurements of the Jacobian and the Kellman estimation of $\sigma$. This calculation gives the co-variance matrix $\mathbf{C}_{\hat{\theta}}$, which includes the variance, and therefore the standard deviation, of the parameters in the signal model, including SD-Water, SD-Fat, and SD-$R_2^*$. SD-PDFF may then be defined via analytical error propagation of SD-Water and SD-Fat. As described in Section 4.2.4, for ease of comparison to the metrics employed in this thesis, we also performed analytical error propagation to determine SD-$T_2^*$ from SD-$R_2^*$.

# F

# The Mahalanobis Distance

The Mahalanobis distance is a measure of the distance between a datapoint and a distribution which is commonly used to quantify separation in a multivariate space. For a distribution with mean $\boldsymbol{\mu}$ and co-variance matrix $\mathbf{S}$, the Mahalanbois distance between a point $\boldsymbol{x}$ and the distribution is

$$D_M{}^2 = \left(\boldsymbol{x} - \boldsymbol{\mu}\right) \mathbf{S}^{-1} \left(\boldsymbol{x} - \boldsymbol{\mu}\right)^\top. \tag{F.1}$$

The Mahalanobis distance can also be used to compare the separation between two distributions. In this case, for distributions $A$ and $B$,

$$D_M{}^2 = \left(\boldsymbol{\mu}_\mathbf{A} - \boldsymbol{\mu}_\mathbf{B}\right) \mathbf{S}_{\mathbf{Pooled(A,B)}}{}^{-1} \left(\boldsymbol{\mu}_\mathbf{A} - \boldsymbol{\mu}_\mathbf{B}\right)^\top. \tag{F.2}$$

where $\mathbf{S}_{\mathbf{Pooled(A,B)}}$ is the pooled co-variance matrix of the two distributions in the multivariate space and $\boldsymbol{\mu}_\mathbf{A}$ and $\boldsymbol{\mu}_\mathbf{B}$ are the means of distributions A and B respectively.

In Chapter 8, $D_M$ is used to quantify separation in the bi-variate PDFF-$T_2^*$ space between pixels in perilesional and reference breast adipose tissue. In this case, computation of the Mahalanobis distance is preferable to simply finding the Euclidean distance ( $= \sqrt{|\left(\boldsymbol{\mu}_\mathbf{A} - \boldsymbol{\mu}_\mathbf{B}\right)\left(\boldsymbol{\mu}_\mathbf{A} - \boldsymbol{\mu}_\mathbf{B}\right)^\top|}$ ), as $D_M$ accounts for any correlation between the two metrics, and provides a unitless measurement which is invariable to scale changes, such as reporting $T_2^*$ in milliseconds versus seconds.

In this work, the Mahalanobis distance $D_M$ was defined as

$$D_M{}^2 = \left(\boldsymbol{\mu}_{\text{Peri}} - \boldsymbol{\mu}_{\text{Ref}}\right) \mathbf{S}_{\mathbf{Pooled(Peri,Ref)}}{}^{-1} \left(\boldsymbol{\mu}_{\text{Peri}} - \boldsymbol{\mu}_{\text{Ref}}\right)^{\top}. \tag{F.3}$$

where $\boldsymbol{\mu}_{\text{Peri}}$ and $\boldsymbol{\mu}_{\text{Ref}}$ are 2×1 vectors containing the mean PDFF and $T_2^*$ of the perilesional and reference adipose tissue, whilst $\mathbf{S}_{\mathbf{Pooled(Peri,Ref)}}$ is the pooled co-variance matrix between the adipose tissue depots.

# References


[1] Cancer Research UK. *Breast cancer statistics – Breast cancer incidence (invasive).* Accessed: 2026-01-22. URL: https://www.cancerresearchuk.org/health-professional/cancer-statistics/statistics-by-cancer-type/breast-cancer.

[2] Cancer Research UK. *Breast cancer statistics – Breast cancer risk.* Accessed: 2026-01-22. URL: https://www.cancerresearchuk.org/health-professional/cancer-statistics/statistics-by-cancer-type/breast-cancer.

[3] Rui Sha et al. "Global burden of breast cancer and attributable risk factors in 204 countries and territories, from 1990 to 2021: results from the Global Burden of Disease Study 2021". In: *Biomarker Research* 12.87 (Aug. 2024). DOI: 10.1186/S40364-024-00631-8.

[4] Joanne Kim et al. "Global patterns and trends in breast cancer incidence and mortality across 185 countries". In: *Nature Medicine* 31 (Feb. 2025), pp. 1154–1162. DOI: 10.1038/S41591-025-03502-3.

[5] Lindsey A. Torre et al. "Global cancer in women: Burden and trends". In: *Cancer Epidemiology, Biomarkers & Prevention* 26.4 (Apr. 2017), pp. 444–457. DOI: 10.1158/1055-9965.EPI-16-0858.

[6] Marta Bonotto et al. "Measures of Outcome in Metastatic Breast Cancer: Insights From a Real-World Scenario". In: *The Oncologist* 19.6 (May 2014), pp. 608–615. DOI: 10.1634/THEONCOLOGIST.2014-0002.

[7] Nathalie J. Massat et al. "Impact of Screening on Breast Cancer Mortality: The UK Program 20 Years On". In: *Cancer Epidemiology, Biomarkers & Prevention* 25 (Mar. 2016), pp. 455–462. DOI: 10.1158/1055-9965.EPI-15-0803.

[8] Thomas M. Kolb, Jacob Lichy, and Jeffrey H. Newhouse. "Comparison of the Performance of Screening Mammography, Physical Examination, and Breast US and Evaluation of Factors that Influence Them: An Analysis of 27,825 Patient Evaluations". In: *Radiology* 225.1 (Oct. 2002), pp. 165–175. DOI: 10.1148/RADIOL.2251011667.

[9] Elsebeth Lynge et al. "Breast density and risk of breast cancer". In: *International Journal of Cancer* 152.6 (Mar. 2023), pp. 1150–1158. DOI: 10.1002/ijc.34316.

[10] Brian L. Sprague et al. "Variation in Mammographic Breast Density Assessments Among Radiologists in Clinical Practice: A Multicenter Observational Study". In: *Annals of Internal Medicine* 165.7 (July 2016), pp. 457–464. DOI: 10.7326/M15-2934.

[11] Bang J. Guo, Zhen L. Yang, and Long J. Zhang. "Gadolinium Deposition in Brain: Current Scientific Evidence and Future Perspectives". In: *Frontiers in Molecular Neuroscience* 11.335 (Sept. 2018). DOI: 10.3389/fnmol.2018.00335.

[12] S. Mussurakis et al. "Observer variability in the interpretation of contrast enhanced MRI of the breast". In: *British Journal of Radiology* 69.827 (Nov. 1996), pp. 1009–1016. DOI: 10.1259/0007-1285-69-827-1009.

[13] Nicole D. Agaronnik, Areej El-Jawahri, and Lisa I. Iezzoni. "Implications of Physical Access Barriers for Breast Cancer Diagnosis and Treatment in Women With Mobility Disability". In: *Journal of Disability Policy Studies* 33.1 (May 2021), pp. 46–54. DOI: 10.1177/10442073211010124.

[14] Gajanan A. Rodge et al. "Quantification of Liver Fat by MRI-PDFF Imaging in Patients with Suspected Non-alcoholic Fatty Liver Disease and Its Correlation with Metabolic Syndrome, Liver Function Test and Ultrasonography". In: *Journal of Clinical and Experimental Hepatology* 11.5 (Sept. 2021), pp. 586–591. DOI: 10.1016/j.jceh.2020.11.004.

[15] Alexandre Triay Bagur et al. "Magnitude-intrinsic water–fat ambiguity can be resolved with multipeak fat modeling and a multipoint search method". In: *Magnetic Resonance in Medicine* 82.1 (July 2019), pp. 460–475. DOI: 10.1002/mrm.27728.

[16] Jane S. Hankins et al. "R2* magnetic resonance imaging of the liver in patients with iron overload". In: *Blood* 113.20 (May 2009), pp. 4853–4855. DOI: 10.1182/BLOOD-2008-12-191643.

[17] Ryan Kolb and Weizhou Zhang. "Obesity and Breast Cancer: A Case of Inflamed Adipose Tissue". In: *Cancers* 12.6, 1686 (June 2020). DOI: 10.3390/CANCERS12061686.

[18] Fengliang Wang et al. "Mammary Fat of Breast Cancer: Gene Expression Profiling and Functional Characterization". In: *PloS One* 9.10, e109742 (Oct. 2014). DOI: 10.1371/JOURNAL.PONE.0109742.

[19] Andrew Kowalski and Eloka Okoye. "Breast Cyst". In: *StatPearls Publishing* (Sept. 2023). Accessed: 2025-01-25. URL: https://www.ncbi.nlm.nih.gov/books/NBK562196/.

[20] Sandeep Reddy Ramala et al. "A Comprehensive Review of Breast Fibroadenoma: Correlating Clinical and Pathological Findings". In: *Cureus* 15.12 (Dec. 2023), e49948. DOI: 10.7759/CUREUS.49948.

[21] American Cancer Society. *Types of Breast Cancer*. Accessed: 2026-01-22. Nov. 2021. URL: https://www.cancer.org/cancer/types/breast-cancer/about/types-of-breast-cancer.

[22] Karla Kerlikowske. "Epidemiology of Ductal Carcinoma In Situ". In: *Journal of the National Cancer Institute Monographs* 2010.41 (Oct. 2010), pp. 139–141. DOI: 10.1093/JNCIMONOGRAPHS/LGQ027.

[23] Cancer Research UK. *Hormone therapy for breast cancer*. Accessed: 2026-01-20. July 2023. URL: https://www.cancerresearchuk.org/about-cancer/breast-cancer/treatment/hormone-therapy.

[24] Franco Lumachi, Davide A Santeufemia, and Stefano MM Basso. "Current medical treatment of estrogen receptor-positive breast cancer". In: *World Journal of Biological Chemistry* 6.3 (Aug. 2015), pp. 231–239. DOI: 10.4331/wjbc.v6.i3.231.

[25] Margot P. Cleary and Michael E. Grossmann. "Obesity and Breast Cancer: The Estrogen Connection". In: *Endocrinology* 150.6 (June 2009), pp. 2537–2542. DOI: 10.1210/en.2009-0070.

[26] Neil M. Iyengar, Clifford A. Hudis, and Andrew J. Dannenberg. "Obesity and Cancer: Local and Systemic Mechanisms". In: *Annual Review of Medicine* 66 (Jan. 2015), pp. 297–309. DOI: 10.1146/annurev-med-050913-022228.

[27] Shuwen Dong et al. "Metabolic Syndrome and Breast Cancer: Prevalence, Treatment Response, and Prognosis". In: *Frontiers in Oncology* 11, 629666 (Mar. 2021). DOI: 10.3389/fonc.2021.629666.

[28] Burhan Wani et al. "Metabolic syndrome and breast cancer risk". In: *Indian Journal of Medical and Paediatric Oncology* 38.4 (Oct. 2017), pp. 434–439. DOI: 10.4103/ijmpo.ijmpo_168_16.

[29] Gordon P. Watt et al. "Association of breast cancer with MRI background parenchymal enhancement: the IMAGINE case-control study". In: *Breast Cancer Research* 22, 138 (Dec. 2020). DOI: 10.1186/s13058-020-01375-7.

[30] C. J. D'Orsi et al. *ACR BI-RADS® Atlas, Breast Imaging Reporting and Data System.* 2013.

[31] Jose D. Cardona Ortegón et al. "Exploring Dense Breast Density in Mammography: A Comparative Analysis of Breast Cancer Risk". In: *Cureus* 16.11, e74026 (Nov. 2024). DOI: 10.7759/cureus.74026.

[32] Creative Commons. *Deed - Attribution 4.0 International (CC BY 4.0).* URL: https://creativecommons.org/licenses/by/4.0/.

[33] Norman F. Boyd et al. "Breast Tissue Composition and Susceptibility to Breast Cancer". In: *Journal of the National Cancer Institute* 102.16 (Aug. 2010), pp. 1224–1237. DOI: 10.1093/jnci/djq239.

[34] Norman Boyd et al. "The origins of breast cancer associated with mammographic density: A testable biological hypothesis". In: *Breast Cancer Research* 20, 17 (Mar. 2018). DOI: 10.1186/s13058-018-0941-y.

[35] M. C. Pike et al. "'Hormonal' risk factors, 'breast tissue age' and the age-incidence of breast cancer". In: *Nature* 303.5920 (June 1983), pp. 767–770.

[36] O. M. Ginsburg, L. J. Martin, and N. F. Boyd. "Mammographic density, lobular involution, and risk of breast cancer". In: *British Journal of Cancer* 99 (Sept. 2008), pp. 1369–1374. DOI: 10.1038/sj.bjc.6604635.

[37] Jonathan Tyrer, Stephen W. Duffy, and Jack Cuzick. "A breast cancer prediction model incorporating familial and personal risk factors". In: *Statistics in Medicine* 23.1 (Apr. 2004), pp. 1111–1130. DOI: 10.1002/sim.1668.

[38] *Tyrer-Cuzick Risk Calculator for Breast Cancer Risk Assessment | MagView.* Accessed: 2025-01-29. URL: https://ibis-risk-calculator.magview.com/.

[39] Adam R. Brentnall et al. "Long-term Accuracy of Breast Cancer Risk Assessment Combining Classic Risk Factors and Breast Density". In: *JAMA Oncology* 4.9 (Sept. 2018), e180174. DOI: 10.1001/JAMAONCOL.2018.0174.

[40] Volpara Health. *TruDensity – Volpara Health.* URL: https://www.volparahealth.com/science/algorithms/density.

[41] Ryan Kolb, Fayyaz S. Sutterwala, and Weizhou Zhang. "Obesity and cancer: inflammation bridges the two". In: *Current Opinion in Pharmacology* 29 (Aug. 2016), pp. 77–89. DOI: 10.1016/J.COPH.2016.07.005.

[42] Gillian K. Reeves et al. "Cancer incidence and mortality in relation to body mass index in the Million Women Study: cohort study". In: *BMJ* 335, 1134 (Nov. 2007). DOI: 10.1136/BMJ.39367.495995.AE.

[43] Peiting Li et al. "Association between metabolic syndrome and prognosis of breast cancer: A meta-analysis of follow-up studies". In: *Diabetology & Metabolic Syndrome* 12, 10 (Jan. 2020). DOI: 10.1186/s13098-019-0514-y.

[44] Avital Horwitz and Ruth Birk. "Adipose Tissue Hyperplasia and Hypertrophy in Common and Syndromic Obesity—The Case of BBS Obesity". In: *Nutrients* 15.15, 3445 (Aug. 2023). DOI: 10.3390/NU15153445.

[45] M. Dobbins, K. Decorby, and B. C. K. Choi. "The Association between Obesity and Cancer Risk: A Meta-Analysis of Observational Studies from 1985 to 2011". In: *International Scholarly Research Notices* 2013, 680536 (Apr. 2013). DOI: 10.5402/2013/680536.

[46] Mark F. Munsell et al. "Body Mass Index and Breast Cancer Risk According to Postmenopausal Estrogen-Progestin Use and Hormone Receptor Status". In: *Epidemiologic Reviews* 36.1 (Jan. 2014), pp. 114–136. DOI: 10.1093/EPIREV/MXT010.

[47] Daniela Laudisio et al. "Obesity and breast cancer in premenopausal women: Current evidence and future perspectives". In: *European journal of obstetrics, gynecology, and reproductive biology* 230 (Nov. 2018), pp. 217–221. DOI: 10.1016/J.EJOGRB.2018.03.050.

[48] Sebastiano Andò et al. "Obesity, Leptin and Breast Cancer: Epidemiological Evidence and Proposed Mechanisms". In: *Cancers* 11.1 (Jan. 2019). DOI: 10.3390/CANCERS11010062.

[49] Reena S. Cecchini et al. "Body Mass Index and the Risk for Developing Invasive Breast Cancer Among High-Risk Women in NSABP P-1 and STAR Breast Cancer Prevention Trials". In: *Cancer Prevention Research* 5.4 (Apr. 2012), pp. 583–592. DOI: 10.1158/1940-6207.CAPR-11-0482.

[50] Petra H. Lahmann et al. "Body size and breast cancer risk: findings from the European Prospective Investigation into Cancer And Nutrition (EPIC)". In: *International Journal of Cancer* 111.5 (Sept. 2004), pp. 762–771. DOI: 10.1002/IJC.20315.

[51] Piet A. van den Brandt et al. "Pooled analysis of prospective cohort studies on height, weight, and breast cancer risk". In: *American Journal of Epidemiology* 152.6 (Sept. 2000), pp. 514–527. DOI: 10.1093/AJE/152.6.514.

[52] Laura García-Estévez et al. "Obesity and Breast Cancer: A Paradoxical and Controversial Relationship Influenced by Menopausal Status". In: *Frontiers in Oncology* 11, 705911 (Aug. 2021). DOI: 10.3389/FONC.2021.705911.

[53] Mitch Dowsett and Elizabeth Folkerd. "Reduced progesterone levels explain the reduced risk of breast cancer in obese premenopausal women: a new hypothesis". In: *Breast Cancer Research and Treatment* 149 (Jan. 2015), pp. 1–4. DOI: 10.1007/s10549-014-3211-4.

[54] Rehana Qureshi et al. "The Major Pre- and Postmenopausal Estrogens Play Opposing Roles in Obesity-Driven Mammary Inflammation and Breast Cancer Development". In: *Cell Metabolism* 31.6 (June 2020), pp. 1154–1172. DOI: 10.1016/J.CMET.2020.05.008.

[55] D. S. M. Chan et al. "Body mass index and survival in women with breast cancer – systematic literature review and meta-analysis of 82 follow-up studies". In: *Annals of Oncology* 25.10 (Oct. 2014), pp. 1901–1914. DOI: 10.1093/ANNONC/MDU042.

[56] Marianne Ewertz et al. "Effect of Obesity on Prognosis After Early-Stage Breast Cancer". In: *Journal of Clinical Oncology* 29.1 (Jan. 2011), pp. 25–31. DOI: 10.1200/JCO.2010.29.7614.

[57] Nathalie Druesne-Pecollo et al. "Excess body weight and second primary cancer risk after breast cancer: A systematic review and meta-analysis of prospective studies". In: *Breast Cancer Research and Treatment* 135 (Oct. 2012), pp. 647–654. DOI: 10.1007/s10549-012-2187-1.

[58] Béatrice Dirat et al. "Cancer-Associated Adipocytes Exhibit an Activated Phenotype and Contribute to Breast Cancer Invasion". In: *Cancer Research* 71.7 (Apr. 2011), pp. 2455–2465. DOI: 10.1158/0008-5472.CAN-10-3323.

[59] Charu Kothari, Caroline Diorio, and Francine Durocher. "The Importance of Breast Adipose Tissue in Breast Cancer". In: *International Journal of Molecular Sciences* 21.16, 5760 (Aug. 2020). DOI: 10.3390/ijms21165760.

[60] Priscila Pagnotta et al. "Peritumoral adipose tissue promotes lipolysis and white adipocytes browning by paracrine action". In: *Frontiers in Endocrinology* 14, 1144016 (Apr. 2023). DOI: 10.3389/fendo.2023.1144016.

[61] Neil M. Iyengar et al. "Obesity and Cancer Mechanisms: Tumor Microenvironment and Inflammation". In: *Journal of Clinical Oncology* 34.35 (Nov. 2016), pp. 4270–4276. DOI: 10.1200/JCO.2016.67.4283.

[62] Sila Ulus et al. "A New Technical Mode in Mammography: Self-Compression Improves Satisfaction". In: *European Journal of Breast Health* 15.4 (Oct. 2019), pp. 207–212. DOI: 10.5152/EJBH.2019.4480.

[63] Anna Pawłowska et al. "Curated benchmark dataset for ultrasound based breast lesion analysis". In: *Scientific Data* 11, 148 (Jan. 2024). DOI: 10.1038/S41597-024-02984-Z.

[64] Christiane K. Kuhl et al. "Supplemental Breast MR Imaging Screening of Women with Average Risk of Breast Cancer". In: *Radiology* 283.2 (May 2017), pp. 361–370. DOI: 10.1148/RADIOL.2016161444.

[65] Francesco Sardanelli et al. "The paradox of MRI for breast cancer screening: high-risk and dense breasts – available evidence and current practice". In: *Insights into Imaging* 15, 96 (Mar. 2024). DOI: 10.1186/s13244-024-01653-4.

[66] Marije F. Bakker et al. "Supplemental MRI Screening for Women with Extremely Dense Breast Tissue". In: *New England Journal of Medicine* 381.22 (Nov. 2019), pp. 2091–2102. DOI: 10.1056/nejmoa1903986.

[67] Pascal A. T. Baltzer and Francesco Sardanelli. "The Mantra about Low Specificity of Breast MRI". In: *Breast MRI for High-risk Screening*. Ed. by Francesco Sardanelli and Franca Podo. Springer Cham, Oct. 2020, pp. 11–21. DOI: 10.1007/978-3-030-41207-4_2.

[68] S. Vinnicombe et al. "Introduction of an abbreviated breast MRI service in the UK as part of the BRAID trial: practicalities, challenges, and future directions". In: *Clinical Radiology* 76.6 (June 2021), pp. 427–433. DOI: 10.1016/j.crad.2021.01.020.

[69] OECD. *Magnetic resonance imaging (MRI) units*. Accessed 2026-01-21. URL: https://www.oecd.org/en/data/indicators/magnetic-resonance-imaging-mri-units.

[70] Clemens G. Kaiser et al. "Cost-effectiveness of MR-mammography vs. conventional mammography in screening patients at intermediate risk of breast cancer - A model-based economic evaluation". In: *European Journal of Radiology* 136, 109355 (Mar. 2021). DOI: 10.1016/j.ejrad.2020.109355.

[71] Stefanie G. A. Veenhuizen et al. "Re-attendance in supplemental breast MRI screening rounds of the DENSE trial for women with extremely dense breasts". In: *European Radiology* 34 (Oct. 2024), pp. 6334–6347. DOI: 10.1007/s00330-024-10685-9.

[72] Robert W. Brown et al. *Magnetic resonance imaging: physical principles and sequence design*. eng. Second edition. John Wiley & Sons, Incorporated, 2014. DOI: 0.1002/9781118633953.

[73] Donald W. McRobbie et al. *MRI from Picture to Proton*. eng. Third edition. Cambridge University Press, 2017. DOI: 10.1017/9781107706958.

[74] Matt A. Bernstein, Kevin Franklin. King, and Xiaohong Joe. Zhou. *Handbook of MRI pulse sequences*. eng. First edition. Academic Press, 2004.

[75] Adnan Trakic. "Numerical modelling of the electromagnetic field – material interactions in magnetic resonance imaging". PhD thesis. University of Queensland, 2007. DOI: 10.14264/158585.

[76] Darryl McClymont. "Computer assisted detection and characterisation of breast cancer in MRI". PhD thesis. University of Queensland, 2015. DOI: 10.14264/uql.2015.459.

[77] Jo Schlemper et al. "A Deep Cascade of Convolutional Neural Networks for MR Image Reconstruction". In: *IEEE Transactions on Medical Imaging* 37.2 (Feb. 2018), pp. 491–503. DOI: 10.1109/TMI.2017.2760978.

[78] Leon Kaufman et al. "Measuring Signal-to-Noise Ratios In MR Imaging". In: *Radiology* 173.1 (Oct. 1989), pp. 265–267. DOI: 10.1148/radiology.173.1.2781018.

[79] Marijke Welvaert and Yves Rosseel. "On the definition of signal-to-noise ratio and contrast-to-noise ratio for fMRI data". In: *PLoS ONE* 8.11, e77089 (Nov. 2013). DOI: 10.1371/journal.pone.0077089.

[80] E. A. Morris, C. E. Comstock, and C. H. Lee et al. *ACR BI-RADS® Magnetic Resonance Imaging. In: ACR BI-RADS® Atlas, Breast Imaging Reporting and Data System*. 2013.

[81] Harrison Kim. "Variability in Quantitative DCE-MRI: Sources and Solutions". In: *Journal of Nature and Science* 4.1 (2018), e484.

[82] Christiane Katharina Kuhl et al. "Dynamic Breast MR Imaging: Are Signal Intensity Time Course Data Useful for Differential Diagnosis of Enhancing Lesions?" In: *Radiology* 211.1 (Apr. 1999), pp. 101–110. DOI: 10.1148/RADIOLOGY.211.1.R99AP38101.

[83] Sibel Kul et al. "Contribution of Diffusion-Weighted Imaging to Dynamic Contrast-Enhanced MRI in the Characterization of Breast Tumors". In: *American Journal of Roentgenology* 196.1 (Jan. 2011), pp. 210–217. DOI: 10.2214/AJR.10.4258.

[84] Li Zhang et al. "Accuracy of Combined Dynamic Contrast-Enhanced Magnetic Resonance Imaging and Diffusion-Weighted Imaging for Breast Cancer Detection: A Meta-Analysis". In: *Acta Radiologica* 57.6 (Aug. 2015), pp. 651–660. DOI: 10.1177/0284185115597265.

[85] Alexey Surov, Hans Jonas Meyer, and Andreas Wienke. "Can apparent diffusion coefficient (ADC) distinguish breast cancer from benign breast findings? A meta-analysis based on 13 847 lesions". In: *BMC Cancer* 19, 955 (Oct. 2019). DOI: 10.1186/s12885-019-6201-4.

[86] Wen Jie Tang et al. "Abbreviated Versus Full-Protocol MRI for Breast Cancer Neoadjuvant Chemotherapy Response Assessment: Diagnostic Performance by General and Breast Radiologists". In: *AJR. American journal of roentgenology* 220.6 (Feb. 2023), pp. 817–825. DOI: 10.2214/AJR.22.28686.

[87] María Liliana Hernández et al. "Abbreviated magnetic resonance imaging in breast cancer: A systematic review of literature". In: *European Journal of Radiology Open* 8, 100307 (Dec. 2020). DOI: 10.1016/J.EJRO.2020.100307.

[88] North Bristol NHS Trust. *FAST MRI Research Programme*. URL: https://www.nbt.nhs.uk/FASTMRI.

[89] Cyrielle Caussy et al. "Noninvasive, Quantitative Assessment of Liver Fat by MRI-PDFF as an Endpoint in NASH Trials". In: *Hepatology* 68.2 (Aug. 2018), pp. 763–772. DOI: 10.1002/hep.29797.

[90] Alexandre Triay Bagur. "Augmented Mapping and Analysis of Pancreatic Fat by Quantitative MRI". PhD thesis. University of Oxford, 2022. DOI: 10.5287/ora-nyvjrgxnn.

[91] Thomas Baum et al. "Assessment of whole spine vertebral bone marrow fat using chemical shift-encoding based water-fat MRI". In: *Journal of Magnetic Resonance Imaging* 42.4 (Feb. 2015), pp. 1018–1023. DOI: 10.1002/jmri.24854.

[92] Tong-yu Wang et al. "Proton density fat fraction measurements of rotator cuff muscles: Accuracy, repeatability, and reproducibility across readers and scanners". In: *Magnetic Resonance Imaging* 92 (Oct. 2022), pp. 260–267. DOI: 10.1016/J.MRI.2022.05.013.

[93] Andrea Dennis et al. "A composite biomarker using multiparametric magnetic resonance imaging and blood analytes accurately identifies patients with non-alcoholic steatohepatitis and significant fibrosis". In: *Nature Scientific Reports* 10, 15308 (Sept. 2020). DOI: 10.1038/s41598-020-71995-8.

[94] John C. Wood et al. "MRI R2 and R2* mapping accurately estimates hepatic iron concentration in transfusion-dependent thalassemia and sickle cell disease patients". In: *Blood* 106.4 (Aug. 2005), pp. 1460–1465. DOI: 10.1182/BLOOD-2004-10-3982.

[95] Elisabeth Pickles. "Applying Quantitative Imaging to Liver Cancer". PhD thesis. University of Oxford, 2022. DOI: 10.5287/ora-1a11bzkrz.

[96] M. J. Silvennoinen et al. "Comparison of the dependence of blood $R_2$ and $R_2^*$ on oxygen saturation at 1.5 and 4.7 Tesla". In: *Magnetic Resonance in Medicine* 49.1 (Jan. 2003), pp. 47–60. DOI: 10.1002/mrm.10355.

[97] Mirinae Seo et al. "Estimation of T2* Relaxation Time of Breast Cancer: Correlation with Clinical, Imaging and Pathological Features". In: *Korean Journal of Radiology* 18.1 (Feb. 2017), pp. 238–248. DOI: 10.3348/KJR.2017.18.1.238.

[98] Sonia P. Li et al. "Primary human breast adenocarcinoma: Imaging and histologic correlates of intrinsic susceptibility-weighted MR imaging before and during chemotherapy". In: *Radiology* 257.3 (Dec. 2010), pp. 643–652. DOI: 10.1148/radiol.10100421.

[99] Evanthia Kousi et al. "Pre-treatment functional MRI of breast cancer: T2* evaluation at 3T and relationship to dynamic contrast-enhanced and diffusion-weighted imaging". In: *Magnetic Resonance Imaging* 52 (Oct. 2018), pp. 53–61. DOI: 10.1016/j.mri.2018.05.014.

[100] NHS Health Research Authority. *IMOGEN*. Accessed: 2025-01-29. URL: https://www.hra.nhs.uk/planning-and-improving-research/application-summaries/research-summaries/imogen/.

[101] NHS Health Research Authority. *RADIUS*. Accessed: 2025-01-29. URL: https://www.hra.nhs.uk/planning-and-improving-research/application-summaries/research-summaries/radius/.

[102] Siemens. *MRI Acronyms Cross-Vendor Comparison*. Accessed: 2025-01-29. URL: www.usa.siemens.com/healthcare.

[103] Pascal Baltzer et al. "Diffusion-weighted imaging of the breast—a consensus and mission statement from the EUSOBI International Breast Diffusion-Weighted Imaging working group". In: *European Radiology* 30.3 (Mar. 2020), pp. 1436–1450. DOI: 10.1007/s00330-019-06510-3.

[104] W. T. Dixon. "Simple Proton Spectroscopic Imaging". In: *Radiology* 153.1 (1984), pp. 189–194. DOI: 10.1148/radiology.153.1.6089263.

[105] P. Clauser et al. "Fat saturation in dynamic breast MRI at 3 Tesla: Is the Dixon technique superior to spectral fat saturation? A visual grading characteristics study". In: *European Radiology* 24 (May 2014), pp. 2213–2219. DOI: 10.1007/s00330-014-3189-7.

[106] Huong Le-Petross et al. "Fast three-dimensional dual echo Dixon technique improves fat suppression in breast MRI". In: *Journal of Magnetic Resonance Imaging* 31.4 (Apr. 2010), pp. 889–894. DOI: 10.1002/JMRI.22067.

[107] Georg J. Wengert et al. "Influence of fat-water separation and spatial resolution on automated volumetric MRI measurements of fibroglandular breast tissue". In: *NMR in Biomedicine* 29.6 (June 2016), pp. 702–708. DOI: 10.1002/NBM.3516.

[108] Araminta E.W. Ledger et al. “Comparison of dixon sequences for estimation of percent breast fibroglandular tissue”. In: *PLoS ONE* 11.3, e0152152 (Mar. 2016). DOI: 10.1371/journal.pone.0152152.

[109] Scott B. Reeder et al. “Multicoil Dixon Chemical Species Separation with an Iterative Least-Squares Estimation Method”. In: *Magnetic Resonance in Medicine* 51.1 (2004), pp. 35–45. DOI: 10.1002/mrm.10675.

[110] Isobel Gordon et al. “Proton Density Fat Fraction of Breast Adipose Tissue: Comparison of the Effect of Fat Spectra and Initial Evaluation as a Biomarker”. In: *Medical Image Understanding and Analysis. Lecture Notes in Computer Science*. Vol. 13413. Springer, July 2022, pp. 28–45. DOI: 10.1007/978-3-031-12053-4_3.

[111] Chia-Ying Liu et al. “Fat quantification with IDEAL gradient echo imaging: Correction of bias from $T_1$ and noise”. In: *Magnetic Resonance in Medicine* 58.2 (Aug. 2007), pp. 354–364. DOI: 10.1002/mrm.21301.

[112] Xiaoke Wang et al. “$T_1$-corrected quantitative chemical shift-encoded MRI”. In: *Magnetic Resonance in Medicine* 83.6 (June 2020), pp. 2051–2063. DOI: 10.1002/mrm.28062.

[113] Jung Kyu Ryu et al. “Estimation of T2* Relaxation Times for the Glandular Tissue and Fat of Breast at 3T MRI System”. In: *Journal of the Korean Society of Magnetic Resonance in Medicine* 18.1 (Mar. 2014), pp. 1–6. DOI: 10.13104/jksmrm.2014.18.1.1.

[114] Houchun Harry Hu et al. “ISMRM workshop on fat-water separation: Insights, applications and progress in MRI”. In: *Magnetic Resonance in Medicine* 68.2 (Aug. 2012), pp. 378–388. DOI: 10.1002/MRM.24369.

[115] Gavin Hamilton et al. “In vivo triglyceride composition of abdominal adipose tissue measured by $^1$H MRS at 3T”. In: *Journal of Magnetic Resonance Imaging* 45.5 (May 2017), pp. 1455–1463. DOI: 10.1002/jmri.25453.

[116] Rebecca Rakow-Penner et al. “Relaxation times of breast tissue at 1.5T and 3T measured using IDEAL”. In: *Journal of Magnetic Resonance Imaging* 23.1 (Jan. 2006), pp. 87–91. DOI: 10.1002/jmri.20469.

[117] Cayden Beyer et al. “Quantitative MRI for Monitoring Metabolic Dysfunction-Associated Steatotic Liver Disease: A Test–Retest Repeatability Study”. In: *Journal of Magnetic Resonance Imaging* 61.4 (Apr. 2025), pp. 1947–1955. DOI: 10.1002/jmri.29610.

[118] Diego Hernando et al. “On the confounding effect of temperature on chemical shift-encoded fat quantification”. In: *Magnetic Resonance in Medicine* 72.2 (Aug. 2014), pp. 464–470. DOI: 10.1002/mrm.24951.

[119] Diego Hernando et al. “Multisite, multivendor validation of the accuracy and reproducibility of proton-density fat-fraction quantification at 1.5T and 3T using a fat–water phantom”. In: *Magnetic Resonance in Medicine* 77.4 (Apr. 2017), pp. 1516–1524. DOI: 10.1002/mrm.26228.

[120] Nathan T. Roberts et al. “Noise properties of proton density fat fraction estimated using chemical shift–encoded MRI”. In: *Magnetic Resonance in Medicine* 80.2 (Aug. 2018), pp. 685–695. DOI: 10.1002/mrm.27065.

[121] Gary H. Glover and Norbert J. Pelc. *Method for Correcting Image Distortion due to Gradient Nonuniformity*. US Patent 4591789, Assignee: General Electric. May 1986.

[122] Adam Kerr. *Updated Anatomical T1 Data on Flywheel | Center for Cognitive and Neurobiological Imaging*. June 2022. URL: https://cni.su.domains/updated-anatomical-t1-data-on-flywheel/.

[123] Davide Giavarina. "Understanding Bland Altman analysis". In: *Biochemia Medica* 25.2 (2015), pp. 141–151. DOI: 10.11613/BM.2015.015.

[124] Mark Bydder et al. "Relaxation Effects in the Quantification of Fat using Gradient Echo Imaging". In: *Magnetic Resonance Imaging* 26.3 (Apr. 2008), pp. 347–359. DOI: 10.1016/j.mri.2007.08.012.

[125] Scott B. Reeder and Claude B. Sirlin. "Quantification of Liver Fat with Magnetic Resonance Imaging". In: *Magnetic Resonance Imaging Clinics of North America* 18.3 (Aug. 2010), pp. 337–357. DOI: 10.1016/J.MRIC.2010.08.013.

[126] Scott B. Reeder, Houchun H. Hu, and Claude B. Sirlin. "Proton Density Fat-Fraction: A Standardized MR-Based Biomarker of Tissue Fat Concentration". In: *Journal of Magnetic Resonance Imaging* 36.5 (Nov. 2012), p. 1011. DOI: 10.1002/JMRI.23741.

[127] Leah C. Henze Bancroft et al. "Proton density water fraction as a reproducible MR-based measurement of breast density". In: *Magnetic Resonance in Medicine* 87.4 (Apr. 2022), pp. 1742–1757. DOI: 10.1002/mrm.29076.

[128] Houchun H. Hu, Henry Szu Meng Chen, and Diego Hernando. "Linearity and bias of proton density fat fraction across the full dynamic range of 0–100%: a multiplatform, multivendor phantom study using 1.5T and 3T MRI at two sites". In: *Magnetic Resonance Materials in Physics, Biology and Medicine* 37 (Feb. 2024), pp. 551–563. DOI: 10.1007/s10334-024-01148-9.

[129] Sarah Eskreis-Winkler et al. "IDEAL-IQ in an oncologic population: meeting the challenge of concomitant liver fat and liver iron". In: *Cancer Imaging* 18, 51 (Dec. 2018). DOI: 10.1186/S40644-018-0167-3.

[130] Xiaoke Wang, Diego Hernando, and Scott B. Reeder. "Sensitivity of Chemical Shift-Encoded Fat Quantification to Calibration of Fat MR Spectrum". In: *Magnetic Resonance in Medicine* 75.2 (Feb. 2016), p. 845. DOI: 10.1002/MRM.25681.

[131] Jens Peter Kühn et al. "Effect of multipeak spectral modeling of fat for liver iron and fat quantification: Correlation of biopsy with MR imaging results". In: *Radiology* 265.1 (Oct. 2012), pp. 133–142. DOI: 10.1148/radiol.12112520.

[132] Cheng William Hong et al. "MRI proton density fat fraction is robust across the biologically plausible range of triglyceride spectra in adults with nonalcoholic steatohepatitis". In: *Journal of magnetic resonance imaging* 47.4 (Apr. 2018), pp. 995–1002. DOI: 10.1002/JMRI.25845.

[133] Gavin Hamilton et al. "Dependence of liver R2* on the fat spectral model." In: *Proceedings of the International Soceity for Magnetic Resonance in Medicine* 30, 0600 (Apr. 2022). DOI: 10.58530/2022/0600.

[134] Pierre Daudé et al. "Comparative review of algorithms and methods for chemical-shift-encoded quantitative fat-water imaging". In: *Magnetic Resonance in Medicine* 91.2 (Feb. 2024), pp. 741–759. DOI: 10.1002/mrm.29860.

[135] G. T. Malcolm et al. "Fatty acid composition of adipose tissue in humans: differences between subcutaneous sites". In: *The American Journal of Clinical Nutrition* 50 (Aug. 1989), pp. 288–291. DOI: 10.1093/AJCN/50.2.288.

[136] J. L. Calvo-Gallego et al. "Comparison of the viscoelastic properties of human abdominal and breast adipose tissue and its incidence on breast reconstruction surgery. A pilot study". In: *Clinical Biomechanics* 71 (Jan. 2020), pp. 37–44. DOI: 10.1016/J.CLINBIOMECH.2019.10.009.

[137] Véronique Chajes et al. "Fatty-acid composition of breast and iliac adipose tissue in breast-cancer patients". In: *International Journal of Cancer* 50.3 (Feb. 1992), pp. 405–408. DOI: 10.1002/ijc.2910500314.

[138] Sachi Hisanaga et al. "Peritumoral fat content correlates with histological prognostic factors in breast carcinoma: A study using iterative decomposition of water and fat with echo asymmetry and least-squares estimation (ideal)". In: *Magnetic Resonance in Medical Sciences* 20.1 (Mar. 2021), pp. 28–33. DOI: 10.2463/mrms.mp.2019-0201.

[139] Tabea Borde et al. "Assessing breast density using the chemical-shift encoding-based proton density fat fraction in 3-T MRI". In: *European Radiology* 33 (Dec. 2022), pp. 3810–3818. DOI: 10.1007/s00330-022-09341-x.

[140] Melanie Freed et al. "Evaluation of breast lipid composition in patients with benign tissue and cancer by using multiple gradient-echo MR imaging". In: *Radiology* 281.1 (Oct. 2016), pp. 43–53. DOI: 10.1148/radiol.2016151959.

[141] Jimin Ren et al. "Composition of adipose tissue and marrow fat in humans by $^{1}$H NMR at 7 Tesla". In: *Journal of Lipid Research* 49.9 (Sept. 2008), pp. 2055–2062. DOI: 10.1194/jlr.D800010-JLR200.

[142] Gavin Hamilton et al. "*In vivo* characterization of the liver fat $^{1}$H MR spectrum". In: *NMR in biomedicine* 24.7 (Aug. 2011), pp. 784–790. DOI: 10.1002/NBM.1622.

[143] Alexandre Triay Bagur et al. "PDFF and R2* Reconstruction Error Mapping using Cramér-Rao Lower Bounds for Quality Assessment In-Vivo". In: *Proceedings of the International Society for Magnetic Resonance in Medicine* 31, 1810 (May 2023). DOI: 10.58530/2023/1810.

[144] Nobuyuki Otsu. "A Threshold Selection Method from Gray-Level Histograms". In: *IEEE Transactions on Systems, Man, and Cybernetics* 9.1 (Jan. 1979), pp. 62–66. DOI: 10.1109/TSMC.1979.4310076.

[145] Isobel Gordon et al. "Quantitative calculation of breast density with proton density fat fraction enables distinction between latest subjective BI-RADS categories". In: *Proceedings of the International Soceity for Magnetic Resonance in Medicine* 31, 2732 (May 2023). DOI: 10.58530/2023/2732.

[146] George P. Ralli, Gerard R. Ridgway, and Sir Michael Brady. "Segmentation of the Biliary Tree from MRCP Images via the Monogenic Signal". In: *Medical Image Understanding and Analysis. Communications in Computer and Information Science*. Vol. 1248. Springer, July 2020, pp. 105–117. DOI: 10.1007/978-3-030-52791-4_9.

[147] Michael S. Middleton. *The ability to predict histological response from MR parameters: lessons learned from phase 2 trials*. July 2019. URL: https://paris-mash.org/assets/data/2019/NASH-2019-MIDDLETON-M.pdf.

[148] Paul A. Yushkevich et al. "User-Guided 3D Active Contour Segmentation of Anatomical Structures: Significantly Improved Efficiency and Reliability". In: *Neuroimage* 31.3 (2006), pp. 1116–1128. DOI: 10.1016/j.neuroimage.2006.01.015. URL: www.itksnap.org.

[149] Dong Wei et al. "Three-Dimensional Whole Breast Segmentation in Sagittal and Axial Breast MRI with Dense Depth Field Modeling and Localized Self-Adaptation for Chest-Wall Line Detection". In: *IEEE Transactions on Biomedical Engineering* 66.6 (June 2019), pp. 1567–1579. DOI: 10.1109/TBME.2018.2875955.

[150] Ruvini Navaratna et al. "Temperature-Corrected Proton Density Fat Fraction Estimation using Chemical Shift-Encoded MRI in Phantoms". In: *Magnetic Resonance in Medicine* 86.1 (July 2021), pp. 69–81. DOI: 10.1002/mrm.28669.

[151] Mark Bydder et al. "Constraints in estimating the proton density fat fraction". In: *Magnetic Resonance Imaging* 66 (Feb. 2020), pp. 1–8. DOI: 10.1016/J.MRI.2019.11.009.

[152] Mark Bydder et al. "Constraining the initial phase in water-fat Separation". In: *Magnetic Resonance Imaging* 29.2 (Feb. 2011), pp. 216–221. DOI: 10.1016/J.MRI.2010.08.011.

[153] Huanzhou Yu et al. "Field map estimation with a region growing scheme for iterative 3-point water-fat decomposition". In: *Magnetic Resonance in Medicine* 54.4 (Oct. 2005), pp. 1032–1039. DOI: 10.1002/mrm.20654.

[154] Chloe Hutton et al. "Validation of a standardized MRI method for liver fat and T2* quantification". In: *PLoS ONE* 13.9, e0204175 (Sept. 2018). DOI: 10.1371/journal.pone.0204175.

[155] Diego Hernando et al. "Robust water/fat separation in the presence of large field inhomogeneities using a graph cut algorithm". In: *Magnetic Resonance in Medicine* 63.1 (Jan. 2010), pp. 79–90. DOI: 10.1002/mrm.22177.

[156] Huanzhou Yu et al. "Combination of complex-based and magnitude-based multiecho water-fat separation for accurate quantification of fat-fraction". In: *Magnetic Resonance in Medicine* 66.1 (July 2011), pp. 199–206. DOI: 10.1002/mrm.22840.

[157] Diego Hernando, Zhi Pei Liang, and Peter Kellman. "Chemical shift-based water/fat separation: A comparison of signal models". In: *Magnetic Resonance in Medicine* 64.3 (Sept. 2010), pp. 811–822. DOI: 10.1002/MRM.22455.

[158] William M. Haufe et al. "Accuracy of PDFF estimation by magnitude-based and complex-based MRI in children with magnetic resonance spectroscopy as a reference". In: *Journal of Magnetic Resonance Imaging* 46.6 (Dec. 2017), pp. 1641–1647. DOI: 10.1002/JMRI.25699.

[159] Jung Kyu Ryu et al. "Estimation of $T_2^*$ Relaxation Times for the Glandular Tissue and Fat of Breast at 3T MRI System ". In: *Journal of the Korean Society of Magnetic Resonance in Medicine* 18.1 (Mar. 2014), pp. 1–6. DOI: 10.13104/jksmrm.2014.18.1.1.

[160] GE Healthcare. *IDEAL IQ Body MRI Application*. Accessed: 2025-09-06. URL: https://www.gehealthcare.com/products/magnetic-resonance-imaging/mr-applications/ideal-iq-body.

[161] GE Healthcare. *IDEAL IQ 510(k) Premarket Notification Submission*. Accessed: 2025-09-06. Mar. 2011. URL: https://www.accessdata.fda.gov/cdrh_docs/pdf10/K103411.pdf.

[162] Yuan Tian et al. "Hepatic MR imaging using IDEAL-IQ sequence: Will Gd-EOB-DTPA interfere with reproductivity of fat fraction quantification?" In: *World Journal of Clinical Cases* 11.25 (Sept. 2023), pp. 5887–5896. DOI: 10.12998/WJCC.V11.I25.5887.

[163] Elin Lundström et al. "Magnetic Resonance Imaging Cooling-Reheating Protocol Indicates Decreased Fat Fraction via Lipid Consumption in Suspected Brown Adipose Tissue". In: *PLoS ONE* 10.4, e0126705 (Apr. 2015), p. 126705. DOI: 10.1371/journal.pone.0126705.

[164] Sebastian Bidhult et al. "Validation of a new T2* algorithm and its uncertainty value for cardiac and liver iron load determination from MRI magnitude images". In: *Magnetic Resonance in Medicine* 75.4 (Apr. 2016), pp. 1717–1729. DOI: 10.1002/MRM.25767.

[165] Arturo Cárdenas-Blanco et al. "Noise in magnitude magnetic resonance images". In: *Concepts in Magnetic Resonance: Part A* 32A.6 (Nov. 2008), pp. 409–416. DOI: 10.1002/CMR.A.20124.

[166] Debra E. Horng et al. "Comparison of $R_2^*$ correction methods for accurate fat quantification in fatty liver". In: *Journal of Magnetic Resonance Imaging* 37.2 (Feb. 2013), pp. 414–422. DOI: 10.1002/jmri.23835.

[167] Chen Cui et al. "Fat water decomposition using GlObally Optimal Surface Estimation (GOOSE) algorithm". In: *Magnetic Resonance in Medicine* 73.3 (Mar. 2015), pp. 1289–1299. DOI: 10.1002/MRM.25193.

[168] Isobel Gordon et al. "Assessment of Breast Density with Hybrid-Based Proton Density Fat Fraction Calculation Enables Distinction between BI-RADS Categories". In: *British and Irish Chapter of the International Society for Magnetic Resonance in Medicine Postgraduate Symposium 2023* (Apr. 2023).

[169] Isobel Gordon et al. "In-vitro evaluation of the performance of PDFF against classification-based algorithms in calculation of breast density". In: *Proceedings of the International Soceity for Magnetic Resonance in Medicine* 32, 0845 (May 2024). DOI: 10.58530/2024/0845.

[170] Valerie A. McCormack and Isabel Dos Santos Silva. "Breast density and parenchymal patterns as markers of breast cancer risk: a meta-analysis". In: *Cancer epidemiology, biomarkers & prevention : a publication of the American Association for Cancer Research, cosponsored by the American Society of Preventive Oncology* 15.6 (June 2006), pp. 1159–1169. DOI: 10.1158/1055-9965.EPI-06-0034.

[171] A. Redondo et al. "Inter- and intraradiologist variability in the BI-RADS assessment and breast density categories for screening mammograms". In: *British Journal of Radiology* 85.1019 (Nov. 2012), pp. 1465–1470. DOI: 10.1259/BJR/21256379.

[172] Wendie A. Berg et al. "Breast imaging reporting and data system: Inter- and intraobserver variability in feature analysis and final assessment". In: *American Journal of Roentgenology* 174.6 (Nov. 2012), pp. 1769–1777. DOI: 10.2214/ajr.174.6.1741769.

[173] S. Ciatto et al. "Categorizing breast mammographic density: intra- and interobserver reproducibility of BI-RADS density categories". In: *The Breast* 14.4 (Aug. 2005), pp. 269–275. DOI: 10.1016/J.BREAST.2004.12.004.

[174] Karla Kerlikowske et al. "Variability and Accuracy in Mammographic Interpretation Using the American College of Radiology Breast Imaging Reporting and Data System". In: *JNCI: Journal of the National Cancer Institute* 90.23 (Dec. 1998), pp. 1801–1809. DOI: 10.1093/JNCI/90.23.1801.

[175] Leah H. Portnow et al. "Persistent inter-observer variability of breast density assessment using BI-RADS® 5th edition guidelines". In: *Clinical Imaging* 83 (Mar. 2022), pp. 21–27. DOI: 10.1016/J.CLINIMAG.2021.11.034.

[176] Wijdan Alomaim et al. "Variability of Breast Density Classification Between US and UK Radiologists". In: *Journal of Medical Imaging and Radiation Sciences* 50.1 (Mar. 2019), pp. 53–61. DOI: 10.1016/J.JMIR.2018.11.002.

[177] S. Reed et al. "Robustness of interactive intensity thresholding based breast density assessment in MR-mammography". In: *Proceedings of SPIE Medical Imaging*. Vol. 7624. SPIE, Mar. 2010. DOI: 10.1117/12.844337.

[178] Gokhan Ertas, S. Reed, and Martin O Leach. "Comparison of Breast Density Assessments Based on Interactive Thresholding and Automated Fast Fuzzy c-means Clustering in Three-Dimensional MR Imaging". In: *IFMBE Proceedings*. Vol. 25. 4. Springer, Berlin, Heidelberg, Sept. 2009, pp. 1893–1896. DOI: 10.1007/978-3-642-03882-2_503.

[179] Michael Khazen et al. "A Pilot Study of Compositional Analysis of the Breast and Estimation of Breast Mammographic Density Using Three-Dimensional $T_1$-Weighted Magnetic Resonance Imaging". In: *Cancer Epidemiology, Biomarkers & Prevention* 17.9 (Sept. 2008), pp. 2268–2274. DOI: 10.1158/1055-9965.EPI-07-2547.

[180] Alberto Tagliafico et al. "Breast Density Assessment Using a 3T MRI System: Comparison among Different Sequences". In: *PLoS ONE* 9, e99027 (6 June 2014). DOI: 10.1371/JOURNAL.PONE.0099027.

[181] Simon J. Doran et al. "Breast MRI segmentation for density estimation: Do different methods give the same results and how much do differences matter?" In: *Medical Physics* 44.9 (Sept. 2017), pp. 4573–4592. DOI: 10.1002/mp.12320.

[182] C. Klifa et al. "Quantification of breast tissue index from MR data using fuzzy clustering". In: *Annual International Conference of the IEEE Engineering in Medicine and Biology*. Vol. 26. 2004, pp. 1667–1670. DOI: 10.1109/IEMBS.2004.1403503.

[183] Huanjun Ding et al. "Breast density quantification using magnetic resonance imaging (MRI) with bias field correction: A postmortem study". In: *Medical Physics* 40 (12 2013). DOI: 10.1118/1.4831967,.

[184] M. N. Ahmed et al. "A modified fuzzy C-means algorithm for bias field estimation and segmentation of MRI data". In: *IEEE Transactions on Medical Imaging* 21.3 (Mar. 2002), pp. 193–199. DOI: 10.1109/42.996338.

[185] D. J. Kroon. *Bias Field Corrected Fuzzy C-Means*. URL: https://www.mathworks.com/matlabcentral/fileexchange/25712-bias-field-corrected-fuzzy-c-means.

[186] Nicholas J. Tustison and James Gee. "N4ITK: Nick's N3 ITK Implementation For MRI Bias Field Correction". In: *The Insight Journal* (Dec. 2010). DOI: 10.54294/JCULXW.

[187] Rik. *Bland-Altman*. Accessed: 2026-01-22. URL: https://github.com/thrynae/BlandAltmanPlot.

[188] Tess V. Clendenen et al. "Comparison of 3-point dixon imaging and fuzzy C-means clustering methods for breast density measurement". In: *Journal of Magnetic Resonance Imaging* 38.2 (Aug. 2013), pp. 474–481. DOI: 10.1002/jmri.24002.

[189] Andreas Fieselmann et al. "Volumetric breast density measurement for personalized screening: accuracy, reproducibility, consistency, and agreement with visual assessment". In: *Journal of Medical Imaging* 6.3 (Feb. 2019), p. 031406. DOI: 10.1117/1.JMI.6.3.031406.

[190] Ralph Highnam et al. "Robust Breast Composition Measurement - Volpara™". In: *Digital Mammography, Lecture Notes in Computer Science*. Vol. 6136. Springer, Berlin, Heidelberg, 2010, pp. 342–349. DOI: 10.1007/978-3-642-13666-5_46.

[191] Susan P. Weinstein et al. "ACR Appropriateness Criteria® Supplemental Breast Cancer Screening Based on Breast Density". In: *Journal of the American College of Radiology* 18.11 (Nov. 2021), S456–S473. DOI: 10.1016/J.JACR.2021.09.002.

[192] Ritse M. Mann et al. "Breast cancer screening in women with extremely dense breasts recommendations of the European Society of Breast Imaging (EUSOBI)". In: *European Radiology* 32.6 (June 2022), pp. 4036–4045. DOI: 10.1007/s00330-022-08617-6.

[193] Lisa V. Paulis et al. "ACR Appropriateness Criteria® Supplemental Breast Cancer Screening Based on Breast Density: 2024 Update". In: *Journal of the American College of Radiology* 22.5 (May 2025), S405–S423. DOI: 10.1016/J.JACR.2025.02.023.

[194] Irmgard Schiller-Fruehwirth et al. "The Long-Term Effectiveness and Cost Effectiveness of Organized versus Opportunistic Screening for Breast Cancer in Austria". In: *Value in Health* 20.8 (Sept. 2017), pp. 1048–1057. DOI: 10.1016/J.JVAL.2017.04.009.

[195] DenseBreast-info. *Comparative Analysis of National Breast Screening Guidelines in Europe*. Oct. 2024. URL: https://densebreast-info.org/wp-content/uploads/2024/12/Table-Europe-Guidelines122724.pdf.

[196] Janice Hopkins Tanne. "US women must be told breast density after mammogram, says FDA". In: *BMJ* 386, q2045 (Sept. 2024). DOI: 10.1136/BMJ.Q2045.

[197] D. Franz et al. "Association of proton density fat fraction in adipose tissue with imaging-based and anthropometric obesity markers in adults". In: *International Journal of Obesity* 42 (Feb. 2018), pp. 175–182. DOI: 10.1038/ijo.2017.194.

[198] Yongbin Yang et al. "Chemical-shift water-fat MRI of white adipose depots: inability to resolve cell size differences". In: *International journal of body composition research* 11.1 (May 2013), pp. 9–16.

[199] Satyam Ghodasara. *3D Gray Level Co-Occurence Matrix*. Accessed: 2025-01-25. URL: https://github.com/sxg/3D-Gray-Level-Co-Occurrence-Matrix.

[200] Robert M. Haralick. "Statistical and structural approaches to texture". In: *Proceedings of the IEEE* 67.5 (1979), pp. 786–804. DOI: 10.1109/PROC.1979.11328.

[201] Brian L. Sprague et al. "Prevalence of Mammographically Dense Breasts in the United States". In: *Journal of the National Cancer Institute* 106.10, dju255 (Oct. 2014). DOI: 10.1093/JNCI/DJU255.

[202] C. J. D'Orsi, E. B. Mendelson, and D. M. Ikeda et al. *ACR BI-RADS® Atlas, Breast Imaging Reporting and Data System.* 2003.

[203] Aysegul Akdogan Gemici et al. "Comparison of breast density assessments according to BI-RADS 4th and 5th editions and experience level". In: *Acta Radiologica Open* 9.7, 205846012093738 (July 2020). DOI: 10.1177/2058460120937381.

[204] Jie Ding et al. "Reproducible automated breast density measure with no ionizing radiation using fat-water decomposition MRI". In: *Journal of Magnetic Resonance Imaging* 48.4 (Oct. 2018), pp. 971–981. DOI: 10.1002/jmri.26041.

[205] Rosie Goodburn et al. "An automated approach for the optimised estimation of breast density with Dixon methods". In: *The British Journal of Radiology* 93.1106, 20190639 (Feb. 2020). DOI: 10.1259/BJR.20190639.

[206] Isobel Gordon et al. "Non-Invasive Assessment of Breast Adipose Tissue with Quantitative MRI May Enable Detection of Cancer and Contribute to the Assessment of Cancer Risk". In: *Meeting Abstracts from the British Society of Breast Radiology Annual Scientific Meeting 2022, Breast Cancer Research* 25.S1(O4) (June 2023). DOI: 10.1186/s13058-023-01659-8.

[207] Neil M. Iyengar et al. "Menopause is a Determinant of Breast Adipose Inflammation". In: *Cancer Prevention Research* 8.5 (May 2015), pp. 349–358. DOI: 10.1158/1940-6207.CAPR-14-0243.

[208] Gerald V. Denis and Martin S. Obin. "'Metabolically healthy obesity': Origins and implications". In: *Molecular Aspects of Medicine* 34.1 (Feb. 2013), p. 59. DOI: 10.1016/J.MAM.2012.10.004.

[209] Jodi M. Carter et al. "Macrophagic "Crown-like Structures" Are Associated with an Increased Risk of Breast Cancer in Benign Breast Disease". In: *Cancer Prevention Research* 11.2 (Feb. 2018), pp. 113–119. DOI: 10.1158/1940-6207.CAPR-17-0245.

[210] Naiara Cubelos-Fernández et al. "Burden of postmenopausal breast cancer attributable to excess body weight: comparative study of body mass index and CUN-BAE in MCC-Spain study". In: *Journal of Epidemiology and Community Health* 79 (Dec. 2024), pp. 64–71. DOI: 10.1136/jech-2023-220706.

[211] Julie Anne Côté et al. "Computed tomography-measured adipose tissue attenuation and area both predict adipocyte size and cardiometabolic risk in women". In: *Adipocyte* 5.1 (Dec. 2015), pp. 35–42. DOI: 10.1080/21623945.2015.1106057.

[212] Klara J. Rosenquist et al. "Fat Quality and Incident Cardiovascular Disease, All-Cause Mortality, and Cancer Mortality". In: *The Journal of Clinical Endocrinology and Metabolism* 100.1 (Jan. 2015), pp. 227–234. DOI: 10.1210/JC.2013-4296.

[213] Dominik Weidlich et al. "Lipid droplet–size mapping in human adipose tissue using a clinical 3T system". In: *Magnetic Resonance in Medicine* 86.3 (Sept. 2021), pp. 1256–1270. DOI: 10.1002/MRM.28755.

[214] Julius Honecker et al. "Transcriptome and fatty-acid signatures of adipocyte hypertrophy and its non-invasive MR-based characterization in human adipose tissue". In: *EBioMedicine* 79, 104020 (2022). DOI: 10.1016/j.ebiom.2022.104020.

[215] Navin Michael et al. "Adipose Tissue Hydration as a Potential Non-invasive Marker for Adipose Tissue Hypertrophy". In: *Proceedings of the International Soceity for Magnetic Resonance in Medicine* 23, 0840 (2015).

[216] M. Digirolamo and J. L. Owens. "Water content of rat adipose tissue and isolated adipocytes in relation to cell size". In: *American Journal of Physiology - Legacy Content* 231.5 (1976), pp. 1568–1572. DOI: 10.1152/AJPLEGACY.1976.231.5.1568.

[217] Magdalena Pasarica et al. "Reduced Adipose Tissue Oxygenation in Human Obesity: Evidence for Rarefaction, Macrophage Chemotaxis, and Inflammation Without an Angiogenic Response". In: *Diabetes* 58.3 (Mar. 2009), pp. 718–725. DOI: 10.2337/DB08-1098.

[218] Emma Börgeson, Jeremie Boucher, and Carolina E. Hagberg. "Of mice and men: Pinpointing species differences in adipose tissue biology". In: *Frontiers in Cell and Developmental Biology* 10, 1003118 (Sept. 2022). DOI: 10.3389/FCELL.2022.1003118.

[219] Sam Virtue and Antonio Vidal-Puig. "Adipose tissue expandability, lipotoxicity and the Metabolic Syndrome — An allostatic perspective". In: *Biochimica et Biophysica Acta (BBA) - Molecular and Cell Biology of Lipids* 1801.3 (Mar. 2010), pp. 338–349. DOI: 10.1016/J.BBALIP.2009.12.006.

[220] Peter Arner and Mikael Rydén. "Human white adipose tissue: A highly dynamic metabolic organ". In: *Journal of Internal Medicine* 291.5 (May 2022), pp. 611–621. DOI: 10.1111/JOIM.13435.

[221] Carolina E. Hagberg et al. "Flow Cytometry of Mouse and Human Adipocytes for the Analysis of Browning and Cellular Heterogeneity". In: *Cell Reports* 24.10 (Sept. 2018), pp. 2746–2756. DOI: 10.1016/J.CELREP.2018.08.006.

[222] Suneeta Chaudhary et al. “Estimation of fatty acid composition in mammary adipose tissue using deep neural network with unsupervised training”. In: *Magnetic Resonance in Medicine* 93.5 (May 2025), pp. 2163–2175. DOI: 10.1002/MRM.30401.

[223] Mark Bydder et al. “Sources of Systematic Error in Proton Density Fat Fraction (PDFF) Quantification in the Liver Evaluated From Magnitude Images With Different Numbers of Echoes”. In: *NMR in Biomedicine* 31.1 (Jan. 2018), 10.1002/nbm.3843. DOI: 10.1002/NBM.3843.

[224] Henry H. Ong et al. “Fat-water MRI of a diet-induced obesity mouse model at 15.2T”. In: *Journal of Medical Imaging* 3.2, 026002 (May 2016). DOI: 10.1117/1.jmi.3.2.026002.

[225] Chongru Zhao et al. “Cancer-associated adipocytes: Emerging supporters in breast cancer”. In: *Journal of Experimental and Clinical Cancer Research* 39.1, 156 (Aug. 2020). DOI: 10.1186/s13046-020-01666-z.

[226] Su Myung Jung, Joan Sanchez-Gurmaches, and David A. Guertin. “Brown Adipose Tissue Development and Metabolism”. In: *Handbook of Experimental Pharmacology* 251 (2019), pp. 3–36. DOI: 10.1007/164_2018_168.

[227] Martin Paré et al. “Breast cancer mammospheres secrete Adrenomedullin to induce lipolysis and browning of adjacent adipocytes”. In: *BMC Cancer* 20, 784 (Aug. 2020). DOI: 10.1186/s12885-020-07273-7.

[228] Mariana Gantov et al. “Beige adipocytes contribute to breast cancer progression”. In: *Oncology Reports* 45.1 (Jan. 2021), pp. 317–328. DOI: 10.3892/or.2020.7826.

[229] Francesc Villarroya et al. “Brown adipose tissue as a secretory organ”. In: *Nature reviews. Endocrinology* 13 (Jan. 2017), pp. 26–35. DOI: 10.1038/NRENDO.2016.136.

[230] Daniela Franz et al. “Differentiating supraclavicular from gluteal adipose tissue based on simultaneous PDFF and $T_2^*$ mapping using a 20-echo gradient-echo acquisition”. In: *Journal of Magnetic Resonance Imaging* 50.2 (Aug. 2019), pp. 424–434. DOI: 10.1002/JMRI.26661.

[231] Houchun H. Hu et al. “Characterization of Human Brown Adipose Tissue by Chemical-Shift Water-Fat MRI”. In: *American Journal of Roentgenology* 200.1 (Jan. 2013), pp. 177–183. DOI: 10.2214/AJR.12.8996.

[232] Natsumi Hirano Tani et al. “Peritumoral Fat Content Identified Using Iterative Decomposition of Water and Fat with Echo Asymmetry and Least-squares Estimation (IDEAL) Correlates with Breast Cancer Prognosis”. In: *Magnetic Resonance in Medical Sciences* 24.1 (2025), pp. 112–121. DOI: 10.2463/mrms.mp.2023-0127.

[233] Isabelle Miran et al. “Adipose Tissue Properties in Tumor-Bearing Breasts”. In: *Frontiers in Oncology* 10 (Aug. 2020). DOI: 10.3389/fonc.2020.01506.

[234] Jessica L. Dobbs et al. “Confocal fluorescence microscopy to evaluate changes in adipocytes in the tumor microenvironment associated with invasive ductal carcinoma and ductal carcinoma in situ”. In: *International Journal of Cancer* 139.5 (Sept. 2016), pp. 1140–1149. DOI: 10.1002/ijc.30160.

[235] Edoardo Isnaldi et al. “Digital analysis of distant and cancer-associated mammary adipocytes”. In: *The Breast* 54 (Dec. 2020), pp. 179–186. DOI: 10.1016/J.BREAST.2020.10.004.

[236] Jeremy Williams et al. “Tumor cell-adipocyte gap junctions activate lipolysis and contribute to breast tumorigenesis”. In: *Nature Communications* 16, 7438 (Aug. 2025). DOI: 10.1038/s41467-025-62486-3.

[237] Aurelie D. Laidevant et al. “Compositional breast imaging using a dual-energy mammography protocol”. In: *Medical physics* 37.1 (Jan. 2010), pp. 164–174. DOI: 10.1118/1.3259715.

[238] Simone Mennella et al. “Magnetic resonance imaging of breast cancer: does the time interval between biopsy and MRI influence MRI-pathology discordance in lesion sizing?” In: *Acta Radiologica* 58.7 (July 2017), pp. 800–808. DOI: 10.1177/0284185116674498.

[239] Luca Nicosia et al. “Contrast-enhanced mammography BI-RADS: a case-based approach to radiology reporting”. In: *Insights into Imaging* 15, 37 (Feb. 2024). DOI: 10.1186/S13244-024-01612-Z.

[240] Jiaqing Hao et al. “Development of a humanized anti-FABP4 monoclonal antibody for potential treatment of breast cancer”. In: *Breast Cancer Research* 26, 119 (July 2024). DOI: 10.1186/S13058-024-01873-Y.

[241] Muwei Jiang et al. “CD36 as a double-edged sword in cancer”. In: *Immunology Letters* 265 (Feb. 2024), pp. 7–15. DOI: 10.1016/J.IMLET.2023.12.002.

[242] Ludivine Bochet et al. “Cancer-associated adipocytes promotes breast tumor radioresistance”. In: *Biochemical and Biophysical Research Communications* 411.1 (July 2011), pp. 102–106. DOI: 10.1016/J.BBRC.2011.06.101.

[243] Matías Ferrando et al. “Renal peritumoral adipose tissue undergoes a browning process and stimulates the expression of epithelial-mesenchymal transition markers in human renal cells”. In: *Scientific Reports* 12, 8687 (May 2022). DOI: 10.1038/s41598-022-12746-9.

[244] Qiuling Cai et al. “Cancer-associated adipocytes in the ovarian cancer microenvironment”. In: *American Journal of Cancer Research* 14.7 (July 2024), pp. 3259–3279. DOI: 10.62347/XZRI9189.

[245] Isobel Gordon et al. “The “MR Bra”: Development of a support device for supine breast imaging with commercially available flexible body coils”. In: *Proceedings of the International Soceity for Magnetic Resonance in Medicine* 32, 4766 (May 2024). DOI: 10.58530/2024/4766.

[246] Ritse M. Mann, Nariya Cho, and Linda Moy. “Breast MRI: State of the art”. In: *Radiology* 292.3 (Sept. 2019), pp. 520–536. DOI: 10.1148/radiol.2019182947.

[247] Peter Siegler et al. “Supine breast MRI”. In: *Journal of Magnetic Resonance Imaging* 34 (5 Nov. 2011), pp. 1212–1217. DOI: 10.1002/jmri.22605.

[248] Block Imaging. *MRI Coil Cost Price Guide*. Accessed: 2026-01-22. URL: https://www.blockimaging.com/blog/mri-coil-price-cost-guide.

[249] Ga Young Yoon et al. “Feasibility of supine MRI (Magnetic Resonance Imaging)-navigated ultrasound in breast cancer patients”. In: *Asian Journal of Surgery* 43.8 (Aug. 2020), pp. 787–794. DOI: 10.1016/j.asjsur.2019.09.007.

[250] Tanja Alderliesten et al. "On the feasibility of MRI-guided navigation to demarcate breast cancer for breast-conserving surgery". In: *Medical Physics* 37 (6Part1 June 2010), pp. 2617–2626. DOI: 10.1118/1.3429048.

[251] Luca Alessandro Carbonaro et al. "Contrast enhanced breast MRI: Spatial displacement from prone to supine patient's position. Preliminary results". In: *European Journal of Radiology* 81.6, e771–e774 (June 2012). DOI: 10.1016/j.ejrad.2012.02.013.

[252] Lena Nohava et al. "Supine breast MRI using a wearable coil facilitates the translation of MR imaging findings to clinical practice". In: *European Journal of Radiology* 184, 111974 (Mar. 2025). DOI: 10.1016/J.EJRAD.2025.111974.

[253] Eren D. Yeh et al. "Positioning in Breast MR Imaging to Optimize Image Quality". In: *Radiographics* 34.1 (Jan. 2014), E1–E17. DOI: 10.1148/rg.341125193.

[254] Camille Meullenet et al. "Evaluation of Image Quality of Motion-Corrected Supine Breast MRI". In: *Current Problems in Diagnostic Radiology* 52.6 (Dec. 2023), pp. 493–500. DOI: 10.1067/J.CPRADIOL.2023.05.013.

[255] Alfonso Fausto et al. "Feasibility, Image Quality and Clinical Evaluation of Contrast-Enhanced Breast MRI Performed in a Supine Position Compared to the Standard Prone Position". In: *Cancers* 12.9, 2364 (Aug. 2020). DOI: 10.3390/cancers12092364.

[256] Michael Obermann et al. "Panoramic Magnetic Resonance Imaging of the Breast with a Wearable Coil Vest". In: *Investigative Radiology* 58.11 (Nov. 2023), pp. 799–810. DOI: 10.1097/RLI.0000000000000991.

[257] Jana Vincent et al. "Ultra-Flexible, High-Resolution, 60-Channel RF Coil for Supine Breast Imaging". In: *Proceedings of the International Society for Magnetic Resonance in Medicine* 29, 1591 (Apr. 2021). URL: https://archive.ismrm.org/2021/1591.html.

[258] Autodesk. *Autodesk Inventor: Mechanical deisgn software for ambitious ideas.* Accessed: 2025-07-23. URL: https://www.autodesk.com/uk/products/inventor/overview.

[259] GE Healthcare. *AIR Technology Coils for Magnetic Resonance Imaging.* Accessed: 2025-07-24. URL: https://www.gehealthcare.co.uk/products/magnetic-resonance-imaging/air-technology-coils.

[260] Sheye O. Aliu et al. "Repeatability of Quantitative MRI Measurements in Normal Breast Tissue". In: *Translational Oncology* 7.1 (Feb. 2014), pp. 130–137. DOI: 10.1593/TLO.13841.

[261] Maeve Mullooly et al. "Temporal changes in mammographic breast density and breast cancer risk among women with benign breast disease". In: *Breast Cancer Research* 26.1, 52 (Mar. 2024). DOI: 0.1186/s13058-024-01764-2.

[262] Jeon-Hor Chen et al. "Reduction of Breast Density Following Tamoxifen Treatment Evaluated by 3-D MRI: Preliminary Study". In: *Magnetic Resonance Imaging* 29.1 (Jan. 2011), pp. 91–98. DOI: 10.1016/J.MRI.2010.07.009.

[263] Jack Cuzick et al. "Tamoxifen-Induced Reduction in Mammographic Density and Breast Cancer Risk Reduction: A Nested Case–Control Study". In: *Journal of the National Cancer Institute* 103.9 (May 2011), pp. 744–752. DOI: 10.1093/JNCI/DJR079.

[264] Natasja N. Y. Janssen et al. "Supine Breast MRI Using Respiratory Triggering". In: *Academic Radiology* 24.7 (July 2017), pp. 818–825. DOI: 10.1016/j.acra.2017.01.003.

[265] Amy Herlihy et al. "Prone and Supine Quantitative MRI Measurement of Breast Density: Preliminary Results from Ongoing IMOGEN Study". In: *Meeting Abstracts from the British Society of Breast Radiology Annual Scientific Meeting 2022, Breast Cancer Research* 25.S1(P6) (June 2023). DOI: 10.1186/s13058-023-01659-8.

[266] Katie Albus. *MRI Exam-Specific Parameters: Breast*. Accessed: 2025-07-28. Mar. 2025. URL: https://accreditationsupport.acr.org/support/solutions/articles/11000114407-mri-exam-specific-parameters-breast-revised-3-19-2025.

[267] UK Biobank. *Health research data for the world*. URL: https://www.ukbiobank.ac.uk/.

[268] Yifei Jin, Markus Henningsson, and Carolina Fernandes. "Towards Accurate, Reproducible PDFF Quantification Using a 3D Dual-Echo Dixon Body Composition Sequence: Validation in Phantoms". In: *British and Irish Chapter of the International Society for Magnetic Resonance in Medicine Annual Meeting 2024* (2024).

[269] Yifei Jin, Markus Henningsson, and Carolina Fernandes. "Towards Accurate, Reproducible PDFF Quantification in the Liver Using a 3D Dual-Echo Dixon Body Composition Sequence". In: *British and Irish Chapter of the International Society for Magnetic Resonance in Medicine Annual Meeting 2024* (2024).

[270] Yifei Jin et al. "A Dixon MAGO method for Accurate and Reproducible Fat Quantification Using a 3D Dual-Echo Dixon Sequence". In: *British and Irish Chapter of the International Society for Magnetic Resonance in Medicine Postgraduate Symposium 2025* (2025).

[271] Wojciech Danysz et al. "Browning of white adipose tissue induced by the ß3 agonist CL-316,243 after local and systemic treatment - PK-PD relationship". In: *Biochimica et Biophysica Acta (BBA) - Molecular Basis of Disease* 1864.9 (Sept. 2018), pp. 2972–2982. DOI: 10.1016/J.BBADIS.2018.06.007.

[272] Maggie Chung et al. "Deep Learning to Simulate Contrast-enhanced Breast MRI of Invasive Breast Cancer". In: *Radiology* 306.3 (Mar. 2023). DOI: 10.1148/RADIOL.213199.

[273] Perspectum Ltd. *LiverMultiScan*. URL: https://www.perspectum.com/our-products/livermultiscan.

[274] Nicholas J. Schneiders. "Solutions of two paramagnetic ions for use in nuclear magnetic resonance phantoms". In: *Medical Physics* 15.1 (1988), pp. 12–16. DOI: 10.1118/1.596155.

[275] P. S. Tofts, B. Shuter, and J. M. Pope. "Ni-DTPA doped agarose gel – A phantom material for Gd-DTPA enhancement measurements". In: *Magnetic Resonance Imaging* 11.1 (1993), pp. 125–133. DOI: 10.1016/0730-725X(93)90420-I.

[276] Paul Tofts. "Chapter 3. QA: Quality Assurance, Accuracy, Precision and Phantoms". In: *Quantitative MRI of the Brain: Measuring Changes Caused by Disease* (July 2004), pp. 55–81. DOI: 10.1002/0470869526.ch3.

[277] A. D. Elster. *Relaxation time, T1, T2 - Questions and Answers in MRI*. Accessed: 2026-01-22. URL: https://mri-q.com/why-is-t1--t2.html.

[278] J. Sijbers and A. J. Den Dekker. "Maximum Likelihood Estimation of Signal Amplitude and Noise Variance from MR Data". In: *Magnetic Resonance in Medicine* 51.3 (Mar. 2004), pp. 586–594. DOI: 10.1002/MRM.10728.

[279] Peter Kellman, Andrew E. Arai, and Hui Xue. "T1 and extracellular volume mapping in the heart: Estimation of error maps and the influence of noise on precision". In: *Journal of Cardiovascular Magnetic Resonance* 15.1, 56 (Jan. 2013). DOI: 10.1186/1532-429X-15-56.